Universidad de Huelva

Departamento de Ciencias Integradas

Estudios de coexistencia de forma nuclear y su relación con las transiciones de fase cuánticas

Memoria para optar al grado de doctora
presentada por:

Esperanza Maya Barbecho

Fecha de lectura: 6 de mayo de 2026

Bajo la dirección del doctor:

José Enrique García Ramos

Huelva, 2026

Doctorado en Ciencia y Tecnología Industrial y Ambiental

Tesis doctoral

Estudios de coexistencia de forma nuclear y su relación con las transiciones de fase cuánticas

Facultad de Ciencias Experimentales

Curso 2025/2026

Autora: Esperanza Maya Barbecho
Director: José Enrique García Ramos

Doctorado en Ciencia y Tecnología Industrial y Ambiental

PhD Thesis

STUDIES OF NUCLEAR SHAPE COEXISTENCE AND ITS RELATIONSHIP WITH QUANTUM PHASE TRANSITIONS

Facultad de Ciencias Experimentales

Curso 2025/2026

Author: Esperanza Maya Barbecho
Director: José Enrique García Ramos

To the people who came before,
to the books that led us here,
to the chances we take,
to the dreams we chase.

...
A mi abuela Victoria.

Agradecimientos

Sin lugar a dudas, estas son las líneas que mas trabajo me ha costado escribir de esta tesis, y es que condensar todo el agradecimiento que siento a todas las personas que me han acompañado en este proceso en unas simples líneas me parece una tarea casi imposible. Pero por algún sitio hay que empezar.

En primer lugar me gustaría agradecer a mi director de tesis José Enrique, ya que es por él que esta experiencia me ha resultado tan grata. Dudo que ninguna otra persona hubiera podido hacer un mejor trabajo a la hora de orientarme, ayudarme cuando nada parecía cuadrar y redirigirme cuando en mi cabezonería insistía en coger el camino largo (y en muchas ocasiones desordenado). Gracias además por encontrar siempre una forma de que no me haya faltado financiación en todos estos años, sé que no siempre ha sido tarea sencilla.

No quiero tampoco dejar de agradecer a todos mis compañeros de Departamento, por haberme hecho sentir como una más desde el primer momento y hacer de mis horas un tiempo mucho mas agradable. Disculpad que no ponga los nombres de todos, pero soy consciente de que si lo hiciera se me olvidaría nombrar a alguno. Aún así Pablo, mereces un lugar especial, por todas nuestras discusiones sobre la física de esta tesis (y la que no aparece aquí), en un abrir y cerrar de ojos serás tú el que esté escribiendo sus propios agradecimientos. Has sido un compañero de tesis inigualable. Y por supuesto Juan, tú que has estado conmigo desde que entramos en la carrera, gracias por todo, sobre todo por haberme sacado más de una sonrisa cuando menos lo pensaba, has sido un verdadero amigo para mí.

También quiero agradecer el apoyo de mis padres. Sé que no ha sido fácil. Gracias. Por aguantarme todo este tiempo, por hacer que todo haya sido mas fácil, posiblemente sin vosotros este trabajo no existiría.

Finalmente, Juanjo, no son tus palabras las que están escritas aquí, pero sí eres el que ha escuchado cada una de las mías. Tú mas que nadie has estado ahí en cada agobio y en cada problema. Espero tener toda una vida por delante en la que me sienta tan agradecida de tenerte a mi lado como me he sentido todos estos años.

Abstract

This thesis approaches the study of shape coexistence, the onset of deformation, and their connection with quantum phase transitions (QPTs) in medium-mass nuclei around the $Z \approx 40$ region, based on algebraic models, as the IBM and its extensions with configuration mixing (IBM-CM) together with the intrinsic frame description that the Interacting Boson-Fermion Model with configuration mixing (IBFM-CM) provides. The main objective is to provide a consistent interpretation of the structural changes observed experimentally in this mass region.

After introducing the basic concepts of nuclear structure, from mean-field and shell-model approaches to collective and algebraic descriptions in which the models that will be used are based, the IBM and IBFM formalisms are presented in detail. Their algebraic structure, dynamical symmetries, transition operators, and geometric interpretation are discussed, with particular attention paid to the configuration mixing scheme used to describe shape coexistence. A general intrinsic-frame formalism for the IBFM-CM is also developed, applicable to both single- and multiple-j shells and to axial and triaxial shapes, representing one of the main contributions of this thesis.

The even-even isotopic chains of Sr, Mo, and Ru are analyzed within the IBM-CM framework, where the Hamiltonian parameters are obtained from the available experimental excitation energies and absolute B(E2) transition rates, reproducing the evolution of such energy spectra and B(E2) transition rates, together with moments of inertia, nuclear radii, isotopic shifts, and two-neutron separation energies, showing that in Sr isotopes, a clear crossing between regular and intruder configurations occurs at neutron number $N = 60$, marking the onset of deformation. These features are also interpreted as signatures of a Type II QPT driven by configuration crossing. In Mo isotopes, shape coexistence is shown to remain relevant, but showing a smoother systematics and placing Mo at the boundary of the coexistence region. In contrast, Ru isotopes show a gradual evolution, with intruder configurations at higher excitation energies and a second order Type I QPT associated with a single configuration.

The study is extended to odd-even nuclei through an intrinsic-frame analysis of both an schematic and a more realistic case centered in Nb isotopes within the IBFM-CM. In the latter, crossing between regular and intruder configurations is found at $N = 60$ for both positive and negative-parity states, leading to a Type II QPT in the ground state, and showing that the presence of the odd proton enhances the abruptness of the transition and plays a role in the development of triaxial shapes for positive-parity states.

In conclusion, this thesis shows that configuration mixing within algebraic models offers a framework for describing shape coexistence, the onset of deformation, and QPTs in nuclei around $Z \approx 40$. The combined analysis of even-even and odd-even isotopes also provides

a consistent picture of the structural evolution and clarifies the origin of some values for the experimental data in this region.

Resumen

Esta tesis aborda el estudio de fenómenos fisicos como la coexistencia de forma, el origen de la deformación nuclear y su relación con las transiciones de fase cuánticas (QPTs por sus siglas en inglés) en núcleos situados en la región en torno a $Z \approx 40$. Todo esto se realiza mediante modelos algebraicos como el Modelo de Bosones en Interacción (IBM) y su extensión considerando mezcla de configuraciones (IBM-CM), junto con la descripción en el sistema intrínseco que proporciona el Modelo de Bosón-Fermión en Interacción, añadiendo mezcla de configuraciones (IBFM-CM). El objetivo principal es explicar de una forma coherente con estos modelos los cambios estructurales observados experimentalmente en esta región.

Tras introducir los conceptos básicos de estructura nuclear, como son el modelo de capas, el modelo colectivo y los modelos algebraicos, que además son la base de los modelos empleados, se presentan en detalle los formalismos del IBM-CM y del IBFM-CM. Para ello se hace énfasis en su estructura algebraica, las simetrías dinámicas, los operadores y su interpretación geométrica, prestando especial atención al esquema de mezcla de configuraciones utilizado para describir la coexistencia de formas. Asimismo, se desarrolla un formalismo general en el sistema intrínseco del IBFM-CM, aplicable tanto a capas de una sola j como de múltiples j, y no necesariamente restringidos a simetría axial, lo cual es una de las principales aportaciones originales de esta tesis.

Se analizan además los isótopos par-par de Sr, Mo y Ru dentro del marco del IBM-CM, donde los parámetros del Hamiltoniano se obtienen a partir de las energías de excitación experimentales disponibles y de las probabilidades absolutas de transición B(E2). Reproduciendo así la evolución de los espectros de energía, B(E2), momentos de inercia, radios nucleares, y energías de separación de dos neutrones, mostrando que en los isótopos de Sr se produce un cruce entre las configuraciones regulares e intrusas para $N = 60$, lo que marca el origen de la deformación. Estas características se interpretan además como señales propias de una QPT de Tipo II impulsada por el cruce de configuraciones. En los isótopos de Mo, la coexistencia de formas sigue jugando un papel relevante, aunque con una sistemática mucho menos abrupta que para el caso del Sr, lo que sitúa al Mo en el límite de la región donde puede identificarse la aparición de la coexistencia de forma. Por otro lado, los isótopos de Ru muestran una evolución más gradual, con configuraciones intrusas situadas en energías mucho más elevadas, con lo cual sólo puede identificarse una QPT de Tipo I de segundo orden asociada además a una única configuración.

Esta tesis se extiende además a núcleos impar-par mediante un análisis en el sistema intrínseco tanto para un caso esquemático como para otro más realista centrado en los isótopos de Nb y empleando el IBFM-CM. En este último caso, se puede observar además un cruce entre configuraciones regulares e intrusas en $N = 60$ para estados tanto de

paridad positiva como negativa, dando lugar a una QPT de Tipo II en el estado fundamental, y mostrando que la presencia de un nucleón extra incrementa el carácter abrupto de la transición y desempeña un papel importante en la aparicición de triaxialidad en los estados de paridad positiva.

En conclusión, esta tesis muestra que la mezcla de configuraciones dentro de los modelos algebraicos proporciona un marco adecuado para describir la coexistencia de forma, el origen de la deformación nuclear y las QPTs en núcleos en torno a $Z \approx 40$. El análisis conjunto de isótopos par-par e impar-par ofrece además una imagen coherente de la evolución estructural en dicha zona y ayuda a esclarecer el origen de algunos valores experimentales observados en esta región.

Publications included in this thesis

This doctoral thesis is based on the following publications

Journal articles

1. E. Maya-Barbecho and J. E. García-Ramos, *Shape coexistence in Sr isotopes*, Phys. Rev. C **105**, 034341 (2022). DOI: 10.1103/PhysRevC.105.034341.

2. E. Maya-Barbecho, S. Baid, J. M. Arias, and J. E. García-Ramos, *At the borderline of shape coexistence: Mo and Ru*, Phys. Rev. C **108**, 034316 (2023). DOI: 10.1103/PhysRevC.108.034316.

3. E. Maya-Barbecho and J. E. García-Ramos, *An intrinsic-state formalism for the Interacting Boson-Fermion Model with configuration mixing*, Physics Letters B **868**, 139724 (2025). DOI: 10.1016/j.physletb.2025.139724.

4. E. Maya-Barbecho and J. E. García-Ramos, *Nuclear shapes of Nb isotopes*, Phys. Rev. C. *To be published.*

Conference proceedings

1. E. Maya-Barbecho and J. E. García-Ramos, *Sr isotopes: the interplay between shape coexistence and quantum phase transitions*, EPJ Web of Conferences **290**, 02022 (2023).

2. E. Maya-Barbecho, S. Baid, J. M. Arias, and J. E. García-Ramos, *At the edge of shape coexistence in the $Z = 40$ region*, EPJ Web of Conferences **329**, 02011 (2025).

3. E. Maya-Barbecho and J. E. García-Ramos, *The enhancement of deformation in odd-even nuclei around $A = 100$*, EPJ Web of Conferences **324**, 00027 (2025).

Contents

Chapter 1

Introduction

1.1 The Atomic Nucleus: A Complex Many Body System

The atomic nucleus can be considered as a quantum many body system composed of protons and neutrons. However, even in the case of not considering other constituents, the atomic nucleus is a complex system, which also displays a great variety of phenomena, e.g., as single particle excitations or collective motions such as rotations and vibrations. Moreover, the nuclear interaction, governed by the strong interaction, makes the description of the nucleus and its properties an inherently complex problem, as this interaction is not yet known with the same precision or completeness as, for instance, the electromagnetic interaction.

The complexity of the problem manifests itself also in the presence of features such as deformed shapes, vibrational and rotational spectra, pairing correlations, shape coexistence, and quantum phase transitions. Understanding how those phenomena arise from the underlying nucleons dynamic remains to be one major challenge in nuclear physics

1.2 Modeling Nuclear Structure: From Mean-Field to Algebraic Approaches

In order to give a suitable description of the nuclear properties and features, a variety of theoretical frameworks have been developed for nuclei. The most significant one being the *Collective Model* [1, 2, 3, 4], together with the *Independent Particle model* [5, 6, 7].

The Collective Model is particularly convenient, as it reduces the problem to only some degrees of freedom, focusing on phenomena resulting from collective behavior such as ro-

tations and vibrations [8, 9]. On the other hand, the Independent Particle Model assumes that nucleons move freely on an average potential created by their mutual interaction that results in a specially convenient method for obtaining magic numbers or single particle excitations, being its most representative example the Shell Model [10].

However, even though both models describe the most essential aspects and properties of nuclei, some cases can result in contradictory descriptions for the same properties coming from the results obtained with these two different models. This motivates the research for more unified models that could describe the nucleus in a more consistent way, being the algebraic models one of these attempts.

1.3 Algebraic Models: The Interacting Boson Model

As we introduced earlier, the nuclear structure can be studied using algebraic models, which make good use of symmetries and group theory to describe collective phenomena.

One of such approach is the *Interacting Boson Model* (IBM), introduced in the 1970s by Arima and Iachello [11, 12, 13, 14]. This model is based on mapping fermion pairs coupled to angular momentum $L = 0$ (s bosons) and $L = 2$ (d bosons) into bosons [15]. This coupling leads to an U(6) framework, which allows an exact algebraic solution in several dynamical symmetry limits.

Using this model, it is possible to describe low-lying collective states in even-even nuclei, reproducing rotational and vibrational bands through different symmetry limits.

Originally, this model made no distinction between proton and neutron bosons, being known today as the IBM-1. It was later extended to IBM-2 [15, 16], where it takes into account proton or neutron degrees of freedom separately, together with more extensions as the IBM-3 and IBM-4 [17, 18].

To make this model applicable to odd-mass nuclei, the *Interacting Boson-Fermion Model* (IBFM) was developed [19]. In this version of the model, the even-even core is described by the IBM, while the odd nucleon is treated as a fermion moving in a single particle orbital, but anyway interacting with the bosonic core.

1.4 Configuration Mixing and Shape Coexistence

In recent years, it has become increasingly evident that atomic nuclei may exhibit markedly different intrinsic shapes within a relatively narrow energy range. In particular, there exist nuclear eigenstates lying close in energy with associated geometries that can highly

differ, ranging from nearly spherical configurations to strongly deformed ones as found in [20, 21, 22]. This situation may appear somewhat paradoxical, since it is often implicitly assumed that all states of a given nucleus share approximately the same equilibrium shape. This phenomenon is known as shape coexistence and in nuclear physics it was first proposed by Morinaga [23] to explain the nature of the first excited state in ^{16}O, a 0^+ state which was assumed to be deformed though the ground state is obviously spherical because the nucleus is doubly magic. This state corresponds to a proton 2p-2h excitation across the $Z = 8$ shell closure and, therefore, it is a intruder state with a deformed structure. This idea was also supported by the early works [24, 25, 26] for oxygen isotopes. Moreover, one of the most explicit example of such shape coexistence is observed experimentally in ^{40}Ca and is very well described through shell model calculations involving mp-nh excitations[27, 28, 29].

Furthermore, shape coexistence is by no means an exclusive feature of atomic nuclei, as it is not difficult to find analogous phenomena in molecular physics, like isomerism, being a familiar example the limonene, whose different isomers are responsible for the distinct flavors of oranges and lemons. In nuclei, however, shape coexistence arises from the subtle interplay between single-particle and collective degrees of freedom, pairing correlations, and shell effects, making its microscopic origin a subject of intense theoretical and experimental investigation.

This phenomenon is usually associated with the presence of configurations, that will be know as intruder configurations, which come from $2p$–$2h$ or higher-order particle-hole excitations across the shell gaps. These configurations lead to the formation of bands with different deformations coexisting within the same nucleus, usually one spherical-like and the other deformed [30].

This means that for a theoretical modeling of this phenomenon, we require extending the IBM framework to allow for multiple boson configurations. This is accomplished through the IBM with Configuration Mixing (IBM-CM) [31], which incorporates mixing between a regular configuration space $[N]$ and an intruder space $[N + 2]$ corresponding to two additional bosons associated with $2p$–$2h$ excitations.

From the point of view of experimental data, shape coexistence can be observed from changes in observables like:

- The energy of the first excited 0^+ state.
- Quadrupole transition rates B(E2).
- Nuclear radii and isotopic shifts.
- Two-neutron separation energies.

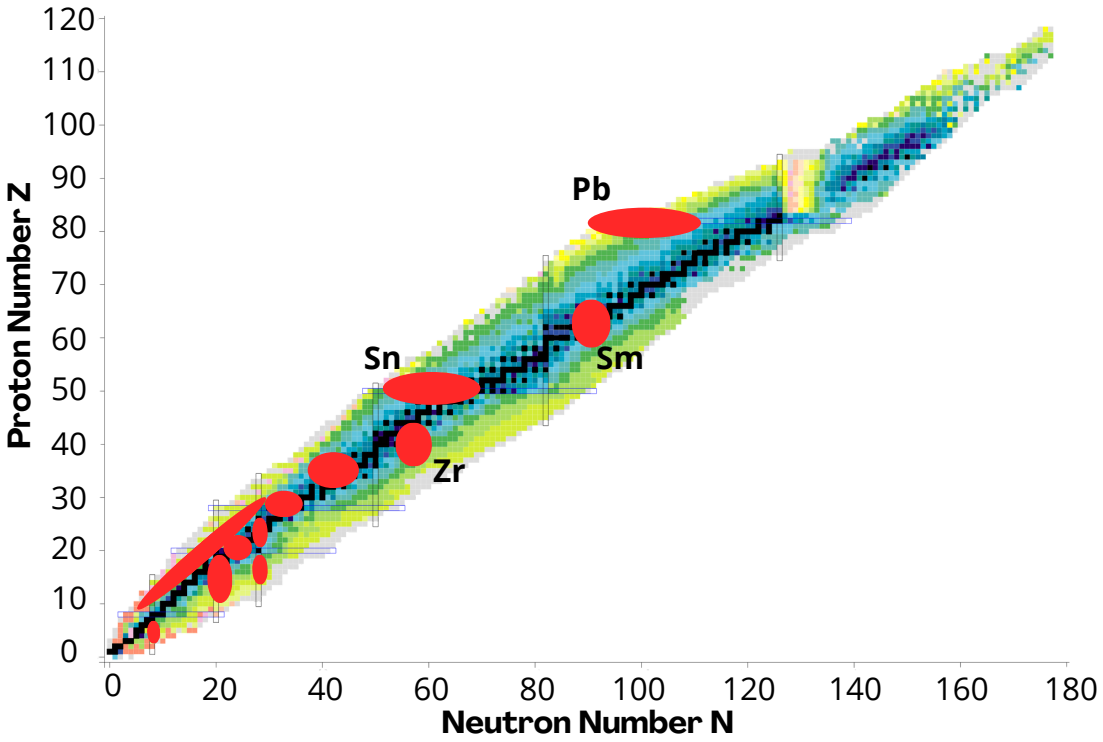

Figure 1.1: Regions where shape coexistence has been encountered.

One of the regions in which it has been proven to present isotopes that exhibit shape coexistence occurs around neutron number $N = 60$ and proton number $Z \approx 40$, in isotopes such as Sr, Zr, Mo, and Ru, although it is not the only region where this phenomenon is encountered, as can be observed in Fig. 1.1, where a particular prevalence around neutron and proton shell closures [30, 32] is observed. The result is that in the $N = 60$ region, a sudden change from spherical to deformed shapes is observed, as seen in the evolution of the energy spectrum and collective observables, suggesting the crossing of regular and intruder configurations.

1.5 Quantum Phase Transitions in Nuclear Systems

Closely related to the phenomenon of shape coexistence we can find the concept of Quantum Phase Transition (QPT), which refers to a qualitative change in the ground state of a quantum system induced by the variation of a control parameter, in principle at zero temperature [33]. However, in nuclear systems, such control parameters are more often associated with changes in the number of valence nucleons or with the evolution of effective interaction strengths, leading to QPTs manifesting themselves as for instance, abrupt changes in the equilibrium shape of the nucleus.

Moreover, depending on the underlying physical mechanism, we can classify the two types of QPTs [34]. In this way, type I QPTs occur within a single configuration space and

correspond to shape transitions driven by a continuous evolution of the Hamiltonian parameters, while type II QPTs, on the other hand, arise from the mixing of different configurations, usually associated with regular and intruder particle-hole excitations. In addition, in certain situations, both types of transitions may coexist and influence each other, giving rise to so-called intertwined QPTs. The first documented example of this phenomenon was found in even-even Zr isotopes [35], and similar behavior has subsequently been identified in Sr [36] and Mo isotopes [37].

QPTs have been extensively studied in finite quantum systems, as could be atomic nuclei, where they provide an specially convenient framework for understanding rapid structural changes along isotopic chains.

1.6 Quantum Phase Transitions in the IBM and IBFM Frameworks

Within the framework of the IBM, QPTs are described in terms of the competition between Hamiltonians associated with different dynamical symmetries: the spherical U(5), the γ-unstable O(6), and the axially deformed SU(3) limits. The concept of QPT has been extensively explored in the IBM and its configuration-mixing extension (IBM-CM) [38, 39, 40]. In this context, Type I QPTs correspond to shape transitions within a single boson configuration, while Type II QPTs emerge from the interaction and mixing of multiple boson configurations.

Seminal works on the IBM-CM [41, 39] have demonstrated that the resulting phase diagram is particularly rich, allowing for the occurrence of both first- and second-order QPTs. Remarkably, in the presence of two configurations, a first-order QPT may occur even for the quadrupole operator parameter $\chi = 0$, a situation that is forbidden in the single-configuration IBM. In this regime, the phase structure becomes highly sensitive to the energy offset Δ^{N+2}; for sufficiently large values of this parameter, the phase transition may disappear altogether. The origin of this first-order behavior can be traced back to the topology of the ground-state energy surface, which, according to Catastrophe Theory [42], exhibits a "butterfly" germ characterized by a β^6 dependence.

The situation becomes considerably more intricate when unpaired fermions are present, as in odd-mass nuclei. In such cases, the coupling between the odd particle and the bosonic core, described within the IBFM, may either favor or hinder the onset of a phase transition. For the IBFM with a single configuration, Refs. [43, 44] showed that, for Hamiltonians depending continuously on a single control parameter, the presence of the odd fermion can enhance or suppress the phase transition depending on the m-projection of the fermionic level.

An analysis of the different boson-fermion interaction terms reveals that the monopole and exchange interactions generate contributions proportional to $\beta^2/(1+\beta^2)$, which can be effectively absorbed into the one-body boson term. In contrast, the quadrupole interaction introduces not only this same $\beta^2/(1+\beta^2)$ dependence but also an additional term proportional to $\beta/(1+\beta^2)$, that plays a crucial role, as it can induce a first-order QPT even in a single configuration scenario with $\chi = 0$ in the bosonic sector of the Hamiltonian.

Recent developments in the IBFM-CM, particularly through the use of the intrinsic state formalism, have enabled a more detailed study of these phenomena, showing that the odd fermion can significantly modify the topology of the energy surfaces, leading to complex phase structures arising from the competition between regular and intruder configurations, as schematically illustrated in Fig. 1.2. As a result, determining the phase diagram of the IBFM-CM constitutes a highly nontrivial problem, requiring a combination of analytical approaches based on Catastrophe Theory and detailed numerical calculations.

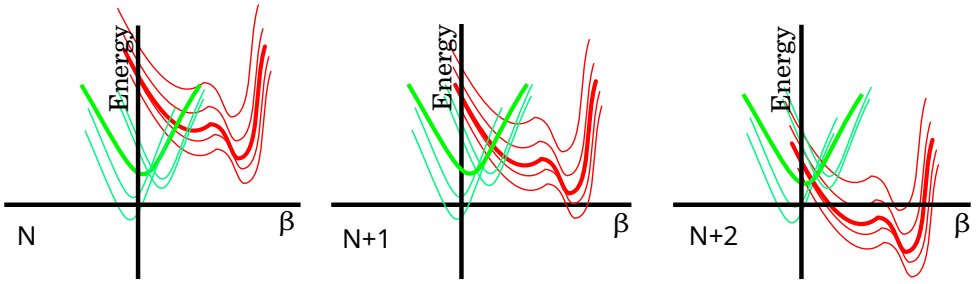

Figure 1.2: Schematic evolution of unperturbed regular (spherical, green lines) and intruder (deformed, red lines) configurations for the IBFM. The thick lines correspond to the boson energy surfaces while the thin ones to the fermion levels.

1.7 Motivation of this Thesis

Within this context, the main motivation of this thesis is the study of nuclear shape coexistence employing the IBM and the IBFM with configuration mixing, IBM-CM and IBFM-CM.

As we introduced before, the description of shape coexistence requires an extension of the model, leading to the IBM-CM. In this framework, different bosonic configurations are considered, associated with particle-hole excitations across a major shell gap. These so-called intruder configurations that originate from excitations across closed shells are expected to play a significant role in regions close to proton or neutron shell closures, such as around $Z = 82$ (lead region) or $Z = 40$ (zirconium-strontium region).

The IBM-CM therefore constitutes one of the main theoretical tools for the development of the objectives of this thesis. In particular, a central contribution exposed here is the

analysis of both intrinsic and laboratory frame description of nuclei, which has moreover lead us to expand the intrinsic frame formalism of the IBFM-CM for odd-even nuclei. The expansion of this formalism for odd-even nuclei provides a framework that makes possible to study in such intrinsic frame, cases with different j-values and of course not only restricted to axial symmetry cases.

The new formalism is first explored and validated through schematic applications, showing for a clear study its capability to describe configuration mixing in odd-even systems. Subsequently, the model is applied to a more realistic nuclear system, which is the niobium isotopic chain.

In addition to the study of odd-even nuclei, this thesis also includes a detailed analysis of even-even systems, focusing on the strontium and molybdenum isotopes. These nuclei are investigated in close comparison with their neighboring zirconium and ruthenium isotopes, in order to elucidate the systematics of shape coexistence, QPTs, and the evolution of nuclear structure along isotopic chains. Special attention is devoted to the interpretation of these phenomena within both the laboratory and intrinsic frames, providing a coherent geometric understanding of collective observables and underlying nuclear shapes.

Throughout this thesis, the results obtained within the IBM and IBM-CM frameworks are discussed in close connection with the two other standard approaches to nuclear structure, namely the Nuclear Shell Model and the Collective Model, and its relation to QPTs in atomic nuclei, using algebraic models, primarily in order to provide a comprehensive and consistent description of shape coexistence and structural evolution in atomic nuclei.

1.8 Structure of the Thesis

The thesis is structured as follows:

- **Chapter 2** presents a concise but comprehensive review of the nuclear structure models that are most relevant for the present work. The chapter begins with an introduction to the Nuclear Shell Model, discussing the mean-field concept and the emergence of single-particle potentials. The role of the residual interaction and the construction of effective Hamiltonians are subsequently addressed, together with a discussion of the scope and intrinsic limitations of the shell-model approach.We then introduce in this chapter the Collective Model, focusing on collective coordinates and the formulation of the collective Hamiltonian. Finally, the Nilsson model is presented, including its extension with BCS pairing correlations, providing a bridge between single-particle and collective descriptions and setting the stage for the algebraic approaches discussed in later chapters.

- **Chapter 3** introduces in detail the IBM, which constitutes one of the main theoretical frameworks employed throughout this thesis. The chapter starts by defining the bosonic basis states and the general structure of the IBM Hamiltonian, as well as the electromagnetic transition operators. Then, the multipole expansion and the Consistent-Q Formalism are discussed in detail, followed by a systematic presentation of the bosonic algebra and its subalgebras, together with the construction of basis states associated with the different algebraic chains. The concept of dynamical symmetries is introduced through Casimir operators and group chains, and analytical expressions for the energy spectra in the U(5), SU(3), and O(6) limits are derived. The geometrical interpretation of the IBM is then developed using coherent states and coset spaces, allowing for a direct connection between algebraic structures and nuclear shapes. The chapter concludes with the formulation of the IBM-CM, which is essential for the description of shape coexistence phenomena.

- **Chapter 4** extends the discussion to odd-even nuclei through the IBFM. After introducing boson and fermion operators and the corresponding basis states, the physical operators of the model are constructed, including the Hamiltonian, transition operators, and the boson fermion interaction. In addition, fermion algebras are discussed for both single-j and multiple-j configurations, together with their associated basis states, then coupled boson fermion algebras and their dynamical symmetries are presented. The chapter ends with the development of the IBFM with configuration mixing, presenting one of the original contribution of this thesis. As a matter of fact, the formalism is extended to incorporate configuration mixing effects, and a microscopic interpretation of the model is also included.

- **Chapter 5** presents the application of the IBM-CM to even-even nuclei, with a particular focus on the strontium and molybdenum isotopic chains, and their comparison with neighboring zirconium and ruthenium nuclei. After a general introduction, shape coexistence is analyzed. Furthermore, experimental energy spectra and electromagnetic transition rates are described, followed by a detailed description of the fitting procedure used to reproduce excitation energies and absolute B(E2) transition probabilities. The accuracy of the fits is assessed through a systematic comparison with experimental data, where in addition, the structure of the wave functions is analyzed in depth, emphasizing the role of configuration mixing and the role of perturbed/unperturbed configurations. Additional observables, including charge radii, isotopic shifts, and two-neutron separation energies, are studied. Finally, nuclear deformation is studied through mean-field energy surfaces and deformation parameters, providing an intrinsic-frame interpretation of the results, which are concluded with a discussion of the relationship between shape coexistence and QPTs, including a comparison between the Sr-Zr region and the Pt-Hg nuclei.

- **Chapter 6** presents the results obtained for odd-even nuclei using the intrinsic formalism for the IBFM with configuration mixing. Here, we begin with schematic calculations illustrating the crossing of configurations. Then, the formalism is applied to a more realistic case, focusing on the niobium isotopic chain. The evolution of nuclear shapes is analyzed in detail, separately for positive and negative parity states. Finally, the results are discussed in terms of QPTs, energy curves and surfaces, providing insight into the collective dynamics, and configuration mixing in odd-even nuclei.
- Finally, **Chapter 7** summarizes the main conclusions obtained in the development of this thesis.

Chapter 2

Models of significance

2.1 The Nuclear Shell Model

2.1.1 Introduction

The Shell Model (SM) [10] is one of the most important frameworks for describing nuclear structure. Its basic assumption is the existence of an average potential in which the nucleons move almost independently [45]. In this way, each particle occupies a single-particle orbit that is only weakly perturbed by the presence of the others. This is a picture inspired by the success of the atomic shell model, in which electrons move in a central Coulomb field.

However, the nuclear case is less obvious, mainly because nuclei do not present any central field, moreover the nuclear force is short-ranged and repulsive at small distances, so strong fluctuations would be expected in the motion of nucleons rather than a smooth mean field. Despite these assumptions, the liquid drop model [8] was successful in describing some physical properties of nuclei such as binding energies or some collective behavior, but this model was based on a picture of nuclei that suggested that they were similar to a liquid drop, meaning that those nuclei should be considered as highly correlated systems [46], while, several experimental observations, as they were the existence of magic numbers, deviations from liquid-drop model predictions, and separation energies, suggested a shell structure in nuclei.

The key to connect theory and experiment was the introduction of a strong spin-orbit term in the Hamiltonian. This idea, developed independently by M. Goeppert-Mayer [5, 6] and by Haxel, Jensen and Suess [7], explained the stability of magic numbers $2, 8, 20, 28, 50, 82, 126$, and established the Shell Model as a powerful microscopic description of nuclei.

2.1.2 The Mean Field and Single-Particle Potentials

In the shell model, the motion of nucleons is described by the time-independent Schrödinger equation,

$$\left[-\frac{\hbar^2}{2m}\nabla^2 + V(r)\right]\phi_i = \epsilon_i\phi_i, \tag{2.1}$$

where $V(r)$ is the average potential and ϕ_i are single-particle wave functions. The nuclear wave function is then built as a Slater determinant of these orbits, consistent with the Pauli exclusion principle.

Several forms of the mean potential have been considered:

- **Square well**: which originates from the assumption:

$$V(r) = \begin{cases} -V_0 & \text{para } r \leq R_0 \\ +\infty & \text{para } r > R_0 \end{cases}, \tag{2.2}$$

  where $V_0 \approx 50 - 60$ MeV and $R_0 = r_0 A^{1/3}$ ($r_0 \approx 1.2$ fm and A is the mass number). This potential reproduces some low magic numbers but is not realistic for nuclear surfaces.

- **Harmonic oscillator**: In this case the potential considered is

$$V(r) = -V_0\left[1 - \left(\frac{r}{R_0}\right)^2\right] = \frac{m}{2}\omega_0^2\left(r^2 - R_0^2\right), \tag{2.3}$$

  that presents a simple analytic solution [47],

$$E = \hbar\omega(2k + \ell + 3/2) = \hbar\omega(N + 3/2), \tag{2.4}$$

  where the quantum numbers that appear are defined as:

$$\begin{aligned} &N = 0, 1, 2, \ldots \\ &\ell = N, N-2, \ldots 1 \text{ or } 0, \\ &k = (N - \ell)/2, \end{aligned} \tag{2.5}$$

  being N is the principal quantum number, l is the orbital angular momentum quantum number, and k is the radial quantum number.

  It should be noted that both the square well and the harmonic oscillator potential do not provide a fully realistic description of the nuclear potential. In this way, when continuum states are relevant, additional assumptions or approximations must be introduced in order to account for their contribution.

- **Woods-Saxon** [48]: That describes charge and matter distributions more accurately, based on the assumption that the nuclear potential must verify that,

$$V(r) = \begin{cases} \left(\frac{\partial V(r)}{\partial r}\right)_{r=0} = 0 \\ \left(\frac{\partial V(r)}{\partial r}\right)_{r<R_0} > 0 \\ V(r)_{r>R_0} \approx 0 \end{cases}, \tag{2.6}$$

  One of the potentials that behaves according to such conditions is,

$$V(r) = \frac{-V_0}{1 + \exp\left(\frac{r-R_0}{a}\right)}, \tag{2.7}$$

  with $a \approx 0.5$fm.

None of these potentials alone explain all the observed shell closures, and as we have introduced earlier, the decisive improvement comes from adding a strong spin-orbit interaction,

$$H = H_{\text{central}} + \kappa\, \vec{L} \cdot \vec{S}, \tag{2.8}$$

which correctly reproduces the full sequence of magic numbers. Moreover, the existence of this spin-orbit splitting is strongly supported by experimental data. This result also supports the level scheme presented in Fig. 2.1.

2.1.3 Residual Interaction and Effective Hamiltonians

Even though nucleons move in a mean field, they still interact with each other, where this residual interaction lifts degeneracies and mixes configurations. The full Hamiltonian considering residual interactions can be written as

$$H = H_0 + H_{\text{res}}, \tag{2.9}$$

where H_0 is the mean-field Hamiltonian and H_{res} represents residual two-body interactions.

There are different strategies to reproduce H_{res}:

1. **Phenomenological approach:** adjust two-body matrix elements to reproduce selected experimental data as single particle energies.
2. **Realistic interactions:** start from nucleon-nucleon forces and modify them to account for the nuclear medium.
3. **Schematic forces:** where we use simplified interactions (Gaussian, contact, Yukawa,

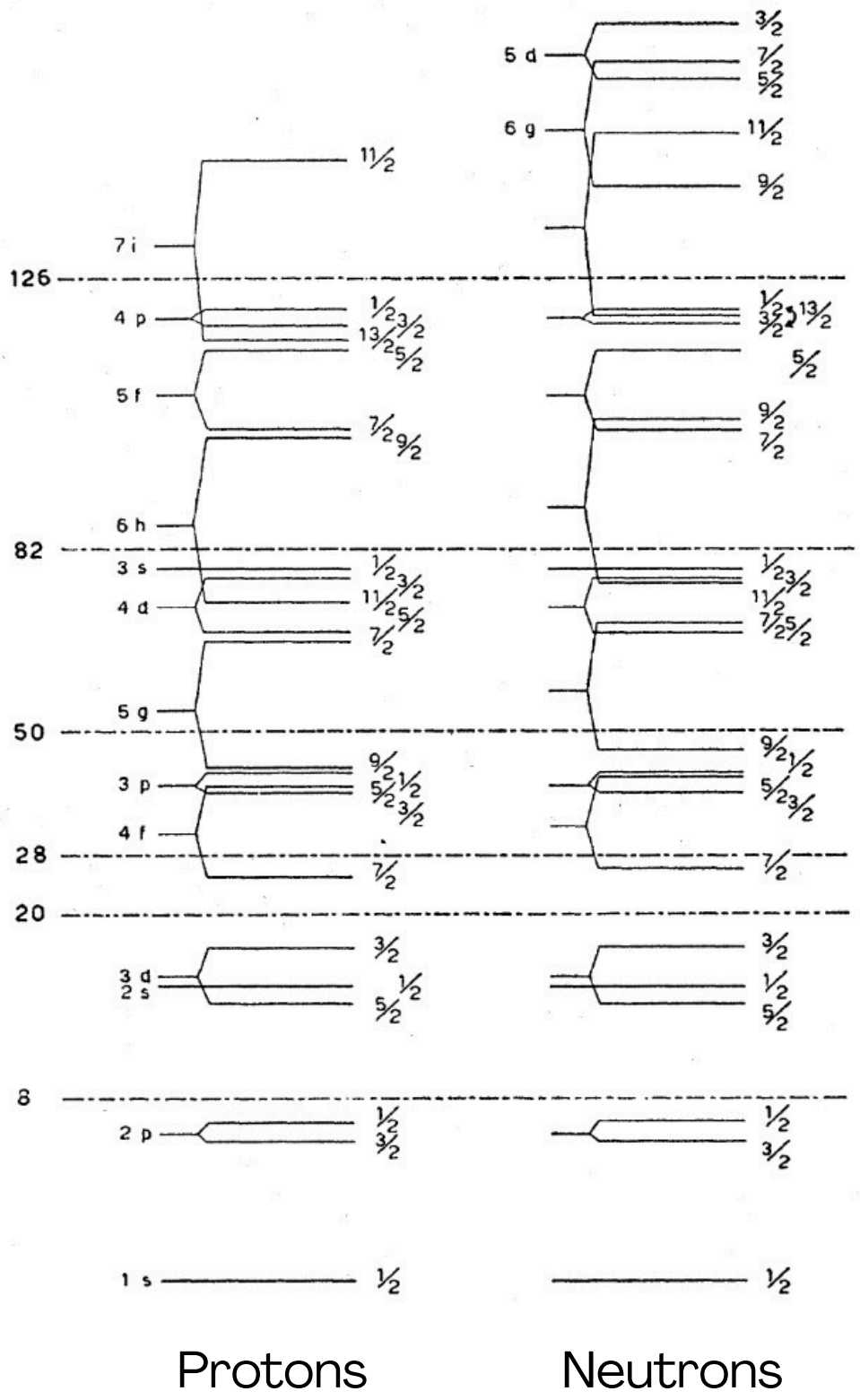

Figure 2.1: Single-particle levels for a Hamiltonian formed by central potential plus a spin-orbit term.

Skyrme) whose parameters are adjusted to experimental trends in a given mass region.

2.1.4 Scope and Limitations

The SM has been extremely successful in explaining nuclear properties near closed shells and across wide mass ranges, providing a unified framework for both single-particle behavior and collective effects.

However, its main limitation is computational: the dimension of the Hilbert space grows rapidly with the number of valence nucleons, making diagonalizations challenging. Moreover, strongly collective excitations, such as giant resonances or large deformations, often require orbitals from several major shells.

Despite these difficulties, the nuclear SM remains one of the central tools of nuclear theory, combining physical insight with modern computational techniques to explore nuclei from stability to the limits of the nuclear chart.

2.2 The Collective Model

The SM has the great advantage compared with other approaches to nuclear structure of providing a complete framework that does not leave out any nuclear degrees of freedom. This allows phenomena to be described involving only a few nucleons as well as those in which all nucleons participate simultaneously. However, applying the SM to the description of collective excitations becomes extremely complex, since it requires dealing with a vast number of configurations and diagonalizing matrices of huge dimensions. For this reason, phenomenological models were developed, in which collective properties emerge naturally. Nonetheless, in principle, a "complete" SM calculation would always contain such features, although extracting them may be very cumbersome.

The existence of a central mean field in which the nucleons move is itself a collective effect arising from all nucleons. Moreover, several experimental observations point to collective behavior in nuclei. For instance, quadrupole moments that are an order of magnitude larger than those expected for a single nucleon indicate significant nuclear deformation. Likewise, the appearance of rotational spectra, with energy levels following a sequence proportional to $J(J+1)$, provides evidence of cooperative motion among nucleons. In summary, the nucleus exhibits long–range interactions that induce collective effects, giving rise to deformations and vibrational-rotational dynamics [8, 9].

The Collective Model (CM) is a phenomenological framework tailored to describe low-energy (< 8 MeV) excitations of medium and heavy even-even nuclei. In this model,

the nucleus is considered an incompressible liquid droplet, meaning that single-particle excitations are ignored. Instead, the nuclear surface is parametrized by a set of variables, leading to a "classical" description in which the main modes of excitation are vibrations and rotations.

2.2.1 Collective Coordinates

For medium and heavy nuclei it is not necessary to use the full set of orbital degrees of freedom. Instead, we can introduce a reduced set of coordinates, α_μ, which are sufficient to describe the essential collective properties. These are known as *collective coordinates*, and most importantly, the explicit relation between the nucleonic and collective coordinates is not required.

The nuclear surface can be parametrized as:

$$R(\theta,\phi) = R_0\left(1+\alpha_{00}+\sum_{\lambda=1}^{\infty}\sum_{\mu=-\lambda}^{\lambda}\alpha^*_{\lambda\mu}Y_{\lambda\mu}(\theta,\phi)\right), \tag{2.10}$$

where $Y_{\lambda\mu}$ are spherical harmonics and R_0 is the radius of a sphere with the same volume as the nucleus. For small deformations, truncating to the quadrupole terms ($\lambda = 2$) is sufficient, leading to

$$R(\theta,\phi) = R_0\left[1+\sum_{\mu=-2}^{2}\alpha^*_{2\mu}Y_{2\mu}(\theta,\phi)\right]. \tag{2.11}$$

The parameters $\alpha_{2\mu}$ are known as *deformation parameters*. After suitable rotations in order to reduce the number of deformation parameters, only two independent parameters remain, usually expressed in terms of the Hill–Wheeler [49] variables β and γ:

$$\alpha_{20} = \beta\cos\gamma, \qquad \alpha_{22} = \frac{1}{\sqrt{2}}\beta\sin\gamma. \tag{2.12}$$

Here β quantifies the overall deformation, while γ characterizes the deviation from axial symmetry. Specific values correspond to different nuclear shapes: $\gamma = 0°$ gives a prolate ellipsoid, $\gamma = 60°$ corresponds to an oblate ellipsoid, and intermediate values describe triaxial shapes. In contrast, in the γ-unstable case the energy is essentially independent of γ, implying the absence of a preferred orientation in the γ degree of freedom.

2.2.2 The Collective Hamiltonian

For quadrupole deformations, the collective Hamiltonian can be written as

$$H = \frac{1}{2}B\sum_{\mu}|\dot{\alpha}_{2\mu}|^2 + V(\alpha_{2\mu}), \tag{2.13}$$

where B is an inertial parameter and V is a generic collective potential. In the harmonic approximation, this Hamiltonian reduces to that of a five-dimensional oscillator, corresponding to a spherical nucleus undergoing vibrations while preserving spherical symmetry.

A more general expression, derived by Bohr [2, 3], reads

$$H_{BM} = \sum_{\kappa=1}^{3}\frac{\hat{M}'^2_{\kappa}}{2\mathcal{I}_{\kappa}(\beta,\gamma)} + -\frac{\hbar^2}{2B_2}\left(\frac{1}{\beta^4}\frac{\partial}{\partial\beta}\beta^4\frac{\partial}{\partial\beta} + \frac{1}{\beta^2}\frac{1}{\sin 3\gamma}\frac{\partial}{\partial\gamma}\sin 3\gamma\frac{\partial}{\partial\gamma}\right) + V\left(\alpha_{2\mu}\right). \tag{2.14}$$

This formulation is known as the Bohr–Mottelson Hamiltonian, and the entire approach is sometimes referred to as the Bohr–Mottelson Model.

Depending on the potential $V(\beta,\gamma)$, the spectrum exhibits rotational and vibrational bands. For example, β-vibrations correspond to oscillations in the magnitude of the deformation, while γ-vibrations represent departures from axial symmetry. The coupling of these modes gives rise to rich nuclear excitation spectra, including the well-known vibrational-rotational structures.

2.3 The Nilsson Model

A widely used framework to describe the spectra of odd-even deformed nuclei is the Nilsson model [50], in which single-particle states are determined by solving the Schrödinger equation for a nucleon moving in a deformed mean field. The corresponding single-particle Hamiltonian is

$$H = \frac{p^2}{2m} + V_c(r)\left[1 + \beta Y^{(2)}(\theta)\right] + V_{so}(r)\,\mathbf{l}\cdot\mathbf{s}, \tag{2.15}$$

where β is the quadrupole deformation parameter, $Y^{(2)}$ is the harmonic spherical, $V_c(r)$ denotes the central potential generated by the even-even core, and $V_{so}(r)$ represents the spin–orbit interaction.

Within perturbation theory, the single-particle energy levels take the approximate form

$$\epsilon_{jK} \approx \epsilon_j^{(0)} + \beta\, P_j\left(3K^2 - j(j+1)\right)\langle j\|V_c(r)Y^{(2)}\|j\rangle, \tag{2.16}$$

where $\epsilon_j^{(0)}$ are the eigenvalues of the spherical Hamiltonian

$$H_0 = \frac{p^2}{2m} + V_c(r) + V_{so}(r)\,\mathbf{l}\cdot\mathbf{s}. \tag{2.17}$$

In general, the full solution requires diagonalization since the quadrupole term $Y^{(2)}$ couples states with different j values.

An important point is that the Nilsson model can be regarded as the classical limit of the IBFM when only a quadrupole boson–fermion interaction is present. In this correspondence, the effective quadrupole interaction strength is related to the parameters of the Nilsson potential as

$$\Gamma \propto \frac{1}{N_B\,\beta^2}\langle j\|V_c(r)Y^{(2)}\|j\rangle, \tag{2.18}$$

with N_B denoting the number of bosons in the even-even core. After applying the appropriate scale transformation between the geometric deformation parameter of Bohr and the bosonic deformation parameter of the IBFM, one obtains a direct mapping between the two descriptions.

2.3.1 The Nilsson Model with BCS Pairing

While the Nilsson model captures the gross features of single-particle spectra in deformed nuclei, it does not reproduce the correct ordering of levels. To remedy this, it is necessary to incorporate residual interactions. A natural choice is a pairing force acting in the deformed basis, characterized by an effective strength G_{def}. Within this scheme, a Bardeen–Cooper–Schrieffer (BCS) calculation [51] provides the quasiparticle energies

$$E_{jK} = \sqrt{(\epsilon_{jK} - \lambda_F)^2 + \Delta^2}, \tag{2.19}$$

where λ_F is the Fermi energy and Δ the pairing gap. These quantities are fixed self-consistently by imposing particle-number conservation,

$$N = \sum_K 2v_K^2, \tag{2.20}$$

where v_K^2 is the occupation probability of the state labeled by K.

The Nilsson+BCS scheme leads to a more realistic description of odd-even nuclei and can be related, at the classical limit, to the IBFM including both quadrupole and exchange boson–fermion interactions. By equating the resulting single-particle levels, one can establish explicit connections between the interaction strengths of the two approaches.

Finally, it is worth noting a fundamental conceptual difference between the Nilsson model and the IBFM. In the latter, single-particle energies saturate to constant values at large

deformations due to the finite boson number N_B, which reflects the underlying microscopic structure of the nucleus. In contrast, in the Nilsson model the energies associated with a given j-orbit diverge as β increases, since the deformed field is treated as an external potential rather than as one generated microscopically by the finite number of nucleons. This distinction becomes crucial when comparing both models at large deformations and following this discussion, detailed comparisons of the properties of the Nilsson model and the IBFM can be found in [52, 53].

Chapter 3

The Interacting Boson Model

As it was exposed before, the IBM was introduced in the 1970s as an algebraic model that would be functioning both in the vibrational U(5) limit so in the rotational SU(3) (introduced by J. P. Elliot). In the IBM, all collective excitations of nuclei are described by bosons, as this model stems from low-lying collective states being described in terms of boson with angular momenta $L = 0$ and $L = 2$ resulting from the coupling of nucleons.

From this point, it is clear that the appropriate formalism for this model is no other than second quantization, where we describe the system in terms of a monopole boson with angular momentum and parity $J^P = 0^+$, which will be called s, and a quadrupole boson with $J^P = 2^+$, referred as d bosons, as depicted schematically in Fig. 3.1.

Thus, the system is built through the following blocks

$$\begin{cases} s^\dagger, d^\dagger_\mu & (\mu = 0, \pm 1, \pm 2) \\ s, d_\mu & (\mu = 0, \pm 1, \pm 2) \end{cases}. \tag{3.1}$$

It is also convenient to introduce a more compact notation for those bosons operators

$$\gamma^\dagger_{lm}(\gamma_{lm}) \quad with \quad l = 0, 2 \quad and \quad m = -l, -l+1, ..., l. \tag{3.2}$$

Where lm can be considered as a single index, that can be named, for instance as α, which ranges from 1 to 6, covering the possible cases.

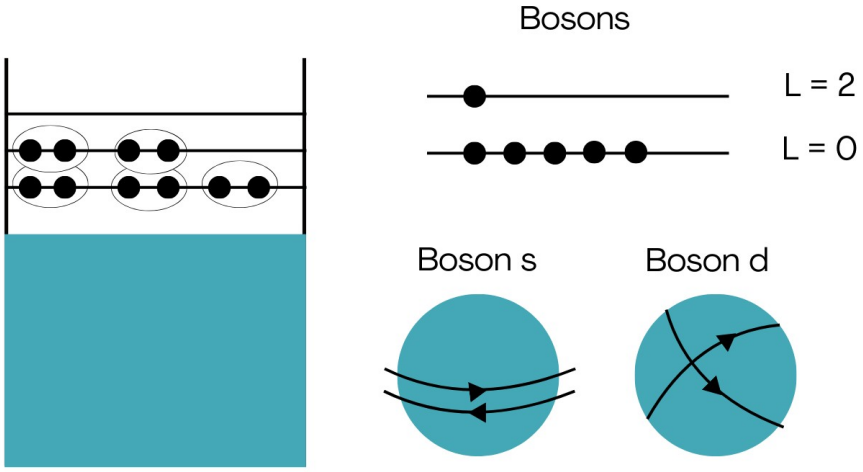

Figure 3.1: Bosons s and d depicted schematically.

In this way, commutation relations are the following ones,

$$\begin{aligned} &\left[b_{l,m}, b^{\dagger}_{l',m'}\right] = \delta_{ll'}\delta_{mm'}, \\ &[b_{l,m}, b_{l',m'}] = \left[b^{\dagger}_{l,m}, b^{\dagger}_{l',m'}\right] = 0, \\ &\text{or as} \\ &\left[b_{\alpha}, b^{\dagger}_{\alpha'}\right] = \delta_{\alpha\alpha'}; \quad [b_{\alpha}, b_{\alpha'}] = \left[b^{\dagger}_{\alpha}, b^{\dagger}_{\alpha'}\right] = 0. \end{aligned} \tag{3.3}$$

This results in 36 operators that can be mapped into an U(6) algebra,

$$d^{\dagger}_{\mu}d_{\mu'} \quad d^{\dagger}_{\mu}s \quad s^{\dagger}d_{\mu} \quad s^{\dagger}s. \tag{3.4}$$

That can be written in a more general way as:

$$\hat{G}_{ij} = \gamma^{\dagger}_{i}\gamma_{j}, \quad i,j = 1,\ldots,6, \tag{3.5}$$

that verifies

$$\left[\hat{G}_{ij}, \hat{G}_{kl}\right] = \hat{G}_{il}\delta_{jk} - \hat{G}_{jk}\delta_{il}. \tag{3.6}$$

For applying this model, it is convenient to define the group generators that are able to transform adequately under rotations. In the case of $\gamma^{\dagger}_{lm}$, they can be considered as a spherical tensor of degree l that under rotations transforms as basis vectors of a $2l+1$ dimensional group,

$$\mathcal{R}\gamma^{\dagger}_{lm}\mathcal{R}^{-1} = \sum_{m'} \mathcal{D}^{l}_{m'm}\gamma^{\dagger}_{lm'}. \tag{3.7}$$

However, in the case of the γ_{lm} operator, we encounter the difficulty that they do not behave correctly under rotations, so in order to construct spherical tensors, one needs to introduce the following

$$\tilde{\gamma}_{lm} = (-1)^{l+m}\gamma_{l-m}. \tag{3.8}$$

Now that we have spherical tensors, it is possible to apply the tensor product to obtain another spherical tensors[54]:

$$\hat{T}^L_M = \left[\hat{T}^{L_1} \times \hat{T}^{L_2}\right]^L_M = \sum_{M_1 M_2} \langle L_1 M_1 L_2 M_2 \mid LM\rangle \, \hat{T}^{L_1}_{M_1} \hat{T}^{L_2}_{M_2}, \tag{3.9}$$

where $\langle L_1 M_1 L_2 M_2 \mid LM\rangle$ indicates the Clebsch Gordan coefficient.

A particular case is the scalar product, usually denoted by a round bracket in the following way,

$$U^{(k)} \cdot V^{(k)} = (-)^k (2k+1)^{\frac{1}{2}} \left[U^{(k)} \times V^{(k)}\right]^{(0)}_0 . \tag{3.10}$$

3.1 Basis States

It is essential to operate correctly with the IBM to define a basis of states, which in this work will be constructed in the usual way by repeatedly applying bosons operators on a boson vacuum $|0\rangle$

$$b^\dagger_\alpha b^\dagger_{\alpha'} ... \, |0\rangle \, . \tag{3.11}$$

Also, it is specially convenient to construct states with good angular momentum, for this reason we couple the boson operators appropriately.

$$\left[b^\dagger_l \times b^\dagger_{l'} \times ...\right]^{(L)}_M |0\rangle \, . \tag{3.12}$$

It is important to note that the angular momentum alone itself is not sufficient to characterize a state uniquely, as it is possible to find states with the same angular momentum L for a certain number of bosons N. The issue of finding appropriate labels will be addressed in the following sections. Moreover, many calculations are performed using a spherical basis in which the s and s bosons are treated separately,

$$s^{\dagger n_s} \left[d^{\dagger n_d}\right]_{\nu n_\Delta L M_L} |0\rangle \, , \tag{3.13}$$

where the parameters n_s, n_d correspond with the total number of bosons s and d, respectively, and verify that $N = n_s + n_d$ and the quantum numbers ν, n_Δ will be discussed in the next sections.

3.2 The Hamiltonian Operator

As we want to describe a physical system composed by bosons, it is necessary to write all operators in terms of boson operators, including the Hamiltonian. In this case and considering that the Hamiltonian operator conserves the total boson number, we write,

$$H = E_0 + \sum_{\alpha\beta} \epsilon_{\alpha\beta} b^\dagger_\alpha b_\beta + \sum_{\alpha\beta\gamma\delta} \frac{1}{2} u_{\alpha\beta\gamma\delta} b^\dagger_\alpha b^\dagger_\beta b_\gamma b_\delta + ..., \tag{3.14}$$

where the one-body contribution is represented here with the term $b^\dagger b$, the two-body one is $b^\dagger b^\dagger bb$ and so on, it is also for the presence of these terms that these models are named interacting boson models, moreover the interactions in equation (3.14) are always number conserving.

In addition, to make apparent that the Hamiltonian is invariant under rotations, we write

$$H = E_0 + \sum_l \varepsilon_l b^\dagger_l \cdot \tilde{b}_l + \sum_{L,l'l'l'''} \frac{1}{2} u^{(L)}_{ll'l''l'''} \left[\left[b^\dagger_l \times b^\dagger_{l'} \right]^{(L)} \times \left[\tilde{b}_{l''} \times \tilde{b}_{l'''} \right]^{(L)} \right]^{(0)}_0 + \cdots . \tag{3.15}$$

As in many calculations, only up to two terms are retained, in that case, equation (3.15) can be written in terms of bosons s and d as,

$$\begin{aligned} H =& E_0 + \varepsilon_s s^\dagger \cdot \tilde{s} + \varepsilon_{\mathrm{d}} d^\dagger \cdot \tilde{d} \\ &+ \sum_{L=0,2,4} \frac{1}{2} (2L+1)^{\frac{1}{2}} c_L \left[\left[d^\dagger \times d^\dagger \right]^{(L)} \times [\tilde{d} \times \tilde{d}]^{(L)} \right]^{(0)}_0 \\ &+ \frac{1}{\sqrt{2}} v_2 \left[\left[d^\dagger \times d^\dagger \right]^{(2)} \times [\tilde{d} \times \tilde{s}]^{(2)} + \left[d^\dagger \times s^\dagger \right]^{(2)} \times [\tilde{d} \times \tilde{d}]^{(2)} \right]^{(0)}_0 \\ &+ \frac{1}{2} v_0 \left[\left[d^\dagger \times d^\dagger \right]^{(0)} \times [\tilde{s} \times \tilde{s}]^{(0)} + \left[s^\dagger \times s^\dagger \right]^{(0)} \times [\tilde{d} \times \tilde{d}]^{(0)} \right]^{(0)}_0 \\ &+ u_2 \left[\left[d^\dagger \times s^\dagger \right]^{(2)} \times [\tilde{d} \times \tilde{s}]^{(2)} \right]^{(0)}_0 + \frac{1}{2} u_0 \left[\left[s^\dagger \times s^\dagger \right]^{(0)} \times [\tilde{s} \times \tilde{s}]^{(0)} \right]^{(0)}_0 , \end{aligned} \tag{3.16}$$

where it has also been considered that the Hamiltonian is an Hermitian operator.

3.3 Transition Operators

In addition to the Hamiltonian, transition operators can also be written in terms of boson operators,

$$T^{(L)} = t^{(0)}_0 \delta_{L0} + \sum_{\alpha\beta} t^{(L)}_{\alpha\beta} b^\dagger_\alpha b_\beta + \cdots . \tag{3.17}$$

Now, transforming this to tensor operators of rank L, as transition operators must have

good quantum number L,

$$T_{\mu}^{(L)} = t_0^{(0)}\delta_{L0} + \sum_{ll'} t_{ll'}^{(L)} \left[b_l^{\dagger} \times \tilde{b}_{l'}\right]_{\mu}^{(L)} + \cdots . \tag{3.18}$$

It is specially convenient to use the coupled form for the generators, where again in our case of s and d bosons the transition operators for the different multipolarities are written as,

$$\begin{aligned}
T_0^{(\mathrm{E0})} &= \gamma_0 + \alpha_0 \left[s^{\dagger} \times \tilde{s}\right]_0^{(0)} + \beta_0 \left[d^{\dagger} \times \tilde{d}\right]_0^{(0)}, \\
T_{\mu}^{(\mathrm{M1})} &= \beta_1 \left[d^{\dagger} \times \tilde{d}\right]_{\mu}^{(1)}, \\
T_{\mu}^{(\mathrm{E2})} &= \alpha_2 \left[d^{\dagger} \times \tilde{s} + s^{\dagger} \times \tilde{d}\right]_{\mu}^{(2)} + \beta_2 \left[d^{\dagger} \times \tilde{d}\right]_{\mu}^{(2)}, \\
T_{\mu}^{(\mathrm{M3})} &= \beta_3 \left[d^{\dagger} \times \tilde{d}\right]_{\mu}^{(3)}, \\
T_{\mu}^{(\mathrm{E4})} &= \beta_4 \left[d^{\dagger} \times \tilde{d}\right]_{\mu}^{(4)}.
\end{aligned} \tag{3.19}$$

In equation (3.19), it can be observed that if only one-body operators are considered (with s and d bosons), transition operators with multipolarity up to four can be constructed. Moreover, the coefficients $\gamma_0, \alpha_L(L = 0, 2), \beta_L(L = 0, ..., 4)$ specify the strength of the corresponding operators.

3.3.1 Choice of Phases

As it has been specified, the parameters in equations (3.16) and (3.19) have been chosen to be Hermitian and real, but there is some phase ambiguity, as the operators s and d could undergo a gauge transformation [55],

$$\begin{aligned}
s &\to s\mathrm{e}^{-\mathrm{i}\phi}, \quad s^{\dagger} \to s^{\dagger}\mathrm{e}^{+\mathrm{i}\phi}, \\
d &\to d\mathrm{e}^{-\mathrm{i}\psi}, \quad d^{\dagger} \to d^{\dagger}\mathrm{e}^{+\mathrm{i}\psi}.
\end{aligned} \tag{3.20}$$

This gauge transformation affects the first term in the E2 operator in equation (3.19) in the following way,

$$\left[d^{\dagger} \times \tilde{s} + s^{\dagger} \times d\right]_{\mu}^{(2)} \to e^{i(\psi-\phi)} \left[d^{\dagger} \times \tilde{s} + e^{-2i(\psi-\phi)} s^{\dagger} \times d\right]_{\mu}^{(2)}, \tag{3.21}$$

where the standard choice is $\psi = \phi = 0$ and it is the choice that will be used through this work, but it is also possible to choose a phase that verifies $\psi - \phi = \dfrac{\pi}{2}$, that would transform the transition operator in:

$$T_{\mu}^{(\mathrm{E2})} = \alpha_2 i \left[d^{\dagger} \times \tilde{s} - s^{\dagger} \times d\right]_{\mu}^{(2)} + \beta_2 \left[d^{\dagger} \times d\right]_{\mu}^{(2)}, \tag{3.22}$$

which is Hermitian but also complex.

3.4 Multipole Expansion and the Consistent-Q Formalism

Usually the Hamiltonian and transition operators are written in multiple ways, one of the most employed are the known as multipole expansion, in which two ways of writing the Hamiltonian exist.

$$\begin{aligned} H =& E'_0 + \varepsilon_{\mathrm{d}}\hat{n}_{\mathrm{d}} + a_0\hat{\mathcal{P}}^\dagger\cdot\hat{\mathcal{P}} + a_1\hat{L}\cdot\hat{L} + a_2\hat{Q}\cdot\hat{Q} \\ &+ a_3\hat{U}\cdot\hat{U} + a_4\hat{V}\cdot\hat{V}, \end{aligned} \tag{3.23}$$

and

$$\begin{aligned} H =& E'_0 + \varepsilon\hat{n}_{\mathrm{d}} + a_0\hat{\mathcal{P}}^\dagger\cdot\hat{\mathcal{P}} + a_1\hat{L}\cdot\hat{L} + a_2\hat{Q}\cdot\hat{Q} \\ &+ a_3\hat{U}\cdot\hat{U} + a_5\hat{n}_{\mathrm{d}}^2, \end{aligned} \tag{3.24}$$

where,

$$\begin{aligned} \hat{n}_d &= d^\dagger\cdot\tilde{d}, \\ \hat{\mathcal{P}} &= \frac{1}{2}d\cdot\tilde{d} - \frac{1}{2}\tilde{s}\cdot\tilde{s}, \\ \hat{L} &= (10)^{\frac{1}{2}}\left[d^\dagger\times d\right]^{(1)}, \\ \hat{Q} &= \left[d^\dagger\times\tilde{s} + s^\dagger\times d\right]^{(2)} - \chi\left[d^\dagger\times d\right]^{(2)}, \\ \hat{U} &= \left[d^\dagger\times d\right]^{(3)}, \\ \hat{V} &= \left[d^\dagger\times d\right]^{(4)}, \end{aligned} \tag{3.25}$$

are often referred to as multipole operators.

Another important parametrization that will also be used in the calculations in this thesis is the known as the extended Consistent-Q formalism [56], in which the Hamiltonian is written as,

$$H = E'_0 + \varepsilon\hat{n}_{\mathrm{d}} + c_1\hat{L}\cdot\hat{L} + c_2\hat{Q}^\chi\cdot\hat{Q}^\chi + c_3\hat{U}\cdot\hat{U} + c_4\hat{V}\cdot\hat{V} \tag{3.26}$$

and the operators, $\hat{n}_d$, $\hat{L}$, $\hat{U}$ and $\hat{V}$ are the same as for the multipole expansion. Moreover, the transition operator is now written as,

$$\hat{Q}^\chi = \left[d^\dagger\times\tilde{s} + s^\dagger\times\tilde{d}\right]^{(2)} + \chi\left[d^\dagger\times\tilde{d}\right]^{(2)}. \tag{3.27}$$

So, the transition operator is given by:

$$T^{(E2)} = \alpha_2\hat{Q}^\chi \tag{3.28}$$

This parameterization is especially convenient as it reduces the number of parameters by one, given that the quadrupole operator is the same and used in both the Hamiltonian and the transition operator.

3.5 Bosonic Algebra

Employing the already defined bilinear products of boson creation and annihilation operators

$$\hat{G}_{ij} = \gamma_i^\dagger \gamma_j, \quad i,j = 1,\ldots,6, \tag{3.29}$$

That satisfy the commutation relations

$$\left[\hat{G}_{ij}, \hat{G}_{kl}\right] = \hat{G}_{il}\delta_{jk} - \hat{G}_{kj}\delta_{li}. \tag{3.30}$$

Moreover, for problems where angular momentum is preserved, it is more convenient to use the coupled form,

$$\hat{G}_{LM}\left(l,l'\right) = \left[\gamma_l^\dagger \times \tilde{\gamma}_{l'}\right]^L_M, \quad l,l' = 0,2, \tag{3.31}$$

that verifies the commutation relations,

$$\begin{aligned}
&\left[\hat{G}_{LM}\left(l,l'\right), \hat{G}_{L'M'}\left(l'',l'''\right)\right] = \\
&\quad \sum_{L''M''} \sqrt{2L+1}\sqrt{2L'+1}\left\langle LML'M' \mid L''M''\right\rangle (-1)^{L-L'} \\
&\quad \times \left[(-1)^{L+L'+L''} \begin{Bmatrix} L & L' & L'' \\ l''' & l & l' \end{Bmatrix} \delta_{l'l''} \hat{G}_{L''M''}\left(l,l'''\right)\right. \\
&\quad \left. - \begin{Bmatrix} L & L' & L'' \\ l'' & l' & l \end{Bmatrix} \delta_{ll'''} \hat{G}_{L''M''}\left(l'',l'\right)\right],
\end{aligned} \tag{3.32}$$

where the curly brackets denotes a Wigner 6-j symbol, being those the generators of U(6) in Racah's form. It is also possible to write them in terms of s and d bosons, having each

tensor a total of $(2l+1)$ components as indicated

$$\begin{aligned}
G_0^{(0)}(s,s) &= \left[s^\dagger \times \tilde{s}\right]_0^{(0)}, \\
G_0^{(0)}(d,d) &= \left[d^\dagger \times d\right]_0^{(0)}, \\
G_\mu^{(1)}(d,d) &= \left[d^\dagger \times d\right]_\mu^{(1)}, \\
G_\mu^{(2)}(d,d) &= \left[d^\dagger \times d\right]_\mu^{(2)}, \\
G_\mu^{(3)}(d,d) &= \left[d^\dagger \times d\right]_\mu^{(3)}, \\
G_\mu^{(4)}(d,d) &= \left[d^\dagger \times d\right]_\mu^{(4)}, \\
G_\mu^{(2)}(d,s) &= \left[d^\dagger \times \tilde{s}\right]_\mu^{(2)}, \\
G_\mu^{(2)}(s,d) &= \left[s^\dagger \times d\right]_\mu^{(2)}.
\end{aligned} \tag{3.33}$$

3.6 Bosonic Subalgebras

We define a subalgebra h as a subset of a given algebra g, closed under commutation, which schematically can be written as,

$$\begin{aligned}
&X \in g, \quad Y \in h, \quad g \supset h, \\
&[Y_i, Y_j] = \sum_k C_{ij}^k Y_k.
\end{aligned} \tag{3.34}$$

As this model is made to work within the field of nuclear physics, it is compulsory that states are characterized by a good value of angular momentum. This implies that the algebra of tridimensional rotations, O(3), must always be included as a subalgebra of U(6). In the particular case of coupled form generator, working with them in such a way, will ensure automatically the inclusion of O(3) as a subalgebra, as the operators $G_\mu^{(1)}(d,d)$ are no other but the generators of the O(3) algebra.

3.6.1 Boson Subalgebra I

The easiest subalgebra that can be obtained is U(5), composed by the generators that only include d bosons:

$$\begin{aligned}
\hat{G}_{00}(2,2) &= \left[d^\dagger \times \tilde{d}\right]_0^0, \\
\hat{G}_{1\mu}(2,2) &= \left[d^\dagger \times \tilde{d}\right]_\mu^1, \\
\hat{G}_{2\mu}(2,2) &= \left[d^\dagger \times \tilde{d}\right]_\mu^2, \\
\hat{G}_{3\mu}(2,2) &= \left[d^\dagger \times \tilde{d}\right]_\mu^3, \\
\hat{G}_{4\mu}(2,2) &= \left[d^\dagger \times \tilde{d}\right]_\mu^4.
\end{aligned} \tag{3.35}$$

Again, from the resulting 25 generators, we can choose 10 that close under commutation, being the O(5) algebra:

$$\begin{aligned} \hat{G}_{1\mu}(2,2) &= \left[d^\dagger \times \tilde{d}\right]^1_\mu, \\ \hat{G}_{3\mu}(2,2) &= \left[d^\dagger \times \tilde{d}\right]^3_\mu, \end{aligned} \tag{3.36}$$

where can be rapidly noticed that the O(3) generators are enclosed, so the O(5) algebra contains intrinsically the O(3) one,

$$\hat{G}_{1\mu}(2,2) = \left[d^\dagger \times \tilde{d}\right]^1_\mu. \tag{3.37}$$

This results in the following chain of subalgebras, together with their labels,

$$\begin{array}{ccccccc} U(6) & \supset & U(5) & \supset & O(5) & \supset & O(3) \\ \downarrow & & \downarrow & & \downarrow & & \downarrow \\ [N] & & n_d & & \tau & \nu_\Delta & L \end{array} \tag{3.38}$$

So, the states are characterized by

$$|[N] n_d \tau \nu_\Delta L\rangle \,. \tag{3.39}$$

3.6.2 Boson Subalgebra II

Obtaining the second subalgebra it not so obvious as the first one, since it involves the consideration of linear combinations of the operators, given the case of

$$\begin{aligned} &\hat{G}_{00}(0,0) + \sqrt{5}\hat{G}_{00}(2,2) = \left[s^\dagger \times \tilde{s}\right]^0_0 + \sqrt{5}\left[d^\dagger \times \tilde{d}\right]^0_0, \\ &\hat{G}_{1\mu}(2,2) = \left[d^\dagger \times \tilde{d}\right]^1_\mu, \\ &\hat{G}_{2\mu}(0,2) + \hat{G}_{2\mu}(2,0) \pm \frac{\sqrt{7}}{2}\hat{G}_{2\mu}(2,2) = \\ &\quad \left[s^\dagger \times \tilde{d}\right]^2_\mu + \left[d^\dagger \times \tilde{s}\right]^2_\mu \pm \frac{\sqrt{7}}{2}\left[d^\dagger \times \tilde{d}\right]^2_\mu. \end{aligned} \tag{3.40}$$

It can be proven that they close under the U(3) algebra using the commutation relations. Furthermore, we can notice that the $\hat{G}_{00}(0,0) + \sqrt{5}\hat{G}_{00}(2,2)$ operator, is the total number operator $\hat{N}$, which means that in the particular case of an application to nuclei with

conserved total N, the algebra SU(3) is more convenient,

$$\begin{aligned}
&\hat{G}_{1\mu}(2,2) = \left[d^\dagger \times \tilde{d}\right]^1_\mu, \\
&\hat{G}_{2\mu}(0,2) + \hat{G}_{2\mu}(2,0) \pm \frac{\sqrt{7}}{2}\hat{G}_{2\mu}(2,2) = \\
&\quad \left[s^\dagger \times \tilde{d}\right]^2_\mu + \left[d^\dagger \times \tilde{s}\right]^2_\mu \pm \frac{\sqrt{7}}{2}\left[d^\dagger \times \tilde{d}\right]^2_\mu,
\end{aligned} \tag{3.41}$$

where again O(3) is a subalgebra formed by,

$$\hat{G}_{1\mu}(2,2) = \left[d^\dagger \times \tilde{d}\right]^1_\mu. \tag{3.42}$$

Resulting in the chain of subalgebras,

$$\begin{array}{ccccc}
\mathrm{U}(6) & \supset & \mathrm{SU}(3) & \supset & \mathrm{O}(3) \\
\downarrow & & \downarrow & & \downarrow \\
[N] & & (\lambda,\mu), \tilde{\chi} & & L
\end{array} \tag{3.43}$$

3.6.3 Boson Subalgebra III

The third possibility is to consider the following 15 operators which close under the O(6) algebra of orthogonal transformations.

$$\begin{aligned}
&\hat{G}_{1\mu}(2,2) = \left[d^\dagger \times \tilde{d}\right]^1_\mu, \\
&\hat{G}_{3\mu}(2,2) = \left[d^\dagger \times \tilde{d}\right]^3_\mu, \\
&\hat{G}_{2\mu}(0,2) + \hat{G}_{2\mu}(2,2) = \left[s^\dagger \times \tilde{d} + d^\dagger \times \tilde{s}\right]^2_\mu,
\end{aligned} \tag{3.44}$$

where if the generators $\hat{G}_{2\mu}(0,2) + \hat{G}_{2\mu}(2,2)$ are deleted, we encounter the 10 generators of the O(5) algebra:

$$\begin{aligned}
\hat{G}_{1\mu}(2,2) &= \left[d^\dagger \times \tilde{d}\right]^1_\mu, \\
\hat{G}_{3\mu}(2,2) &= \left[d^\dagger \times \tilde{d}\right]^3_\mu.
\end{aligned} \tag{3.45}$$

Where again, O(3) is a subalgebra,

$$\hat{G}_{1\mu}(2,2) = \left[d^\dagger \times \tilde{d}\right]^1_\mu. \tag{3.46}$$

This results in the following chain of subalgebras, that will be detailed in the following

sections,

$$\begin{array}{ccccccc} U(6) & \supset & O(6) & \supset & O(5) & \supset & O(3) \\ \downarrow & & \downarrow & & \downarrow & & \downarrow \\ [N] & & \sigma & & \tau, \nu_\Delta & & L \end{array} \tag{3.47}$$

3.7 Basis States of Every Algebra

The main reason for obtaining the set of nested subalgebras exposed before is that they allow constructing basis in which the Hamiltonian operator can be diagonalized. For constructing a basis, the main problem that needs to be addressed is the decomposition of the representation $[N]$ of U(6) into representations of subgroups, which we now present its solution for every chain of subalgebras.

3.7.1 Chain I

The quantum numbers that characterize the representation of groups appearing in this chain are [57]

$$\begin{aligned} &\mathrm{U}(6) \quad [N,0,0,0,0,0] \equiv [N], \\ &\mathrm{U}(5) \quad (n_\mathrm{d},0,0,0,0) \equiv (n_\mathrm{d}), \\ &\mathrm{O}(5) \quad (\nu,0) \equiv \nu, \\ &O(3) \quad L. \end{aligned} \tag{3.48}$$

Note that we are considering only fully symmetric irreducible representations.

Given a certain representation of U(6), $[N]$, the values n_d are obtained as

$$n_d = N, N-1, ...1, 0 \tag{3.49}$$

and the values of ν in that certain representation of U(5)

$$\nu = n_d, n_d - 2, ..., 1 \quad or \quad 0. \tag{3.50}$$

The representations of U(6), U(5), and O(3) are all completely symmetric, so there is no ambiguity in how the states are labeled in these groups.

When reducing O(5) to O(3), a more subtle issue appears, namely, a single O(5) representation, labeled by the quantum number ν, may contain several different states with the same angular momentum L. This means that the labels provided by O(5) are not sufficient to uniquely identify all states once the reduction to O(3) is performed.

In general, when this happens for a group reduction G to G', one says that G is not fully reducible with respect to G'. In this case, O(5) is not fully reducible with respect to

O(3).

To uniquely classify the states, an additional quantum number is required. There are infinitely many possible ways to choose this quantum number, but for classification purposes it is convenient to choose it as the number of boson triplets coupled to zero angular momentum, denoted by n_Δ.

To determine the values of L contained in each O(5) representation ν, the following algorithm is followed,

$$n_d = 2n_\beta + 3n_\Delta + \lambda, \tag{3.51}$$

where,

$$n_\beta = (n_d - \nu)/2. \tag{3.52}$$

Considering the values that ν takes in the equation (3.50), then n_β

$$n_\beta = 0, 1, ..., n_d/2 \quad or \quad (n_d - 1)/2, \tag{3.53}$$

and

$$L = \lambda, \lambda + 1, ..., 2\lambda - 2, 2\lambda. \tag{3.54}$$

This can be written in the following scheme

$$\begin{array}{ccccccc} U(6) & \supset & U(5) & \supset & O(5) & \supset & O(3) \\ \downarrow & & \downarrow & & \downarrow & & \downarrow \\ [N] & & n_d & & \nu, n_\Delta & & L \end{array} \tag{3.55}$$

As an example, the values of the quantum numbers for $N = 1, 2$ and 3 are included in table 3.1.

3.7.2 Chain II

In this case the labels needed to classify the states in this chain are [58]

$$\begin{array}{rl} \mathrm{U}(6) & [N, 0, 0, 0, 0, 0] \equiv [N], \\ \mathrm{SU}(3) & (\lambda, \mu), \\ O(3) & L. \end{array} \tag{3.56}$$

Thus, a generic state can be fully specified by the set of quantum numbers

$$|[N]\,(\lambda, \mu)\,\kappa\,L\rangle\,. \tag{3.57}$$

U(6) N	U(5) n_{d}	O(5) v	$\tilde{n}_\Delta$	O(3) L
1	0	0	0	0
	1	1	0	2
2	0	0	0	0
	1	1	0	2
	2	2	0	4, 2
		0	0	0
3	0	0	0	0
	1	1	0	2
	2	2	0	4, 2
		0	0	0
	3	3	0	6, 4, 3
			1	0
		1	0	2

Table 3.1: Quantum numbers for the group chain I.

The allowed values of the labels $(\lambda, \mu, \kappa, L)$ can be obtained from the structure of Elliott's SU(3) model and are summarized as

$$(\lambda, \mu) = \big(2N - 4n_x - 6n_y,\ 2n_x\big), \tag{3.58}$$

where $n_x, n_y = 0, 1, 2, \ldots$ satisfy the condition

$$2N - 4n_x - 6n_y \geq 0. \tag{3.59}$$

The remaining labels are defined as follows:

$$\kappa = \min\{\lambda, \mu\},\ \min\{\lambda, \mu\} - 2, \ldots, 1 \text{ or } 0, \tag{3.60}$$

$$L = \kappa,\ \kappa + 1,\ \ldots,\ \kappa + \max\{\lambda, \mu\}, \qquad (\kappa \neq 0), \tag{3.61}$$

$$L = 0,\ 2,\ 4,\ \ldots,\ \max\{\lambda, \mu\}, \qquad (\kappa = 0). \tag{3.62}$$

Here, κ is sometimes referred to as the *missing label*. The set of states defined by these quantum numbers constitutes the so-called Elliott basis [59], which is not orthogonal in its original form. By applying an appropriate orthogonalization procedure, one obtains the Vergados basis [60], in which the label K emerges as a specific combination of κ values.

Schematically, we can write again

$$\begin{array}{ccccc} U(6) & \supset & SU(3) & \supset & O(3) \\ \downarrow & & \downarrow & & \downarrow \\ [N] & & (\lambda,\mu),\kappa & & L \end{array} \tag{3.63}$$

As an example, the values of the quantum numbers for $N = 1, 2$ and 3 are included in Table 3.2.

U(6) N	SU(3) (λ,μ)	κ	O(3) L
0	(0,0)	0	0
1	(2,0)	0	2,0
2	(4,0)	0	4, 2, 0
	(0,2)	0	2, 0
3	(6,0)	0	6, 4, 2, 0
	(2,2)	0	4, 2, 0
	(2,2)	2	3, 2
	(0,0)	0	0

Table 3.2: Quantum numbers for the group chain II.

3.7.3 Chain III

The labels that are needed to characterize the representations of the group in this chain are [61]:

$$\begin{array}{ll} \mathrm{U}(6) & [N,0,0,0,0,0] \equiv [N], \\ \mathrm{O}(6) & (\sigma,0,0,0) \equiv (n_{\mathrm{d}})\,, \\ \mathrm{O}(5) & (\tau,0) \equiv \tau, \\ O(3) & L. \end{array} \tag{3.64}$$

So, the basis state is

$$|[N]\,\sigma\,\tau\,\nu_\Delta\,L\rangle\,. \tag{3.65}$$

The possible values of the quantum number σ are then,

$$\sigma = N, N-2, ..., 1, \quad or \quad 0, \tag{3.66}$$

and the values of τ given the O(6) representation are,

$$\tau = \sigma, \sigma - 1, ..., 0, 1. \tag{3.67}$$

Again, the step from O(5) to O(3) is not fully reducible, and an additional quantum number is needed, that will be ν_Δ, which verifies,

$$\tau = 3\nu_\Delta + \lambda, \quad \nu_\Delta = 0, 1, ... \tag{3.68}$$

and now the quantum number L

$$L = \lambda, \lambda + 1, ..., 2\lambda - 2, 2\lambda. \tag{3.69}$$

Finally, the complete classification scheme for chain III can be written as,

$$\begin{array}{ccccccc} U(6) & \supset & O(6) & \supset & O(5) & \supset & O(3) \\ \downarrow & & \downarrow & & \downarrow & & \downarrow \\ [N] & & \sigma & & \tau, \nu_\Delta & & L \end{array} \tag{3.70}$$

Moreover, the algorithm previously written gives as a result the quantum numbers presented in table 3.3.

U(6) N	O(6) σ	O(5) τ	ν_Δ	O(3) L
0	0	0	0	0
1	1	1	0	2
	1	0	0	0
2	0	0	0	0
	1	1	0	2
	2	2	0	4, 2
3	3	3	0	6, 4, 3
		3	1	0
		2	0	4, 2
		1	0	2
		0	0	0
	1	1	0	2
		0	0	0

Table 3.3: Quantum numbers for the group chain III.

3.8 Dynamical Symmetries, Casimir Operators and Group Chains in the Interacting Boson Model

Within the framework of the IBM, the Hamiltonian in its most general form typically requires numerical diagonalization in one of the basis explained before. However, under certain conditions, the problem becomes analytically tractable. These special situations, known as *dynamical symmetries*, occur when the Hamiltonian can be expressed entirely in terms of *Casimir operators* of a nested chain of groups:

$$G \supset G' \supset G'' \supset \cdots \tag{3.71}$$

3.8.1 Casimir Operators and Group Chains

Definition:

For a given Lie algebra with generators $\{X_a\}$, a *Casimir operator* $\hat{C}$ is defined as

$$\hat{C}, X_a] = 0 \quad \forall\, a. \tag{3.72}$$

Casimir operators are invariants of the group: they commute with all elements of the algebra and therefore are constant within a given irreducible representation. The rank of the algebra equals the number of independent Casimir operators, corresponding to the number of integer labels that specify its irreducible representations.

Order of Casimir Operators:

Casimir operators are classified by their order, p, in the generators, denoted $\hat{C}_p(G)$. Some examples are:

- First-order: proportional to the total number operator.
- Second-order: quadratic forms such as L^2 in O(3).
- Higher-order: cubic, quartic, etc., combinations.

Only unitary groups U(n) possess first-order invariants.

3.9 Hamiltonian in Terms of Casimir Operators

In IBM-1, the dynamical algebra is U(6) and its possible nested subalgebras finishing in O(3), as explained in previous sections are,

$$U(6) \supset U(5) \supset O(5) \supset O(3), \quad U(6) \supset SU(3) \supset O(3), \quad U(6) \supset O(6) \supset O(5) \supset O(3).$$

The eigenvalues of the corresponding Casimir operators are,

$$\langle \hat{C}_1[U(6)] \rangle = \hat{N} = \hat{n}_s + \hat{n}_d, \tag{3.73}$$
$$\langle \hat{C}_2[O(3)] \rangle = L(L+1), \tag{3.74}$$
$$\langle \hat{C}_2[SU(3)] \rangle = \lambda^2 + \mu^2 + \lambda\mu + 3(\lambda + \mu), \tag{3.75}$$
$$\langle \hat{C}_2[O(6)] \rangle = \sigma(\sigma + 4), \tag{3.76}$$
$$\langle \hat{C}_2[O(5)] \rangle = \nu(\nu + 3). \tag{3.77}$$

An important consequence is that the most general IBM-1 Hamiltonian up to quadratic order can be expressed as

$$H = \sum_i \alpha_i \, \hat{C}_{p_i}(G_i), \tag{3.78}$$

where G_i are the groups that belong to the relevant nested chains. If all G_i belong to the same chain, H is diagonal in that chain's basis, and the eigenvalues are given directly by the Casimir eigenvalues. Otherwise, a numerical diagonalization is required.

3.9.1 Energy Eigenvalues in the Three Dynamical Symmetry Chains

$U(5)$ Chain: Vibrational Limit

In this symmetry limit, the most general Hamiltonian written in terms of the Casimir operators is,

$$H = e_0 + e_1\hat{C}_1(U(6)) + e_2\hat{C}_2(U(6)) + \epsilon\hat{C}_1(U(5)) + \alpha\hat{C}_2(U(5)) + \beta\hat{C}_2(O(5)) + \gamma\hat{C}_2(O(3)). \tag{3.79}$$

and their eigenvalues are,

$$E\,(N, n_d, v, n_\Delta,\ L, M_L) = E_0 + \epsilon n_d + \alpha n_d(n_d+4) + \beta\nu(\nu+3) + \gamma\, L(L+1), \tag{3.80}$$

where in E_0 has been included

$$E_0 = e_0 + e_1 N + e_2 N(N+5). \tag{3.81}$$

The structure of this expression shows that, in the U(5) limit, the energy levels are mainly organized according to the d-boson number n_d, with smaller splittings coming from the O(5) and O(3) quantum numbers. This behavior can be clearly seen in Fig. 3.2, where the energy spectrum for $N = 4$ bosons is displayed.

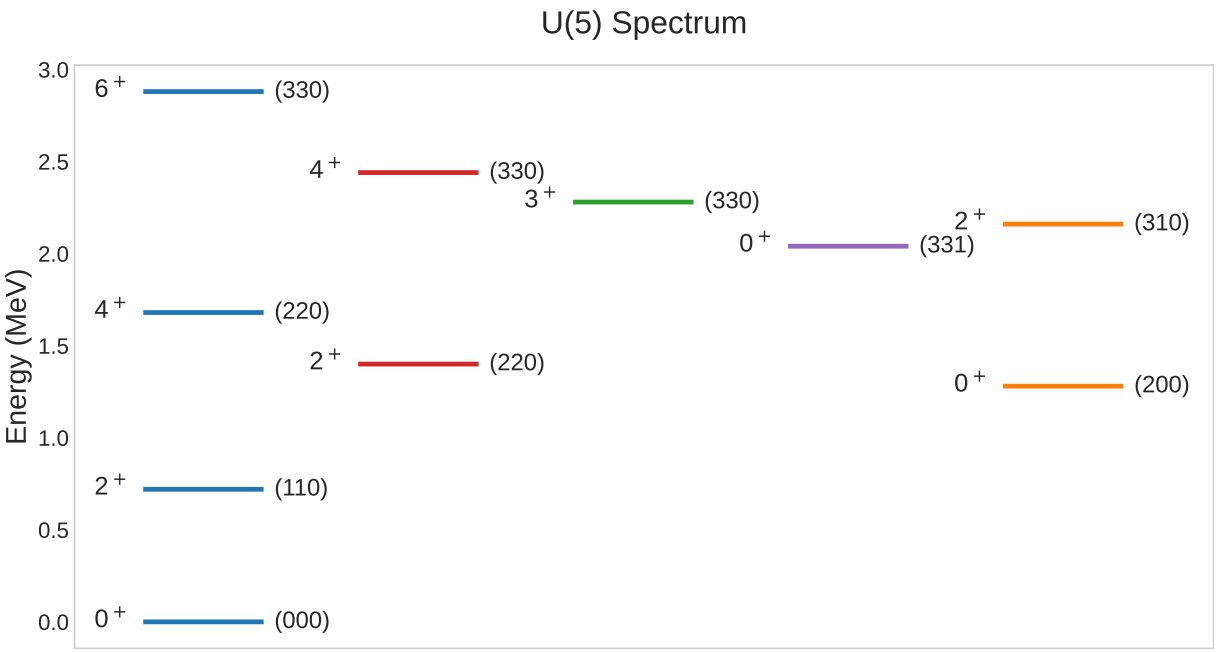

Figure 3.2: Energy spectrum in the U(5) dynamical symmetry of the IBM for $N = 4$ bosons. Levels are arranged in columns according to the d-boson number n_d. Each horizontal line represents a state with angular momentum L^+ (shown on the left), while the labels on the right indicate the quantum numbers $(n_d\, v\, n_\Delta)$. The ground-state energy is shifted to zero.

SU(3) Chain: Rotational Limit

In this case, the Hamiltonian that we are considering in terms of Casimir operators:

$$H = e_0 + e_1\hat{C}_1(U(6)) + e_2\hat{C}_2(U(6)) + \delta\hat{C}_2(SU(3)) + \gamma\,\hat{C}_2(O(3)). \tag{3.82}$$

Again, this Hamiltonian is diagonal in the basis 3.63, which gives the following energy eigenvalues:

$$E^{(II)}\left(N, \lambda, \mu, \tilde{\chi}, L, M_L\right) = E_0 + \gamma L(L+1) + \delta\left(\lambda^2 + \mu^2 + \lambda\mu + 3\lambda + 3\mu\right), \tag{3.83}$$

and the value of E_0 is given by equation (3.81).

From this expression it follows that, in the SU(3) limit, the energies are mainly determined by the SU(3) quantum numbers (λ, μ), while the angular momentum term produces the rotational splitting within each SU(3) multiplet. This characteristic structure is illustrated in Fig. 3.3, which shows the energy spectrum for $N = 3$ bosons.

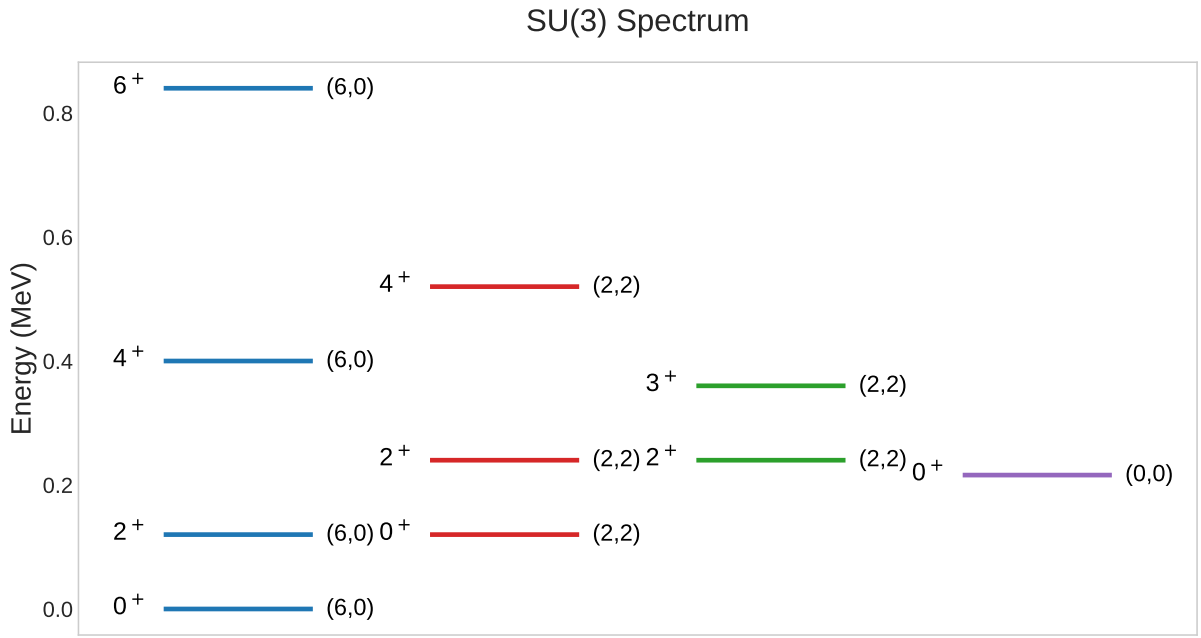

Figure 3.3: Energy spectrum in the SU(3) dynamical symmetry of the IBM for $N = 3$ bosons. Levels are displayed in separate columns following the SU(3) irreducible representations. The angular momentum L^+ is indicated on the left of each level, and the labels on the right correspond to the SU(3) quantum numbers (λ, μ). Energies are normalized such that the lowest state is located at zero.

O(6) Chain: γ-Unstable Rotational Limit

The Hamiltonian considered is,

$$H = e_0 + e_1\hat{C}_1(U(6)) + e_2\hat{C}_2(U(6)) + \eta\hat{C}_2(O(6)) + \beta\,\hat{C}_2(O(5)) + \gamma\,\hat{C}_2(O(3)). \tag{3.84}$$

The energy eigenvalues obtained in the basis 3.47 are,

$$E^{(III)}\,(N, \sigma, \tau, \nu_\Delta, L, M_L) = E_0 + \beta\tau(\tau+3) + \gamma L(L+1) + \eta\sigma(\sigma+4), \tag{3.85}$$

This expression shows that, in the O(6) limit, the spectrum is mainly organized according to the O(6) quantum number σ, with additional splittings associated with the O(5) quantum number τ and the angular momentum L. This structure is illustrated in Fig. 3.4, where the energy spectrum for $N = 3$ bosons is shown.

3.10 Intrinsic State Formalism for the IBM

The IBM possesses an intrinsic geometric structure, a characteristic shared by all models with a well-defined underlying group G. Each group is associated with an algebra $\mathfrak{g}$ and a topology, which together define the possible geometric properties of the system.

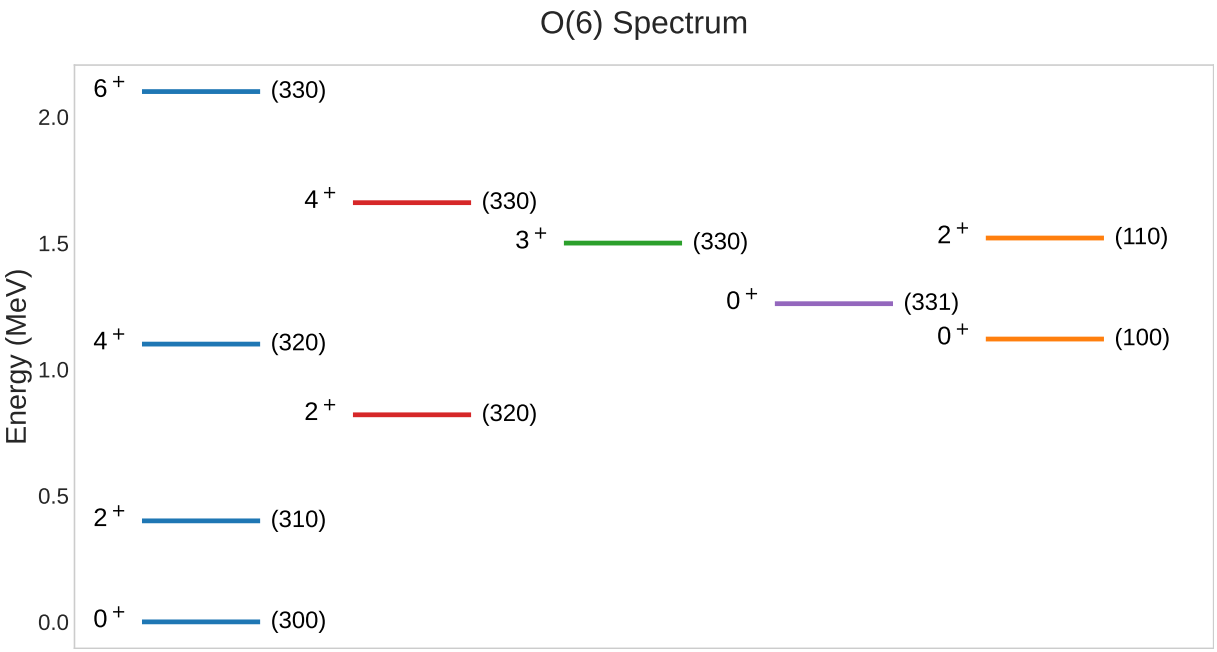

Figure 3.4: Energy spectrum in the O(6) dynamical symmetry of the IBM for $N = 3$ bosons. States are arranged in columns according to their position in the O(6) chain. Each level is labeled by its angular momentum L^+ on the left, while the right-hand labels indicate the quantum numbers $(\sigma\,\tau\,n_\Delta)$. The ground state is taken as the zero of energy.

The geometric approach is important because it enables a direct connection between the IBM and the description of collective nuclear states through shape variables (β, γ), originally introduced by Bohr and Mottelson [2, 3, 62]. Furthermore, coherent or intrinsic states form the central mathematical tool for exploring both static and dynamical properties within this geometric framework.

3.10.1 Coherent States

In practice, it is more convenient to use a type of coherent state, known as "projective state", to work with the geometric properties of the IBM. In relation with the collective model, they were introduced by Bohr and Mottelson [62], Ginocchio and Kirson [63] and Dieperink, Scholten and Iachello [64]. The projective coherent states, better known as intrinsic states are:

$$|N;\alpha_\mu\rangle = \left(s^\dagger + \sum_\mu \alpha_\mu d^\dagger_\mu\right)^N |0\rangle, \tag{3.86}$$

where α_μ are five complex parameters.

This set of parameters can be used to study both static or dynamic problems, with the essential difference that for static problem α_μ is a real parameter while for dynamic must be taken as complex.

In the first place, we will address static problems, where α_μ can be expressed in terms

of Euler angles $(\theta_1, \theta_2, \theta_3)$ defining the intrinsic frame orientation, and the Bohr shape variables (β, γ),

$$\alpha_\mu = \sum_\nu a_\nu \mathcal{D}^{(2)}_{\mu\nu}(\Omega). \tag{3.87}$$

Being $\mathcal{D}^{(2)}_{\mu\nu}$ the Wigner-$\mathcal{D}$ function and $\Omega = (\theta_1, \theta_2, \theta_3)$ are the Euler angles and

$$a_0 = \beta \cos\gamma, \tag{3.88}$$

$$a_{\pm 2} = \frac{\beta}{\sqrt{2}} \sin\gamma, \tag{3.89}$$

$$a_{\pm 1} = 0, \tag{3.90}$$

Now, in terms of the intrinsic variables β, γ the intrinsic state is written as:

$$|N : \beta, \gamma\rangle = \frac{1}{\sqrt{N!}} \left(\frac{1}{\sqrt{1+\beta^2}} \left(s^\dagger + \beta \cos\gamma \, d^\dagger_0 + \frac{1}{\sqrt{2}} \beta \sin\gamma \, (d^\dagger_2 + d^\dagger_{-2}) \right) \right)^N |0\rangle, \tag{3.91}$$

Once defined the intrinsic state it is possible to evaluate many nuclear properties, such as the ground state energy,

$$E(N; \beta, \gamma) = \frac{\langle N; \beta, \gamma | H | N; \beta, \gamma \rangle}{\langle N; \beta, \gamma | N; \beta, \gamma \rangle}, \tag{3.92}$$

where H must is the IBM Hamiltonian.

It is also possible to obtain the equilibrium shape of the system. For doing so, $E(N; \beta, \gamma)$ must be minimized with respect to β and γ.

The expectation value of the Hamiltonian in an intrinsic state defines the energy surface. Moreover, minimization with respect to β and γ yields the equilibrium shape. This procedure, analogous to the Hartree–Fock method, is known as the *Hartree–Bose* approach.

For the most general Hamiltonian H, which can be obtained using the method detailed in Appendix B, the energy surface reads,

$$\begin{aligned} E(N; \beta, \gamma) =& E_0 + \frac{N}{(1+\beta^2)} \left(\varepsilon_{\mathrm{s}} + \varepsilon_{\mathrm{d}} \beta^2 \right) \\ &+ \frac{N(N-1)}{(1+\beta^2)^2} \left(f_1 \beta^4 + f_2 \beta^3 \cos 3\gamma + f_3 \beta^2 + \frac{1}{2} u_0 \right), \end{aligned} \tag{3.93}$$

with

$$\begin{aligned} f_1 &= \frac{1}{10}c_0 + \frac{1}{7}c_2 + \frac{9}{35}c_4, \\ f_2 &= -2\left(\frac{1}{35}\right)^{\frac{1}{2}}\tilde{v}_2, \\ f_3 &= \left(\frac{1}{5}\right)^{\frac{1}{2}}(\tilde{v}_0 + u_2), \end{aligned} \tag{3.94}$$

where it is important to notice that those variables β and γ are not the same as the ones introduced by Bohr and Mottelson, but are related in the following way,

$$\begin{aligned} \gamma_{CM} &= \gamma_{IBM}, \\ \beta_{CM} &= c\,\beta_{IBM}. \end{aligned} \tag{3.95}$$

3.10.2 Shape Structure of the Dynamical Symmetries

The three dynamical symmetry chains of the IBM lead to distinct equilibrium geometries.

Chain I (U(5) limit). The energy functional is γ-independent and its minimization leads to $\beta = 0$, corresponding to a spherical shape. In the (β, γ) plane, lines of equal energy are concentric circles, meaning an spherical nucleus. The expression for the mean field energy in this case equals to

$$E_{U(5)}(N;\beta,\gamma) = E_0 + \epsilon_d N\frac{\beta^2}{1+\beta^2} + f_1 N(N-1)\frac{\beta^4}{(1+\beta^2)^2}. \tag{3.96}$$

This limit is known as the vibrational limit, due to the fact that the only collective behavior possible are vibrations.

Chain II (SU(3) limit). Considering a Hamiltonian composed by the terms:

$$H = -\kappa'\hat{C}_2[O(3)] - \kappa\hat{Q}\cdot\hat{Q}, \tag{3.97}$$

with $\chi = -\sqrt{7}/2$ to have explicitly the second order SU(3) Casimir operator, the energy functional is,

$$\begin{aligned} E(N;\beta,\gamma)_{SU(3)} = &-2\kappa\left[\frac{N}{1+\beta^2}\left(5+\frac{11}{4}\beta^2\right) + \frac{N(N-1)}{(1+\beta^2)^2}\right. \\ &\left.\times\left(\frac{\beta^4}{2} + 2\sqrt{2}\beta^3\cos 3\gamma + 4\beta^2\right)\right] - \kappa'\frac{6N\beta^2}{1+\beta^2}. \end{aligned} \tag{3.98}$$

Observing this functional, we may take notice that the minimum occurs at $\gamma = 0°$ and

$\beta \neq 0$, representing an axially symmetric prolate shape. A sign change in the χ parameter of the quadrupole operator reverses the symmetry to $\gamma = 60°$ (oblate shape). Furthermore, in the case of $N \to \infty$, the value of beta obtained is $\beta_0 = \sqrt{2}$. This limit is known as the rotational limit and both vibrations and rotations are possible.

Chain III (O(6) limit). Considering the Hamiltonian,

$$H = A\hat{P}^{\dagger}\hat{P} + C\hat{C}_2[O(3)] + B\hat{C}_2[O(5)], \tag{3.99}$$

The resulting energy is,

$$E(N;\beta,\gamma)_{O(6)} = (144B + 6C)\frac{N\beta^2}{1+\beta^2} + \frac{A}{4}N(N-1)\left(\frac{1-\beta^2}{1+\beta^2}\right)^2, \tag{3.100}$$

The energy is γ-independent but minimized at $\beta \neq 0$, corresponding to a γ-soft deformed shape. In the limit $N \to \infty$ the equilibrium value of β is $\beta_0 = 1$. Finally, in this case, known as γ-unstable, the only possible collective excitations are the β-vibrations and the rotations.

3.11 The Interacting Boson Model with Configuration Mixing Formalism

In the case of a large number of nuclei, when studying the experimental data of the same energy region, it is possible to find different structures coexisting in the spectrum. These structures, that may appear close in energy, cannot be treated as independent, due to the interactions between them, which lead to observable configuration mixing.

With the objective of describing how these different configurations affect the global description of nuclei, the IBM-CM is introduced. This model constitutes a natural extension of the original IBM [11]. Its essential feature is the possibility of treating, within the same algebraic framework, different bosonic configurations that correspond to different particle–hole excitations across a closed shell or subshell [31, 65]. By doing so, the IBM-CM provides a powerful scheme to describe phenomena such as shape coexistence and configuration mixing.

The philosophy of the method is based on performing a general description of both configurations within the IBM, and then mixing the results obtained through an appropriate IBM mixing Hamiltonian

To describe the technique, it is necessary to keep in mind that in the IBM works with valence nucleons treated as bosons.This means that the total number of bosons, N, is ob-

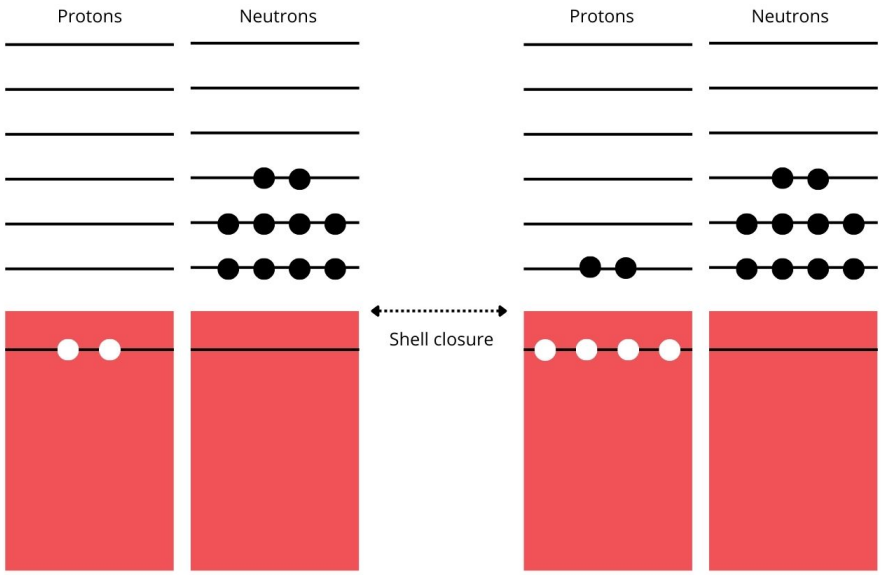

Figure 3.5: Example of a regular proton and neutron configuration (left side) and the same nucleus when a proton pair has been excited across the shell. White dots refers to hole, while black ones refer to particles

tained as one half of the total number of valence nucleons, counting protons and neutrons, regardless its particle or hole character i.e.,

$$N = \tfrac{1}{2}\big(N_\pi + N_\nu\big), \tag{3.101}$$

where N_π and N_ν denote the number of valence protons and neutrons, respectively.

As we introduced earlier, two simultaneous structures arising from different boson configurations are considered. These configurations will be named as regular or intruder configuration, where the regular one comes from the standard IBM picture while the intruder has its origin in exciting a pair of fermions above the shell gap. This is schematically depicted in Fig. 3.5

This means that the Hilbert space for the resulting Hamiltonian is (taking into account the two extra bosons from the intruder configuration) the direct sum

$$\mathcal{H} = [N] \ \oplus \ [N+2]. \tag{3.102}$$

Moreover, as we also expect to have some mixing between configurations, it is necessary to introduce a part to reproduce this behavior. In the cases treated in this thesis, this

term is considered as the most general, composed by two terms as follows,

$$\hat{V}_{\rm mix}^{N,N+2} = \omega_0^{N,N+2}\left(s^\dagger \times s^\dagger + s \times s\right)^{(0)} + \omega_2^{N,N+2}\left(d^\dagger \times d^\dagger + \tilde{d} \times \tilde{d}\right)^{(0)}, \tag{3.103}$$

where $\omega_0^{N,N+2}$ and $\omega_2^{N,N+2}$ denote the mixing strengths, respectively.

We also need to introduce a new parameter which gives the energy needed to excite a boson into the next major shell, this will be the parameter that will be represented as Δ

Accordingly, the Hamiltonian of the IBM-CM is written as

$$\hat{H} = \hat{P}_N^\dagger\, \hat{H}^{(N)}\, \hat{P}_N \;+\; \hat{P}_{N+2}^\dagger \left(\hat{H}^{(N+2)} + \Delta^{N+2}\right) \hat{P}_{N+2} \;+\; \hat{V}_{\rm mix}^{N,N+2}, \tag{3.104}$$

where $\hat{P}_N$ and $\hat{P}_{N+2}$ are projection operators onto the $[N]$ and $[N+2]$ boson subspaces, respectively, and $\hat{H}^{(N)}$ and $\hat{H}^{(N+2)}$ are the corresponding Hamiltonians.

Moreover, here the operators $\hat{H}^{(i)}_{\rm ECQF}$ $(i = N,\, N+2)$ denote the so-called *extended consistent-Q Hamiltonians* (ECQF) [56], where the definition that we will use is:

$$\hat{H}^{(i)}_{\rm ECQF} = \epsilon_i\, \hat{n}_d + \kappa_i'\, \hat{L}\cdot\hat{L} + \kappa_i\, \hat{Q}(\chi_i)\cdot\hat{Q}(\chi_i), \tag{3.105}$$

with $\hat{n}_d$ the d-boson number operator, $\hat{L}$ the angular momentum operator, and $\hat{Q}(\chi_i)$ the quadrupole operator,

$$\hat{Q}_\mu(\chi_i) = \left[s^\dagger \times \tilde{d} + d^\dagger \times s\right]^{(2)}_\mu + \chi_i \left[d^\dagger \times \tilde{d}\right]^{(2)}_\mu. \tag{3.106}$$

The parameter Δ^{N+2} represents the energy cost to promote two protons across the shell gap (a $2p$-$2h$ excitation), corrected for pairing correlations and monopole shifts

The interaction term $\hat{V}_{\rm mix}^{N,N+2}$ mixes the two boson configurations and is given by Eq. (3.103).

Furthermore, electromagnetic properties which can be described using the E2 transition operator, constructed consistently with the quadrupole operators employed in the Hamiltonian, are in the IBM-CM frame described as:

$$\hat{T}(E2) = \sum_{i=N,N+2} e_i\, \hat{P}_i^\dagger\, \hat{Q}(\chi_i)\, \hat{P}_i, \tag{3.107}$$

where e_i are effective boson charges for the regular and intruder sectors. Importantly, here no cross terms are included, so that E2 transitions are generated independently within each subspace.

In summary, the IBM-CM formalism provides an approach to describe nuclei in regions

where regular and intruder configurations coexist. By incorporating explicit configuration mixing, the model is capable of reproducing not only spectra but also transition rates and properties that cannot be captured within the standard IBM framework.

Chapter 4

The Interacting Boson Fermion Model

The IBM has shown to be a powerful framework for describing the collective properties of nuclei, due to its algebraic structure and its connection with the shell model. The IBM is designed to deal with even-even nuclei. However, it must not be forgotten that more than a half of nuclear species have an odd number of protons and/or neutrons. In those nuclei it is also important to take into consideration the interplay between collective (bosonic) and single-particle (fermionic) degrees of freedom. Under this conditions, it was necessary to extend the IBM into the IBFM.

The IBFM offers a powerful algebraic framework to describe the structure of odd-mass nuclei by coupling collective bosonic degrees of freedom, associated with correlated pairs of valence nucleons, to a single unpaired fermion. In this way the IBFM has proven to be an useful tool successfully reproducing low-lying collective excitations as well as single-particle features in a range of nuclei.

Within the IBM, studies of phenomena like shape coexistence are incorporated through the IBM-CM, which allows for the coexistence and interaction of different boson spaces corresponding to regular ($0p$–$0h$) and intruder ($2p$–$2h$) excitations across closed shells. Extending this concept to odd-mass systems leads naturally to the IBFM-CM, a recently developed formalism that unifies bosonic collective dynamics, single-fermion motion, and configuration mixing effects within a single algebraic framework [35, 66, 67].

From a geometric perspective, the IBFM-CM is particularly appealing because it permits the analysis of energy surfaces, equilibrium shapes, and shape coexistence in odd-mass nuclei in direct analogy with the intrinsic-state formalism of the IBM-CM [68, 69, 41]. In the present thesis, we extend the intrinsic-state methodology originally developed for the IBM-CM to the IBFM-CM, establishing a consistent boson–fermion intrinsic-state

formalism. This development enables the systematic study of shape coexistence, intruder band formation, and collective–single particle interplay in odd-mass nuclei from both an algebraic and a geometric point of view.

Historically, the intrinsic-state formalism of the IBFM was first introduced in the seminal contributions of [70, 71]. The earliest formulation in [70] was restricted to a single-j shell, allowing only for axial shapes. Later, in [71] the formalism was generalized to multi-j shells, but not considering triaxiality.

In more recent studies [43, 44], the intrinsic-state approach has been employed to investigate the role of the odd fermion in the context of QPTs [72]. These works demonstrated that the unpaired particle can significantly alter the collective dynamics, either reinforcing or suppressing the occurrence of a QPT, depending on the details of the boson–fermion coupling and the underlying shell structure.

The formalism presented here represents a significant advancement for several reasons: it is a formalism constructed for the IBFM-CM that (i) is applicable to both single- and multiple-j shells, (ii) consistently incorporates both axial and triaxial shapes, and (iii) explicitly accounts for configuration mixing effects. As such, it provides a theoretical tool to study the interplay of shape coexistence and configuration mixing in odd-mass nuclei.

4.1 Boson and Fermion Operators

In the interacting boson-fermion model, the collective degrees of freedom are described using the boson operators already described in chapter 3, that interact with the single particle degrees of freedom. As single particles that will be considered are fermions (protons or neutrons), the formalism of second quantization is necessary, introducing in this way the fermion creation and annihilation operators

$$\begin{aligned} &a^\dagger_{j,m}, \quad \left(m = \pm\tfrac{1}{2}, \pm\tfrac{3}{2}, \ldots, \pm j\right), \\ &a_{j,m}, \quad \left(m = \pm\tfrac{1}{2}, \pm\tfrac{3}{2}, \ldots, \pm j\right). \end{aligned} \tag{4.1}$$

These operators satisfy anticommutation relations,

$$\begin{aligned} &\left\{a_{j,m}, a^\dagger_{j',m'}\right\} = \delta_{jj'}\delta_{mm'}, \\ &\{a_{j,m}, a_{j',m'}\} = \left\{a^\dagger_{j,m}, a^\dagger_{j',m'}\right\} = 0, \end{aligned} \tag{4.2}$$

were the curly bracket denotes an anticommutator, i.e., $\{A, B\} = AB + BA$.

Moreover, it is assumed that bosons and fermion operators commute, which is a natural model assumption given that both fermions and bosons are considered as elementary

particles.

In the same way as in the IBM, spherical tensors are constructed, leading to the same problem with annihilation operators that was encountered in the IBM-case, i.e., they are not transforming appropriately under rotations, so in an equivalent way we define,

$$\tilde{a}_{j,m} = (-)^{j-m} a_{j,-m}, \tag{4.3}$$

which transforms appropriately under rotations.

4.1.1 Basis States

As we are working in the framework of second quantization, we need to repeatedly apply creation and annihilation operators on a vacuum state to obtain our basis state.

For bosons, in the same way as in the IBM,

$$b^\dagger_\alpha b^\dagger_{\alpha'} ... \left|0\right\rangle , \tag{4.4}$$

while for fermions,

$$a^\dagger_i a^\dagger_{i'} ... \left|0\right\rangle . \tag{4.5}$$

However, it is necessary to keep in mind that in contrary to bosons, it is not possible to put any number of fermions in a certain state but only one for each, implying that,

$$\left(a^\dagger_i\right)^2 \left|0\right\rangle = 0. \tag{4.6}$$

As a result, all indices for fermions must differ, and the resulting boson-fermion state is written in its general form as,

$$a^\dagger_i a^\dagger_{i'} ... b^\dagger_\alpha b^\dagger_{\alpha'} ... \left|0\right\rangle . \tag{4.7}$$

Moreover, to construct states with good angular momentum we couple fermion and boson operators in the same way as we did in the basis state of the IBM,

$$\left[\left[a^\dagger_j \times a^\dagger_{j'} \times \cdots\right]^{(L_\mathbf{F})} \times \left[b^\dagger_l \times b^\dagger_{l'} \times \cdots\right]^{(L_\mathbf{B})}\right]^{(L)}_M \left|0\right\rangle. \tag{4.8}$$

4.2 Physical Operators: Hamiltonian and Transition Operators

4.2.1 Hamiltonian Operator

The IBFM is made for systems that include bosons and fermions, which also interact among themselves. For this reason, the Hamiltonian that will be considered is made of three terms,

$$\hat{H} = \hat{H}_B + \hat{H}_F + \hat{H}_{BF}. \tag{4.9}$$

Being $\hat{H}_B$ the bosonic Hamiltonian, $\hat{H}_F$ the fermionic, and $\hat{H}_{BF}$ the term to account for the interaction between bosons and fermions. The structure of each part of the Hamiltonian is,

$$\begin{aligned} H_{\mathrm{B}} &= E_0 + \sum_{\alpha\beta} \epsilon_{\alpha\beta} b^\dagger_\alpha b_\beta + \sum_{\alpha\alpha'\beta\beta'} \frac{1}{2} u_{\alpha\alpha'\beta\beta'} b^\dagger_\alpha b^\dagger_{\alpha'} b_\beta b_{\beta'} + \cdots , \\ H_{\mathrm{F}} &= \mathcal{E}_0 + \sum_{ik} \eta_{ik} a^\dagger_i a_k + \sum_{ii'kk'} \frac{1}{2} v_{ii'kk'} a^\dagger_i a^\dagger_{i'} a_k a_{k'} + \cdots , \\ V_{\mathrm{BF}} &= \sum_{\alpha i\beta k} w_{\alpha i\beta k} b^\dagger_\alpha a^\dagger_i b_\beta a_k + \cdots . \end{aligned} \tag{4.10}$$

These expressions can be rewritten in order to get a Hamiltonian invariant under rotations as,

$$\begin{aligned} H_{\mathrm{B}} =& E_0 + \sum_l \epsilon_l \sqrt{2l+1} \left[b^\dagger_l \times \tilde{b}_l \right]^{(0)}_0 \\ &+ \sum_{L_{\mathrm{B}}, ll'l''l'''} \frac{1}{2} u^{(L_{\mathrm{B}})}_{ll'l''l'''} \left[\left[b^\dagger_l \times b^\dagger_{l'} \right]^{(L_{\mathrm{B}})} \times \left[\tilde{b}_{l''} \times \tilde{b}_{l'''} \right]^{(L_{\mathrm{B}})} \right]^{(0)}_0 + \cdots , \\ H_{\mathrm{F}} =& \mathcal{E}_0 - \sum_j \eta_j \sqrt{2j+1} \left[a^\dagger_j \times \tilde{a}_j \right]^{(0)}_0 \\ &+ \sum_{L_{\mathrm{F}}, j'j''j'''} \frac{1}{2} v^{(L_{\mathrm{F}})}_{jj'j''j'''} \left[\left[a^\dagger_j \times a^\dagger_{j'} \right]^{(L_{\mathrm{F}})} \right. \\ &\left. \times \left[\tilde{a}_{j''} \times \tilde{a}_{j'''} \right]^{(L_{\mathrm{F}})} \right]^{(0)}_0 + \cdots , \\ V_{\mathrm{BF}} =& - \sum_{J, lj'j'} w^{(J)}_{ljl'j'} \sqrt{2J+1} \left[\left[b^\dagger_l \times a^\dagger_j \right]^{(J)} \right. \\ &\left. \times \left[\tilde{b}_{l'} \times \tilde{a}_{j'} \right]^{(J)} \right]^{(0)}_0 + \cdots . \end{aligned} \tag{4.11}$$

In equation (4.11), the term $w^{(J)}_{ljl'j'}$ corresponds to the boson-fermion interaction matrix-elements, written as,

$$w^{(J)}_{ljl'j'} = \langle b_l a_j; J | \, V_{\mathrm{BF}} \, | b_{l'} a_{j'}; J \rangle \, . \tag{4.12}$$

As the hermiticity of the Hamiltonian must be imposed, this results in certain restrictions over the parameters of equation (4.11). For example, assuming that the parameters of equation (4.12) are real, they must verify that $w^{(J)}_{ljl'j'} = w^{(J)}_{l'j'lj'}$.

4.2.2 Transition Operators

In the same manner as for the Hamiltonian operator, transition operator also must include a part describing bosons and another one describing fermions,

$$T^{(L)} = T^{(L)}_{\mathrm{B}} + T^{(L)}_{\mathrm{F}}. \tag{4.13}$$

Each of them with the following structure,

$$\begin{aligned} T^{(L)}_{\mathrm{B}} &= t^{(0)}_0 \delta_{L0} + \sum_{\alpha\beta} t^{(L)}_{\alpha\beta} b^\dagger_\alpha b_\beta + \cdots, \\ T^{(L)}_{\mathrm{F}} &= f^{(0)}_0 \delta_{L0} + \sum_{ik} f^{(L)}_{ik} a^\dagger_i a_k + \cdots. \end{aligned} \tag{4.14}$$

Again, if we rewrite transition operators to transform as rank L tensors under rotations, we get,

$$\begin{aligned} T^{(L)}_{\mathrm{B},\mu} &= t^{(0)}_0 \delta_{L0} + \sum_{l'} t^{(L)}_{ll'} \left[b^\dagger_l \times \tilde{b}_{l'} \right]^{(L)}_\mu + \cdots, \\ T^{(L)}_{\mathrm{F},\mu} &= f^{(0)}_0 \delta_{L0} + \sum_{jj'} f^{(L)}_{jj'} \left[a^\dagger_j \times \tilde{a}_{j'} \right]^{(L)}_\mu + \cdots. \end{aligned} \tag{4.15}$$

In addition to their behavior under rotations, electromagnetic transition operators also have a well-defined transformation property under parity.

If we consider only bosons with quantum numbers $J^P = 0^+$ and 2^+, their parity is always positive. As a result, the bosonic part of the transition operator, $T^{(L)}_B$, has positive parity and does not change sign under a parity transformation.

In contrast, the fermionic part of the operator, $T^{(L)}_F$, can have either positive or negative parity, depending on the specific fermion states involved.

4.2.3 The Boson-Fermion Interaction

Although we have given an expression for the boson fermion interaction in (4.11), it is convenient to account for a simpler form, especially for working from a phenomenological point of view, as originally proposed in [19]. In first place, the monopole term is written as,

$$V^{\mathrm{MON}}_{\mathrm{BF}} = \sum_j A_j \left[\left[d^\dagger \times \tilde{d} \right]^{(0)} \times \left[a^\dagger_j \times \tilde{a}_j \right]^{(0)} \right]^{(0)}_0. \tag{4.16}$$

Secondly, the quadrupole term is written as,

$$V_{\rm BF}^{\rm QUAD} = \sum_{jj'} \Gamma_{jj'} \left[\left[\left(s^\dagger \times \tilde{d} + d^\dagger \times \tilde{s} \right) + \chi \left(d^\dagger \times \tilde{d} \right) \right]^{(2)} \times \left[a_j^\dagger \times \tilde{a}_{j'} \right]^{(2)} \right]_0^{(0)}, \tag{4.17}$$

where hermiticity implies that $\Gamma_{jj'} = (-1)^{j-j'}\Gamma_{j'j}$, due to the Clebsch-Gordan symmetry properties.

Finally, an interaction that will be called exchange interaction,

$$V_{\rm BF}^{\rm EXC} = \sum_{jj'j''} \Lambda_{jj'}^{j''} : \left[\left[d^\dagger \times \tilde{a}_j \right]^{(j'')} \times \left[\tilde{d} \times a_{j'}^\dagger \right]^{(j'')} \right]_0^{(0)} :, \tag{4.18}$$

where : stands for normal order. This interaction could also include the following terms,

$$\begin{aligned} V_{\rm BF}^{\rm EXC'} = \sum_{jj'} \Lambda_{jj'}^{\prime j'} : \Bigg\{ & \left[\left[d^\dagger \times \tilde{a}_j \right]^{(j')} \times \left[\tilde{s} \times a_{j'}^\dagger \right]^{(j')} \right]_0^{(0)} \\ & + \left[\left[s^\dagger \times \tilde{a}_{j'} \right]^{(j')} \times \left[\tilde{d} \times a_j^\dagger \right]^{(j')} \right]_0^{(0)} \Bigg\} :, \end{aligned} \tag{4.19}$$

and

$$V_{\rm BF}^{\rm EXC''} = \sum_{j} \Lambda_{jj}^{\prime\prime j} : \left[\left[s^\dagger \times \tilde{a}_j \right]^{(j)} \times \left[\tilde{s} \times a_j^\dagger \right]^{(j)} \right]_0^{(0)} : . \tag{4.20}$$

That in case of considering a single orbit j, they can be both included in equations (4.17) and (4.18).

4.3 Fermion Algebras

Previously, we have discussed the algebras constructed in systems composed uniquely by bosons, however in the framework of the IBFM, it is necessary to introduce algebras built with fermion operators in combination with those built with bosons.

In first place, we consider the set of bilinear products of fermion creation and annihilation operators,

$$g: \quad A_{ik} = a_i^\dagger a_k, \quad (i,k = 1, \ldots, n), \tag{4.21}$$

which commutation relations are,

$$[A_{ik}, A_{st}] = A_{it}\delta_{ks} - A_{sk}\delta_{it}, \tag{4.22}$$

that are the generators of the unitary algebra in n dimensions u(n), that in coupled tensor

notation are,

$$g: \quad A^{(\lambda)}_{\mu}(j,j') = \left[a^{\dagger}_{j} \times \tilde{a}_{j'}\right]^{(\lambda)}_{\mu} \tag{4.23}$$

and satisfy the following commutation relation,

$$\begin{aligned}
&\left[A^{(\lambda)}_{\mu}(j,j'), A^{(\lambda')}_{\mu'}(j'',j''')\right] \\
&\qquad = -\sum_{\lambda''\mu''} \sqrt{(2\lambda+1)(2\lambda'+1)}\,(\lambda\mu\lambda'\mu' \mid \lambda''\mu'') \\
&\qquad \times \left[(-)^{\lambda''+j+j'''} \begin{Bmatrix} \lambda & \lambda' & \lambda'' \\ j''' & j & j' \end{Bmatrix} \delta_{j'j''} A^{(\lambda'')}_{\mu''}(j,j''') \right. \\
&\qquad \left. -(-)^{\lambda+\lambda'+j'+j''} \begin{Bmatrix} \lambda & \lambda' & \lambda'' \\ j'' & j' & j \end{Bmatrix} \delta_{jj'''} A^{(\lambda'')}_{\mu''}(j'',j') \right],
\end{aligned} \tag{4.24}$$

being j, j', j'' and j''' half-integers. Moreover, as the algebraic structure in this case is richer that in the case of bosons, it is useful to divide our discussion in two parts, firstly the case in which we only consider a single j, and in second place the case in which we assume more than one value of j.

4.3.1 Single j

When considering a single j-shell, the value of n regarding the definition of creation and annihilation operators, $a^{\dagger}_{j,m}$, $a_{j,m}$, is

$$n = 2j + 1. \tag{4.25}$$

Moreover, the n^2 operators $A^{(\lambda)}_{\mu}(j,j) = \left[a^{\dagger}_{j} \times \tilde{a}_{j}\right]^{(\lambda)}_{\mu}$ are the generators of an U(2j+1) group, which eliminating the case of $\lambda = \mu = 0$ returns the corresponding algebra of an SU(2j+1) group.

Within this algebra it is useful to keep identifying more subalgebras in an equivalent way as we did for the IBM. From equation (4.24), it is possible to notice that operators with odd values of λ close under commutation and they generate the algebra $Sp(n)$ (sympletic), containing $2n(n+1)$ generators.

Moreover, we take into account the isomorphism,

$$SU(2) \simeq O(3), \tag{4.26}$$

which is generated by $A^{(\lambda)}_{\mu}(j,j) = \left[a^{\dagger}_{j} \times \tilde{a}_{j}\right]^{(\lambda)}_{\mu}$ with $\lambda = 1$.

In this way, one naturally obtains a hierarchy of algebras, where each step corresponds to

imposing additional restrictions on the system:

$$U(2j+1) \supset SU(2j+1) \supset Sp(2j+1) \supset SU(2). \tag{4.27}$$

We now can consider some examples of this chains for a certain value of j, we will consider in first place the simplest case for $j = 1/2$ and latter the case of $j = 3/2$, keeping in mind that for higher values of j the same exact process is repeated.

The Case $j = 1/2$

In this case the expression

$$A^{(\lambda)}_{\mu}(j,j) = \left[a^{\dagger}_{j} \times \tilde{a}_{j}\right]^{(\lambda)}_{\mu}, \tag{4.28}$$

results in 4 generators arising from:

$$\begin{aligned} A^{(1)}_{\mu}\left(\frac{1}{2},\frac{1}{2}\right) &= \left[a^{\dagger}_{1/2} \times \tilde{a}_{1/2}\right]^{(1)}_{\mu} \rightarrow 3, \\ A^{(0)}_{0}\left(\frac{1}{2},\frac{1}{2}\right) &= \left[a^{\dagger}_{1/2} \times \tilde{a}_{1/2}\right]^{(0)}_{0} \rightarrow 1, \end{aligned} \tag{4.29}$$

The algebra generated by these four operators is then U(2). Regarding $A^{(1)}_{\mu}\left(\frac{1}{2},\frac{1}{2}\right)$, it is helpful noticing that they are the generators of

$$\mathrm{SU(2)} \approx \mathrm{O(3)} \approx \mathrm{Sp(2)}, \tag{4.30}$$

while the operator

$$A^{(1)}_{0}\left(\frac{1}{2},\frac{1}{2}\right) = \left[a^{\dagger}_{1/2} \times \tilde{a}_{1/2}\right]^{(1)}_{0}, \tag{4.31}$$

generates the algebra O(2) of rotations around an axis.

Finally, the chain of algebras obtained in this particular case is then,

$$\mathrm{U(2)} \supset \mathrm{Sp(2)} \supset \mathrm{O(2)}. \tag{4.32}$$

The Case $j = 3/2$

When moving to higher values of j, it is clear that an equally higher number of generators will be encountered, in the $j = 3/2$ case, we part from an U(4) algebra generated by the

following 16 operators,

$$\begin{aligned} A^{(3)}_{\mu}\left(\frac{3}{2},\frac{3}{2}\right) &= \left[a^{\dagger}_{3/2}\times\tilde{a}_{3/2}\right]^{(3)}_{\mu} \rightarrow 7, \\ A^{(2)}_{\mu}\left(\frac{3}{2},\frac{3}{2}\right) &= \left[a^{\dagger}_{3/2}\times\tilde{a}_{3/2}\right]^{(2)}_{\mu} \rightarrow 5, \\ A^{(1)}_{\mu}\left(\frac{3}{2},\frac{3}{2}\right) &= \left[a^{\dagger}_{3/2}\times\tilde{a}_{3/2}\right]^{(1)}_{\mu} \rightarrow 3, \\ A^{(0)}_{0}\left(\frac{3}{2},\frac{3}{2}\right) &= \left[a^{\dagger}_{3/2}\times\tilde{a}_{3/2}\right]^{(0)}_{0} \rightarrow 1, \end{aligned} \tag{4.33}$$

Moreover, neglecting the case of $\lambda = \mu = 0$ reduces to the SU(4) algebra,

$$\begin{aligned} A^{(3)}_{\mu}\left(\frac{3}{2},\frac{3}{2}\right) &= \left[a^{\dagger}_{3/2}\times\tilde{a}_{3/2}\right]^{(3)}_{\mu} \rightarrow 7, \\ A^{(2)}_{\mu}\left(\frac{3}{2},\frac{3}{2}\right) &= \left[a^{\dagger}_{3/2}\times\tilde{a}_{3/2}\right]^{(2)}_{\mu} \rightarrow 5, \\ A^{(1)}_{\mu}\left(\frac{3}{2},\frac{3}{2}\right) &= \left[a^{\dagger}_{3/2}\times\tilde{a}_{3/2}\right]^{(1)}_{\mu} \rightarrow 3, \end{aligned} \tag{4.34}$$

where it is possible to identify the subalgebras of $Sp(4)$ with 10 generators,

$$\begin{aligned} A^{(3)}_{\mu}\left(\frac{3}{2},\frac{3}{2}\right) &= \left[a^{\dagger}_{3/2}\times\tilde{a}_{3/2}\right]^{(3)}_{\mu} \rightarrow 7, \\ A^{(1)}_{\mu}\left(\frac{3}{2},\frac{3}{2}\right) &= \left[a^{\dagger}_{3/2}\times\tilde{a}_{3/2}\right]^{(1)}_{\mu} \rightarrow 3, \end{aligned} \tag{4.35}$$

then $\mathrm{SU}(2) \approx \mathrm{O}(3)$,

$$A^{(1)}_{\mu}\left(\frac{3}{2},\frac{3}{2}\right) = \left[a^{\dagger}_{3/2}\times\tilde{a}_{3/2}\right]^{(1)}_{\mu}, \tag{4.36}$$

Resulting in the chain,

$$\mathrm{U}(4) \supset \mathrm{SU}(4) \supset \mathrm{Sp}(4) \supset \mathrm{SU}(2). \tag{4.37}$$

4.3.2 Multiple j

When several single-particle angular momenta $j_1, j_2, \ldots$ are involved, the classification of the associated chains of algebras becomes considerably more complicated. For this reason, we will discuss only a few representatives cases.

Each angular momentum j_i contributes with a space of dimension $(2j_i + 1)$. When combined, the total space has dimension:

$$n = \sum_i (2j_i + 1), \tag{4.38}$$

and the most general symmetry generated is the unitary group U(n).

In many situations, the value of n can be quite large, often reaching the order of 20 or 30. Moreover, although the full group U(n) provides the most general description, it is usually too large to be directly useful. Therefore, it becomes necessary to focus on particular subcases, which correspond to specific ways of reducing this large symmetry into smaller subalgebras.

Spinor Algebras

This class appears when the set of angular-momentum values $j_1, j_2, \ldots$ forms a spinor representation of an orthogonal algebra.

A spinor representation is a type of group representation in which states transform differently from the ordinary vector representations. In particular, under a rotation of 360°, spinor states do not return to their original value but instead acquire a minus sign, only recovering their original form after a rotation of 720°. Those representations, which arise naturally in the description of fermions, are associated with spin groups $Spin(n)$.

In our case, the single-particle states transform according to spinor symmetries, being a particularly important example when the values of j are a representation of the algebra,

$$Spin(6) \simeq SU(4). \tag{4.39}$$

The spinor representation of lowest dimensionality is formed by the single value $j = 3/2$, a case that has already been considered when studying single j cases.

The next higher spinor representation includes the set of values $j = \frac{1}{2}, \frac{3}{2}, \frac{5}{2}, \frac{7}{2}$, with a total dimension of $n = \sum(2j + 1) = 20$. This means that the corresponding unitary algebra U(20) therefore contains $20^2 = 400$ generators. Rather than listing these generators explicitly, it is better to describe the symmetry structure through a chain of subgroups:

$$U(20) \supset Spin(6) \simeq SU(4) \supset Spin(5) \simeq Sp(4) \supset Spin(3) \simeq SU(2) \supset Spin(2) \simeq O(2). \tag{4.40}$$

Because of the special properties of spinor groups, this chain has the same structure as a smaller-dimensional case, but starting from U(20) instead of a lower-dimensional unitary group.

Pseudo Spin Algebras

Pseudo-spin algebras arise from a convenient way of reorganizing the single-particle angular momentum j into two separate contributions. Instead of treating j as a single object,

one can consider that it can be decomposed into an integer part, called the pseudo-orbital angular momentum k, and a half-integer part, called the pseudo-spin s [73, 74].

An example can be found in the example provided by the set $j = 1/2, 3/2$. This pair of values can be interpreted as originated from a pseudo-orbital angular momentum $k = 1$, coupled to a pseudo-spin $s = 1/2$, being the total dimension $n_j = 6$.

Algebraically, this decomposition corresponds to the breakage of the unitary algebra U(6) into two smaller unitary algebras, one associated with the pseudo-orbital degree of freedom and one with the pseudo-spin degree of freedom, denoted as $U_k(3)$ and $U_s(2)$, respectively.

More generally, an algebra $\mathrm{U}(\mathrm{n}_j)$ can be decomposed as

$$\mathrm{U}\left(n_j\right) \supset \mathrm{U}_k\left(n_k\right) \otimes \mathrm{U}_s\left(n_s\right), \tag{4.41}$$

where the dimensions of the spaces are given by

$$\begin{aligned} n_j &= \sum_{j_i} \left(2j_i + 1\right), \\ n_k &= \sum_{k_i} \left(2k_i + 1\right), \\ n_s &= \sum_{s_i} \left(2s_i + 1\right). \end{aligned} \tag{4.42}$$

The generators of the pseudo-orbital group $\mathrm{U}_k(n_k)$ (K) and of the pseudo-spin group $\mathrm{U}_s(n_s)$ (S) can be constructed explicitly from the generators of $\mathrm{U}(\mathrm{n}_j)$ (A). This is done by changing the coupling scheme from a j-j coupling to a k-s coupling [75],

$$\begin{aligned} K_\mu^{(\lambda)}\left(k, k'\right) = &- \sum_s \sum_{jj'} \sqrt{\left(2j+1\right)\left(2j'+1\right)} (-)^{j'+\lambda+k+s} \\ &\times \left\{ \begin{array}{ccc} j & j' & \lambda \\ k' & k & s \end{array} \right\} A_\mu^{(\lambda)}\left(j, j'\right), \\ S_\mu^{(\lambda)}\left(s, s'\right) = &\sum_k \sum_{jj'} \sqrt{\left(2j+1\right)\left(2j'+1\right)} (-)^{s'+\lambda+j+k} \\ &\times \left\{ \begin{array}{ccc} s & s' & \lambda \\ j' & j & k \end{array} \right\} A_\mu^{(\lambda)}\left(j, j'\right). \end{aligned} \tag{4.43}$$

The resulting generators satisfy well-defined commutation relations. The commutators among the pseudo-orbital generators close within the $U_k(n_k)$ algebra, those among the pseudo-spin generators close within $U_s(n_s)$, and the mixed commutators between pseudo-

orbital and pseudo-spin generators vanish,

$$\begin{aligned}
&\left[K_{\mu}^{(\lambda)}\left(k,k'\right),K_{\mu'}^{(\lambda')}\left(k'',k'''\right)\right]\\
&=\sum_{\lambda''\mu''}\sqrt{\left(2\lambda+1\right)\left(2\lambda'+1\right)}\left(\lambda\mu\lambda'\mu'\mid\lambda''\mu''\right)\\
&\quad\times\left[(-)^{\lambda''+k+k'''}\left\{\begin{array}{ccc}\lambda & \lambda' & \lambda''\\ k''' & k & k'\end{array}\right\}\delta_{k'k''}K_{\mu''}^{(\lambda'')}\left(k,k'''\right)\right.\\
&\quad\left.-(-)^{\lambda+\lambda'+k'+k''}\left\{\begin{array}{ccc}\lambda & \lambda' & \lambda''\\ k'' & k' & k\end{array}\right\}\delta_{kk'''}K_{\mu''}^{(\lambda'')}\left(k'',k'\right)\right],
\end{aligned}\tag{4.44}$$

$$\begin{aligned}
&\left[S_{\mu}^{(\lambda)}\left(s,s'\right),\ S_{\mu'}^{(\lambda')}\left(s'',s'''\right)\right]\\
&\quad=\sum_{\lambda''\mu''}\sqrt{\left(2\lambda+1\right)\left(2\lambda'+1\right)}\left(\lambda\mu\lambda'\mu'\mid\lambda''\mu''\right)(-)^{s+s'+s''+s'''}\\
&\qquad\times\left[(-)^{\lambda''}\left\{\begin{array}{ccc}\lambda & \lambda' & \lambda''\\ s''' & s & s'\end{array}\right\}\delta_{s's''}S_{\mu''}^{(\lambda'')}\left(s,s'''\right)\right.\\
&\qquad\left.-(-)^{\lambda+\lambda'}\left\{\begin{array}{ccc}\lambda & \lambda' & \lambda''\\ s'' & s' & s\end{array}\right\}\delta_{ss'''}S_{\mu''}^{(\lambda'')}\left(s'',s'\right)\right],
\end{aligned}\tag{4.45}$$

$$\left[K_{\mu}^{(\lambda)}\left(k,k'\right),S_{\mu'}^{(\lambda')}\left(s,s'\right)\right]=0,\tag{4.46}$$

As a result, we can construct chains of nested subalgebras in the usual way, now expressed in terms of pseudo-spin and pseudo-orbital symmetries instead of the original total angular momentum.

4.4 Basis States for Fermions

4.4.1 Single j

In this section we will address the construction and classification of basis states for a single value of the angular momentum j.

The maximum number of fermions that can occupy a single-j shell is following directly the Pauli principle,

$$N_F=2j+1.\tag{4.47}$$

In the case treated for the IBM, the total wave function needed to be symmetric, but this situation changes for fermions, whose total wave function must be antisymmetric. The classification of these antisymmetric states of the unitary algebra U(n) is, in general, nontrivial. A way to label these states is provided by a chain of algebras where each

algebra in the chain contributes with a set of quantum numbers, which may or may not be sufficient to uniquely identify the states.

For a single-j shell, the considered chain is,

$$\mathrm{U}(2j+1) \supset \mathrm{SU}(2j+1) \supset \mathrm{Sp}(2j+1) \supset \mathrm{SU}(2). \tag{4.48}$$

Using this chain, the basis states can be labeled according to the following scheme:

$$\begin{array}{ccccc} \mathrm{U}(n) & \supset & \mathrm{Sp}(n) & \supset & \mathrm{SU}(2) \\ \downarrow & & \downarrow & & \downarrow \\ \{N_{\mathrm{F}}\} & & (n_1, n_2, \ldots, n_{n/2}) & & \nu, J \end{array} \tag{4.49}$$

where N_F denotes the number of fermions and the remaining quantum numbers arise from the successive subalgebras in the chain. In some cases, additional labels ν are required to fully distinguish the states, known as missing labels.

For shells with $j \leq 7/2$, however, no extra labels are needed, since the quantum numbers from chain of nested algebras are sufficient to uniquely characterize all states.

We can also discuss explicitly the two cases introduced earlier.

(i) The case $j = 1/2$.

For $j = 1/2$, the corresponding group chain is

$$\begin{array}{ccc} \mathrm{U}(2) & \supset & \mathrm{Sp}(2) \approx \mathrm{SU}(2). \\ \downarrow & & \\ \{N_{\mathrm{F}}\} & & \end{array} \tag{4.50}$$

where the allowed number of fermions is $N_F = 0, 1, 2$.

In fermionic systems, there exists an equivalence between a configuration with N_F particles and one with $(2j + 1 - N_F)$ particles, known as particle-hole conjugation. As a result, for $j = 1/2$ the configurations with $N_F = 0$ and $N_F = 2$ are equivalent. In this case, the number of fermions alone uniquely specifies the state and no additional quantum numbers are required.

(ii) The case $j = 3/2$.

For $j = 3/2$, the relevant group chain is as we obtained before,

$$\mathrm{U}(4) \supset \mathrm{SU}(4) \supset \mathrm{Sp}(4) \supset \mathrm{SU}(2). \tag{4.51}$$

The decomposition of representations of U(4) into representations of Sp(4) has been worked out explicitly in [76] and the quantum numbers can be written as,

$$\begin{array}{ccccc} \mathrm{U}(4) & \supset & \mathrm{Sp}(4) & \supset & \mathrm{SU}(2) \\ \downarrow & & \downarrow & & \downarrow \\ \{N_{\mathrm{F}}\} & & (n_1, n_2) & & J \end{array} \tag{4.52}$$

At first sight, several quantum numbers appear to be needed to label this state, however, the allowed representations of Sp(4) are subject to strong constraints. In practice, they can be characterized by a single quantum number, denoted by ν_F, that takes the values $v_F = N_F,\ N_F - 2,\ \ldots,\ 1$ or 0,

Thus, the classification of the basis states for $j = 3/2$ remains simple and does not require additional missing labels.

4.4.2 Multiple j

Spinor Algebras

We now turn to systems involving multiple values of j, firstly studying the case of spinor algebras. A physically important example is given by the set $j = \frac{1}{2}, \frac{3}{2}, \frac{5}{2}, \frac{7}{2}$, which is classified using the group chain given in equation (4.40).

The single-particle states associated with these values of j transform as the fundamental representation $\{1\}$ of the unitary group U(20), together with the representation of the spinor algebra Spin(6), which is equivalent to the representation $[2, 1]$ of SU(4).

Many-particle antisymmetric states are obtained by forming appropriate antisymmetrized products of these single-particle representations. The resulting basis states can be classified through the successive reduction of symmetries along the algebra chain,

$$\begin{array}{ccccccc} \mathrm{U}(20) \supset & \mathrm{Spin}(6) & \supset \mathrm{Spin}(5) & \supset \mathrm{Spin}(3) & \supset \mathrm{Spin}(2) \\ \downarrow & \downarrow & \downarrow & \downarrow & \downarrow \\ \{N_{\mathrm{F}}\} & \nu, (\sigma_1, \sigma_2, \sigma_3) & (\tau_1, \tau_2) & \nu', J & M_J \end{array} \tag{4.53}$$

where the intermediate labels denoted by ν and ν', are referred to as missing labels.

Pseudo-Spin Algebras

For pseudo-spin algebras, the construction of basis states is somewhat simpler than in the spinor case because the single-particle space factorizes naturally into a pseudo-orbital part and a pseudo-spin part.

It was shown in [76] that overall antisymmetry under $\mathrm{U}(n_j)$ is preserved when the representations of $\mathrm{U}_k(n_k)$ and $\mathrm{U}_s(n_s)$ are conjugate to each other, meaning that the symmetry pattern in one sector fixes the allowed symmetry in the other.

As an explicit example, we consider the case $j = \frac{1}{2}, \frac{3}{2}$, which is classified using the group chain

$$\begin{array}{ccccccccccc} \mathrm{U}(6) & \supset & \mathrm{SU}_k(3) & \otimes & \mathrm{SU}_s(2) & \supset & \mathrm{O}_k(3) \otimes \mathrm{SU}_s(2) & \supset & \mathrm{SU}_j(2) & \supset & \mathrm{O}_j(2) \\ \downarrow & & \downarrow & & \downarrow & & \downarrow & & \downarrow & & \downarrow \\ \{N_\mathrm{F}\} & & (\lambda, \mu) & & S & & L & & J & & M_J \end{array} \tag{4.54}$$

The requirement of overall antisymmetry under U(6) imposes a constraint linking the allowed $\mathrm{SU}_k(3)$ representations to the corresponding $\mathrm{SU}_s(2)$. As a result, only specific combinations of orbital and spin quantum numbers are allowed.

4.5 Coupled Bose-Fermi Algebras

The algebraic structure of systems containing both bosons and fermions is intrinsically more complex. Nevertheless, the basic idea behind their description is straightforward: the bosonic and fermionic sectors are first treated separately and then combined in the same algebraic framework.

The bosonic degrees of freedom are described in terms of boson creation and annihilation operators,

$$B_{\alpha\beta} = b^\dagger_\alpha b_\beta, \quad (\alpha, \beta = 1, \ldots, n_\mathrm{B})\,. \tag{4.55}$$

In an analogous way, the fermionic sector is described by bilinear products of fermion operators, which generate the unitary algebra $\mathrm{u}_F(n_F)$,

$$A_{ik} = a^\dagger_i a_k, \quad (i, k = 1, \ldots, n_\mathrm{F})\,. \tag{4.56}$$

Moreover, as we have explained, bosons and fermions are usually classified through separate chains of algebras. Hence, for bosons we have,

$$G^\mathrm{B} \supset G'^\mathrm{B} \supset G''^\mathrm{B} \supset \cdots\,, \tag{4.57}$$

while for fermions it verifies,

$$G^\mathrm{F} \supset G'^\mathrm{F} \supset G''^\mathrm{F} \supset \cdots\,. \tag{4.58}$$

Coupling between the two sectors is possible in the case that the algebras in these chains

coincide or are isomorphic. This situation can be visualized by a lattice of algebras, which may admit several distinct coupling routes,

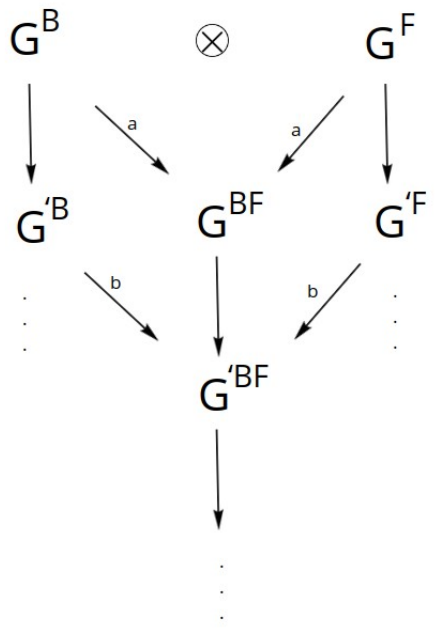

(4.59)

Depending on the structure of the fermion algebra, two cases can arise. Firstly, for spinor algebras, the coupling leads to so-called twofold lattices. For pseudo-spin algebras, the fermion symmetry is further decomposed, resulting in threefold lattices,

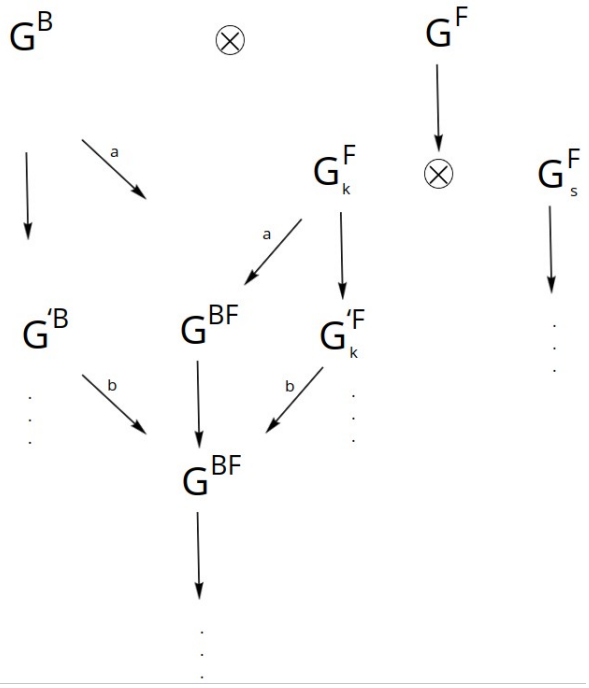

(4.60)

The generators of the coupled Bose-Fermi algebras are constructed as linear combinations of boson and fermion generators and are most conveniently expressed in coupled-tensor

form,

$$B^{(\lambda)}_{\mu}(l,l') = \left[b^{\dagger}_{l} \times \tilde{b}_{l'}\right]^{(\lambda)}_{\mu}, \qquad A^{(\lambda)}_{\mu}(j,j') = \left[a^{\dagger}_{j} \times \tilde{a}_{j'}\right]^{(\lambda)}_{\mu}. \tag{4.61}$$

When the boson and fermion algebras are combined at an early stage of the symmetry chain, the coupling is known as maximal and results in strong restrictions on the form of the Hamiltonian. The case where the coupling is done later, for example at the level of the rotation group, is usually less restrictive.

For pseudo-spin algebras, the coupling requires two steps, in first place the fermion generators are separated into pseudo-orbital and pseudo-spin parts, and secondly the bosonic generators are coupled successively to each of them.

In essence, the coupling of Bose-Fermi algebras is a generalization of the coupling of angular momenta. As an example, combining a boson orbital angular momentum $\mathbf{L}$ with a fermion spin $\mathbf{S}$ leads to the total angular momentum,

$$\mathbf{J} = \mathbf{L} + \mathbf{S}, \tag{4.62}$$

which generates the corresponding coupled rotation algebra.

4.6 Boson-Fermion Basis States

After obtaining the specific algebraic structure for the model, the next step is to construct the corresponding basis states, which are obtained from the representations of the algebras that appear in the dynamical-symmetry chain.

In this way, constructing a basis consists in decomposing the representation of a given algebra into its subalgebras. However, in the case that bosonic and fermionic degrees of freedom are present, the procedure also involves combining representations of different algebras.

Consider as an example the chain:

$$G^{\mathrm{B}} \otimes G^{\mathrm{F}} \supset G'^{\mathrm{B}} \otimes G'^{\mathrm{F}} \supset G'^{\mathrm{BF}} \supset G''^{\mathrm{BF}}. \tag{4.63}$$

The first step would be decomposing bosonic and fermionic algebras separately:

$$G^{\mathrm{B}} \supset G^{\mathrm{B}}, \quad G^{\mathrm{F}} \supset G^{\mathrm{F}}, \tag{4.64}$$

Later, combining bosonic and fermionic representations:

$$G'^{\mathrm{B}} \otimes G'^{\mathrm{F}} \supset G'^{\mathrm{BF}} \tag{4.65}$$

and finally decomposing the combined algebra:

$$G'^{\mathrm{BF}} \supset G''^{\mathrm{BF}}. \tag{4.66}$$

Each step in this chain introduces a set of quantum numbers that characterize the basis states. Schematically,

$$\begin{array}{ccccccccccc} G^{\mathrm{B}} & \otimes & G^{\mathrm{F}} & \supset & G'^{\mathrm{B}} & \otimes & G'^{\mathrm{F}} & \supset & G'^{\mathrm{BF}} & \supset & G''^{\mathrm{BF}} \\ \downarrow & & \downarrow & & \downarrow & & \downarrow & & \downarrow & & \downarrow \\ [N_{\mathrm{B}}] & & \{N_{\mathrm{F}}\} & & \text{labels} & & \text{labels} & & \text{labels} & & \text{labels} \end{array} \tag{4.67}$$

These labels may or may not be sufficient to uniquely specify each physical state. If they are sufficient, the construction ends here. If not, additional labels must be introduced to uniquely distinguish these states.

To combine the representations in practice, one often uses Young tableaux and their multiplication rules [77]. Moreover, in some cases, it is possible to simplify the calculations by exploiting isomorphisms between algebras.

4.7 Dynamical Symmetries for Boson-Fermion Systems

The basis states obtained in the previous section can be used in two different ways. In first place, these bases give a concrete set of states on which one can diagonalize the Hamiltonian numerically. For example, the ODDA code [78] performs calculations in a basis of the type shown in equation (4.67). The second purpose is to find Hamiltonians written in terms of the Casimir of the nested groups, known as dynamical symmetries, which are especially valuable because they provide simple expressions for energies and wave functions.

The method used to obtain analytic solutions is the same as the one followed for the IBM, that is writing the Hamiltonian as a combination of Casimir invariants of the groups that appear in the chosen chain. For example, for the chain in (4.63), the Hamiltonian take the form

$$\begin{aligned} H =& E_0 + \alpha \mathcal{C}\left(G^{\mathrm{B}}\right) + \beta \mathcal{C}\left(G^{\mathrm{F}}\right) + \alpha' \mathcal{C}\left(G^{\mathrm{B}}\right) + \beta' \mathcal{C}\left(G^{\mathrm{F}}\right) \\ &+ \gamma \mathcal{C}\left(G^{\mathrm{BF}}\right) + \delta \mathcal{C}\left(G''^{\mathrm{BF}}\right). \end{aligned} \tag{4.68}$$

It is important to remember that each algebra generally has several Casimir operators (often of different orders), but if the Hamiltonian contains only up to two-body interactions, then only invariants up to second order appear.

Now, evaluating the Hamiltonian in the basis of equation (4.67) gives as a result the energy

$$\begin{aligned} E(\text{ labels }) =& E_0 + \alpha \left\langle \mathcal{C}\left(G^{\mathrm{B}}\right)\right\rangle + \beta \left\langle \mathcal{C}\left(G^{\mathrm{F}}\right)\right\rangle + \alpha' \left\langle \mathcal{C}\left(G^{\mathrm{B}}\right)\right\rangle \\ &+ \beta' \left\langle \mathcal{C}\left(G^{\mathrm{F}}\right)\right\rangle + \gamma \left\langle \mathcal{C}\left(G^{\mathrm{BF}}\right)\right\rangle + \delta \left\langle \mathcal{C}\left(G'^{\mathrm{BF}}\right)\right\rangle . \end{aligned} \tag{4.69}$$

Finally, an important point is that the Casimir invariants of G_B and G_F contribute the same amount to all states because their expectation values depend only on the fixed boson and fermion numbers N_B and N_F. Therefore, these terms do not affect excitation energies but are relevant when computing absolute binding energies.

4.8 Boson-fermion Interaction in the U(5) Limit

The energy structure of odd-even nuclei is governed by the coupling between collective bosonic degrees of freedom and the effect of one unpaired nucleon. This coupling, which is described by the boson-fermion interaction H_{BF}, plays a central role in determining the splitting and ordering of the energy levels. In order to identify the characteristic effects of each element in this interaction, it is useful to analyze its different components separately.

In this section we consider the case in which the boson core has a U(5) dynamical symmetry, corresponding to a spherical, vibrational collective structure. The reason of this choice is that it provides a reference and is consistent with the schematic results presented, where a U(5) behavior of the bosonic sector is assumed.

The boson wave functions are characterized by the quantum numbers $[N_B], n_d, \tau, n_\Delta, L, M_L$, and the boson Hamiltonian H_B is diagonal in this basis, with eigenvalues given in equation (3.80). The fermionic part consists on a single particle occupying one orbit with angular momentum j (here $j = 9/2$), characterized by j and its projection m_j.

A convenient basis for the odd-even system is obtained by coupling boson and fermion states to total angular momentum J, taking into consideration the properties of Clebsch-Gordan coefficients

$$\left|[N_B], n_d, \tau, n_\Delta, L;\, j;\, JM\right\rangle = \sum_{M_L, m_j} (LM_L\, jm_j|JM)\left|[N_B], n_d, \tau, n_\Delta, LM_L\right\rangle\left|jm_j\right\rangle. \tag{4.70}$$

In this basis, both H_B and H_F are diagonal, and the spectral structure is determined entirely by the boson-fermion interaction H_{BF}.

We now discuss separately the effects of the monopole, quadrupole, and exchange terms of H_{BF}.

Monopole term. For a single fermion orbit, the monopole interaction reduces to

$$\hat{H}_{BF}^{\mathrm{MON}} = -\frac{A}{5(2j+1)}\,\hat{n}_d\hat{n}_j, \tag{4.71}$$

where $\hat{n}_d$ and $\hat{n}_j$ are the number operators for d bosons and fermions, respectively. Since $\langle\hat{n}_j\rangle = 1$, this term is diagonal in the basis proposed and leads to the energy shift

$$\Delta E_{n_d} = -\frac{A}{5(2j+1)}\,n_d. \tag{4.72}$$

The monopole interaction therefore just renormalizes the boson excitation energy and does not produce additional splittings of the coupled multiplets, as illustrated in Fig.4.1.

Quadrupole term. The quadrupole interaction couples the quadrupole moments of the boson core and the fermion and it is written as

$$\hat{H}_{BF}^{\mathrm{QUAD}} = \Gamma\, Q_B \cdot q_j/\sqrt{5}. \tag{4.73}$$

In the U(5) basis, this interaction contains a diagonal part,

$$H_{\mathrm{BF}}^{\mathrm{QUAD}} = \chi\Gamma_{jj}\left[\left[d^\dagger\times\tilde{d}\right]^{(2)}\times\left[a_j^\dagger\times\tilde{a}_j\right]^{(2)}\right]^{(0)} \tag{4.74}$$

and an off-diagonal part,

$$\hat{H}_{\mathrm{BF}}^{\mathrm{QUAD}\prime\prime} = \Gamma_{jj}\left[\left[s^\dagger\times\tilde{d}+d^\dagger\times\tilde{s}\right]^{(2)}\times\left[a_j^\dagger\times\tilde{a}_j\right]^{(2)}\right]^{(0)}. \tag{4.75}$$

When ϵ in equation (3.80) is large, the diagonal term dominates. As a consequence, the quadrupole interaction produces a characteristic splitting of the multiplets obtained by coupling a boson state with angular momentum L to the fermion with angular momentum j, as shown schematically in Fig.4.1.

Where a splitting of the multiplet with $n_d = 1$is given by:

$$\Delta E'_{n_{\mathrm{d}}=1}(J) = (\chi\Gamma_{jj})\,\sqrt{5}(-)^{J-j}\begin{Bmatrix} 2 & j & J \\ j & 2 & 2 \end{Bmatrix}. \tag{4.76}$$

Exchange term. The exchange interaction accounts for the exchange of identical particles between the boson core and the unpaired fermion. For a single fermion orbit it is

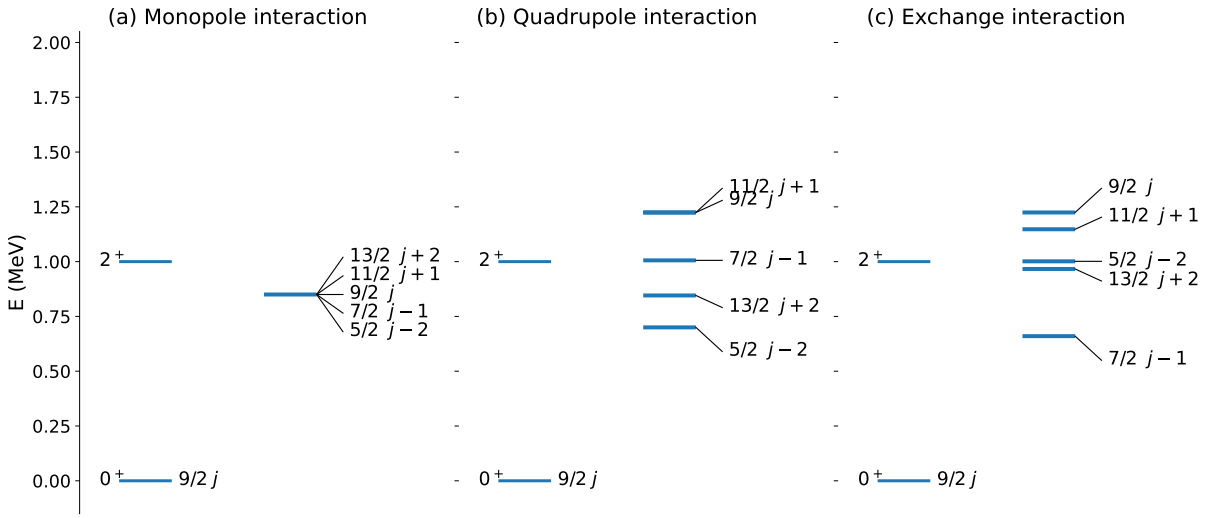

Figure 4.1: Schematic illustration of the effects of the boson–fermion interaction $H_{\rm BF}$ on the energy spectra of odd even nuclei with $j = 9/2$ and $U_{\rm B}(5)$ symmetry:(a) monopole term; (b) quadrupole term; (c) exchange term.

given by

$$\hat{H}_{BF}^{\rm EXC} = \Lambda\Big[[d^\dagger \times a_j]^{(j)} \times [\tilde{d} \times a_j^\dagger]^{(j)}\Big]^{(0)}. \tag{4.77}$$

This term is diagonal in the basis introduced in this section and leads to an additional splitting of the coupled multiplets. For the $n_d = 1$ multiplet, the resulting energy shifts are given by

$$\Delta E''_{n_{\rm d}=1}(J) = \Lambda^j_{jj}\sqrt{2j+1}\begin{Bmatrix} j & 2 & J \\ j & 2 & j \end{Bmatrix}. \tag{4.78}$$

Its qualitative effect is illustrated in Fig. 4.1.

In the U(5) limit the boson core has a spherical character, and the coupling to a single fermion corresponds to the particle-vibration coupling scheme. The analysis of the separate effects of the monopole, quadrupole, and exchange interactions provides a clear interpretation of the spectral structures in this limit.

4.9 Multiple j and Microscopic Interpretation of the IBFM

When operating within the IBFM, it is possible to perform calculations involving single-j or multiple-j situation. In the case of many j calculations, we must be careful with the terms corresponding with the boson-fermion interaction, that are, as it has been previously introduced, the monopole term in equation (4.16), the quadrupole term in (4.17) and finally the exchange interaction in equation (4.18).

The reason is that, when several single-particle orbits are included in the calculation, the independent parameters A_j, $\Gamma_{jj'}$, and $\Lambda^{j''}_{jj'}$ would introduce an excessively large number of free parameters. To overcome this difficulty and reduce the number of free parameters, we will use the microscopic interpretation of the IBFM and assume that these coefficients depend on the angular momentum of a single-particle, j. Moreover, a widely used approach within this interpretation is the generalized seniority scheme, which provides simple expressions for the interaction strengths while preserving the shell-model structure. Within this scheme, the coefficients are expressed in terms of the orbital degeneracy $(2j+1)$, the occupation probabilities of the single-particle states, u_j and v_j, and the matrix elements of the quadrupole operator. The use of this seniority scheme leads to [79]:

$$\begin{aligned} A_j &= -\sqrt{5(2j+1)}A_0, \\ \Gamma_{jj'} &= \sqrt{5}\gamma_{jj'}\Gamma_0, \\ \Lambda^{j''}_{jj'} &= -2\sqrt{\frac{5}{2j''+1}}\beta_{jj''}\beta_{j'j''}\Lambda_0, \end{aligned} \tag{4.79}$$

where

$$\begin{aligned} \gamma_{jj'} &= (u_j u_{j'} - v_j v_{j'})\, Q_{jj'}, \\ \beta_{jj'} &= (u_j v_{j'} + v_j u_{j'})\, Q_{jj'}. \end{aligned} \tag{4.80}$$

Moreover, $Q_{jj'}$ in these equations are matrix elements of the quadrupole operator in the single-particle basis,

$$Q_{jj'} = \left\langle j \left\| Y^{(2)} \right\| j' \right\rangle. \tag{4.81}$$

The occupation amplitudes u_j and v_j are most commonly obtained from a BCS calculation [8], although they can also be obtained using other procedures [80]. When a BCS approach is used, we can obtain within the same calculation the single quasi-particle energies in terms of the particle energies, the Fermi energy λ_F and the energy gap Δ_F, which establishes a direct connection between the microscopic interaction and the effective parameters used in the model.

$$\epsilon_j = \sqrt{(E_j - \lambda_{\mathrm{F}})^2 + \Delta^2_{\mathrm{F}}}. \tag{4.82}$$

The generalized seniority scheme provides a reliable description for nuclei close to closed shells, where the U(5) dynamical symmetry is a good approximation. However, its validity gradually decreases as one moves away from this limit and collective deformation effects are more important.

To improve the description of nuclei outside the U(5) region, this model can be extended by including additional exchange interaction terms. In particular, the exchange interaction associated with deformation plays a crucial role, since its inclusion has a strong impact

on the results and is essential for a proper description of nuclei in regions where the SU(3) limit is more appropriate.

4.10 The Interacting Boson-Fermion Model with Configuration Mixing

In the case of odd-even nuclei close to closed shells, it is not unusual to find cases where different structures coexist within the same energy region. For this reason it is necessary to again enlarge the IBFM formalism to allow core excitations, giving rise to the known as IBFM whith configuration mixing (IBFM-CM) [67, 66].

The Hamiltonian of the IBFM-CM is then written as:

$$\hat{H} = \hat{P}_N^{\dagger}\, \hat{H}^{(N)}\, \hat{P}_N \;+\; \hat{P}_{N+2}^{\dagger} \left(\hat{H}^{(N+2)} + \Delta^{N+2}\right) \hat{P}_{N+2} \;+\; \hat{V}_{BF,\mathrm{mix}}^{N,N+2}, \tag{4.83}$$

where $\hat{P}_N$ and $\hat{P}_{N+2}$ are projection operators onto the $[N]$ and $[N+2]$ boson subspaces, respectively.

Moreover, in this case, the Hamiltonians considered for $[N]$ and $[N+2]$ consist on three parts,

$$\hat{H} = \hat{H}_{\mathrm{B}} + \hat{H}_{\mathrm{F}} + \hat{H}_{\mathrm{BF},} \tag{4.84}$$

being $\hat{H}_B$ the Hamiltonian of the IBM-CM, for which it is important to remember that already contains terms that account for the mixing between the regular and intruder boson configurations, as well as the Δ energy that was required to excite a boson pair across the shell closure; $\hat{H}_F$ represents the fermion Hamiltonian, and $\hat{H}_{BF}$ is the boson-fermion interaction, in which the monopole, quadrupole and exchange terms are included, whose strengths can be expressed in terms of the occupation probabilities (u_j, v_j) using the microscopic interpretation of the IBFM. Finally, the term,

$$\hat{V}_{\mathrm{BF,mix}}^{N,N+2} = \sum_j \hat{n}_j \omega_j \big([s^{\dagger} \times s^{\dagger} + s \times s]^{(0)} + [d^{\dagger} \times d^{\dagger} + \tilde{d} \times \tilde{d}]^{(0)} \big), \tag{4.85}$$

controls the mixing for each orbit.

Furthermore, electromagnetic transition operators contain both bosonic and fermionic contributions. They are therefore written as

$$\hat{T}^{(\sigma L)} = \hat{T}_{\mathrm{b}}^{(\sigma L)} + \hat{T}_{\mathrm{f}}^{(\sigma L)}. \tag{4.86}$$

In the case of electric quadrupole transitions, the bosonic part of the operator is given

by

$$\hat{T}_{\rm b}(E2) = e^{(A)}\hat{Q}_{\chi}^{(N)} + e^{(B)}\hat{Q}_{\chi}^{(N+2)}, \tag{4.87}$$

where the superscripts (N) and $(N+2)$ indicate projections onto the corresponding boson spaces.

4.11 The Intrinsic State Formalism for the IBFM-CM

The intrinsic state formalism provides a powerful geometrical interpretation of the IBM in terms of deformation variables (β, γ). In the IBFM, this approach can be naturally extended to odd-mass nuclei by coupling the bosonic intrinsic state to an unpaired fermion occupying several single-particle orbitals, for which the bosonic condensate, defined in equation (3.91), will be used as an essential component of the basis employed all along our calculations.

In the general case, the odd fermion can occupy several single particle orbitals labeled by j. For this reason, the intrinsic basis is constructed as the direct product of the bosonic intrinsic state and the fermionic single particle states,

$$|N;\beta,\gamma;jm\rangle = |N;\beta,\gamma\rangle \otimes |jm\rangle. \tag{4.88}$$

Taking the expectation value of the Hamiltonian with respect to the bosonic intrinsic state, one obtains an effective fermionic Hamiltonian that depends parametrically on (β, γ) [81],

$$\begin{aligned} \mathcal{H}_{\rm IBFM}(N,\beta,\gamma) &= \langle N;\beta,\gamma|\hat{H}|N;\beta,\gamma\rangle \\ &= \sum_{j_1 m_1 j_2 m_2} \mathcal{M}(N,\beta,\gamma)_{j_1 m_1, j_2 m_2}\, a^{\dagger}_{j_1 m_1} a_{j_2 m_2}. \end{aligned} \tag{4.89}$$

This matrix can be decomposed as

$$\begin{aligned} \mathcal{H}_{IBFM}(N,\beta,\gamma) &= \sum_{j_1,m_1,j_2,m_2} \mathcal{M}(N,\beta,\gamma)_{j_1,m_1,j_2,m_2} a^{\dagger}_{j_1,m_1} a_{j_2,m_2} \\ &= \sum_{j,m} \big(E_B(N,\beta,\gamma) + \epsilon_j\big) a^{\dagger}_{j,m} a_{j,m} \\ &+ \sum_{j_1,m_1,j_2,m_2} E_{BF}(N,\beta,\gamma)_{j_1,m_1,j_2,m_2} \times \frac{a^{\dagger}_{j_1,m_1} a_{j_2,m_2} + a^{\dagger}_{j_2,m_2} a_{j_1,m_1}}{1+\delta_{j_1,j_2}\delta_{m_1,m_2}}. \end{aligned} \tag{4.90}$$

ϵ_j are the fermion single quasi-particle energies, $E_B(N,\beta,\gamma)$ stands for the matrix element of $\hat{H}_B$ with the intrinsic state (3.91), and $E_{BF}(N,\beta,\gamma)_{j_1,m_1,j_2,m_2}$ is the matrix element of $\hat{H}_{BF}$.

The bosonic energy surface is, using the $\hat{H}_{ECQF}$ defined in 3.105:

$$\begin{aligned} E_B(N,\beta,\gamma) = & \frac{N\beta^2}{1+\beta^2}(\varepsilon + 6\kappa') + \frac{N}{1+\beta^2}\,\kappa\,(5+(1+\chi^2)\beta^2) \\ & + \frac{N(N-1)}{(1+\beta^2)^2}\,\kappa\,\left(\frac{2}{7}\chi^2\beta^4 - 4\sqrt{\frac{2}{7}}\chi\beta^3\cos 3\gamma + 4\beta^2\right). \end{aligned} \tag{4.91}$$

Regarding $E_{BF}(N,\beta,\gamma)_{j_1,m_1,j_2,m_2}$, the different contributions are,

$$E_{BF}^{\mathrm{MON}}(N,\beta,\gamma)_{j_1,m_1,j_2,m_2} = -NA_{j_1}/\sqrt{5(2j_1+1)}\delta_{j_1,j_2}\delta_{m_1,m_2}\frac{\beta^2}{1+\beta^2}, \tag{4.92}$$

$$E_{BF}^{\mathrm{QUAD}}(N,\beta,\gamma)_{j_1,m_1,j_2,m_2} = N\frac{\Gamma_{j_1j_2}}{\sqrt{5}}\sum_M (-1)^{j_2+m_2-M} q_{2M}(\beta,\gamma)\langle j_1,m_1;j_2,-m_2|2-M\rangle, \tag{4.93}$$

where

$$\begin{aligned} q_{20}(\beta,\gamma) &= \frac{1}{1+\beta^2}\left(2\beta\cos\gamma - \sqrt{\frac{2}{7}}\beta^2\chi\cos 2\gamma\right), \\ q_{2\pm2}(\beta,\gamma) &= \frac{1}{1+\beta^2}\left(\sqrt{2}\beta\sin\gamma + \sqrt{\frac{1}{7}}\chi\beta^2\sin 2\gamma\right), \\ q_{2\pm1}(\beta,\gamma) &= 0, \end{aligned} \tag{4.94}$$

and

$$\begin{aligned} E_{BF}^{\mathrm{EXC}}(N,\beta,\gamma)_{j_1,m_1,j_2,m_2} = N & \sum_{j''m''} \Lambda_{j_1j_2}^{j''}\frac{(-1)^{j_1+j''}}{\sqrt{2j''+1}}\eta_{m''+m_1}\eta_{m''+m_2} \\ & \times \langle 2,m''+m_1;j_1,-m_1|j''m''\rangle\langle 2,-m_2-m'';j_2,m_2|j''-m''\rangle, \end{aligned} \tag{4.95}$$

where

$$\eta_0 = \frac{\beta\cos\gamma}{\sqrt{1+\beta^2}}, \qquad \eta_1 = \eta_{-1} = 0, \qquad \eta_2 = \eta_{-2} = \frac{\beta\sin\gamma}{\sqrt{2(1+\beta^2)}} \tag{4.96}$$

and $\langle ...|...\rangle$ stand for the Clebsh-Gordan coefficients. Moreover, all these expressions have been obtained by using the method detailed in Appendix B. Hence, solving the problem requires diagonalizing a matrix of dimension $\sum_j(2j+1)$. However, since the Hamiltonian only connects states with $\Delta m = \pm 2$, the matrix can be decomposed into two equivalent blocks, each of dimension $1/2\sum_j(2j+1)$. One block includes states with $m = j, j-2, ..., -(j-1)$, while the other contains the corresponding complementary values.

It is also possible to rewrite this term using the properties of Clebsch-Gordan, Wigner -3j

and -6j coefficients, that have been summarized in Appendix C, resulting in,

$$E_{BF}^{EXC}(N,\beta,\gamma)_{j_1,m_1,j_2,m_2} = -N \sum_{j_1,j_2 j'' \mu JM} \Lambda_{j_1 j_2}^{j''} (-1)^{J-M+j_1-j''+j_2-m} (2J+1)\sqrt{2j''+1} \times \begin{Bmatrix} 2 & 2 & J \\ j_2 & j_1 & j'' \end{Bmatrix} \begin{pmatrix} 2 & 2 & J \\ \mu & -\mu-M & M \end{pmatrix} \begin{pmatrix} j_1 & j_2 & J \\ m_2 & -m_1 & M \end{pmatrix} \eta_\mu \eta_{-\mu-M}. \tag{4.97}$$

Configuration Mixing

In order to take in consideration 2p-2h excitation, it is necessary to include the space we are working with, meaning that the boson space is then $[N] \oplus [N+2]$, and the corresponding Hamiltonian is the one defined in (3.104)

Furthermore, for identifying the space we are working with, an index i is included in expressions introduced before in the following way,

For the bosonic Hamiltonian in each sector, we write

$$\hat{H}_B^i = \varepsilon_i \hat{n}_d + \kappa_i' \hat{L} \cdot \hat{L} + \kappa_i \hat{Q}(\chi_i) \cdot \hat{Q}(\chi_i), \tag{4.98}$$

with $i = N, N+2$, $\hat{n}_d$ the d boson number operator, being

$$\hat{Q}_\mu(\chi_i) = [s^\dagger \times \tilde{d} + d^\dagger \times s]_\mu^{(2)} + \chi_i [d^\dagger \times \tilde{d}]_\mu^{(2)} \ , \tag{4.99}$$

the quadrupole operator.

The fermion Hamiltonian,

$$\hat{H}_F^i = \sum_j \epsilon_j^i \hat{n}_j \tag{4.100}$$

And finally, for the boson-fermion part,

$$\hat{H}_{\rm BF}^i = \hat{H}_{\rm BF}^{{\rm MON},i} + \hat{H}_{\rm BF}^{{\rm QUAD},i} + \hat{H}_{\rm BF}^{{\rm EXC},i}, \tag{4.101}$$

where each term has been defined in section 4.9,

To account for the mixing between regular, N, and intruder $N+2$, configuration, we make use of the operator $\hat{V}_{BF,mix}^{N,N+2}$ for the bosonic sector already defined in equation (4.85) from section 4.10.

Now that two configurations are introduced, we need to enlarge space and as a result the matrix we are working with is now the following,

$$\mathcal{H}^{CM}_{IBFM}(N,\beta,\gamma) = \begin{pmatrix} \mathcal{M}(N,\beta,\gamma) & \Omega_{BF}(\beta) \\ \Omega_{BF}(\beta) & \mathcal{M}(N+2,\beta,\gamma) \end{pmatrix}, \tag{4.102}$$

where $\mathcal{M}(N,\beta,\gamma)$ and $\mathcal{M}(N+2,\beta,\gamma)$ correspond to the matrices of the regular and the intruder Hamiltonian and $\Omega_{BF}(\beta)$ is the matrix form of the mixing operator $V_{mix}(N,\beta)$ written as

$$V_{mix}(N,\beta) = \sum_{j_1,m_1,j_2,m_2} \Omega_{BF}(N,\beta)_{j_1,m_1,j_2,m_2}\; a^{\dagger}_{j_1,m_1} a_{j_2,m_2}. \tag{4.103}$$

The expression of $V_{mix}(N,\beta)$, assuming equal weight for the s and d boson parts, can be written as,

$$\Omega_{BF}(N,\beta)_{j_1,m_1,j_2,m_2} = \delta_{j_1,j_2}\delta_{m_1,m_2}(\omega+\omega_{j_1})\frac{\sqrt{(N+2)(N+1)}}{1+\beta^2}\left(1+\frac{\beta^2}{\sqrt{5}}\right), \tag{4.104}$$

but considering no dependence of ω_j on j, its value can be absorbed in ω, such that $\omega+\omega_j \to \omega$. Therefore, $\Omega_{BF}(N,\beta)$ is a diagonal matrix proportional to the identity.

As previously discussed, the matrix (4.102) has dimension $2\sum_j(2j+1)$ when both the N and $N+2$ sectors are taken into account. However, it can be separated into two identical sub-blocks, so that its diagonalization yields $\sum_j(2j+1)$ eigenvalues, each depending on β and γ, and each appearing with a twofold degeneracy.

For every eigenvalue, the equilibrium deformation parameters (β_0,γ_0) are determined by minimizing the corresponding energy surface. It should be noted that, in general, the equilibrium parameters may differ from one energy surface to another.

As a result, the proposed formalism brings several significant improvements: it takes into account all three parts of the boson–fermion interaction, allows for the inclusion of multiple j values, incorporates both N and $N+2$ configurations, and explicitly considers the triaxial degree of freedom. Altogether, these aspects represent a substantial advance in the formulation of the boson–fermion intrinsic state within the IBFM framework.

Finally, the eigenstates obtained after diagonalizing the Hamiltonian described in (4.90), are denoted by $|\phi(k;\beta,\gamma)\rangle$, and they describe the physical states of the system obtained as mixtures of the two different configurations: a normal configuration, [N] sector, and an intruder configuration, [N+2] sector.

$$\begin{aligned} |\phi(k;\beta,\gamma)\rangle = &\sum_{j,m} a^{k}_{N;j,m}(\beta,\gamma)|N;\beta,\gamma\rangle \otimes |jm\rangle \\ &+ \sum_{j,m} b^{k}_{N+2;j,m}(\beta,\gamma)|N;\beta,\gamma\rangle \otimes |jm\rangle. \end{aligned} \tag{4.105}$$

Note that the wave functions depends on β and γ. It is also convenient to define the

weight of the wave function contained within the [N]-boson subspace, i.e., the sum of the squared amplitudes (similarly it can be defined for the [N+2] sector),

$$w^k(N;\beta,\gamma) = \sum_{j,m} |a^k_{N;j,m}(\beta,\gamma)|^2. \tag{4.106}$$

In addition, for each of the eigenvalues, it is needed to obtain the equilibrium values of β and γ, β_0 and γ_0, which minimize the corresponding energy surface [44]. Those equilibrium values are, supposedly, different among them and different from the boson ones. This fact is very relevant because the wave functions (4.105) corresponding to the equilibrium values will lose their orthogonal character, in principle, which supposes a drawback of the formalism.

Chapter 5

Structure and Shape Evolution in Even–Even Nuclei

5.1 Introduction

The region around the $Z = 40$ subshell closure is one of the most known testing ground to study how nuclear shapes change as neutrons are added. In this mass region, the even-even isotopes of Sr, Zr, Mo, and Ru show different but closely related patterns of structural evolution when they approach neutron number $N \approx 60$. This makes these isotopic chains particularly convenient in order to perform an analysis of deformation and configuration mixing. The origin of this behavior is moreover strongly connected with the filling of the neutron $1g_{7/2}$ orbital and its interaction with the proton $1g_{9/2}$ orbital. This mechanism was first identified in the seminal works of Federman and Pittel [82, 83, 84], who showed that the simultaneous occupation of neutron-proton spin-orbit partner orbitals plays a key role in driving deformation in this mass region.

In general, the shape of a nucleus results from the balance between different nuclear interactions. Pairing correlations tend to stabilize spherical configurations, while quadrupole correlations favor deformed shapes instead. In addition to this competition, the monopole interaction is the term responsible of controlling the evolution of single-particle energies as a function of particle number.

This balance between competing interactions provides the physical basis for the appearance of shape coexistence. The concept of this phenomenon was first introduced by Morinaga [23] to explain the nature of the first excited 0^+ state in ^{16}O and is now known to occur throughout the nuclear chart. Early shell model studies [24, 25, 26] showed that particle-hole excitations across major shell gaps can generate low-lying deformed 0^+ intruder states. These intruder configurations often give rise to rotational

structures coexisting with spherical states. A classical example is ^{40}Ca, where multi particle-hole configurations successfully reproduce the experimentally observed coexistence of very different shapes [27, 28, 29]. Experimentally, some of the clearest signatures of shape coexistence are observed in nuclear radii and isotope shifts, as first evidenced by the odd-even staggering in the mercury isotopes. Later studies confirmed that sudden changes in radii and related observables appear in many light, medium, and heavy nuclei [85, 86, 30, 87, 32].

When a nucleus lies close to a major shell closure, spherical configurations are usually favored and particle-hole excitations across the shell gap require a large amount of energy, this is something that changes as residual interactions become more relevant at the same time that we increase the number of valence nucleons [30]. In such cases, the excitation energy of particle-hole configurations can be strongly reduced, allowing deformed structures to appear at relatively low energy. This effect is especially pronounced when protons are near a shell closure while neutrons occupy mid shell orbitals, or the other way around. Under these conditions, nuclei can show coexisting configurations with different character, that are called regular configurations associated with 0p-0h excitations and intruder configurations involving 2p-2h excitations, as we introduced in previous sections. These configurations can lie close in energy and, in some nuclei, the intruder configurations may even become energetically lower than the regular ones [88].

From a theoretical point of view, many approaches have been used to describe the evolution of nuclear shapes in the $Z \approx 40$ region. Mean-field calculations based on non-relativistic and relativistic energy density functionals, including Skyrme, Gogny, and PC-PK1 interactions, predict a rapid change from spherical to deformed shapes in neutron–rich Sr and Zr isotopes [89, 90, 91]. In contrast, Mo and Ru isotopes generally show a smoother evolution. In these nuclei, different shapes often lie close in energy and triaxial configurations may develop. Furthermore, Hartree-Fock-Bogoliubov calculations [92] describe Mo isotopes as oblate at $N = 58$ and evolving gradually towards triaxial shapes up to $N \approx 68$, forming a wide region of triaxial deformation. Other studies [93, 94] also report nearly degenerate prolate and oblate minima in several Mo and Ru isotopes. In particular, ^{104}Ru stands out because of the flatness of its potential energy surface, which has been associated with an E(5) symmetry.

Moreover, Zr isotopes provide an essential reference for understanding the behavior of Sr, Mo, and Ru. Along the Zr isotopic chain, the competition between spherical, oblate, and prolate configurations is particularly clear, and many of the mechanisms responsible for the structural evolution of Sr and Mo can be most easily identified [95, 88, 96].

Additional theoretical methods support this picture of Mo and Ru being transitional isotopes, like Triaxial projected shell–model calculations [97], the nucleon–pair approx-

imation [98], and several IBM studies [99, 100, 101, 102, 103, 104]. In the Sr isotopic chain, the approach to $N = 60$ is marked by a very abrupt structural change. This is reflected in a strong decrease of the 2_1^+ excitation energy, a sharp increase of the ratio $E(4_1^+)/E(2_1^+)$, and clear anomalies in nuclear radii and two–neutron separation energies [88, 96]. In Mo isotopes, similar observables indicate a rapid but less sudden evolution, where intruder configurations play an important role. In contrast, Ru isotopes show a smoother behavior, although clear signatures of transitional dynamics remain, especially in nuclei such as ^{104}Ru, which display very flat energy surfaces [105, 106].

In the following sections, the results obtained for the even-even Sr, Mo, and Ru isotopes are presented [36, 37, 107, 108]. For completeness, results for Zr will be also shown, although obtained by other authors. By comparing excitation energies, energy ratios, nuclear radii, and configuration mixing patterns, the analysis aims to provide a unified and transparent picture of shape evolution and the role of intruder configurations in the vicinity of the $Z = 40$ subshell closure.

5.2 Motivation: Experimental and Theoretical evidences of Shape Coexistence and the Crossing of Configurations around $Z = 40$

The presence of different configurations in the energy spectrum implies that states with different deformation exist. However, we must keep in mind that nuclear deformation itself cannot be measured directly and must therefore be inferred from experimental observables or theoretical calculations. When studying the evolution of the different configurations along an isotope chain, those can cross, hence, they can induce the onset of deformation along the isotopic chains and even the appearance of QPTs.

5.2.1 The Moment of Inertia

A valuable approach for gaining insights into the evolving collective structure along the yrast band, with a particular focus on deformation, is to examine the variations in the moment of inertia as one progresses up the band structure. In this context, we will specifically investigate the kinematic moment of inertia, denoted as $J^{(1)}$, which is defined as follows [109],

$$J^{(1)} = \frac{\hbar^2}{2}\left(\frac{dE}{d\left(J(J+1)\right)}\right)^{-1} \approx \frac{\hbar^2(2J-1)}{E_\gamma(J \to (J-2))}, \tag{5.1}$$

where $E_\gamma(J \to (J-2))$ is the energy difference $E(J) - E(J-2)$.

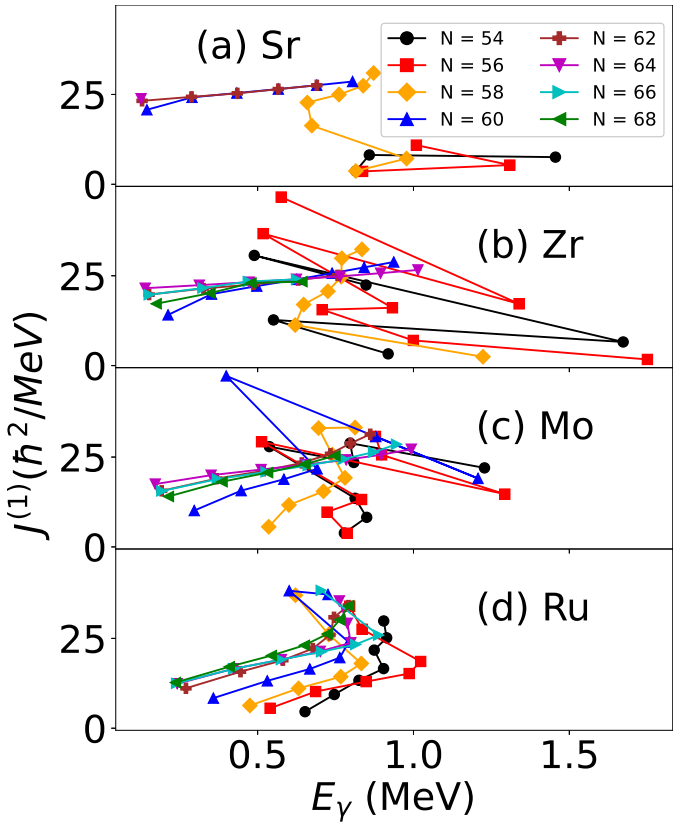

Figure 5.1: Value of the kinematic moment of inertia for Sr, Zr, Mo, and Ru isotopes as a function of the γ energy, for different neutron numbers.

In constructing the experimental values of $J^{(1)}$, we rely on the yrast band energies. However, complexities are encountered at high-spin levels (8^+, 10^+, and 12^+). These complexities arise from the crossing of non-collective states, such as those associated with broken-pair configurations, and the crossing of regular and intruder configurations at specific energy levels. Such crossings can lead to significant variations in the smooth progression of $J^{(1)}$ sometimes resulting in a back-bending pattern.

In Fig. 5.1, we present the kinematic moment of inertia for the different isotope chains. To aid in visualization, it is helpful to note that a purely rotational system exhibits a constant moment of inertia, while a pure vibrational structure appears as a vertical trend. For Sr isotopes a significant change in behavior is observed from N=60 onward, where the moment of inertia demonstrates a relatively smooth trend, indicative of a rotational structure. However, for N=58, it appears that the lowest angular momenta correspond to a more vibrational-like structure, while the highest angular momenta exhibit rotational characteristics. For N=54-56, it is challenging to draw a definitive conclusion, though the substantial values of E_γ (gamma-ray energy) suggest a vibrational system. The results points towards the coexistence of two configurations, with the rotational structure corresponding to the intruder configuration and the vibrational structure to the regular one. For Zr and Mo isotopes, similarly to Sr, the information presented in Fig. 5.1 supports

the existence of two different configurations. From N=60 and onwards, there is a clear presence of a rotational structure. However, for N=54-60, the observed back-bending suggests the coexistence of two structures within the yrast band. In the Ru isotopes, a relatively consistent behavior is observed across the entire chain. Nevertheless, the highest angular momenta exhibit an upward trend, suggesting the presence of a vibrational structure, while the lowest angular momenta maintain a relatively horizontal trend, typical of a more deformed structure. In summary, the kinematic moment of inertia serves as a suitable observable for studying the coexistence of different configurations. For Sr, Zr, and Mo, the data suggests the presence of two crossing configurations, while in Ru, a single configuration exists, showing more of a rotational nature for lower angular momenta and a more vibrational character for higher angular momenta.

5.2.2 The "Crossing" of Configurations

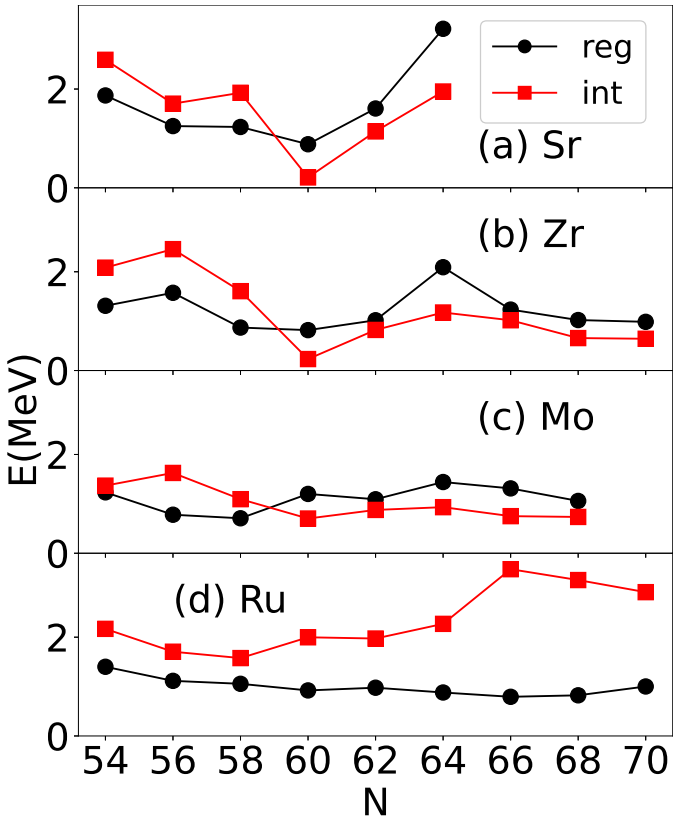

Figure 5.2: Unperturbed regular (black dots and lines) and intruder (red squares and lines) ground-state energies for Sr, Zr, Mo, and Ru isotopes as a function of neutron number.

Distinguishing between regular and intruder states in a nucleus is not straightforward and usually requires the help coming from theoretical description. Initially, we will present results obtained from Sr[36], Zr[88], Mo and Ru [37] (although later they will be presented in more detail), so we can represent in Fig. 5.2 the energies corresponding to the ground

state, employing a calculation in which the interaction mixing the two configuration spaces is switched off. Moreover, the lowest energy states associated with the regular and intruder configurations are shown separately.

As a result, Fig. 5.2 shows that the energy separation between regular and intruder configurations becomes very small in the vicinity of neutron number $N = 60$. In addition, it is possible to observe clear crossings between the two configurations for the Sr, Zr, and Mo isotopic chains. In the Ru isotopes, although a true crossing does not occur, the minimum energy distance between the regular and intruder configurations is also found around $N = 60$, that is a number known for its rapid structural changes and for the presence of a QPT. Therefore, these results justify the study of this region, as it is natural to associate the appearance of these configuration crossings with the underlying QPT [35, 110].

5.3 Experimental Data in the Even-Even Sr, Zr, Mo, and Ru Nuclei

5.3.1 Sr Isotopes

The experimental information available for even-even Sr isotopes in the neutron 50-82 shell covers a wide range of structures, from the closed-shell nucleus ^{88}Sr to the well-deformed ^{102}Sr. Fig. 5.3 summarizes the systematics of positive parity states up to excitation energies of about 3 MeV, in which despite the significant experimental progress achieved in recent years, several isotopes still lack complete spectroscopic information, in particular concerning quadrupole moments.

In Fig. 5.3, we indicate the levels that have been identified in the literature as predominantly regular, or vibrational, in blue, while intruder, rotational states are shown in red. We can observe an evolution of structure along the isotopic chain. In first place, the nucleus ^{88}Sr exhibits the large energy gap characteristic of a closed shell. Then, the isotopes ^{90}Sr and ^{92}Sr display vibrational patterns that become increasingly complex at higher excitation energies. In ^{94}Sr, the energy of the 2_1^+ state remains almost constant, but a noticeable gap develops between the 2_1^+ and 4_1^+ states. Finally, a sudden compression of the spectrum occurs in ^{96}Sr and ^{98}Sr, accompanied by a sharp decrease of the $E(2_1^+)$ energy that ends in ^{100}Sr and ^{102}Sr, where the yrast sequence shows a clear rotational behavior.

For comparison with theoretical calculations, we rely on the evaluated data in Nuclear Data Sheets for $A = 92$ [111], $A = 94$ [112, 113], $A = 96$ [114], $A = 98$ [115, 116], $A = 100$ [117], and $A = 102$ [118]. Moreover, the nuclei $^{88-90}$Sr, being at or too close to the shell

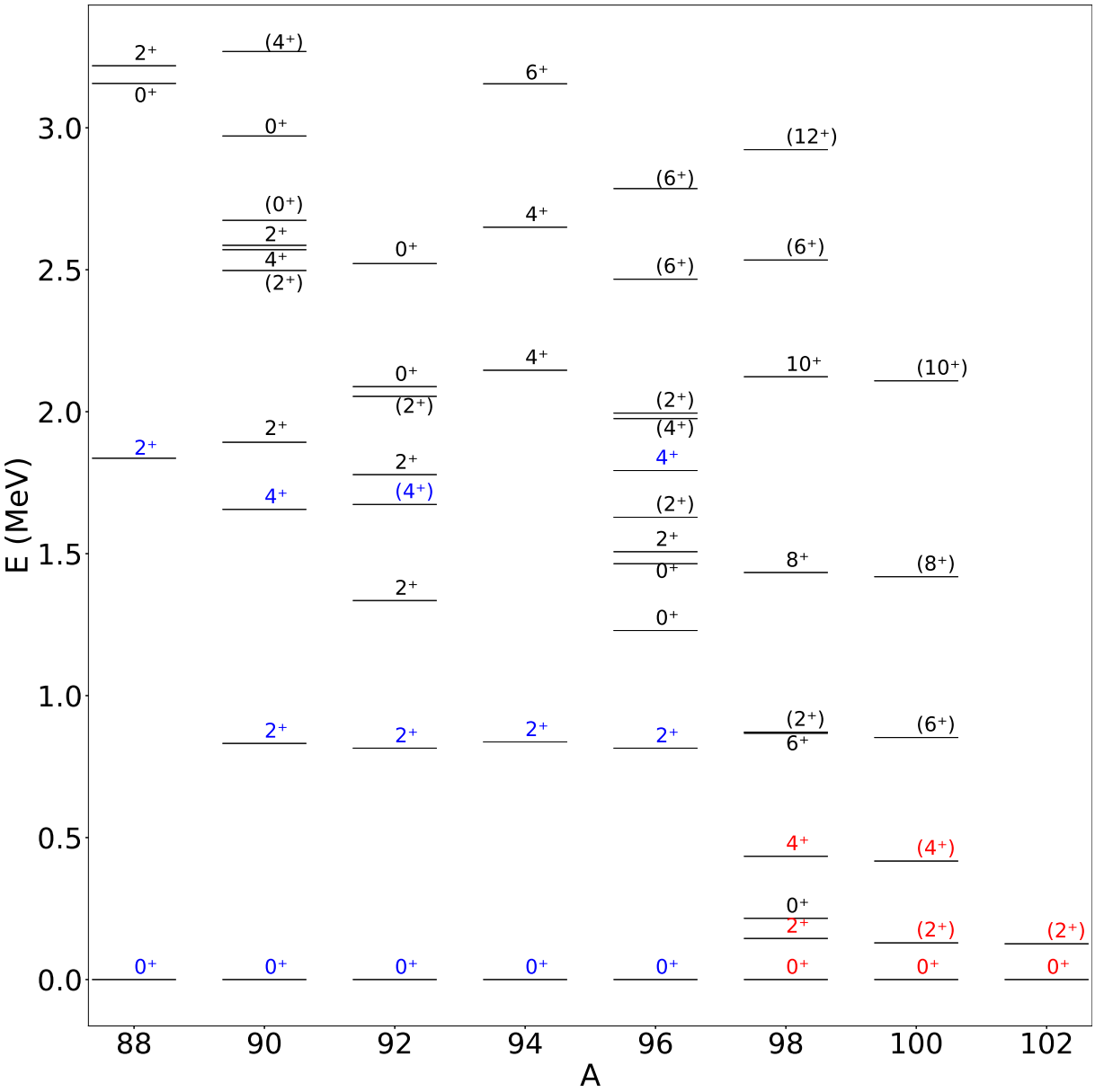

Figure 5.3: Experimental energy level systematics of positive-parity states in Sr isotopes up to $E_x \approx 3$ MeV. Levels labeled in blue correspond to spherical shapes, while those in red correspond to deformed ones (see discussion in Section 5.3).

closure, are excluded from the analysis because the theoretical framework employed (the IBM-CM) is not sufficiently reliable in this region.

A number of experimental works have refined the Sr systematics in recent years. In [119], isotopes ^{92,94,96}Sr were investigated through spontaneous fission of ^{248}Cm, leading to revised spin and parity assignments for several levels. A gamma-ray and internal conversion electron spectroscopy study of ^{98}Sr at TRIUMF-ISAC [120] yielded $\rho^2(E0)$ values for the $0_2^+ \rightarrow 0_1^+$ transition and several B(E2) values, consistent with evaluated data except in the case of $B(E2; 0_2^+ \rightarrow 2_1^+)$. Mixing ratios of 9% for the two lowest 0^+ states and 1.3% for the two lowest 2^+ states were extracted.

Coulomb-excitation experiments at REX-ISOLDE for ^{96,98}Sr [121] provided B(E2) values and spectroscopic quadrupole moments, indicating small mixing between spherical and prolate configurations in ^{98}Sr. A subsequent study with radioactive beams and the MINIBALL array [122] reported a sudden increase in β deformation at ^{98}Sr, with a regular–intruder mixing of about 12%. Lifetime measurements for ^{94,96,98}Sr using the EXILL-FATIMA setup at ILL [123] confirmed the rapid onset of deformation at ^{98}Sr.

Additional insight was obtained from spectroscopic factor measurements for the 0_2^+ and 0_3^+ states in ^{96}Sr [124]. These results are consistent with a mixing amplitude of about 40% and a difference in deformation parameter β of 0.31 between the two states. Delayed γ–ray measurements in ^{97}Sr [125] provided several lifetimes and placed this nucleus at the transition between spherical and deformed structures, corresponding to neutron numbers $N = 58$–60. Finally, Ref. [126] analyzed the 0_2^+ states in ^{98}Sr and ^{100}Zr using spontaneous fission of ^{248}Cm and ^{252}Cf. In that work, the 0^+ states were classified into four categories, and it was concluded that the two lowest 0^+ states correspond to highly deformed 2p-2h neutron excitations involving the $9/2^+$ extruder orbital and low Ω orbitals originating from the $h_{11/2}$ shell.

5.3.2 Zr Isotopes

For completeness, we briefly review the experimental data for zirconium isotopes. Regarding the available data, here we cover a broad range of nuclei, from ^{90}Zr up to neutron-rich isotopes around $A = 110$, where the nucleus ^{90}Zr is close to a closed-shell configuration, while heavier isotopes show more changes in their nuclear structure, we will also restrict ourselves to energies up to 3 MeV, as it has been represented in Fig. 5.4 (figure from [88]).

As we have previously mentioned, some early experimental studies have already reported evidence for the onset of deformation in the mass region around $A \approx 100$, moreover, as the neutron number increases, a clear structural transition is observed. This leads to nuclei with $N \leq 56$ displaying spectra typical of spherical systems, whereas beyond $N \approx 60$ the energy levels rapidly evolve toward a more collective and deformed pattern.

In addition, as in the other isotope chains, this evolution is supported not only by excitation energies but also by electromagnetic observables, isotope shifts, and two-neutron separation energies, which together provide consistent evidence for shape changes along the Zr isotopic chain.

The experimental information is mainly taken from evaluated Nuclear Data Sheets for $A = 92 - 108$ Over the years, several complementary techniques have been applied, including lifetime measurements, neutron scattering, Coulomb excitation, and electron

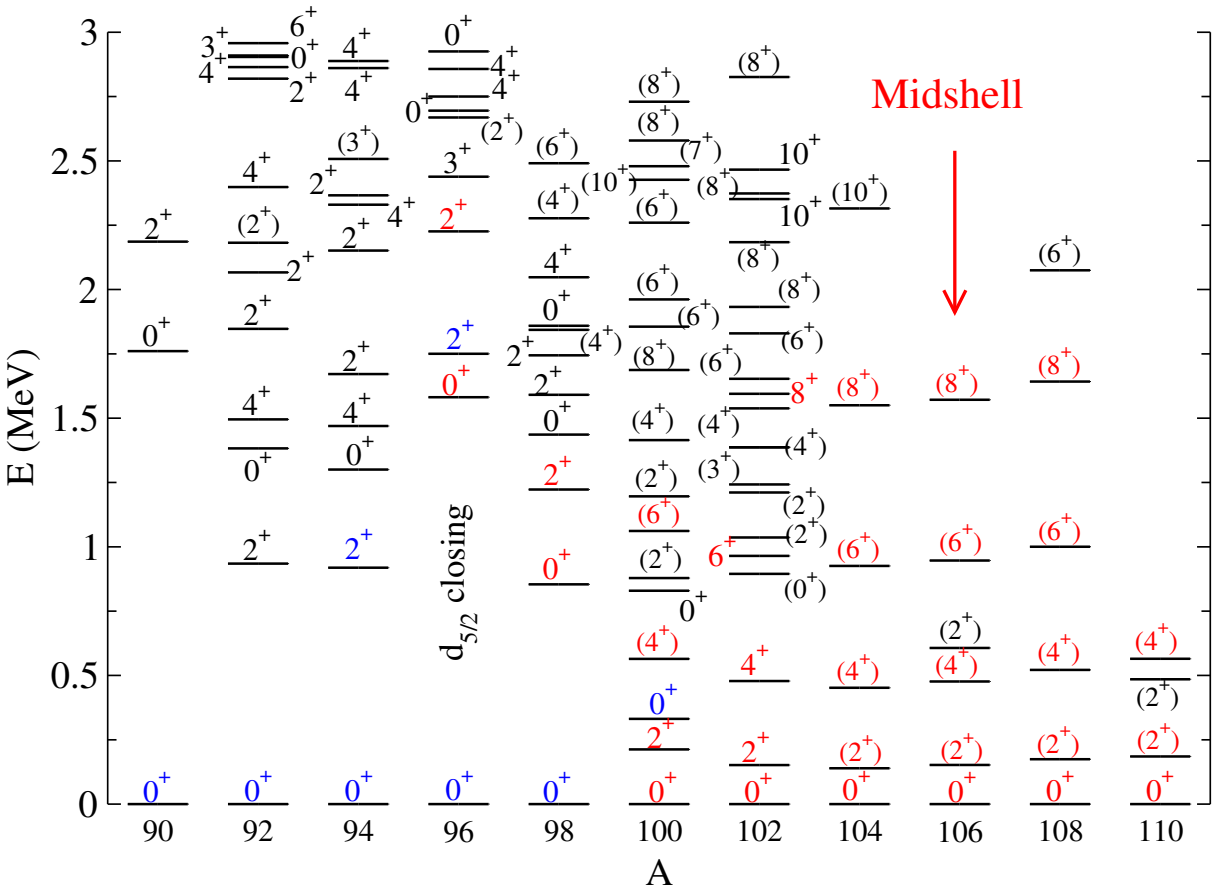

Figure 5.4: Experimental energy level systematics of positive-parity states in Zr isotopes up to $E_x \approx 3$ MeV. Levels labeled in blue correspond to spherical shapes, while those in red correspond to deformed ones (figure from [88].)

scattering experiments. For the most neutron-rich Zr isotopes, prompt γ-ray spectroscopy following fission has provided the available data

5.3.3 Mo Isotopes

The experimental energy systematics from ^{92}Mo to ^{110}Mo below excitation energies of approximately 3 MeV are shown in Fig. 5.5. As the neutron number increases, the density of low lying states grows significantly. The structure evolves smoothly from a vibrational character in the lighter isotopes to a more rotational pattern starting at ^{102}Mo and continuing towards heavier masses. A distinctive feature along the chain is the gradual lowering of the first excited 0^+ state, which reaches its minimum energy in ^{102}Mo. In the heavier isotopes, the near degeneracy of the 4_1^+ and 2_2^+ states, most pronounced in ^{108}Mo, points to an increasing degree of γ softness.

For making a comparison with theory, we use the evaluated Nuclear Data Sheets for $A = 96$ [114], $A = 98$ [115, 116], $A = 100$ [117], $A = 102$ [118], $A = 104$ [127], $A = 106$ [128], $A = 108$ [129], $A = 110$ [118], $A = 112$ [130], and $A = 114$ [131], as well as updated

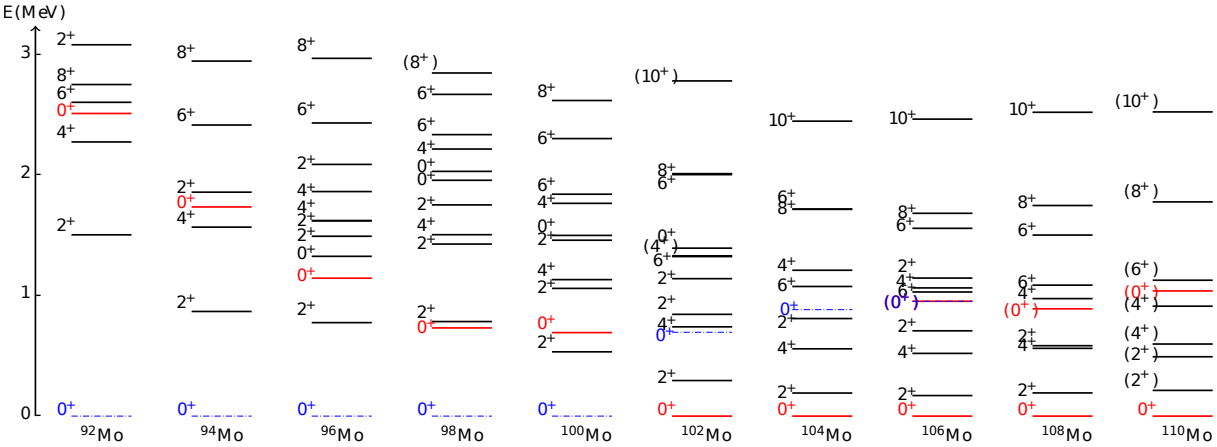

Figure 5.5: Experimental energy systematics of low-lying positive-parity states in Mo isotopes up to about 3 MeV. Levels with dashed blue lines correspond approximately to spherical configurations, and those in red to deformed ones (see Section 5.3).

references when appropriate. A comprehensive overview of experimental data in this mass region, including Mo and Ru isotopes, can be found in [32].

Low-lying states in $^{96-98}$Mo were investigated via $\gamma\gamma$ angular correlations in [132], enabling the determination of angular momenta and mixing ratios. Detailed Coulomb-excitation studies of ^{98}Mo and ^{100}Mo were reported in [133] and [134], respectively. Beta-delayed gamma-ray spectroscopy of $^{106-108-110}$Mo in [135] yielded, for the first time, information on the 0_2^+ band in ^{108,110}Mo. Proton and neutron occupancies in ^{98}Mo and ^{100}Mo were analyzed in [136], revealing a significant change in the filling of the proton $g_{9/2}$ orbital between the two isotopes.

5.3.4 Ru Isotopes

Fig. 5.6 shows the systematics of $^{94-114}$Ru isotopes. A vibrational pattern characterizes $^{94-102}$Ru, gradually leading to a more rotational structure with some degree of γ softness in the heavier nuclei, as suggested by the close spacing between the 4_1^+ and 2_2^+ states. The first excited 0^+ state follows a dropping trend along the chain, reaching its lowest value at ^{102}Ru.

For comparing again with theoretical results, we use the same set of Nuclear Data Sheets references as for Mo, supplemented with the some other recent works. In [137], the 0_2^+ and γ bands in ^{98}Ru were observed using gamma-ray spectroscopy following the β decay of ^{98}Rh and via the ^{100}Ru(p,t) reaction. The 0_2^+ state was proposed to have an intruder character, although mean-field calculations in the same study did not fully support this interpretation. Lifetimes of the 2_1^+, 2_2^+, and 4_1^+ states in ^{98}Ru were measured in [138] to clarify discrepancies regarding the 4_1^+ lifetime.

The 0_2^+ band in ^{102}Ru and its mixing with the 0_1^+ state were analyzed in [139] to investigate

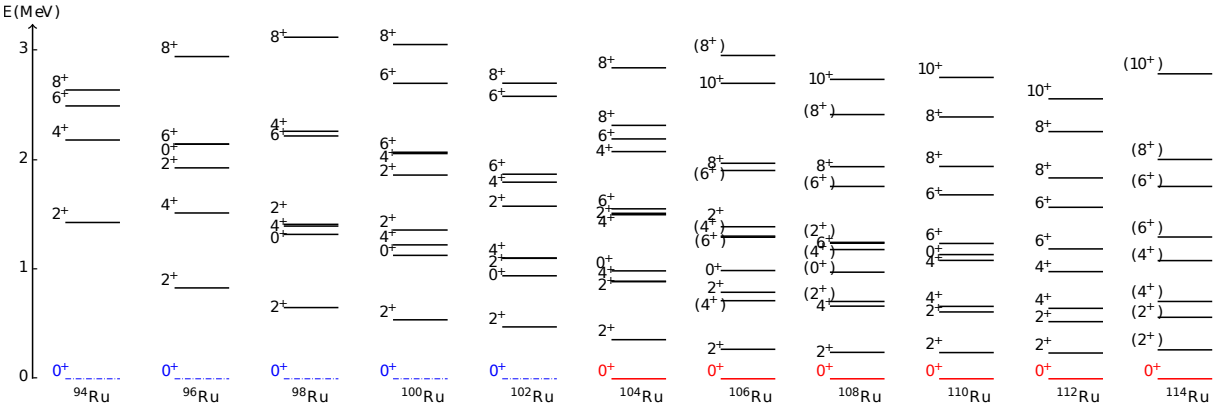

Figure 5.6: Same as Fig. 5.5 but for Ru isotopes.

the evolution of deformation along the Ru chain. Coulomb excitation of ^{104}Ru yielded 28 E2 and 3 M1 matrix elements involving 17 low-lying states [140]. The g-factor of the 2_1^+ state in $^{96-104}$Ru was measured in [141]. More recently, a Coulomb-excitation experiment for ^{102}Ru [142] obtained slightly larger E2 matrix elements than the evaluated values for transitions from the 2_1^+ and 2_2^+ states to the 0_1^+ state, and measured for the first time the matrix element of the $2_3^+ \rightarrow 0_1^+$ transition. The authors concluded that the 0_2^+ state, with $\beta \approx 0.18$, is slightly less deformed than the ground state, with $\beta \approx 0.24$.

5.4 Fitting Procedure: Energy Spectra and Absolute B(E2) Reduced Transition Probabilities

In this Section, we summarize the procedure employed to determine the parameters of the IBM-CM Hamiltonian, written equation (3.104), where the Hamiltonian employed is the one given by Consistent-Q formalism, as we have explained in previous sections.

The same fitting strategy has been applied to the three isotopic chains considered in this work: Sr, Mo, and Ru, and the procedure has been detailed in Appendix A. For each chain, the relevant neutron-rich even-even isotopes within the $50 \leq N \leq 82$ shell have been included, excluding nuclei too close to the neutron shell closure, where the applicability of the IBM is questionable. The fitting is carried out by requiring a simultaneous and coherent description of level energies and absolute B(E2) reduced transition probabilities, using a standard χ^2 minimization procedure as it is detailed in Refs. [143, 144, 145, 88] and also in Appendix A.

In the most general case, the IBM-CM Hamiltonian and the E2 operator involve thirteen parameters, coming from the Hamiltonian operator together with the transition one. In practice, the number of free parameters is smaller for several nuclei, either because some terms are not required or because a subset cannot be unambiguously described by the

available data. Moreover, across the isotopic chains, we impose that the evolution of the parameters develops smoothly as we increase the neutron number or even, when possible, keep a subset of parameters fixed.

5.4.1 Sr Isotopes

For the Sr isotopes, the resulting parameters are listed in Table 5.1. There, it is noticeable that the parameter Δ^{N+2} exhibits a clear evolution: it takes larger values for the lighter isotopes (around 1900 keV) and decreases to 1360 keV for the heavier members of the chain. For $^{100-102}$Sr, all experimentally known low-lying states correspond to the intruder configuration, in consequence, the parameters of the regular configuration cannot be fixed and have been taken from ^{98}Sr.

Similarly, the intruder effective charge for ^{92}Sr and ^{102}Sr has been taken from the values obtained for ^{94}Sr and ^{100}Sr, respectively. The global evolution of the parameters is relatively smooth, although some exceptions appear, being the most notably one the sudden drop in the intruder effective charge e_{N+2} for ^{96}Sr, for which no clear physical explanation is evident.

Table 5.1: Hamiltonian and $\hat{T}(E2)$ parameters resulting from the present study for Sr isotopes. All quantities have dimensions of energy (in keV), except χ_N and χ_{N+2}, which are dimensionless, and e_N and e_{N+2}, given in units of $\sqrt{\text{W.u.}}$.

Nucleus	N	ε_N	κ_N	χ_N	κ'_N	ε_{N+2}	κ_{N+2}	χ_{N+2}	κ'_{N+2}	ω	Δ^{N+2}	e_N	e_{N+2}
^{92}Sr	3	838	-32.01	0.00	-7.84	347.2	-15.00	-0.88	0.00	15	1900	1.53	1.53[a]
^{94}Sr	4	365	-50.00	0.00	75.01	451.7	-41.81	0.00	0.00	15	1800	1.16	1.53
^{96}Sr	5	620	-35.00	0.64	53.43	242.7	-20.00	-0.79	9.84	15	1500	1.33	0.86
^{98}Sr	6	526	-28.19	1.88	18.59	279.1	-34.96	-0.72	0.23	15	1360	0.78	2.22
^{100}Sr	7	526[b]	-28.19[b]	1.88[b]	18.59[b]	387.3	-43.16	-0.77	-2.99	15	1360	0.78[b]	1.93
^{102}Sr	8	526[b]	-28.19[b]	1.88[b]	18.59[b]	387.3	-46.41	-0.77	-2.99	15	1360	0.78[b]	1.93[c]

[a] $\hat{T}(E2)$ intruder parameter taken from ^{94}Sr.
[b] Hamiltonian and $\hat{T}(E2)$ parameters for the regular sector taken from ^{98}Sr.
[c] $\hat{T}(E2)$ intruder parameter taken from ^{100}Sr.

5.4.2 Zr Isotopes

Again for completeness we present the results of the fitting procedure for Zr isotopes (see [88]). Here the IBM-CM parameters were determined again by fitting experimental excitation energies and absolute B(E2) transition probabilities for the isotopes ^{94}Zr to ^{110}Zr. Additionally, the nuclei ^{90,92}Zr were excluded due to their proximity to the $N = 50$ shell closure, where the IBM description becomes less reliable.

In the same philosophy, the fitting procedure aims at a global reproduction of the data while enforcing a smooth evolution of the parameters along the isotopic chain, moreover

whenever possible, they were kept constant. However, for the lightest isotopes, the influence of the $N = 50$ and $N = 56$ closures requires variations in the mixing strength and in the energy offset between configurations, which decrease toward heavier isotopes.

As it is interesting to present the Hamiltonian and $\hat{T}(E2)$ parameters resulting from this fitting procedure, so as to compare with the other cases, they can be regarded in Table 5.2.

Table 5.2: Hamiltonian and $\hat{T}(E2)$ resulting from an IBM-CM calculation for Zr isotopes. All quantities have the dimension of energy (keV), except χ_N and χ_{N+2}, which are dimensionless, and e_N and e_{N+2}, which are given in $\sqrt{\text{W.u.}}$. Taken from [88].

Nucleus	ε_N	κ_N	χ_N	κ'_N	ε_{N+2}	κ_{N+2}	χ_{N+2}	κ'_{N+2}	ω	Δ	e_N	e_{N+2}
^{94}Zr	1201	0.00	1.30	-39.93	0.1	-26.32	-2.35	21.97	150	3200	2.01	-1.36
^{96}Zr	1800	-34.41	1.82	25.12	333.2	-29.18	0.09	-4.50	15	2000	0.90	3.35
^{98}Zr	1044	-25.23	1.80	78.71	439.6	-14.32	0.67	26.48	15	814	1.55	3.11
^{100}Zr	1063	-23.26	2.53	0.00	438.3	-28.76	-0.95	0.00	15	820	0.46	2.26
^{102}Zr	1050	-23.58	2.46	0.00	337.9	-32.01	-0.68	0.00	15	820	0.46	2.32
^{104}Zr	1050[a]	-23.58[a]	2.46[a]	0.00[a]	616.5	-32.00	-1.35	0.00	15	820	0.46[a]	2.04
^{106}Zr	1050[a]	-23.58[a]	2.46[a]	0.00[a]	580.5	-31.03	-0.93	0.00	15	820	0.46[a]	1.79
^{108}Zr	1050[a]	-23.58[a]	2.46[a]	0.00[a]	540.2	-30.00	-0.90	0.00	15	820	0.46[a]	1.79[b]
^{110}Zr	1050[a]	-23.58[a]	2.46[a]	0.00[a]	498.9	-32.00	-0.90	0.00	15	820	0.46[a]	1.79[b]

[a] Hamiltonian and $\hat{T}(E2)$ parameters for the regular sector taken from ^{102}Zr.
[b] Effective charge for the intruder sector taken from ^{106}Zr.

5.4.3 Mo Isotopes

The parameters obtained for the Mo isotopes following the same procedure are presented in Table 5.3. The fitting includes the nuclei $^{96-110}$Mo, and a common value of $\Delta^{N+2} = 1500$ keV is employed for the entire chain, that lies within the typical range used in nearby mass regions, such as Zr ($\Delta^{N+2} = 820$–3200 keV) and Sr ($\Delta^{N+2} = 1360$–1900 keV).

In most Mo isotopes, the mixing strength takes the value $\omega = 15$ keV, while for the lighter nuclei $^{96-100}$Mo a larger value $\omega = 45$ keV is required. For the heaviest isotopes, $^{108-110}$Mo, the experimental information does not allow a reliable determination of the parameters associated with the regular configuration; therefore, those parameters have been fixed to the values obtained for ^{106}Mo.

Overall, a smooth parameter evolution is obtained across the chain, except in those cases where limited experimental information forces the use of fixed values.

5.4.4 Ru Isotopes

Finally, the description of the Ru isotopes is summarized in Table 5.4. Here, the situation is more constrained because we have a lack of experimental signatures of intruder states

Table 5.3: Hamiltonian and $\hat{T}(E2)$ parameters resulting from the study of Mo isotopes in the present work. All quantities have dimensions of energy (keV), except χ_N and χ_{N+2}, which are dimensionless, and e_N and e_{N+2}, which are given in units of $\sqrt{\text{W.u.}}$. The value $\Delta^{N+2} = 1500$ keV is fixed for all isotopes.

Nucleus	ε_N	κ_N	χ_N	κ'_N	ε_{N+2}	κ_{N+2}	χ_{N+2}	κ'_{N+2}	ω	e_N	e_{N+2}
^{96}Mo	695.84	0.00	1.50	15.00	191.56	-9.96	1.12	13.69	45.0	2.48	4.00
^{98}Mo	813.16	0.00	-1.70	-5.00	873.21	-25.08	1.50	-5.00	45.0	2.73	-0.87
^{100}Mo	517.29	-2.00	-1.49	10.00	408.52	-21.98	0.05	4.34	45.0	2.24	2.88
^{102}Mo	470.23	-4.93	-1.50	-5.00	446.78	-35.00	0.14	1.08	15.0	4.00	-2.15
^{104}Mo	150.00	-10.00	-1.34	7.02	450.04	-35.00	0.49	-0.63	15.0	2.11	-2.05
^{106}Mo	294.38	-15.00	-0.58	0.02	263.83	-29.90	0.37	7.68	15.0	1.90	1.93
^{108}Mo	294.38[a]	-15.00[a]	-0.58[a]	0.02[a]	203.58	-28.85	0.12	8.98	15.0	1.90[b]	2.12
^{110}Mo	294.38[a]	-15.00[a]	-0.58[a]	0.02[a]	200.00	-31.79	0.01	7.58	15.0	1.90[b]	2.12[c]

[a] Hamiltonian parameters for the regular sector taken from ^{106}Mo.
[b] $\hat{T}(E2)$ regular parameter taken from ^{106}Mo.
[c] $\hat{T}(E2)$ intruder parameter taken from ^{108}Mo.

along the chain. Only in ^{100}Ru can a few 0^+ states be clearly identified as belonging to the intruder configuration. Consequently, the intruder-sector parameters extracted for ^{100}Ru have been adopted for all other Ru isotopes, and the description of intruder states in this chain must therefore be considered only as an approximation.

In addition, several parameters have been kept fixed along the entire Ru chain: $\chi_N = \chi_{N+2} = 0$, $\kappa'_{N+2} = 0$ keV, and $\omega = 15$ keV. The value of Δ^{N+2} is set to 2200 keV for all isotopes; although this value is only constrained by the limited intruder-state information in ^{100}Ru, it provides a consistent description of the chain as a whole. Finally, the fixed χ parameters imply that both regular and intruder configurations in Ru behave as γ-unstable.

Table 5.4: Hamiltonian and $\hat{T}(E2)$ parameters resulting from the study of Ru isotopes in the present work. All quantities have dimensions of energy (keV), except e_N and e_{N+2}, which are given in units of $\sqrt{\text{W.u.}}$. The values $\chi_N = \chi_{N+2} = 0$, $\kappa'_{N+2} = 0$ keV, $\omega = 15$ keV and $\Delta^{N+2} = 2200$ keV were fixed for all isotopes.

Nucleus	ε_N	κ_N	κ'_N	ε_{N+2}	κ_{N+2}	e_N	e_{N+2}
^{98}Ru	683.60	-15.79	-1.28	410.72[a]	-24.08[a]	2.55	4.00[a]
^{100}Ru	546.85	-19.89	8.60	410.72	-24.08	2.34	4.00
^{102}Ru	535.28	-20.46	4.75	410.72[a]	-24.08[a]	2.27	4.00[a]
^{104}Ru	412.75	-24.34	7.03	410.72[a]	-24.08[a]	2.11	4.00[a]
^{106}Ru	360.60	-26.37	5.67	410.72[a]	-24.08[a]	1.96	4.00[a]
^{108}Ru	298.53	-29.19	7.60	410.72[a]	-24.08[a]	1.67	4.00[a]
^{110}Ru	250.00	-30.00	9.55	410.72[a]	-24.08[a]	1.55	4.00[a]
^{112}Ru	250.00	-30.00	6.43	410.72[a]	-24.08[a]	1.76	4.00[a]
^{114}Ru	299.33	-34.25	5.55	410.72[a]	-24.08[a]	1.80	4.00[a]

[a] Hamiltonian and $\hat{T}(E2)$ parameters for the intruder sector taken from ^{100}Ru.

Taken together, the fitting procedures for Sr, Mo, and Ru provide a coherent set of Hamiltonian and transition-operator parameters that evolve smoothly along each isotopic chain.

5.5 Correlation Energy in the Configuration Mixing Approach

As we have introduced before, the relative position of regular and intruder configurations is governed by the competition between two effects, in first place the energy required to promote particles across a shell or subshell gap, and secondly, the correlation energy gained through boson interactions. In the isotopic chains that we will present here, intruder configurations originate from $2p$-$2h$ excitations across a subshell closure, and although such excitations are expected to lie at higher energies than the regular configurations, their actual placement in the spectrum depends critically on pairing effects and on the additional correlation energy, which is generally larger for intruder states due to their higher boson number.

In the Sr isotopes, the $Z = 40$ shell gap leads to an excitation energy of $\Delta^{N+2} = 1900$ keV in ^{92}Sr, which gradually decreases to about $\Delta^{N+2} = 1340$ keV for $^{98\text{-}102}$Sr. These values already include the gain in pairing energy associated with the formation of two additional 0^+ pairs. However, the energy of the intruder band head is not determined by Δ^{N+2} alone, since both regular and intruder configurations gain correlation energy that increases toward mid-shell. This effect is more pronounced for intruder states, which contain a larger number of bosons, as illustrated in Fig. 5.7 in panel (a) for Sr. Moreover, a similar dynamic can be distinguished for Zr isotopes in panel (b), as the shell gap decreases from $\Delta^{N+2} = 3200$ keV in ^{94}Zr, that decreases to $\Delta^{N+2} = 820$ keV in ^{100}Zr.

A similar situation is found in the Mo and Ru isotopic chains. In Mo isotopes, the $2p$-$2h$ excitation energy is $\Delta^{N+2} = 1500$ keV, while in Ru isotopes it reaches the value of $\Delta^{N+2} = 2200$ keV. These values represent the energetic cost of generating the intruder configurations before additional correlation effects are taken into account, and define the reference energies shown in Figs. 5.9(a) and 5.9(b).

To better isolate the role of correlation energy, it is instructive to temporarily switch off the mixing term in the IBM-CM Hamiltonian. This procedure yields a set of unperturbed energies, allowing the regular and intruder configurations to be analyzed independently. Fig. 5.7 displays the unperturbed energies of the lowest 0_1^+ states in the regular (set to zero) and intruder (set to Δ^{N+2}) spaces for Sr isotopes, where the thick red dashed line indicates the reference energy of the regular ground state.

Furthermore, we have included the case of Zr isotopes in panel b) of Fig.5.7, following the same color code for the energy levels, which have been obtained following a similar procedure in [88].

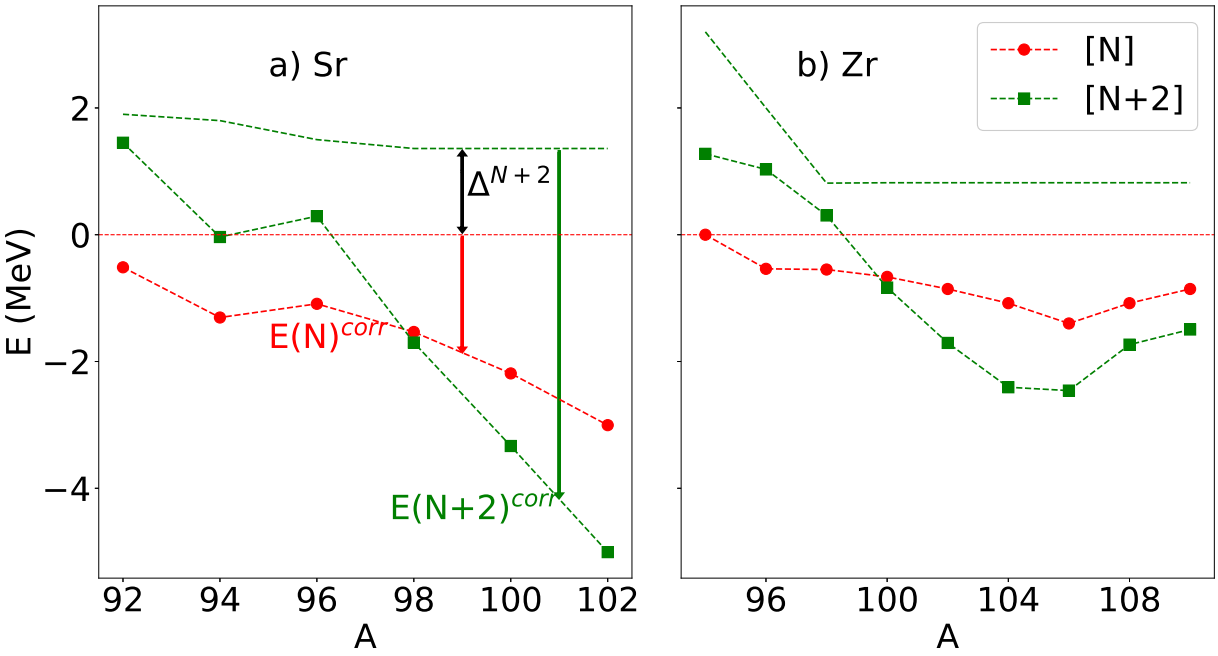

Figure 5.7: Absolute energy of the lowest unperturbed regular and intruder 0_1^+ states for $^{92\text{-}102}$Sr and $^{94\text{-}110}$Zr. The arrows in panel a) indicate the correlation energies in the N and $N+2$ subspaces.

In the Sr chain, the correlation energy of the regular ground state is mainly driven by the strength of $|\kappa_N|$, as reflected by the gradual lowering of the regular curve in Fig. 5.7. In contrast, the intruder configuration already displays a sizable correlation energy at $A = 92$, which increases steadily and reaches a maximum near mid-shell at $A = 102$, as shown by the downward evolution of the intruder curve in the same figure. From $A = 98$ onward, the intruder configuration lies below the regular one, and the energy separation between the two configurations increases with neutron number (Fig. 5.7). The results for $^{100\text{-}102}$Sr should, however, be interpreted with some caution, since the Hamiltonian parameters for the regular configuration could not be fully constrained by the available experimental data.

In contrast to the Sr isotopes discussed above, the Zr isotopic chain, shown in panel b) of Fig. 5.7, exhibits a more pronounced evolution of the relative position of regular and intruder configurations but also driven by $|\kappa_N|$. As is noticeable, in Zr nuclei, the energy required to generate the intruder configuration across the $Z = 40$ shell gap is as well as in Sr isotopes, larger at the beginning of the chain, with $\Delta^{N+2} \approx 3200$ keV in ^{94}Zr, but it decreases rapidly with increasing neutron number, reaching values below 1 MeV around ^{100}Zr. As in the previous case, this reduction is accompanied by a strong increase of the

correlation energy in the intruder sector, driven both by the stronger quadrupole interaction and by the larger effective number of bosons in the $[N+2]$ space. Consequently, the intruder configuration in Zr becomes larger near midshell and eventually drops below the regular one, leading to a crossing of the two configurations. Finally, while the underlying mechanism is common to both chains, the Zr nuclei present a larger decrease of Δ^{N+2} as reported in Ref. [88]. Moreover, it is interesting to notice, that the crossing between regular and intruder configuration is encountered earlier in Zr isotopes. This delayed crossing in the Sr isotopes reflects the slower reduction of Δ^{N+2} and the more gradual build-up of quadrupole correlation energy in the intruder sector, which together postpone the crossing of the intruder configuration with respect to the Zr case.

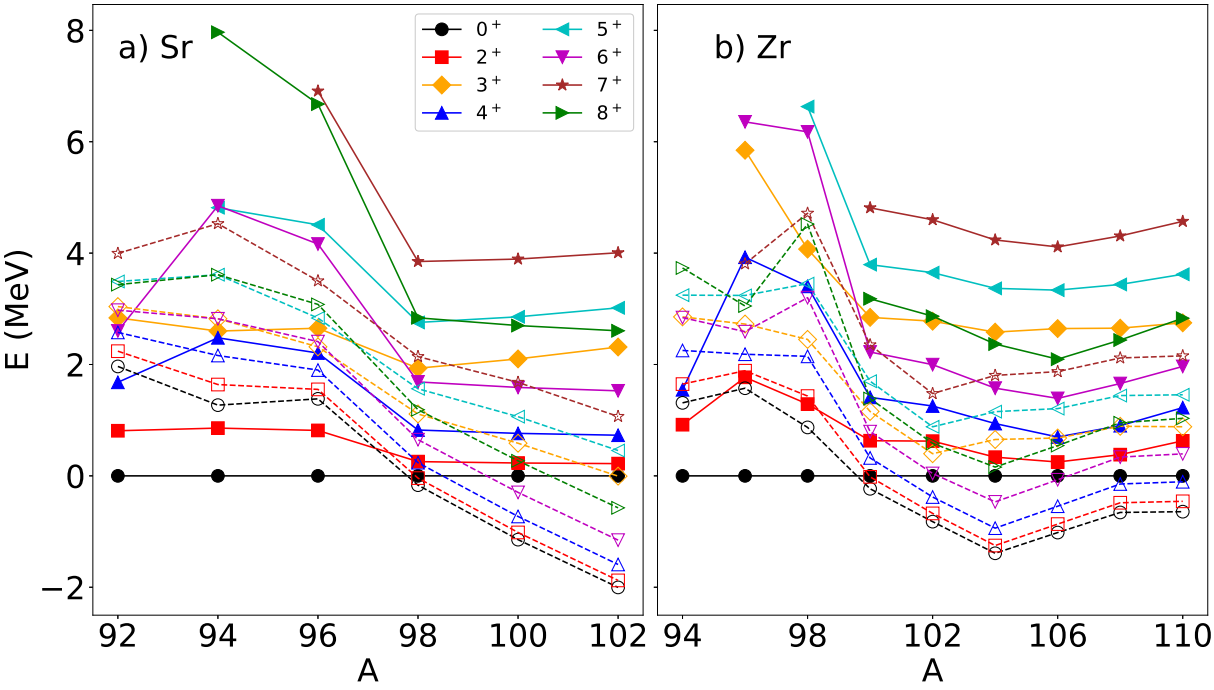

Figure 5.8: Energy spectra obtained from the IBM-CM Hamiltonian of Table 5.1 with the mixing term switched off. The lowest regular (solid lines, closed symbols) and intruder (dashed lines, open symbols) states are shown for each angular momentum. Data in panel (b) taken from [88].

Additional insight into the structure of the unperturbed configurations is obtained from the excitation spectra shown in Fig. 5.8, where in panel a) the unperturbed spectra of Sr isotopes, reveal the progressive lowering of the intruder states relative to the regular ones as neutron number increases, consistent with the behavior observed for the 0_1^+ energies in Fig. 5.7.

To complement the above analysis, the case of Zr isotopes is presented in panel b) of Fig. 5.8, where again, regular and intruder states provide a clear illustration of the parabolic behavior expected for the intruder configurations. In this case, the energy systematics reveal a pronounced kink in the regular configurations around $A = 96$, fol-

lowed by a flatter evolution toward heavier isotopes in both isotopic chains. Meanwhile, the intruder states display an overall parabolic trend, with a minimum in $A \approx 104$ for Zr chain, being this minimum in $A \approx 102$ for the case of Sr.

The same analysis has been applied to the Mo and Ru isotopes. In the Mo chain, the unperturbed energy curves exhibit a clear crossing between the regular and intruder configurations between $A = 100$ and $A = 102$ ($N = 60$), as shown in Fig. 5.9(a). For $A \geq 102$, the intruder configuration becomes energetically favored. While the regular configuration gains correlation energy gradually, the intruder configuration evolves more rapidly due to both its larger boson number and the condition $|\kappa_{N+2}| > |\kappa_N|$, leading to the pronounced downward slope observed near mid-shell in Fig. 5.9(a).

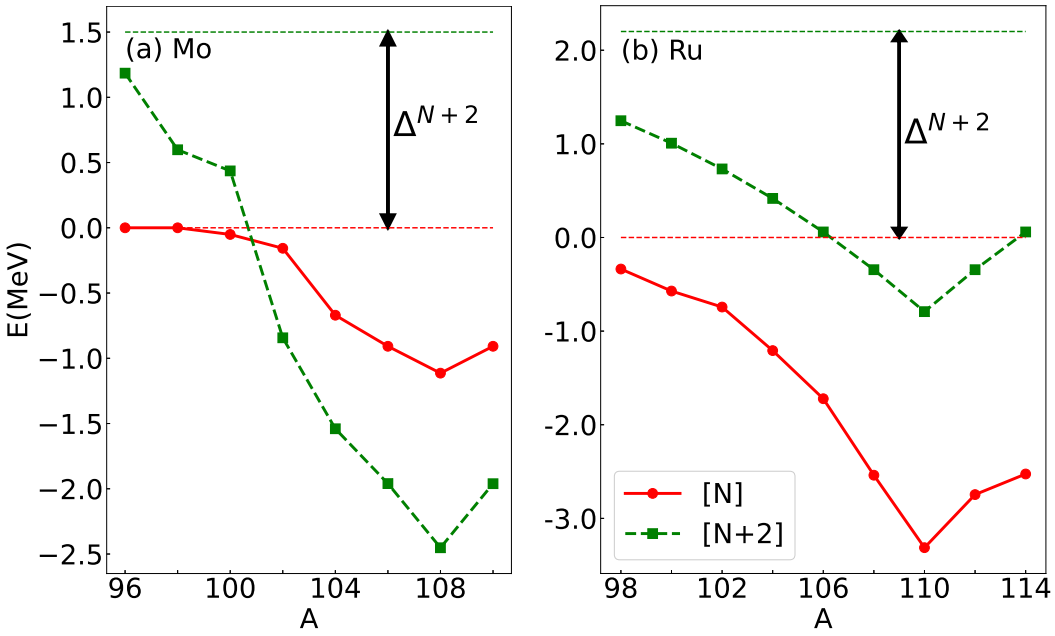

Figure 5.9: Absolute energy of the lowest unperturbed regular (red) and intruder (green) 0_1^+ states for $^{96\text{-}110}$Mo (panel (a)) and $^{98\text{-}114}$Ru (panel (b)). Thin dashed lines indicate the reference energies for the regular and intruder configurations.

In contrast, the Ru isotopes display a markedly different behavior. As shown in Fig. 5.9(b), the regular configuration remains energetically lower throughout the entire isotopic chain and gains more correlation energy than the intruder configuration. The intruder curve exhibits a shallow minimum around $A = 98$-102, followed by a rapid increase in energy for heavier isotopes. Since the intruder Hamiltonian parameters are fixed and taken to be identical to those of ^{100}Ru, the trends shown in Fig. 5.9(b) should be interpreted with some caution.

The impact of these trends on the observable spectra is illustrated in Fig. 5.11. The calculated IBM-CM excitation energies reproduce the experimental systematics, in particular the increasing role of the intruder configuration for $A \geq 98$, consistent with the unperturbed energy analysis discussed above.

Further information on the evolution of collectivity is provided by the unperturbed excitation spectra shown in Fig. 5.10. In the Sr isotopes, the intruder spectrum displays a characteristic kink for $L > 2$, with a maximum around $A = 94$ (Fig. 5.8), which may be related to the filling of the $d_{5/2}$ orbital, as observed in Zr isotopes. This is also observed in the case of Mo, where the regular configuration evolves rapidly from a vibrational to a more rotational pattern, while the intruder configuration shows a smoother evolution and becomes the ground-state configuration for $A \geq 98$, in agreement with Fig. 5.7.

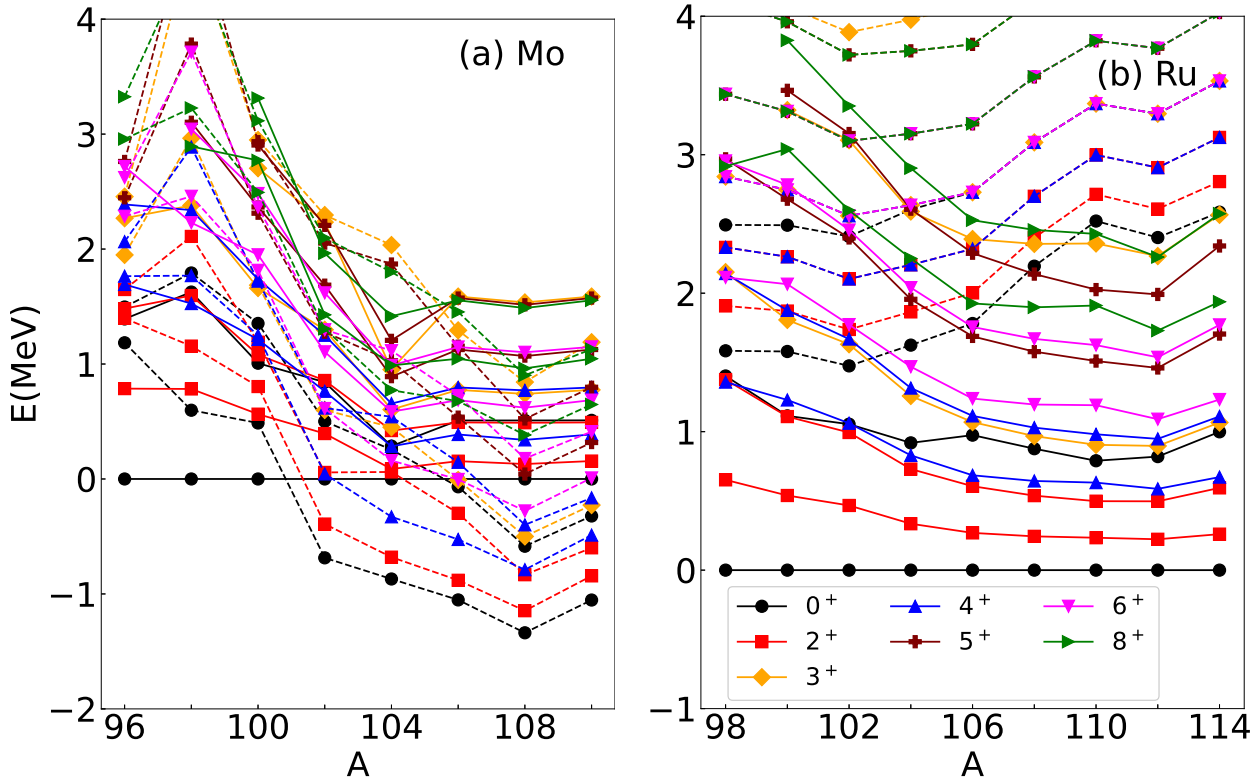

Figure 5.10: Unperturbed energy spectra for Mo (panel (a)) and Ru (panel (b)) isotopes obtained by switching off the mixing term in the IBM-CM Hamiltonian. Solid lines correspond to regular states and dashed lines to intruder states.

In the Mo isotopes, Fig. 5.10(a) shows that the regular configuration is predominantly vibrational in the lighter nuclei and gradually evolves toward a more rotational regime as mass increases. The intruder configuration exhibits a stronger rotational character throughout the chain, becoming particularly pronounced for $A > 100$.

In Ru isotopes, Fig. 5.10(b) shows that the intruder configuration lies substantially higher in energy, with only a shallow minimum around $A = 98$-102, before increasing sharply for heavier isotopes. The regular configuration displays a well-defined vibrational pattern in the lighter nuclei, while a structural transition is observed at $A = 104$ ($N = 60$).

Finally, the combined analysis of correlation energies and unperturbed spectra shown in Figs. 5.7, 5.9, and 5.10 highlights the role of configuration mixing in shaping the low-

energy structure of these nuclei. While Sr, Zr and Mo isotopes exhibit a clear dominance of intruder configurations near mid-shell, Ru isotopes remain governed by regular configurations. Despite these differences, all three isotopic chains display an enhancement of correlation energy around mid-shell, underscoring its fundamental role in the development of nuclear collectivity.

5.6 Detailed Comparison of Energy Spectra and B(E2) Transition Rates

Before discussing the isotopic chains individually, it is useful to outline the global trends observed in Sr, Zr, Mo, and Ru nuclei, as these chains display markedly different structural evolutions. The Sr isotopes undergo a rapid and abrupt transition around $N = 60$, associated with a sudden onset of deformation and the dominance of intruder configurations, being this behavior even more abrupt in the case of Zr isotopes. In contrast, the Mo isotopes exhibit a smoother evolution characterized by configuration mixing together with some signatures of shape coexistence over several isotopes near mid-shell. Finally, Ru isotopes show the most gradual behavior, evolving from vibrational to O(6)-like structures while remaining dominated by regular configurations throughout.

5.6.1 Sr isotopes

In first place, we present a detailed comparison between experimental data and IBM-CM calculations for the Sr isotopes, counting with excitation energies up to $E \approx 3$ MeV. The experimental spectra are shown in Fig. 5.11(a), while the corresponding theoretical results are displayed in Fig. 5.11(b). As discussed in Ref. [143], the excitation energy of the 2_1^+ state was assigned a large weight in the fitting procedure; consequently, its evolution along the isotopic chain closely follows the experimental trend.

For $A = 92$ and $A = 94$, the spectra reflect the influence of the neutron shell closure at $N = 50$ and the subshell closure at $N = 56$, producing noticeable discontinuities in the excitation energies, as seen in Fig. 5.11. The spectrum of ^{92}Sr displays an overall vibrational character, although the members of the two-phonon triplet are widely spread in energy. In ^{94}Sr, the lack of observed excited 0^+ states and the kink in the $4_{1,2}^+$ energies complicate the interpretation, although the IBM-CM reproduces this kink and predicts a low-lying excited 0^+ state, similar in energy to that observed experimentally in ^{96}Sr, this prediction must be treated with caution.

For ^{96}Sr, the agreement between theory and experiment is generally good, despite the 4_2^+ and 6_2^+ states being calculated slightly higher than observed. In ^{98}Sr, the sudden structural change is very well reproduced: the calculated spectrum exhibits a rotational yrast band

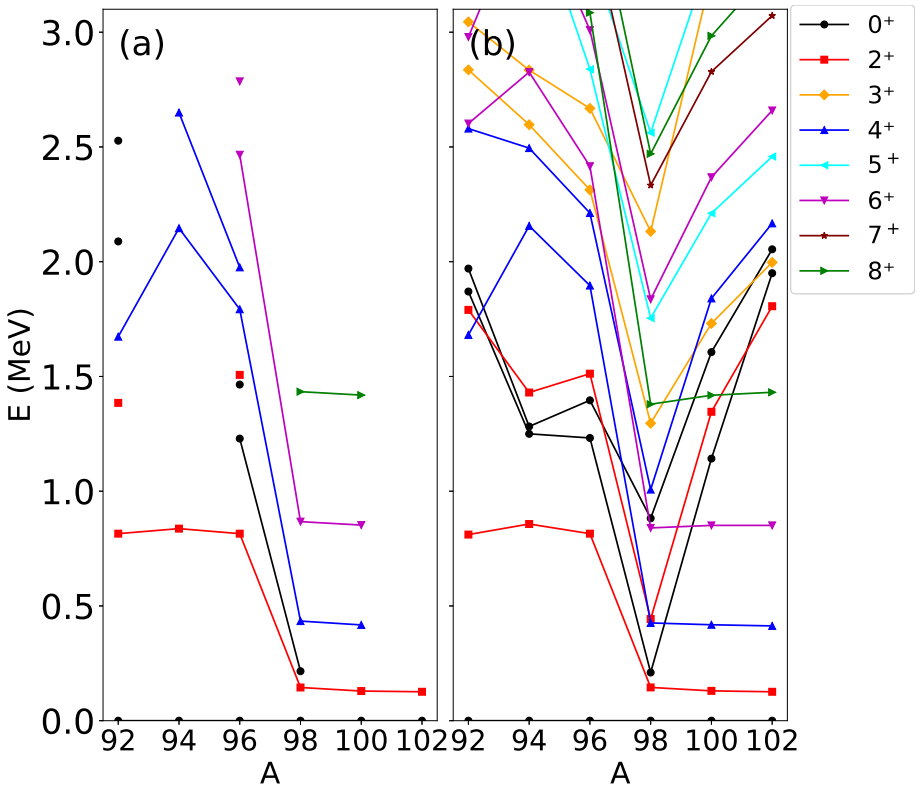

Figure 5.11: Experimental excitation energies (panel (a)) and IBM-CM results (panel (b)) for Sr isotopes up to $E \approx 3$ MeV. Only two excited states (when available experimentally) are shown for each angular momentum.

and a very low-lying first excited 0^+ state. For ^{100}Sr and ^{102}Sr, where experimental information is scarce, the IBM-CM predicts a rotational yrast structure and an intruder configuration whose excitation energy increases away from $N = 60$.

The available experimental B(E2) values, summarized in Table 5.5, allow for a meaningful comparison with the IBM-CM results. The systematics of yrast and non-yrast transitions are shown in Figs. 5.12 and 5.13, respectively. Along the yrast band (Fig. 5.12), the experimental data exhibit a clear increase in collectivity with increasing mass number, with a particularly pronounced change between $A = 96$ and $A = 98$, which is associated with the onset of nuclear deformation. This behavior is well reproduced by the calculations, which display a characteristic peak in the $6_1^+ \rightarrow 4_1^+$ and $8_1^+ \rightarrow 6_1^+$ transitions, linked to the filling of the neutron $d_{5/2}$ orbital.

In contrast, the interband transitions (Fig. 5.13) remain relatively smooth along the isotopic chain, except for the $0_2^+ \rightarrow 2_1^+$ and $2_2^+ \rightarrow 4_1^+$ transitions, which show a maximum around $A = 98$, consistent with the well-known structural change in the Sr isotopes. Conversely, the $2_2^+ \rightarrow 0_2^+$ transition exhibits a sudden increase from $A = 98$ onwards, further supporting the interpretation of a significant modification in the nuclear structure in this mass region.

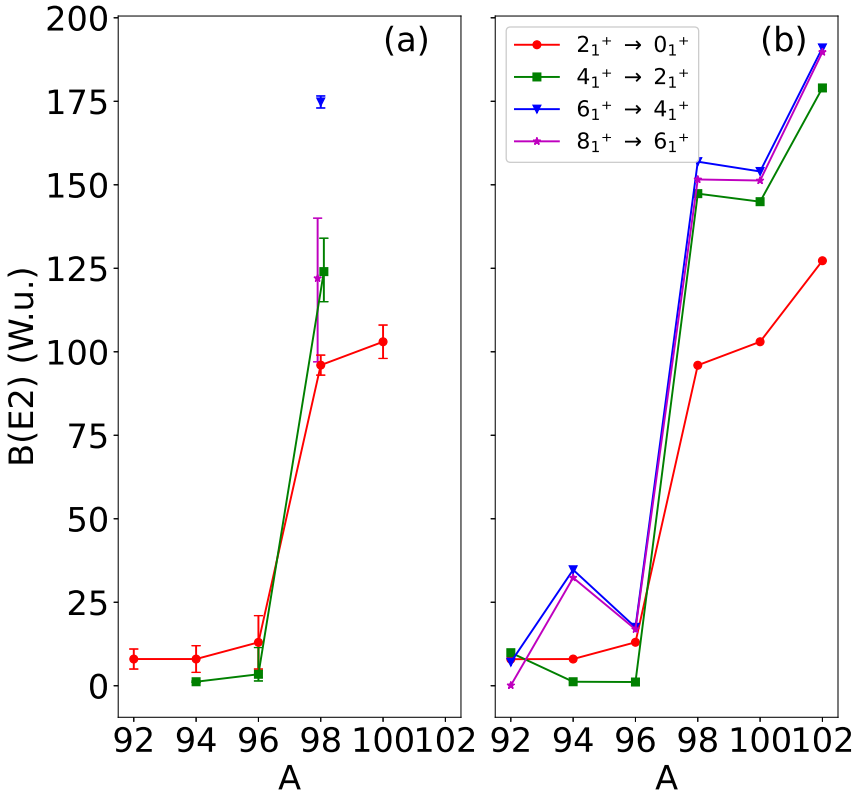

Figure 5.12: Absolute B(E2) transition probabilities along the yrast band (in W.u.) for Sr isotopes. Panel (a) shows the available experimental data and panel (b) the corresponding IBM-CM calculations.

Moreover, Figs. 5.14 and 5.15 present the experimental and theoretical level schemes for the Sr isotopes. In ^{92}Sr, Fig. 5.14 shows a clear vibrational pattern, although the splitting of the two-phonon triplet and the small $B(E2; 2_2^+ \rightarrow 0_1^+)$ value point to significant mixing. In ^{94}Sr, the limited experimental information prevents a firm structural assignment. In ^{96}Sr, deviations from the vibrational limit and the presence of multiple low-lying 0^+ states indicate increasing intruder mixing. In ^{98}Sr, the intruder configuration becomes the ground state, leading to a predominantly rotational spectrum. Finally, ^{100}Sr exhibits a well-developed rotational yrast band, while in ^{102}Sr only the 2_1^+ state has been observed.

5.6.2 Zr isotopes

Again, for offering a complete picture we include in this section an abridge version of the experimental energy spectra and B(E2) transition probabilities compared with the IBM-CM results up to excitation energies below about 3 MeV for the case of Zr (taken from [88].

For the excitation energies, we observe in Fig. 5.16 the excitation energies are well reproduced, in general. Moreover, the peak observed around $A = 96$, which is associated with

Table 5.5: Experimental absolute B(E2) values (in W.u.) compared with the IBM-CM calculations for Sr isotopes. Data from Nuclear Data Sheets [111, 112, 113, 114, 115, 116, 117, 118], supplemented with additional references discussed in Sec. 5.3.

Isotope	Transition	Experiment	IBM-CM
^{92}Sr	$2_1^+ \to 0_1^+$	8(3)	8
	$2_2^+ \to 0_1^+$	0.35(18)	0.00
	$2_3^+ \to 2_1^+$	> 1.2	0.04
	$0_3^+ \to 2_1^+$	0.25(17)	0.28
^{94}Sr	$2_1^+ \to 0_1^+$	8(4)	8
	$4_1^+ \to 2_1^+$	1.2(2)[1]	1.2
^{96}Sr	$2_1^+ \to 0_1^+$	13(8)	13
	$0_2^+ \to 2_1^+$	15.3(16)	9.90
	$0_3^+ \to 2_1^+$	0.028(11)	0.027
	$2_2^+ \to 2_1^+$	> 8.9	8.6
	$4_1^+ \to 2_1^+$	$3(^{+8}_{-2})$[1]	1
^{98}Sr	$2_1^+ \to 0_1^+$	96(3)	96
	$0_2^+ \to 2_1^+$	$62(^{+7}_{-6})$	46
	$4_1^+ \to 2_1^+$	$124(^{+10}_{-9})$	147
	$6_1^+ \to 4_1^+$	174.8(18)	156.9
	$2_2^+ \to 4_1^+$	< 12	2.6
	$2_2^+ \to 0_2^+$	$13(^{+5}_{-4})$	13
	$2_2^+ \to 0_1^+$	$0.8(^{+5}_{-3})$	0.02
	$8_1^+ \to 6_1^+$	$122(^{+25}_{-18})$	152
	$10_1^+ \to 8_1^+$	$126(^{+25}_{-18})$	136
	$6_2^+ \to 4_1^+$	$0.00010(^{+4}_{-3})$	0.00022
^{100}Sr	$2_1^+ \to 0_1^+$	103(5)	103

the $N = 56$ subshell closure, and the rapid energy drop toward $A = 100$, related to the onset of deformation, are both correctly described.

Also it is interesting to note that the origin of the peak observed at $A = 104$ can be understood by analyzing the correlation energy presented before, where both the regular and intruder band-head energies have a minimum at $A = 106$. Moreover, for the intruder configuration, the energies corresponding to $A = 104$ and $A = 106$ are nearly degenerate, however, the regular configuration shows a much steeper dependence on the mass number, with the energy at $A = 104$ lying significantly higher than the minimum reached at $A = 106$.

Furthermore, experimental data reveal the existence of a second 2^+ state in the nuclei with $A = 106$ and $A = 110$ that are not reproduced by the theoretical energy spectra obtained within the present IBM-CM calculations, and it is assumed that they correspond themselves with $4p$-$4h$ excitations, which lie outside the IBM-CM Hilbert space that we consider, being thus not explicitly taken into account in the model. Although, as a matter of fact, it really corresponds to an IBM states once a γ-unstable situation is considered as shown in [35].

Next, we compare the experimental BE(2) values, with the ones obtained from our cal-

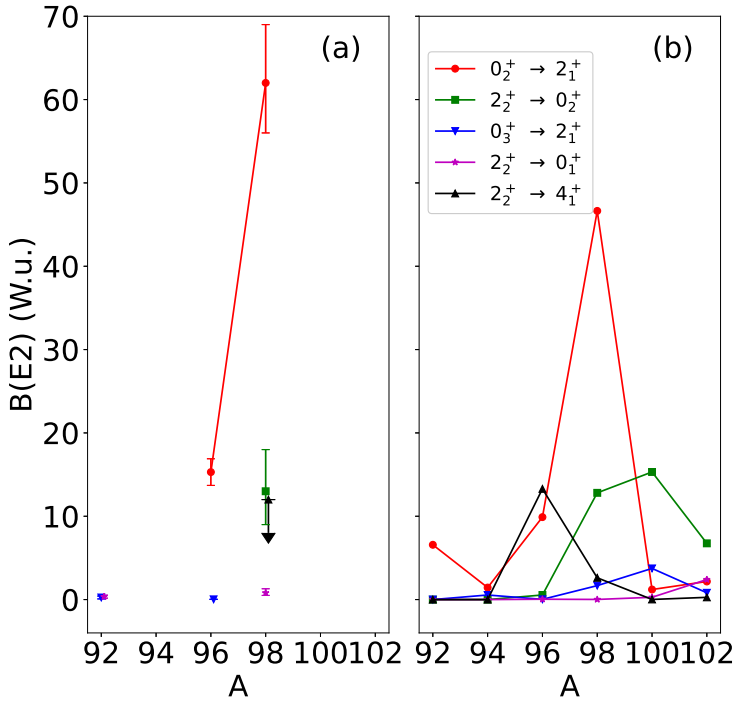

Figure 5.13: Selected absolute B(E2) transition probabilities (in W.u.) for non-yrast intraband transitions in Sr isotopes. Panel (a) shows the available experimental data, while panel (b) presents the IBM-CM results. The arrow in $A = 98$ marks an experimental upper limit.

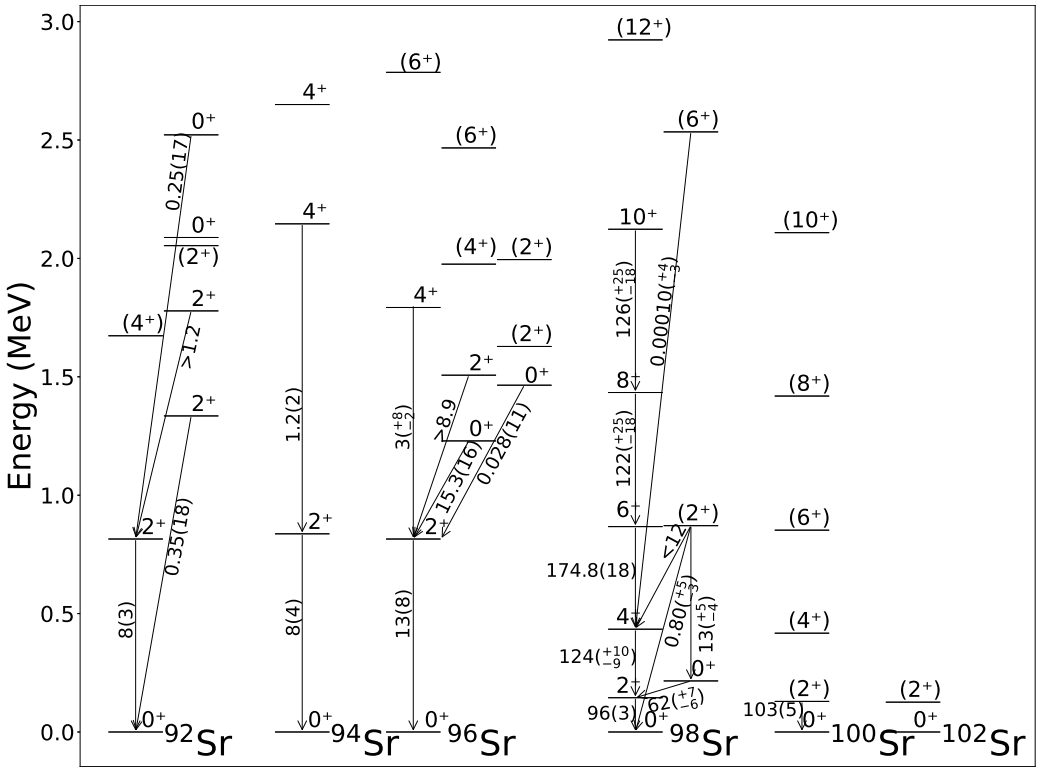

Figure 5.14: Experimental excitation energies and absolute B(E2) values (in W.u.) for selected states in $^{92–102}$Sr.

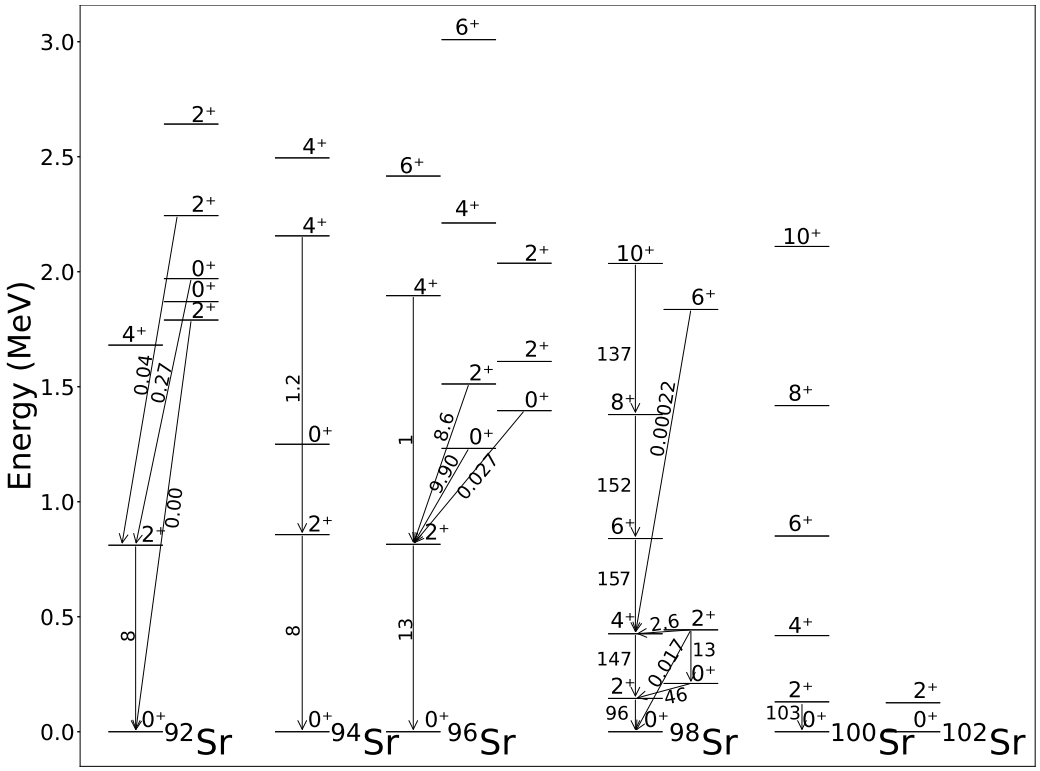

Figure 5.15: Theoretical excitation energies and absolute B(E2) transition rates (in W.u.) for selected states in $^{92\text{-}102}$Sr.

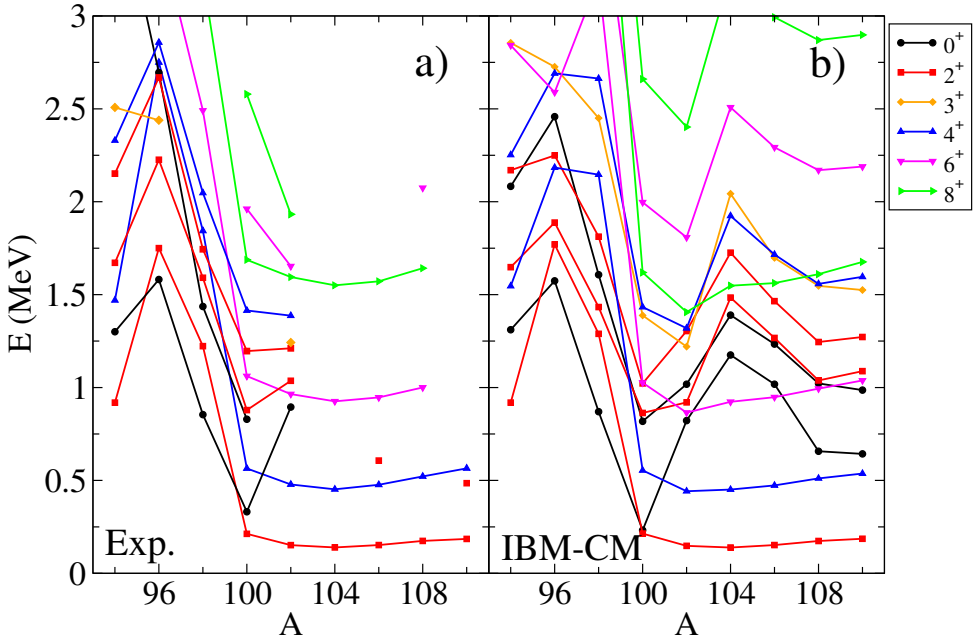

Figure 5.16: Experimental excitation energies up to E≈ 3 MeV for Zr isotopes are represented in panel (a) and theoretical results obtained from an IBM-CM calculation in panel (b) (figure from [88].)

culation in Fig. 5.17 and Fig 5.18.

It is interesting to notice in Fig. 5.17, the way that the collectivity increases as we approach

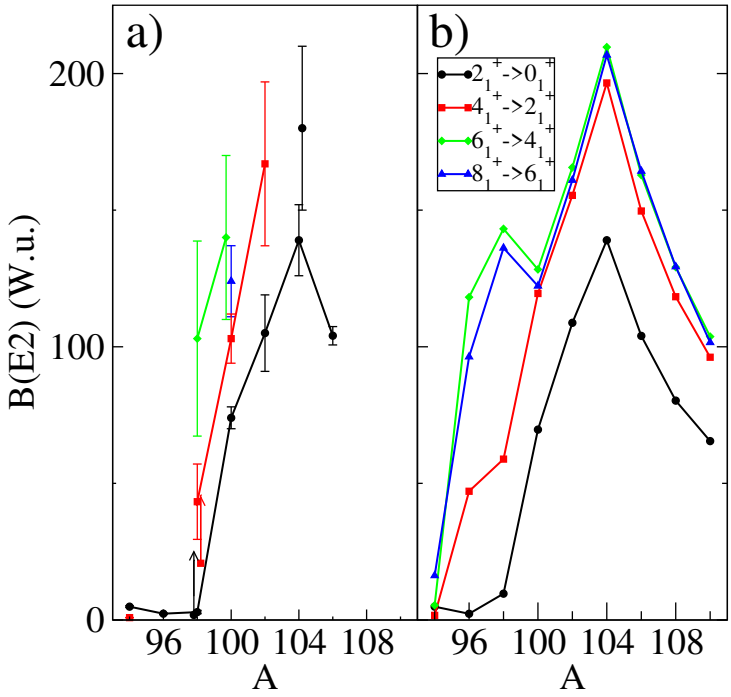

Figure 5.17: Comparison of the absolute B(E2) transition rates probabilities in the yrast band in Zr isotopes. In panel (a) experimental data are presented while in panel (b) we depict the IBM-CM results (taken from [88]).

the midshell, being its maximum located at $A = 104$, which is well reproduced by the IBM-CM calculations. Moreover, in Fig. 5.18 two interband B(E2) transition strengths involving the 0_2^+, 2_1^+, and 2_2^+ states are presented, where due to the limited amount of available experimental information, it is not possible to identify a well-defined systematic trend, nevertheless, the overall agreement with the data is satisfactory.

Finally, the IBM-CM calculations predict the presence of two pronounced peaks: one at $A = 96$, associated with the filling of the $d_{5/2}$ subshell, and another at $A = 104$, corresponding to the midshell region, that indicates a change in the underlying structure of the 0_2^+, 2_1^+, and 2_2^+ states.

5.6.3 Mo isotopes

Here we include the comparison between our theoretical calculations with the experimental data for Mo isotopes. Firstly, in Fig. 5.19 a detailed comparison between theoretical results and experimental data up to 3 MeV is presented, where an important feature that must be noticed is that here, in an equivalent way to the other isotopic chains, the 2_1^+ excitation energy closely matches the experimental data and has been used to normalize the theoretical spectra.

In this case, the lighter Mo isotopes show the characteristics that would be expected to encounter near the 50 sub-shell closure, together with a sudden increase in the excita-

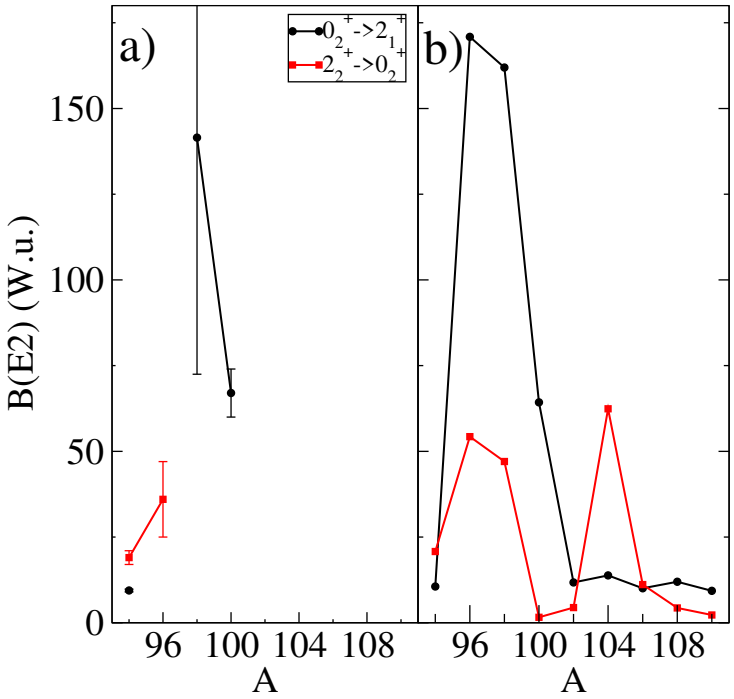

Figure 5.18: Comparison of few nonyrast intraband absolute B(E2) transition rates probabilities in Zr isotopes. In panel (a) experimental data are presented while in panel (b) we depict the IBM-CM results (taken from [88]).

tion energies in certain states, which is associated with the 56 neutron sub-shell closure. The result is a more compressed spectrum, something proper of the evolution to a more collective behavior, that is accurately reproduced by the IBM-CM.

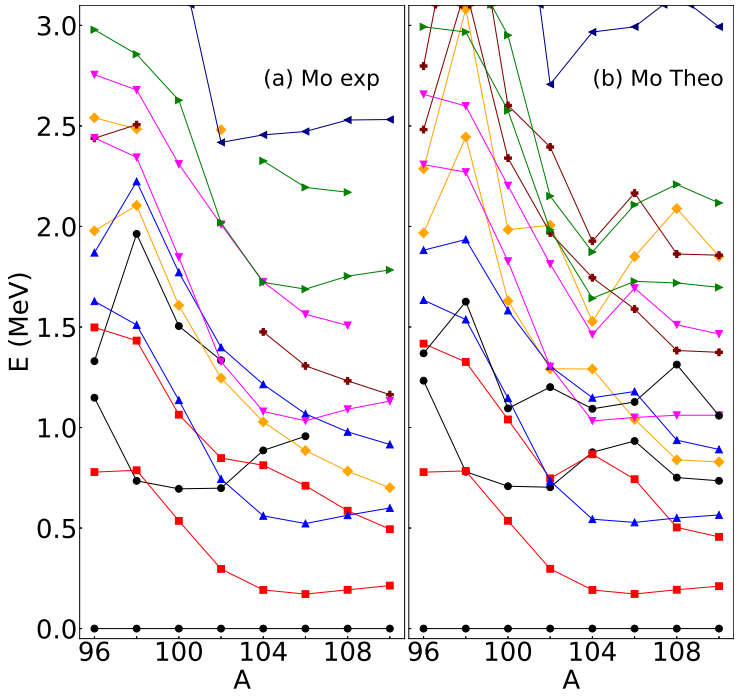

Figure 5.19: Experimental and IBM-CM excitation energies up to $E \approx 3$ MeV for Mo (panel (a) for experimental data and (b) for theoretical results) Only two excited states per angular momentum are shown when available experimentally.

Table 5.6: Comparison of the experimental absolute B(E2) values (given in W.u.) with the IBM-CM Hamiltonian results for Mo isotopes. Data are taken from the Nuclear Data Sheets [114, 115, 116, 117, 118, 127, 128, 129, 118, 130, 131] complemented with references presented in section 5.3.

Isotope	Transition	Experiment	IBM-CM
^{96}Mo	$2_1^+ \to 0_1^+$	20.7(4)	20.7
	$0_2^+ \to 2_1^+$	51(7)	40
	$2_2^+ \to 2_1^+$	16.4(24)	27.5
	$2_2^+ \to 0_1^+$	1.10(11)	0.14
	$2_3^+ \to 2_1^+$	< 28	5
	$2_3^+ \to 0_1^+$	< 0.18	0.32
	$2_4^+ \to 2_1^+$	0.43(20)	0.07
	$2_4^+ \to 0_1^+$	0.080(11)	0.022
	$4_1^+ \to 2_1^+$	41(7)	34
	$4_2^+ \to 4_1^+$	$0.18(^{+9}_{-10})$	14
	$4_2^+ \to 2_2^+$	$22.0(^{+6}_{-10})$	56.4
	$4_2^+ \to 2_1^+$	$1.9(^{+5}_{-9})$	0.0

	$4_3^+ \rightarrow 2_2^+$	< 72	7
	$4_3^+ \rightarrow 2_1^+$	< 0.72	0.08
	$2_5^+ \rightarrow 3_1^+$	$140(^{+30}_{-40})$	115
	$2_5^+ \rightarrow 2_3^+$	$4(^{+8}_{-4})$	12
	$6_1^+ \rightarrow 4_1^+$	< 290	79
	$6_2^+ \rightarrow 4_3^+$	< 52	96
	$6_2^+ \rightarrow 4_2^+$	< 1.1	1.8
	$6_2^+ \rightarrow 4_1^+$	< 47	0.5
	$6_2^+ \rightarrow 6_1^+$	< 65	17
	$3_1^+ \rightarrow 2_2^+$	< 1.8	25
	$3_1^+ \rightarrow 2_1^+$	< 1.3	0.06
	$5_1^+ \rightarrow 4_3^+$	< 1700	20
	$5_1^+ \rightarrow 3_1^+$	< 2000	69
	$5_1^+ \rightarrow 4_2^+$	< 100	3
	$3_3^+ \rightarrow 4_1^+$	$2.7(^{+1.7}_{-2.7})$	0.1
	$3_3^+ \rightarrow 2_3^+$	$4.1(^{+2.4}_{-4.1})$	0.1
	$3_3^+ \rightarrow 2_1^+$	$0.19(^{+10}_{-19})$	0.00
^{98}Mo	$2_1^+ \rightarrow 0_1^+$	20.1(4)	19
	$2_1^+ \rightarrow 0_2^+$	$9.7(^{+10}_{-25})$	6.5
	$4_1^+ \rightarrow 2_1^+$	$42.3(^{+9}_{-8})$	23.5
	$6_1^+ \rightarrow 4_1^+$	10.1(4)	23.3
	$2_2^+ \rightarrow 0_1^+$	$1.02(^{+15}_{-12})$	7.90
	$2_2^+ \rightarrow 0_2^+$	$2.3(^{+5}_{-4})$	2.3
	$2_2^+ \rightarrow 2_1^+$	$48(^{+9}_{-8})$	2
	$4_1^+ \rightarrow 2_2^+$	$15.2(^{+33}_{-30})$	16.6
	$2_3^+ \rightarrow 4_1^+$	14(4)	5
	$2_3^+ \rightarrow 2_2^+$	< 22	3.5
	$2_3^+ \rightarrow 2_1^+$	3.0(7)	30.9
	$2_3^+ \rightarrow 0_2^+$	$7.5(^{+6}_{-5})$	0.0
	$2_3^+ \rightarrow 0_1^+$	$0.032(^{+7}_{-6})$	0.228
^{100}Mo	$2_1^+ \rightarrow 0_1^+$	37.6(9)	37.5
	$0_2^+ \rightarrow 2_1^+$	89(3)	76
	$4_1^+ \rightarrow 2_1^+$	69(6)	71
	$6_1^+ \rightarrow 4_1^+$	$94(^{+16}_{-12})$	100
	$2_2^+ \rightarrow 0_1^+$	0.62(6)	0.03
	$2_2^+ \rightarrow 0_2^+$	$5.7(^{+14}_{-11})$	2.2
	$2_2^+ \rightarrow 2_1^+$	52(7)	70
	$2_3^+ \rightarrow 4_1^+$	$36(^{+34}_{-20})$	42
	$2_3^+ \rightarrow 0_2^+$	$15(^{+5}_{-3})$	70

	$2_3^+ \to 2_1^+$	$0.28(^{+15}_{-9})$	0.11
	$4_2^+ \to 2_2^+$	$30(^{+7}_{-5})$	21
	$8_1^+ \to 6_1^+$	$122(^{+23}_{-17})$	121
^{102}Mo	$2_1^+ \to 0_1^+$	74(9)	74
	$0_2^+ \to 2_1^+$	70(30)	30
	$4_1^+ \to 2_1^+$	89(18)	105
^{104}Mo	$2_1^+ \to 0_1^+$	92(6)	92
	$4_1^+ \to 2_1^+$	110(4)	133
	$6_1^+ \to 4_1^+$	109(4)	144
	$8_1^+ \to 6_1^+$	81(4)	138
^{106}Mo	$2_1^+ \to 0_1^+$	102.3(25)	102.3
	$4_1^+ \to 2_1^+$	140 (30)	146
	$6_1^+ \to 4_1^+$	130(60)	159
	$8_1^+ \to 6_1^+$	89(12)	160
	$10_1^+ \to 8_1^+$	93(13)	66
^{108}Mo	$2_1^+ \to 0_1^+$	140(90)	140

Regarding B(E2) transitions, they are presented in Table 5.6, were we provide a detailed comparison between theory and experiment. Additionally, in Fig. 5.20 and 5.21 we present some intra- and interband transitions.

Overall, we can find a satisfactory agreement between our theoretical predictions and experimental data, with only a few specific discrepancies, such as in ^{98}Mo for which the model predicts a smaller $B(E2; 2_2^+ \to 2_2^+)$ value than observed experimentally. Additionally, it is worth emphasizing the nearly equal B(E2) values found for transitions within the yrast band, and how the natural increase of B(E2) with angular momentum, reaching a maximum at midshell, is accurately reproduced by the model

This result also serves as test for the model. Therefore, the agreement obtained between theory and experiment demonstrates the reliability of the presented calculations, particularly in cases where experimental information is more abundant.

Finally, we incorporate in Fig. 5.22 and 5.23 the detailed excitation energies up to approximately 3 MeV and the B(E2) transition rates for both experimental data and theoretical results. These figures focus on a selected set of Mo isotopes, $^{100–108}$Mo, where the coexistence of two bands is most evident. The separation into bands was performed by first considering the yrast band and then grouping the remaining levels around the 0^+ or 2^+ bandheads, or according to an O(6) scheme.

Furthermore, in the case of ^{100}Mo, the yrast band exhibits a predominantly vibrational character, which is accurately reproduced by the IBM-CM calculation. However, the re-

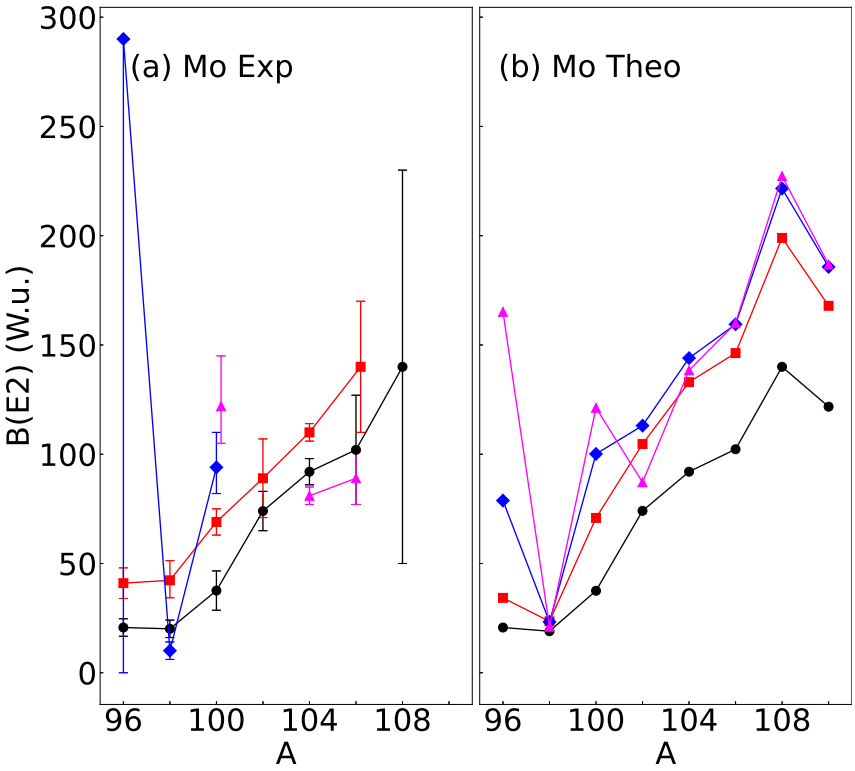

Figure 5.20: Comparison of the absolute B(E2) transition probabilities along the yrast band, given in W.u. for Mo isotopes. Panel (a) corresponds to known experimental data for Mo and panels (b) to the theoretical IBM-CM results

maining states cannot be easily grouped in any obvious manner. The main features of the B(E2) transition rates are generally well reproduced, except for the $B(E2; 2_3^+ \rightarrow 0_2^+)$ transition, where the theoretical model predicts a larger value than observed experimentally. Moving on to ^{102}Mo, the yrast band begins to present a different behavior from the harmonic behavior in terms of both energies and B(E2) values, although the energies and B(E2) values are correctly reproduced by the theoretical calculations. In the cases of ^{104}Mo and ^{106}Mo, the spectra appear quite similar, and the IBM-CM calculations accurately reproduce them. Lastly, in the isotope ^{108}Mo, parts of the spectra exhibit an O(6) character, although there are no known experimental B(E2) values available for comparison.

5.6.4 Ru isotopes

In this section, we continue with the comparison between our theoretical calculations with the experimental data, this time for Ru isotopes, presenting in first place in Fig. 5.24 a detailed comparison between theoretical results and experimental data up to 3 MeV is presented, where once again, the 2_1^+ has been taken to normalize the theoretical spectra.

In the case of Ru isotopes, the theoretical energies quantitatively reproduce the experi-

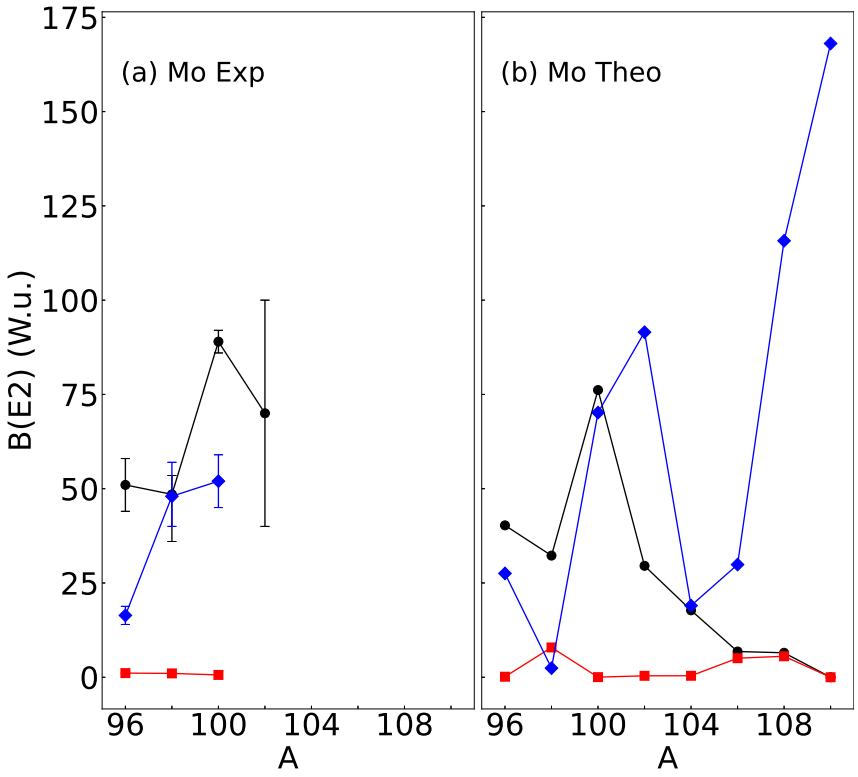

Figure 5.21: Comparison of the few non-yrast intraband absolute B(E2) transition probabilities in Mo given in W.u. Panels (a) corresponds to the known experimental data and panel (b) to the theoretical IBM-CM results

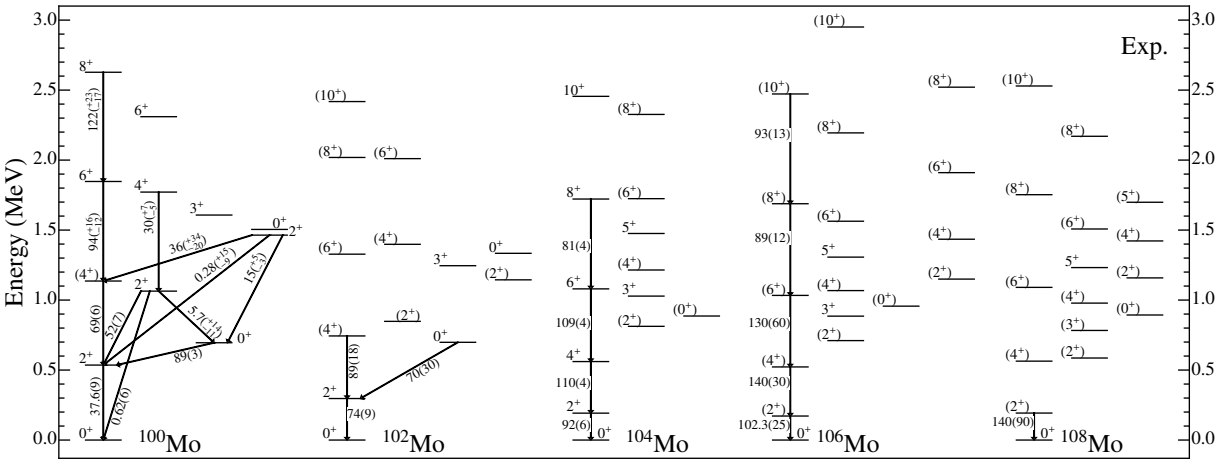

Figure 5.22: Experimental excitation energies and absolute B(E2) transition rates (given in W.u.) for selected states in $^{100-108}$Mo.

mental ones, and it is clear to observe a transition from a purely vibrational-like spectrum (where the one-, two-, and three-phonon states are easily identified) to an O(6) spectrum. However, it should be noted that the experimental levels are more scattered compared to the theoretical ones. Furthermore, there is a notable discrepancy observed for the 0_3^+ state in ^{106}Ru, which appears much higher in energy than predicted by the theoretical model and for this reason was not included in the fitting procedure. Moreover, we find a

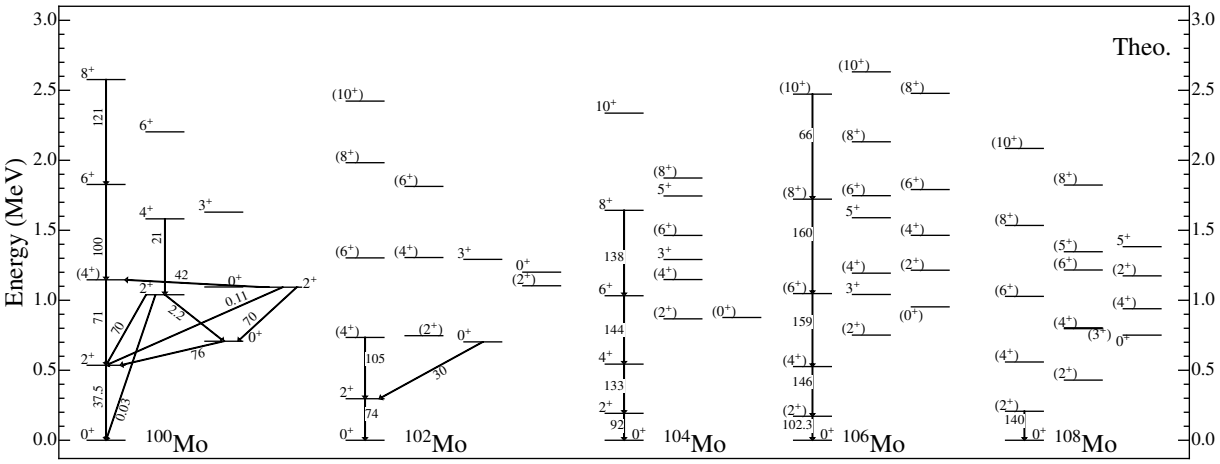

Figure 5.23: The same as Fig. 5.22 but for the theoretical IBM-CM results.

slight discrepancy for the 0_2^+ state in $^{108-110}$Ru, where its energy is slightly higher than the corresponding experimental value.

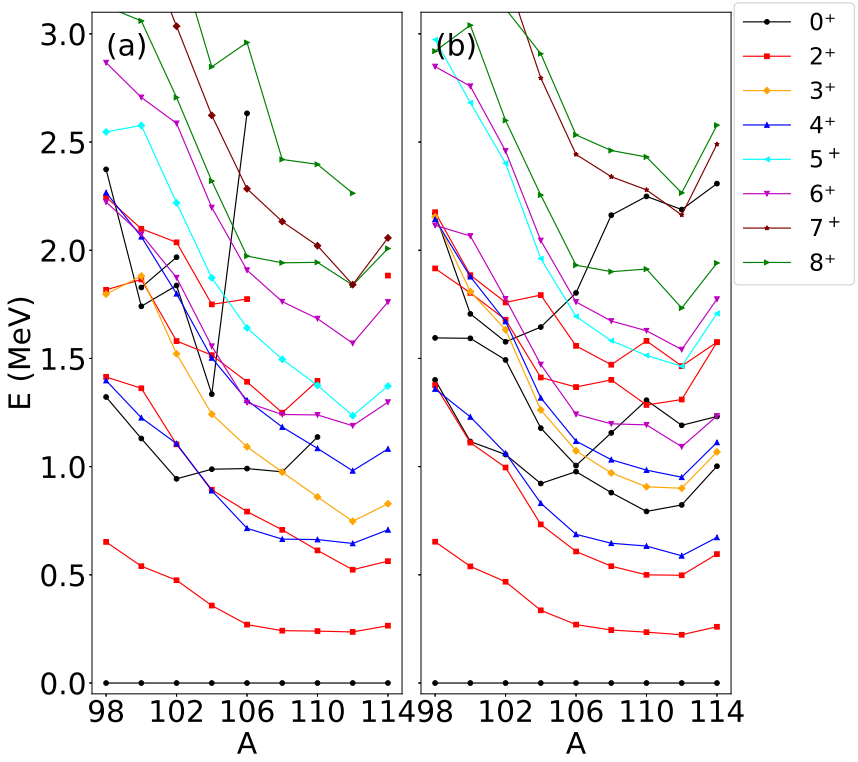

Figure 5.24: Experimental and IBM-CM excitation energies up to $E \approx 3$ MeV for Ru isotopes (panel (a) for experimental data and (b) for theoretical results). Only two excited states per angular momentum are shown when available experimentally.

Table 5.7: Same as Table 5.6 but for Ru isotopes.

Isotope	Transition	Experiment	IBM-CM
^{98}Ru	$2_1^+ \to 0_1^+$	29.8(10)	29.8
	$0_2^+ \to 2_1^+$	42 $(^{+12}_{-11})$	33
	$4_1^+ \to 2_1^+$	57(4)	43
	$6_1^+ \to 4_1^+$	12.8$(^{+17}_{-14})$	40.9
	$2_2^+ \to 0_1^+$	1.04$(^{+17}_{-14})$	0.00
	$2_2^+ \to 2_1^+$	46$(^{+7}_{-6})$	43
	$8_1^+ \to 6_1^+$	2.5$(^{+5}_{-3})$	26
	$10_1^+ \to 8_1^+$	1.27$(^{+31}_{-23})$	0.43
^{100}Ru	$2_1^+ \to 0_1^+$	35.7(3)	35.8
	$0_2^+ \to 2_1^+$	35(5)	32
	$4_1^+ \to 2_1^+$	52(4)	52
	$2_2^+ \to 2_1^+$	31(6)	52
	$2_2^+ \to 0_1^+$	2.0(4)	0.0
	$2_3^+ \to 4_1^+$	17(5)	11
	$2_3^+ \to 0_2^+$	37$(^{+8}_{-9})$	23
	$2_3^+ \to 2_1^+$	1.24$(^{+0.43}_{-0.53})$	0.00
	$2_3^+ \to 0_1^+$	0.43(10)	0.02
	$2_4^+ \to 0_3^+$	270$(^{+60}_{-50})$	196
	$2_4^+ \to 4_1^+$	1.9$(^{+0.6}_{-0.5})$	0.2
	$2_4^+ \to 0_2^+$	1.9(5)	0.0
	$4_2^+ \to 2_2^+$	41$(^{+27}_{-21})$	29
	$4_2^+ \to 4_1^+$	27$(^{+18}_{-14})$	26
	$4_2^+ \to 2_1^+$	1.9$(^{+13}_{-10})$	0.0
	$4_3^+ \to 2_3^+$	77$(^{+32}_{-29})$	7
	$4_3^+ \to 4_1^+$	1.8$(^{+9}_{-8})$	0
	$4_3^+ \to 2_1^+$	0.9(4)	0.3
	$3_1^+ \to 2_2^+$	9.6$(^{+46}_{-41})$	39.2
	$3_1^+ \to 4_1^+$	15(5)	16
	$3_1^+ \to 2_1^+$	3.9$(^{+13}_{-12})$	0
^{102}Ru	$2_1^+ \to 0_1^+$	44.6(7)	44.6
	$0_2^+ \to 2_1^+$	35(6)	36
	$4_1^+ \to 2_1^+$	66(11)	66
	$6_1^+ \to 4_1^+$	68(25)	74
	$2_2^+ \to 0_1^+$	1.14(15)	0.00
	$2_2^+ \to 2_1^+$	32(5)	66

	$8_1^+ \to 6_1^+$	56(19)	70
	$10_1^+ \to 8_1^+$	57(21)	58
^{104}Ru	$2_1^+ \to 0_1^+$	57.9(11)	57.1
	$0_2^+ \to 2_1^+$	25(3)	21
	$4_1^+ \to 2_1^+$	83(9)	81
	$2_2^+ \to 0_1^+$	2.8(5)	0.0
	$2_2^+ \to 2_1^+$	55(6)	81
^{106}Ru	$2_1^+ \to 0_1^+$	66(10)	66
^{108}Ru	$2_1^+ \to 0_1^+$	62(6)	62
	$4_1^+ \to 2_1^+$	102(8)	85
	$2_2^+ \to 0_1^+$	0.5(4)	0.0
	$2_3^+ \to 4_1^+$	0.08(7)	0.00
	$2_3^+ \to 0_1^+$	0.005(3)	0.000
^{110}Ru	$2_1^+ \to 0_1^+$	66(5)	66
	$4_1^+ \to 2_1^+$	86(10)	91
	$6_1^+ \to 4_1^+$	120(50)	101
	$2_2^+ \to 0_1^+$	0.6(3)	0.0
^{112}Ru	$2_1^+ \to 0_1^+$	70(7)	70
	$8_1^+ \to 6_1^+$	82(13)	106
	$10_1^+ \to 8_1^+$	85(13)	100
	$7_1^+ \to 5_1^+$	83(12)	68

Detailed information about theoretical and experimental B(E2) transition rates is also included in Table 5.7 and in Figs. 5.25 and 5.26 we illustrate some intra- and inter-band transitions, where again, the proper increase in the B(E2) values when approaching the midshell and increasing the angular momentum is accurately reproduced by the model.

Finally, in Fig. 5.27 and 5.28 we represent the experimental and theoretical spectra for $^{100-108}$Ru isotopes, where no significant discrepancies are observed, remarking a vibrational-like structure for the isotopes up to ^{104}Ru, allowing the identification of different members of one-, two-, three-, and even four-phonon multiplets. Starting from ^{106}Ru, a transition towards an O(6)-like appears, with ^{104}Ru being the critical point of this transition. Another noteworthy feature is the absence of intruder states, except for the 0_4^+ and 0_5^+ states in ^{100}Ru (not shown in the figure).

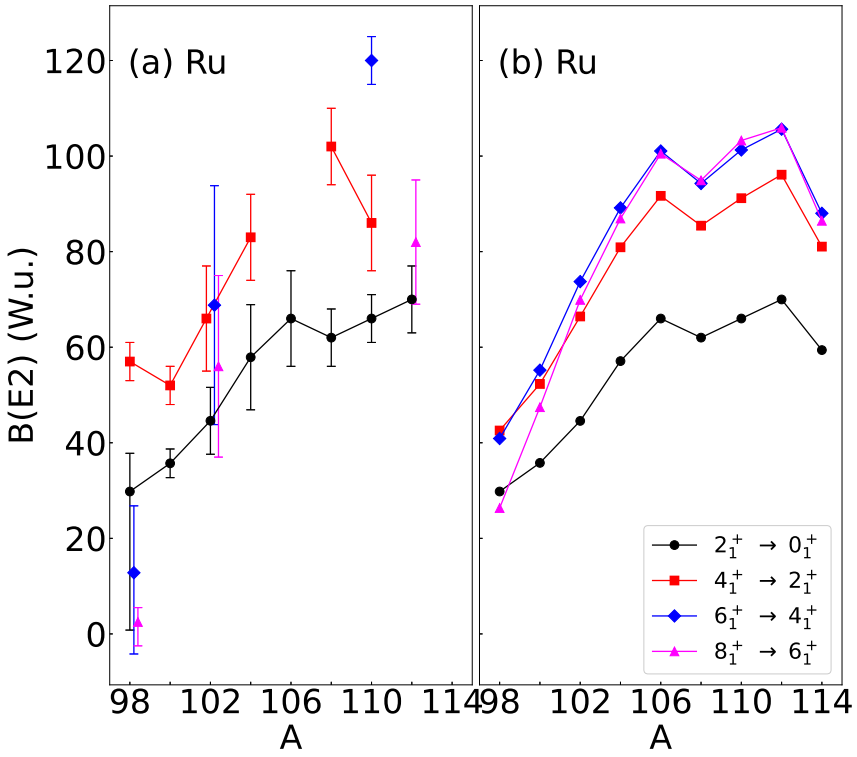

Figure 5.25: Comparison of the absolute B(E2) transition probabilities along the yrast band, given in W.u. for Ru isotopes. Panel (a) corresponds to known experimental data for Mo and panels (b) to the theoretical IBM-CM results

5.7 Wave Function Structure: Configuration Mixing and Unperturbed structure

In order to understand the nature of the calculated states, we analyze now the structure of their wave functions. In particular, we will focus on how much of each wave function belongs to the regular configuration, referred as $[N]$ sector, with the objective of identifying whether a given state is predominantly regular, intruder, or mixed.

As we have previously introduced, within the IBM-CM framework, the wave function of a state can be expressed as a superposition of basis states belonging to the regular and intruder subspaces,

$$\begin{aligned} \Psi(k, JM) &= \sum_i a_i^k(J;N)\,\psi((sd)_i^N; JM) \\ &+ \sum_j b_j^k(J;N+2)\,\psi((sd)_j^{N+2}; JM), \end{aligned} \tag{5.2}$$

where k labels the different states for a given angular momentum J, while the indices i and j run over the basis states in the $[N]$ and $[N+2]$ spaces, respectively.

The contribution of the regular configuration to a given state can be quantified by sum-

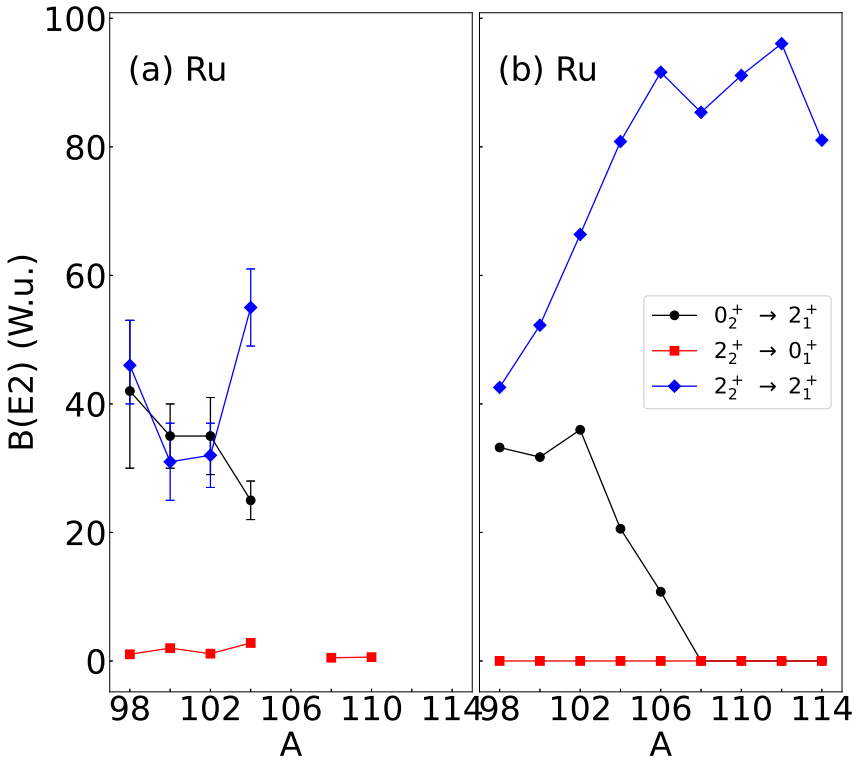

Figure 5.26: Comparison of the few non-yrast intraband absolute B(E2) transition probabilities in Ru given in W.u. Panels (a) corresponds to the known experimental data and panel (b) to the theoretical IBM-CM results

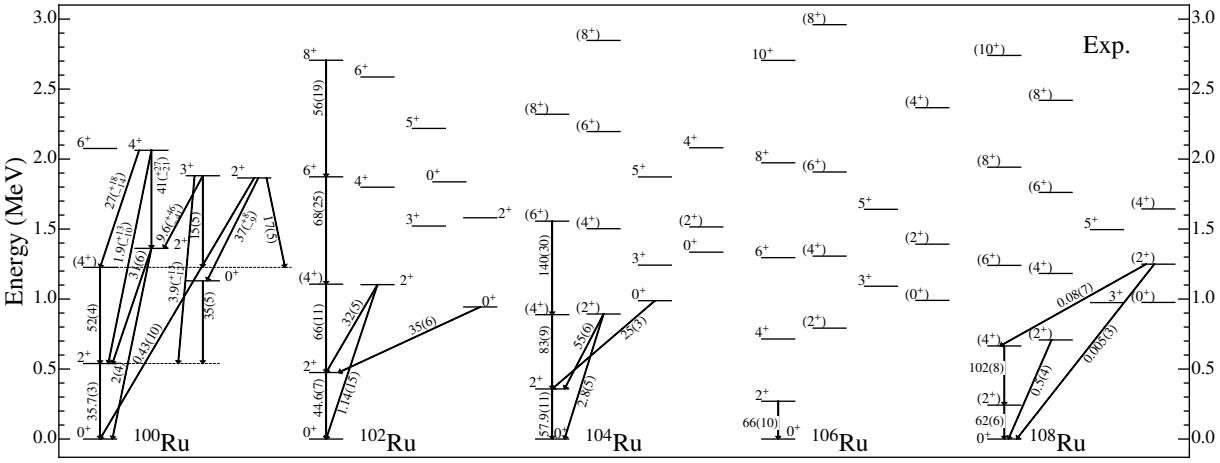

Figure 5.27: Experimental excitation energies and absolute B(E2) transition rates (given in W.u.) for selected states in $^{100-108}$Ru.

ming the squared amplitudes of the components in the $[N]$ sector,

$$w^k(J,N) \equiv \sum_i \left|a_i^k(J;N)\right|^2 . \tag{5.3}$$

This quantity gives a direct measure of the regular content of the wave function.

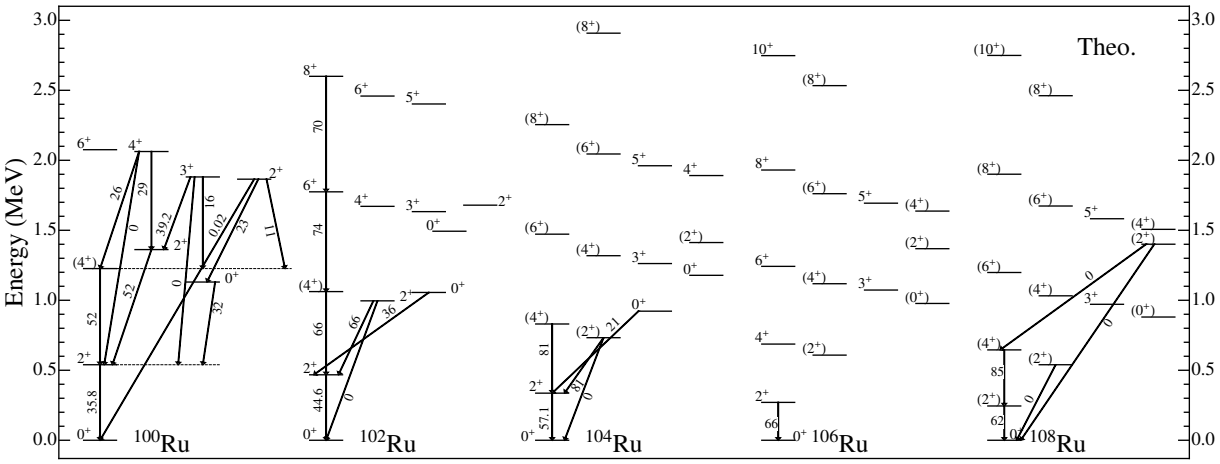

Figure 5.28: The same as Fig. 5.27 but for Ru theoretical results.

5.7.1 Sr Isotopes

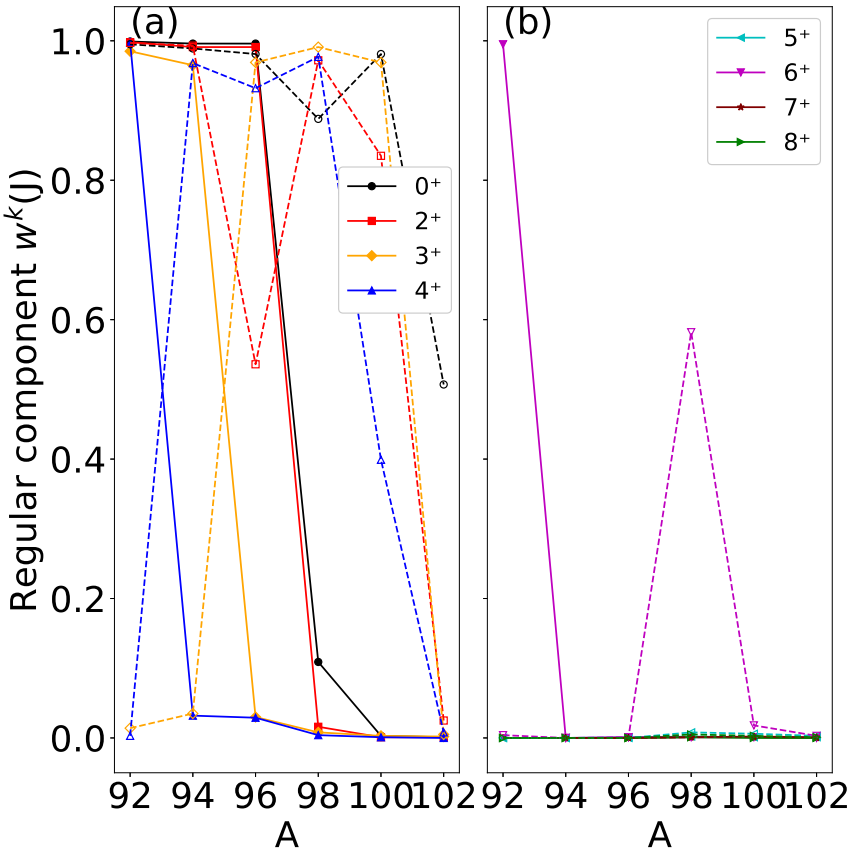

Figure 5.29: Regular content of the two lowest-lying states for each J value for Sr isotopes (full lines with closed symbols correspond with the first state while dashed lines with open symbols correspond with the second state) resulting from the IBM-CM calculation.

Fig. 5.29 shows the evolution of the regular content, $w^k(J)$, for the two lowest states of each angular momentum along the Sr isotopic chain. The ground state displays a very sharp structural change: it is almost purely regular up to $A = 96$, but becomes fully intruder-dominated from $A = 98$ onwards. A similar behavior is observed for the 2_1^+, 3_1^+,

4_1^+, and 6_1^+ states, although the transition occurs at different mass numbers: $A = 98$ for 2_1^+, $A = 96$ for 3_1^+, and already at $A = 94$ for the 4_1^+ and 6_1^+ states.

In contrast, the 5_1^+, 7_1^+, and 8_1^+ states exhibit an intruder character throughout the entire isotopic chain. For the second member of each angular momentum (dashed lines), the behavior is more complex. The 0_2^+ state remains predominantly regular except at $A = 102$. The 2_2^+ state is strongly mixed at $A = 96$, mainly regular for $A = 92$, 94, 98, and 100, and intruder-like at $A = 102$. The 3_2^+ state is regular for $A = 96$, 98, and 100, but intruder for $A = 92$, 94, and 102. The 4_2^+ state is regular for $A = 94$–98, intruder for $A = 92$ and 102, and mixed at $A = 100$. Finally, the 6_2^+ state is regular at $A = 92$, mixed at $A = 98$, and intruder-dominated for the remaining isotopes.

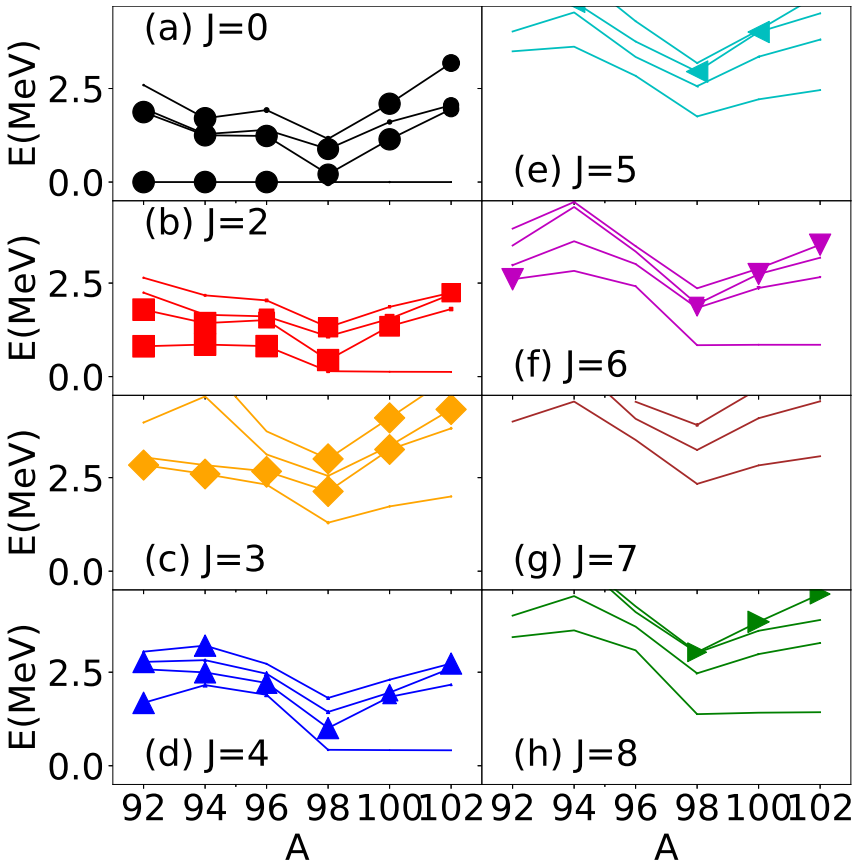

Figure 5.30: Energy systematics of the four lowest states below 4 MeV for Sr isotopes. The size of the symbol is proportional to the value of $w^k(J)$ (see text for details). Each panel corresponds to a given angular momentum, (a) for $J = 0$, (b) for $J = 2$, (c) for $J = 3$, (d) for $J = 4$, (e) for $J = 5$, (f) for $J = 6$, (g) for $J = 7$, and (h) for $J = 8$.

The interpretation of Fig. 5.29 can be obscured by level crossings, which may hide smooth structural trends. In order to overcome this limitation, Fig. 5.30 combines the excitation energies with the regular content of the wave functions. The size of each symbol represents the value of $w^k(J)$. Moreover, as a reference, the 0_1^+ state of ^{92}Sr, which is fully regular, is assigned the maximum symbol size.

This representation clearly shows how the regular character changes between different states as levels cross. For low angular momenta (0^+, 2^+, 3^+, and 4^+), the regular content shifts between the lowest states depending on the isotope. For higher angular momenta (5^+ to 8^+), most low-lying states are intruder in nature, implying that regular configurations are pushed to higher excitation energies and are therefore not visible within the energies shown.

Additional insight can be gained by analyzing the overlap of the physical states with an unperturbed basis. So we can do this, we first diagonalize the Hamiltonian separately in the $[N]$ and $[N+2]$ subspaces, obtaining the states $|l, JM\rangle_N$ and $|m, JM\rangle_{N+2}$. By setting the mixing strength ω to zero, an intermediate basis is defined [146, 147], corresponding to the unperturbed bands shown in Fig. 5.8.

The overlaps squared $|_N\langle l, JM \mid k, JM\rangle|^2$ and $|_{N+2}\langle m, JM \mid k, JM\rangle|^2$ are depicted in Fig. 5.31 for $k = 1, 2$, $(l, m) = 1, 2, 3$, and $J^\pi = 0^+, 2^+, 3^+, 4^+, 5^+, 6^+, 7^+, 8^+$. This way of presenting the wave function shows in a visual form how the structure of the states evolves along the isotope chain. Regarding the first member of the different angular momenta, for the 0^+ and 2^+ states, they correspond to the first regular state, from $A = 92$ up to $A = 96$, but suddenly change to the first intruder one in the range $A = 98 - 102$; in the case of 3^+, the first two isotopes correspond to the first regular state while the rest to the first intruder one; for 4^+ and 6^+, only $A = 92$ fully overlaps with the first regular state and the rest of isotopes overlap with the first intruder one; finally, for 5^+, 7^+ and 8^+, all the states present a complete overlap with the first intruder state. Therefore, the first member of the different angular momenta have a very pure structure without noticeable mixing, presenting a sudden transition when passing from $A = 96$ to $A = 98$, but moving to lower atomic mass values as J increases.

The second member of each angular momentum shows a much richer behavior, with frequent changes between regular, intruder, and mixed character. In this way, the 0^+ state has a complete overlap with the second regular member for $A = 92 - 96$, with the first regular state for $A = 98 - 100$, being a mixture of the first regular and the second intruder state for $A = 102$; the state 2^+ for $A = 92 - 94$ has a full overlap with the second regular state, for $A = 96$ it is a mixture of the second regular and the first intruder state, for $A = 98 - 100$, it overlaps with the first regular state, and for $A = 102$, with the second intruder one; 3^+ is a rather pure state corresponding to the first intruder, first regular and second intruder member for $A = 92 - 94$, $A = 96 - 100$, and $A = 102$, respectively; 4^+ is also rather pure except for $A = 100$ where a mixture between the first regular and the second intruder state exits, having for $A = 92$, $A = 94 - 98$, and $A = 102$ a complete overlap with the first intruder, the first regular and the second intruder state, respectively; for 5^+, 6^+, 7^+, and 8^+, in most of the cases, there is a full overlap with the

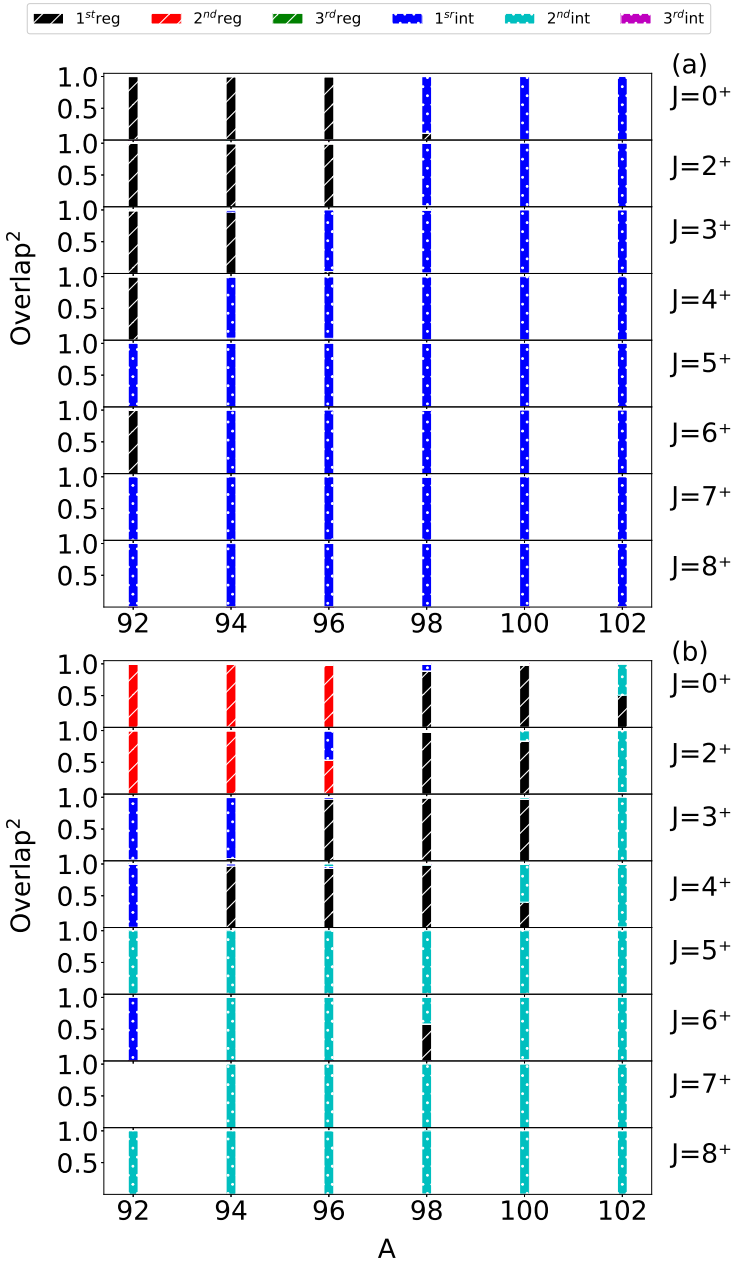

Figure 5.31: Overlap of the wave functions with the wave functions describing the unperturbed basis for Sr isotopes. Panel (a): overlaps for first $0^+, 2^+, 3^+, 4^+, 5^+, 6^+, 7^+, 8^+$ state ($k = 1$), panel (b): overlaps for the corresponding second state ($k = 2$) (see also text).

second intruder state but with some exceptions.

5.7.2 Zr Isotopes

Following the same scheme, we include here the analysis of the structure of the low-lying states is analyzed in terms of the regular ($[N]$) and intruder ($[N+2]$) components of the IBM-CM wave functions, since the evolution of these components along the Zr isotopic chain provides direct insight into the onset of deformation and shape coexistence.

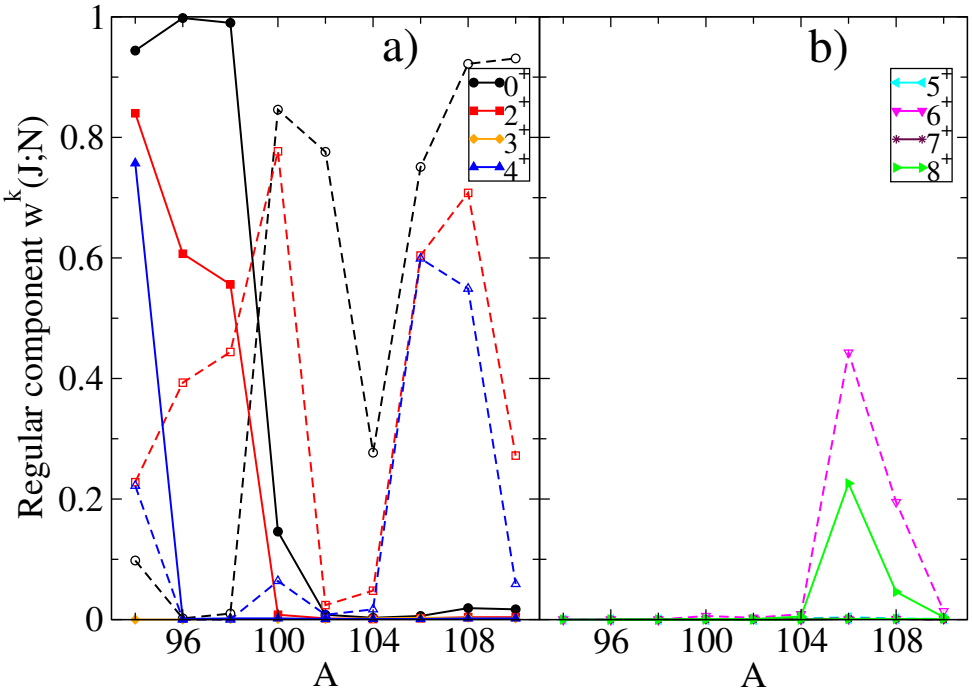

Figure 5.32: Regular content of the two lowest-lying states for each J value for Zr isotopes (full lines with closed symbols correspond with the first state while dashed lines with open symbols correspond with the second state) resulting from the IBM-CM calculation. (figure from [88].)

Fig. 5.32 shows the weight of the regular component for the lowest states with angular momenta $J^\pi = 0^+, 2^+, 3^+, 4^+$ in panel (a) and $J^\pi = 5^+ - 8^+$ in panel (b), where we can easily observe that for the light isotopes ($A = 94$–98), the ground state and the 2_1^+ state are predominantly regular, nonetheless, from $A = 100$ onward, these states become dominated by intruder configurations, which is a sign of a clear structural change. Moreover, the excited 0^+ and 2^+ states show a complementary behavior, with strong mixing appearing around the transition region.

Again, the wave function content with the excitation energies, shown in Fig. 5.33 presents the energy systematics together with the size of the regular component, representing how regular configurations move from low-lying states in the lighter isotopes to higher energies for $A \geq 100$, reflecting the crossing and mixing of states with different intrinsic character, especially for 0, 2, and 4, while for most other angular momenta, the lowest states are almost purely intruder, being regular states higher in energy.

A more detailed decomposition is obtained by projecting the calculated states onto unperturbed regular and intruder sectors. Fig. 5.34 displays the squared overlaps for the first two states of each angular momentum with the lowest regular and intruder bands. This analysis confirms a sudden transition from regular to intruder dominated structures around $A \approx 100$, where we notice that the 0^+ and 2^+ states exhibit the strongest mixing, while most higher states show a dominant overlap with intruder configurations.

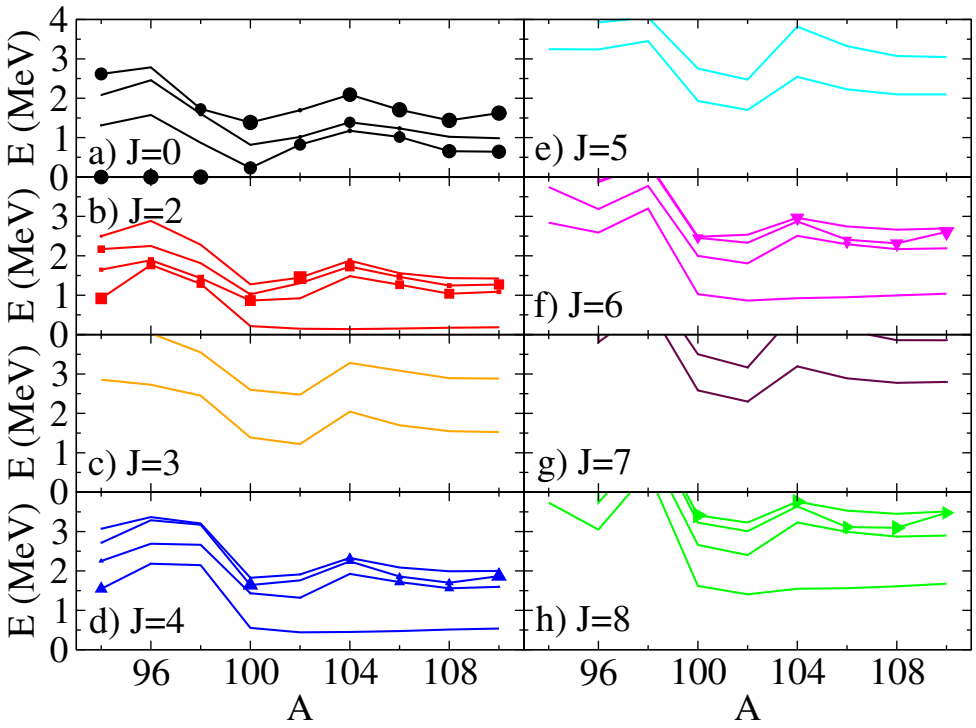

Figure 5.33: Energy systematics of the four lowest states below 4 MeV. The size of the symbol is proportional to the value of $w^k(J)$ (see text for details) for Zr isotopes. Each panel corresponds to a given angular momentum, (a) for $J = 0$, (b) for $J = 2$, (c) for $J = 3$, (d) for $J = 4$, (e) for $J = 5$, (f) for $J = 6$, (g) for $J = 7$, and (h) for $J = 8$. (figure from [88].)

Overall, the wave-function analysis demonstrates the predominance of intruder configurations in the low-lying spectra of the heavier Zr isotopes, together with strong regular–intruder mixing in the transitional region. This is fully consistent with the observed energy spectra and E2 transition rates discussed previously.

5.7.3 Mo isotopes

In analogous form to the results presented for the chain of Sr isotopes presented in Fig. 5.29, we illustrate in Fig. 5.35 the first two states of each angular momentum for Mo isotopes, again representing with full line the first state and with dashed line the second one.

In this case, the ground state undergoes a rapid transition from an almost entirely regular structure till $A = 100$ isotope, to a fully intruder one from $A = 102$ onwards. This trend is also observed for the 2_1^+, 4_1^+, 6_1^+, and 8_1^+ states, with the exception of $A = 96$, where the 6_1^+ and 8_1^+ states correspond to intruder configurations. No clear trend can be observed for odd angular momenta, both for the first and second members.

Also, the second 0^+ state predominantly exhibits an intruder character in most cases, except for $A = 102 - 104$, where it is fully regular. Moreover, the second 2^+ state shows

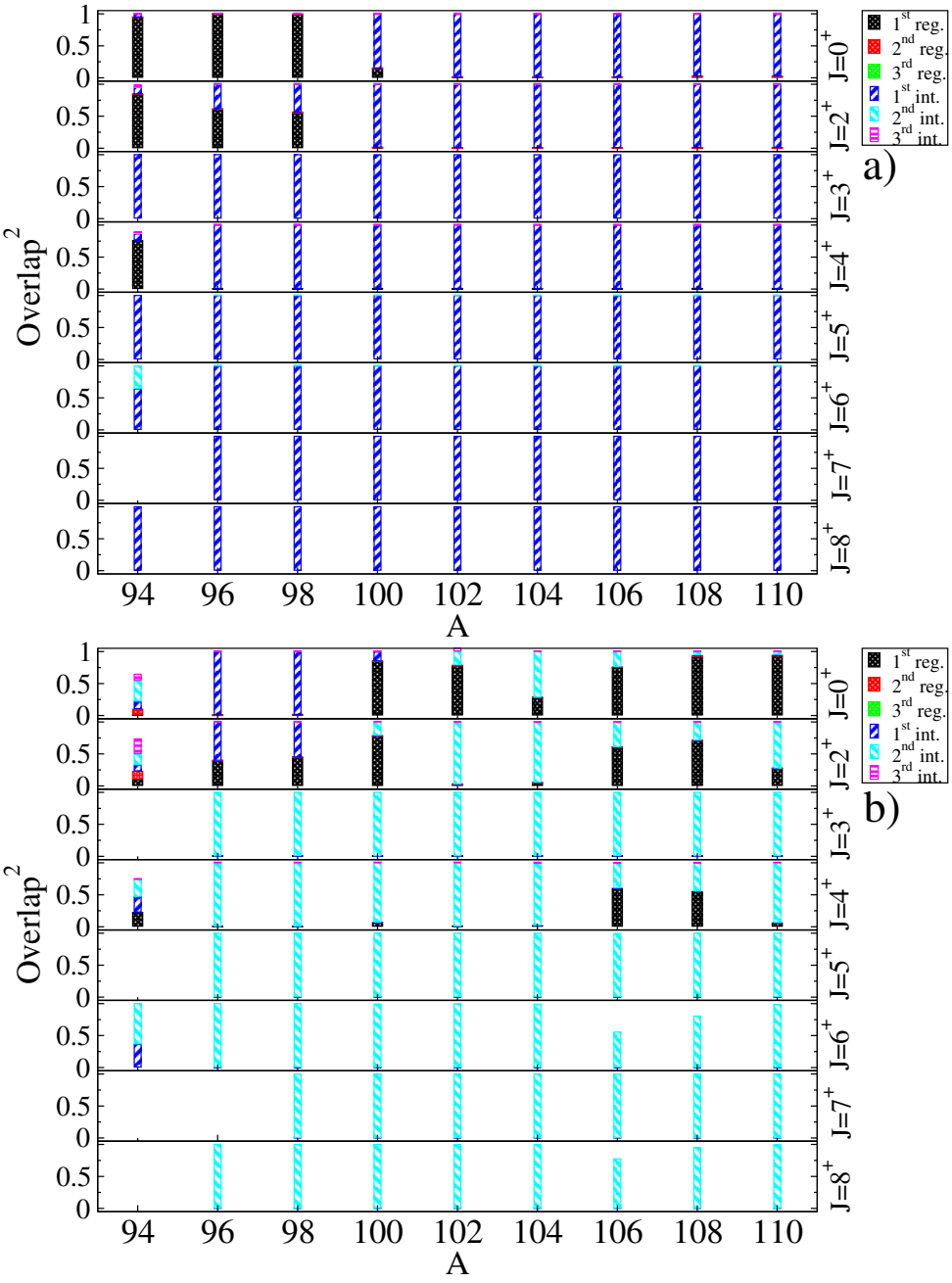

Figure 5.34: Overlap of the wave functions with the wave functions describing the unperturbed basis for Zr isotopes. Panel (a): overlaps for first $0^+, 2^+, 3^+, 4^+, 5^+, 6^+, 7^+, 8^+$ state ($k = 1$), panel (b): overlaps for the corresponding second state ($k = 2$) (figure from [88].)

significant mixing for $A = 96 - 100$ and 104, while being almost purely intruder for the remaining cases.

As in the previous cases, combining excitation energies with regular content provides a clearer picture (Fig. 5.36), where again, the size of each dot associated with a state is proportional to the regular content of its wave function. In this case, the reference point is the size of the dot for the 0_1^+ states in ^{96}Mo (panel (i)) which corresponds to 100% of

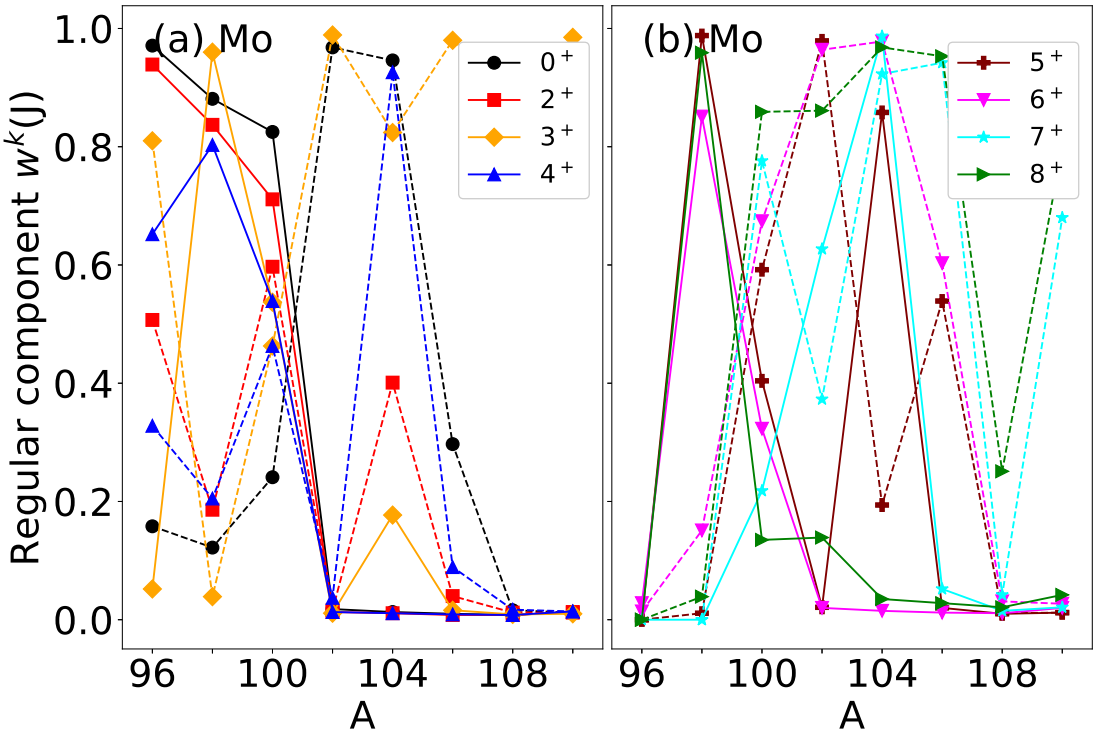

Figure 5.35: Regular content of the Mo isotopes for the two lowest-lying states for each J value (full lines with closed symbols correspond with the first state while dashed lines correspond with the second state) resulting from the IBM-CM calculation.

regular content.

In Fig. 5.36, it is evident how the regular content of the 0_1^+ state transitions from the ground state in $^{96-100}$Mo to the first and second excited 0^+ states in $^{102-104}$Mo and $^{106-110}$Mo, respectively. Similarly, for the 2^+ and 4^+ states, the regular content transitions from the first member in $^{96-102}$Mo to the second or third member in $^{104-110}$Mo. For angular momenta 6^+ and 8^+, the regular content is mainly concentrated in the second and third members throughout the isotopic chain.

5.7.4 Ru isotopes

Finally, we repeat the same analysis for the wave function structure for Ru isotopes. Firstly, we illustrate in Fig. 5.37 the first two states of each angular momentum, again representing with full line the first state and with dashed line the second one.

Analyzing the trend for these isotopes, a simpler pattern is observed, as regular wave functions dominates for the first member of all angular momentum. However, for the second member some cases present a transition from an intruder character to a regular one, being in most cases from $A = 104$ and onwards.

Finally, we also depict the excitation energies with the regular content in order to provide

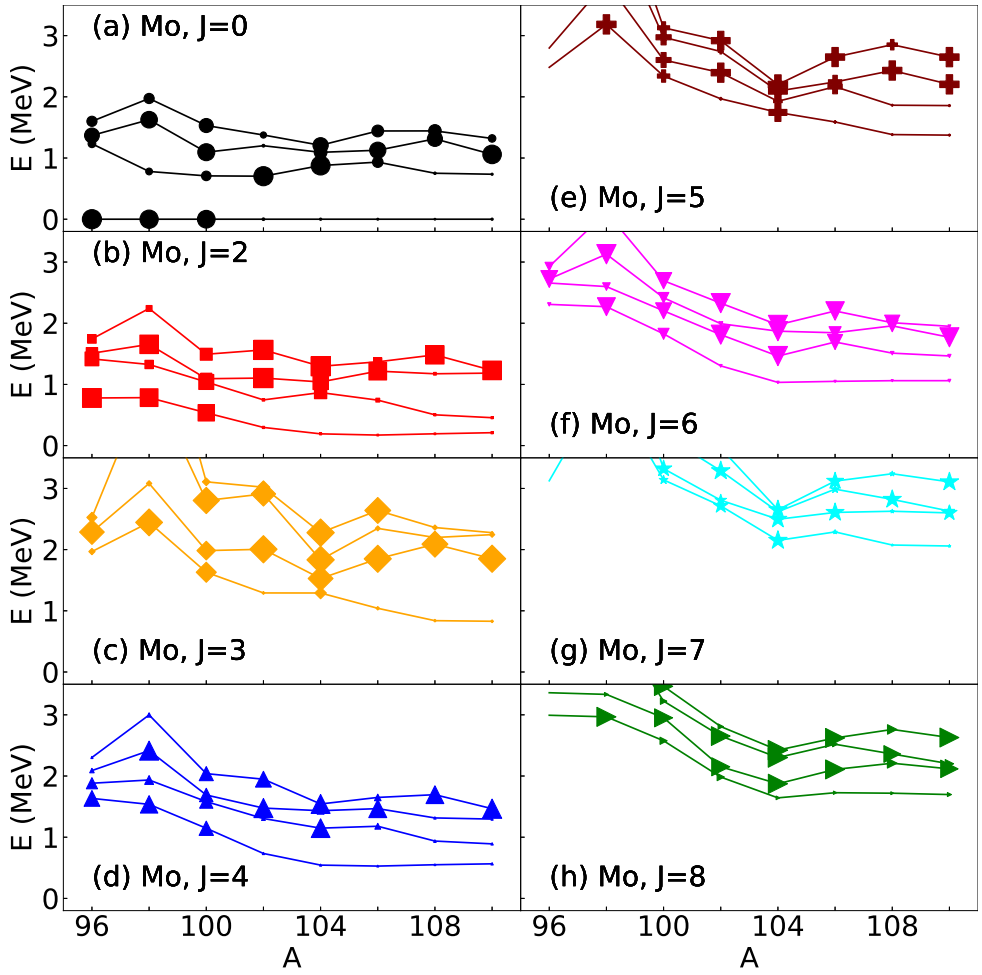

Figure 5.36: Energy systematics of the four lowest states below 4 MeV for Mo isotopes. Each panel corresponds to a specific angular momentum: (a) for $J = 0$, (b) for $J = 2$, (c) for $J = 3$, (d) for $J = 4$, (e) for $J = 5$, (f) for $J = 6$, (g) for $J = 7$, and (h) for $J = 8$. The size of each symbol is proportional to the fraction of the wave function lying in the regular sector. The dot for the state 0_1^+ in ^{96}Mo corresponds to 100%.

a clearer picture (Fig. 5.38), where again, the size of each dot associated with a state is proportional to the regular content of its wave function. In this case, the reference point is the size of the dot for the 0_1^+ states in ^{98}Ru (panel (i)) which corresponds to 100% of regular content.

For Ru isotopes, in contrast to the other isotopic chains studied, the situation is much simpler, with the majority of states belonging to the regular sector, as indicated by their significant regular content.

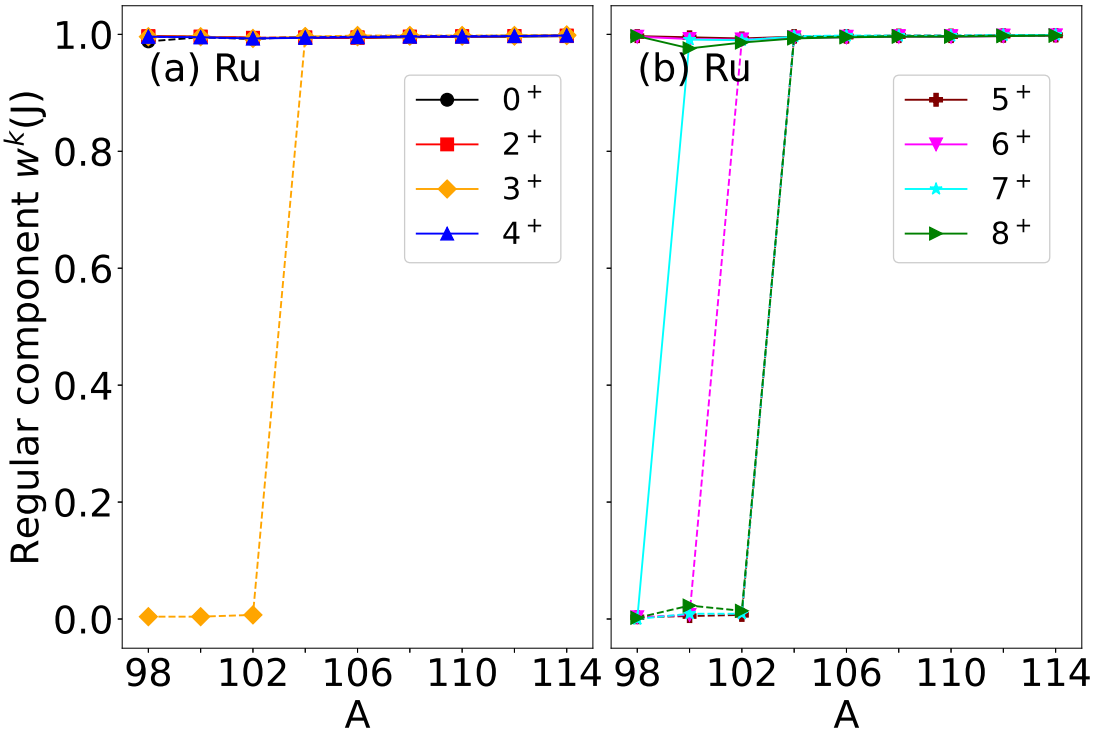

Figure 5.37: Regular content of the Ru isotopes for the two lowest-lying states for each J value (full lines with closed symbols correspond with the first state while dashed lines correspond with the second state) resulting from the IBM-CM calculation.

5.8 Study of other Observables: Radii, Isotopic Shifts, and Two-Neutron Separation Energies

5.8.1 Radii and Isotopic Shifts

Experimental observables such as nuclear charge radii provide an additional and very sensitive probe of structural changes along isotopic chains. In particular, abrupt variations in the radius are expected to occur around neutron number $N = 60$, where a rapid onset of deformation is known to take place. In this section, we compare the available experimental data on charge radii and isotopic shifts with the results obtained from our IBM-CM calculations.

Within the IBM-CM framework, the nuclear radius is closely connected to the expectation value of the $\hat{n}_d$ operator in the ground state. This contribution is imposed on a smooth, approximately linear dependence on the number of bosons. Since the model explicitly includes both regular and intruder configurations, both contributions must be taken into account. The squared charge radius operator can therefore be written as

$$r^2 = r_c^2 + \hat{P}_N^\dagger \left(\gamma_N \hat{N} + \beta_N \hat{n}_d\right) \hat{P}_N + \hat{P}_{N+2}^\dagger \left(\gamma_{N+2} \hat{N} + \beta_{N+2} \hat{n}_d\right) \hat{P}_{N+2}, \tag{5.4}$$

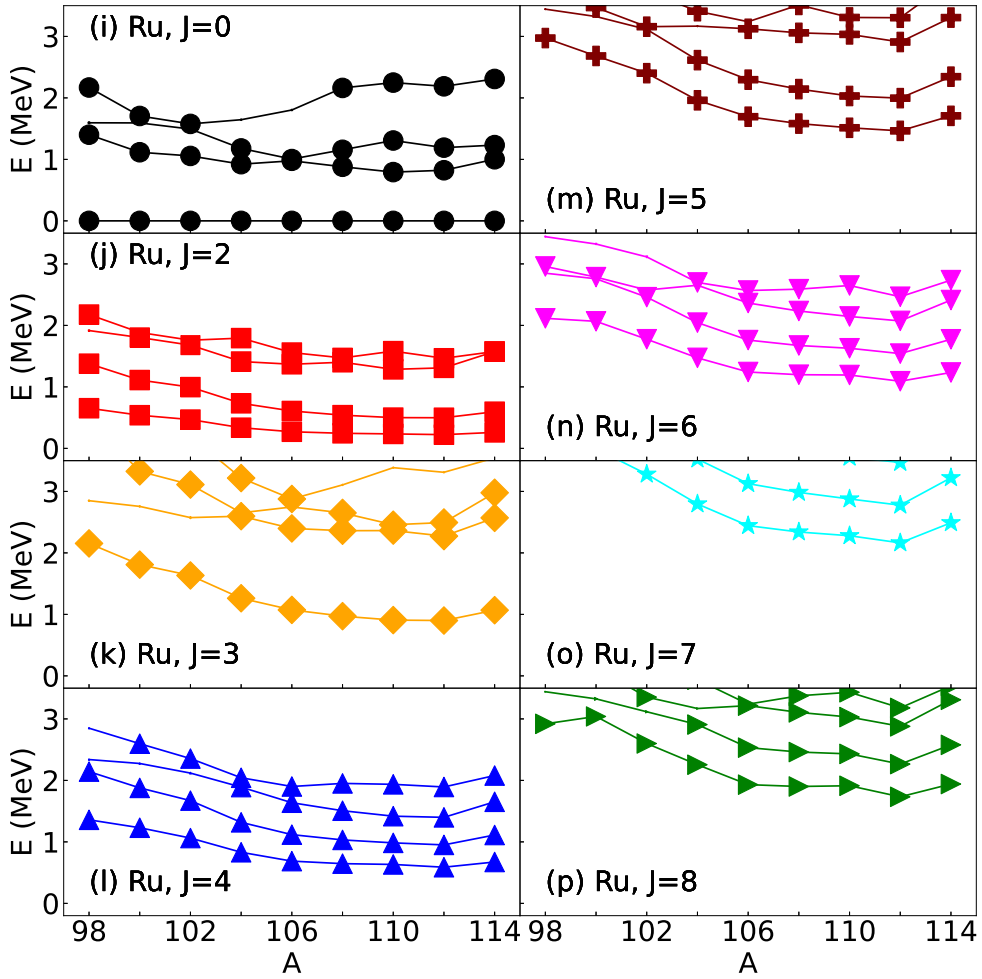

Figure 5.38: Energy systematics of the four lowest states below 4 MeV for Ru isotopes. Each panel corresponds to a specific angular momentum: (a) for $J = 0$, (b) for $J = 2$, (c) for $J = 3$, (d) for $J = 4$, (e) for $J = 5$, (f) for $J = 6$, (g) for $J = 7$, and (h) for $J = 8$. The size of each symbol is proportional to the fraction of the wave function lying in the regular sector. The dot for the state 0_1^+ in ^{98}Ru corresponds to 100%.

where $\hat{P}_N$ and $\hat{P}_{N+2}$ denote projection operators onto the regular and intruder subspaces, respectively.

Sr and Zr isotopes

For the Sr isotopic chain, the parameters entering equation (5.4) are taken to be common to all nuclei considered and are determined by a global fit to the experimental data, which are given relative to ^{88}Sr. The constant term r_c^2 is fixed so as to reproduce the radius of ^{92}Sr. The resulting parameter values are $\gamma_N = 0.23$ fm^2, $\beta_N = -0.028$ fm^2, $\gamma_{N+2} = 0.294$ fm^2, and $\beta_{N+2} = -0.16$ fm^2. A similar strategy was adopted in Ref. [148], although only a single configuration was considered in that work.

The IBM-CM results for both the absolute radii and the isotopic shifts show good overall agreement with the experimental data, as illustrated in panels (a) and (b) of Fig. 5.39. In

particular, the calculations successfully reproduce the sudden increase in the charge radius at ^{98}Sr, which signals the onset of deformation. This behavior can be directly linked to the crossing of two configurations with markedly different deformation, leading to an abrupt change in the ground-state structure and, consequently, in the nuclear radius.

For the Zr isotopic chain, the parameters entering equation (5.4) have been determined through a fit to the available experimental charge radii of the even-even nuclei in the mass range $A = 94$-106, which are given relative to ^{90}Zr [149]. The fit has been performed using the Hamiltonian parameters previously extracted, and restricting the analysis to the first half of the neutron shell ($N = 50 - 82$), in order to avoid possible changes of the radius parameters when crossing midshell. The resulting values are $\gamma_N = 0.245$ fm^2, $\beta_N = 0.195$ fm^2, $\gamma_{N+2} = 0.275$ fm^2, and $\beta_{N+2} = -0.09$ fm^2, with the constant term r_c^2 fixed so as to reproduce the experimental radius of ^{90}Zr.

The IBM-CM results for the Zr isotopes are displayed in Fig. 5.39(c) and (d), where both the absolute charge mean-square radii and the corresponding isotopic shifts are compared with the experimental data. A very good overall agreement is obtained, in particular regarding the abrupt increase of the radius when moving from ^{98}Zr to ^{100}Zr. This pronounced change, which is significantly larger than those observed in other regions of shape coexistence, is a clear fingerprint of a sudden onset of strong deformation at $N = 60$.

A comparison between the Sr and Zr isotopic chains reveals some common features in the evolution of nuclear radii in the $A \approx 100$ region. In both cases, the IBM-CM calculations reproduce the pronounced increase of the charge radius at $N = 60$, reflecting the sudden onset of deformation driven by the mixing of regular and intruder configurations. However, the effect is significantly more pronounced in the Zr isotopes, where both the absolute radii and the isotopic shifts exhibit a sharper and larger variation than in Sr. This indicates a more abrupt structural reorganization in Zr nuclei, consistent with a stronger dominance of the intruder configuration in the ground state beyond $N = 60$.

Mo and Ru isotopes

The same fitting procedure is applied to the Mo and Ru isotopic chains. In both cases, the parameters are assumed to be constant along each chain and are adjusted to best reproduce the experimental data, which are referenced to ^{108}Mo and ^{104}Ru, respectively. For Mo isotopes, the fitted values are $\gamma_N = 0.221$ fm^2, $\beta_N = -0.627$ fm^2, $\gamma_{N+2} = 0.215$ fm^2, and $\beta_{N+2} = -0.024$ fm^2. For Ru isotopes, the values are $\gamma_N = 0.248$ fm^2 and $\beta_N = 0.018$ fm^2. In this case, no explicit contribution from the intruder configuration is required. This treatment closely follows the approach of Ref. [148], where only the regular configuration was considered.

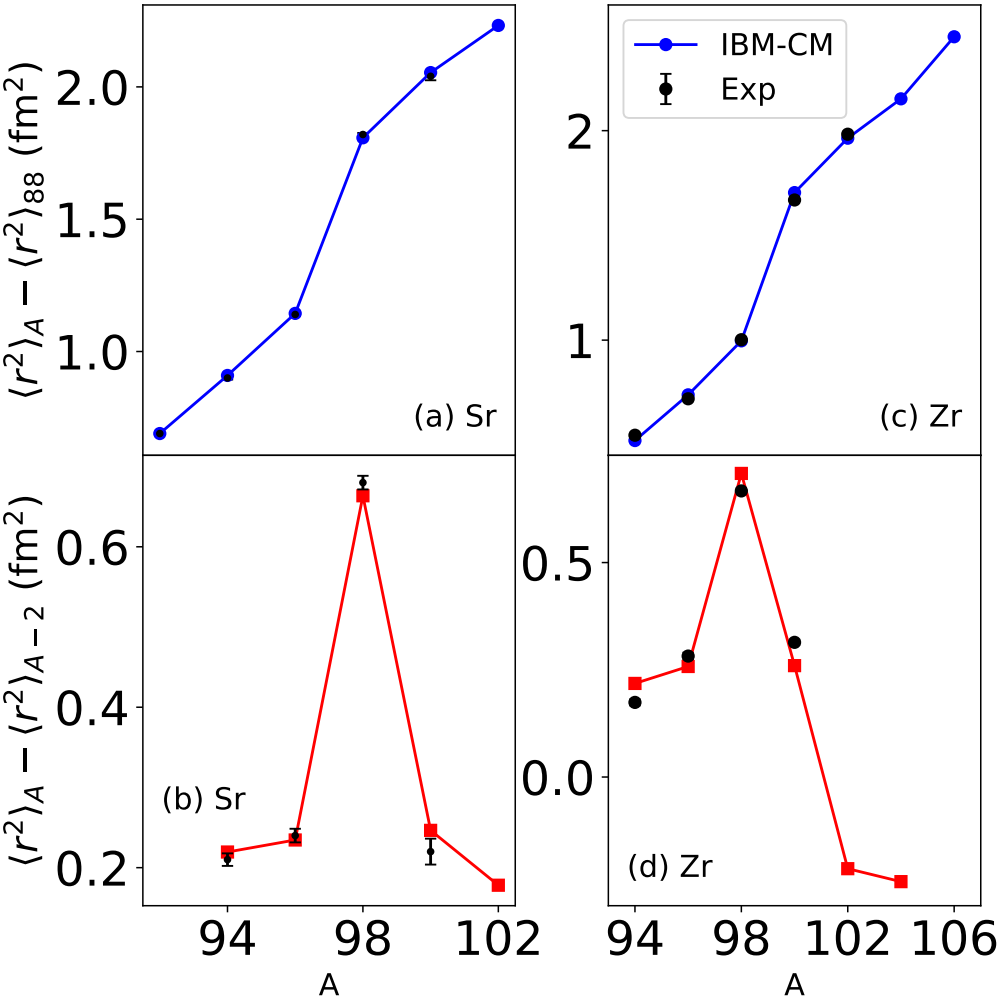

Figure 5.39: Charge mean-square radii for the Sr nuclei (a) and for Zr (c). Together with the isotopic shift for the Sr nuclei (b) and Zr (d). The data are taken from [149]. Lines are used for theoretical results and dots with error bars for experimental values. Data for Zr isotopes taken from [88].

For Mo isotopes, the IBM-CM calculations reproduce the overall trend of the radii and capture the sudden increase observed at ^{102}Mo, associated with the onset of deformation. However, the theoretical values do not fully overlap with the experimental error bars, in agreement with previous studies [150, 144, 145, 88, 36]. In particular, the calculations tend to predict a slightly stronger and more abrupt deformation than observed experimentally. This discrepancy may be related to the theoretical prediction of a similar degree of deformation for $^{104-108}$Mo, whereas the experimental data suggest a more gradual evolution.

In contrast, the situation for Ru isotopes is simpler. Since only the regular configuration contributes, the calculated radii follow a smooth linear trend that agrees well with the experimental data, and no abrupt structural changes are observed. Note that different

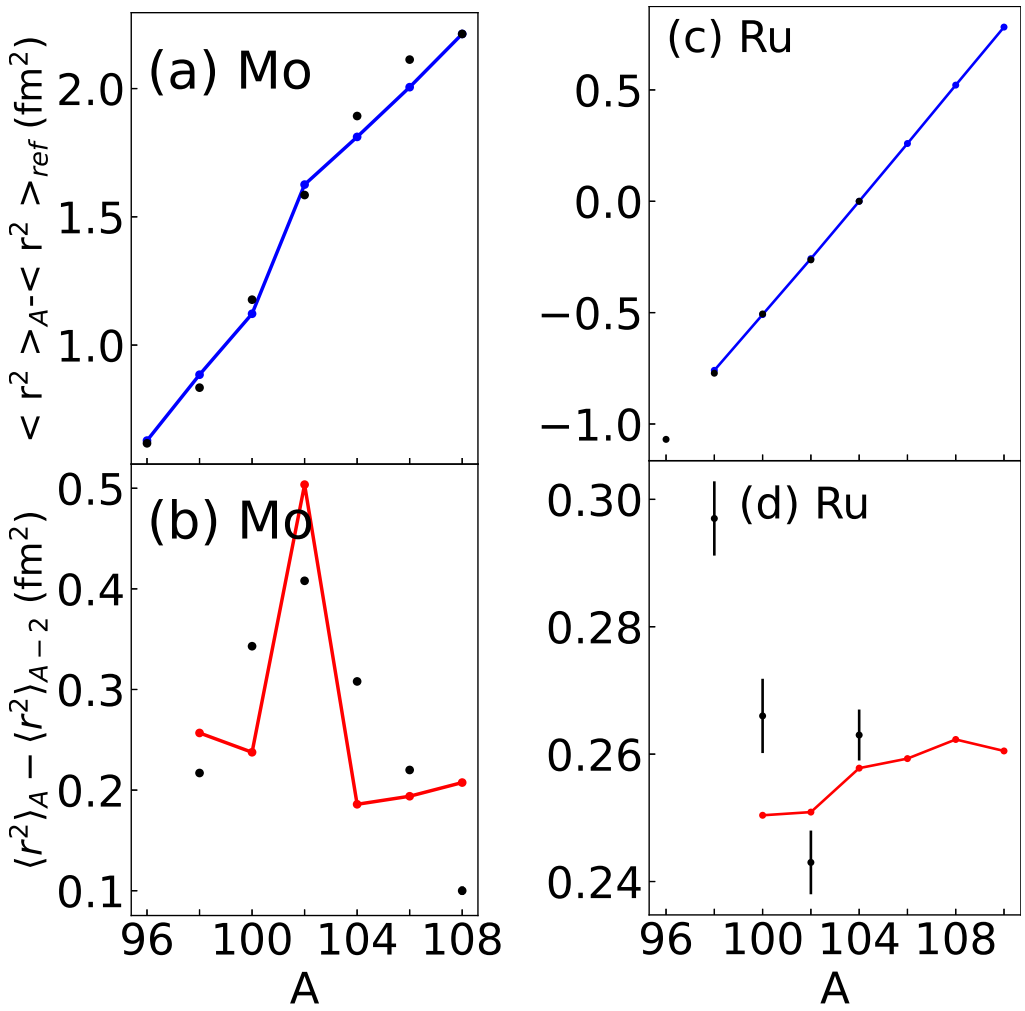

Figure 5.40: Charge mean-square radii for the Mo (a) and Ru nuclei (c) and isotopic shift for the Mo (b) and Ru nuclei (d). The data are taken from [149]. For Mo, $\langle r^2 \rangle_{ref}$ is fixed to reproduce the value of $\langle r^2 \rangle$ in ^{96}Mo, while for Ru to reproduce ^{96}Ru.

vertical scales are used in panels (a) and (c) and also in (b) and (d) of Fig. 5.40.

5.8.2 Two-Neutron Separation Energies

The two-neutron separation energy, S_{2n}, is defined as the difference between the binding energies of two nuclei differing by two mass units,

$$S_{2n}(A) = BE(A) - BE(A-2), \tag{5.5}$$

where $BE(A)$ denotes the binding energy of the nucleus with mass number A. This observable is particularly sensitive to changes in nuclear structure and is therefore perfect for identifying regions of rapid structural evolution.

Within the IBM framework, to the binding energy obtained from the Hamiltonian we must add an additional contribution depending on N and N^2, which does not affect excitation

energies. This leads to an extra linear term in the expression for S_{2n} [151]. As a result, the two-neutron separation energy can be written as

$$S_{2n}(A) = \mathcal{A} + \mathcal{B}A + BE^{\mathrm{lo}}(A) - BE^{\mathrm{lo}}(A-2), \tag{5.6}$$

where BE^{lo} is the local binding energy obtained from the IBM Hamiltonian, and the coefficients $\mathcal{A}$ and $\mathcal{B}$ are taken to be constant along a given isotopic chain [151].

In the IBM-CM approach, the effective number of bosons contributing to the ground state may be modified by the presence of intruder configurations. To account for this effect, we introduce the following ansatz:

$$S_{2n}(A) = \mathcal{A} + \mathcal{B}\,(A + 2(1-w)) + BE^{\mathrm{lo}}(A) - BE^{\mathrm{lo}}(A-2), \tag{5.7}$$

where $w \equiv w^1(0)$ is the regular component of the ground-state wave function, $w^k(J) = \sum_i |a_i^k(J)|^2$. Once the local binding energies are known, the parameters $\mathcal{A}$ and $\mathcal{B}$ are determined through a least-squares fit to the experimental S_{2n} values, following the procedure described in Refs. [151, 144, 88].

Sr and Zr isotopes

For the Sr isotopic chain, the fitted values of the two-neutron separation energy are $\mathcal{A} = 52.9$ MeV and $\mathcal{B} = -0.441$ MeV. The comparison between experimental data and IBM-CM results is shown in Fig. 5.41 panel (a), where a very good overall agreement is observed. In particular, a clear change in the slope of the S_{2n} curve can be noticed when approaching neutron number $N = 60$ ($A \approx 98$), which is approximately reproduced by the theoretical calculations. This behavior manifests itself as a flattening of the S_{2n} systematics and is commonly interpreted as a signature of a rapid structural change in the ground state or a quantum phase transition (QPT) [152], as previously suggested for Zr isotopes [96].

A comparison between the Sr and Zr isotopic chains shows that both exhibit a pronounced change in the slope of the two-neutron separation energy around $N = 60$, reflecting a sudden modification of the underlying nuclear structure. In Zr isotopes, this feature has been previously associated with a crossing between configurations of different deformation and interpreted as a clear signature of a QPT. In the case of Sr, a similar flattening of the S_{2n} curve is observed, although the effect is slightly less abrupt, suggesting a more gradual evolution of the ground-state structure. This difference is consistent with the trends observed in other observables, such as charge radii, and points to a smoother interplay between regular and intruder configurations in Sr as compared to Zr.

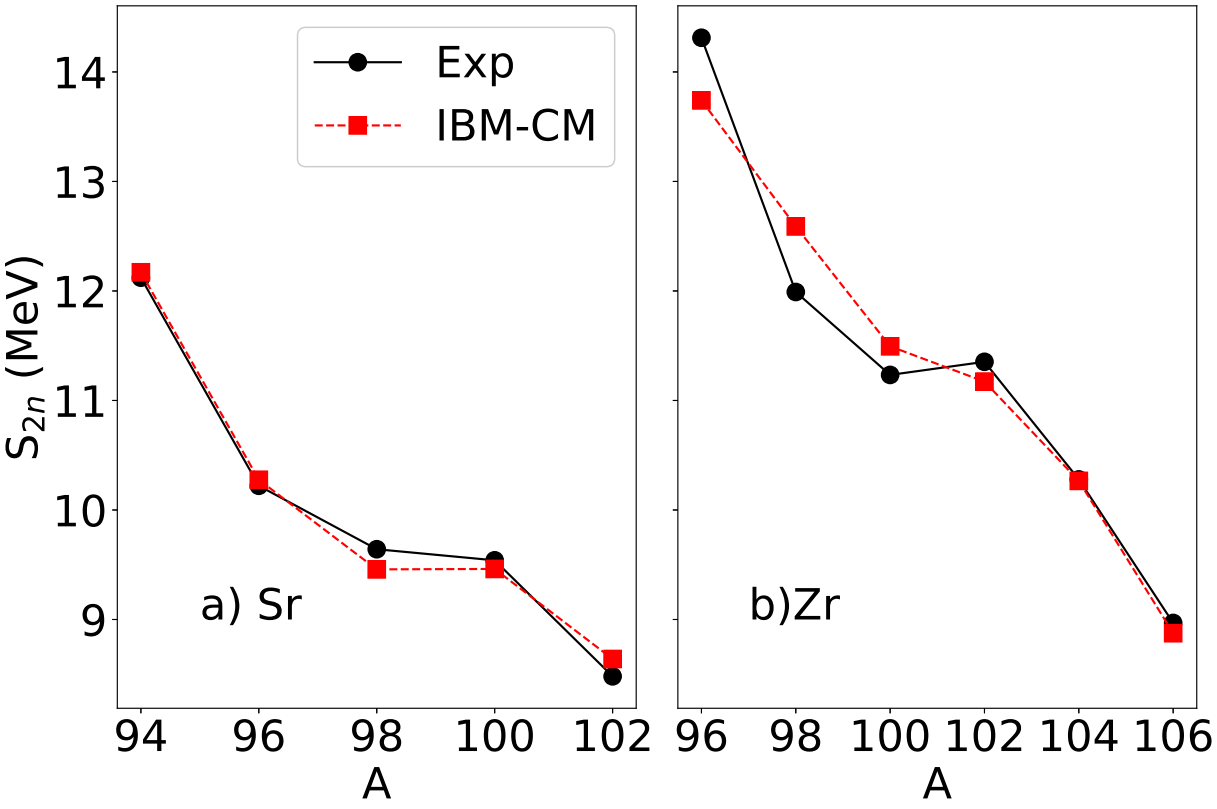

Figure 5.41: Comparison of experimental and theoretical two-neutron separation energies for Sr isotopes in panel (a) and for Zr ones in panel (b).

Mo and Ru isotopes

Applying the same fitting procedure to the Mo and Ru isotopic chains, we obtain $\mathcal{A} = 55.2$ MeV and $\mathcal{B} = -0.407$ MeV for Mo, and $\mathcal{A} = 65.7$ MeV and $\mathcal{B} = -0.499$ MeV for Ru. As in the Sr case, only the first part of the neutron shell is used to determine these parameters.

The comparison between theory and experiment is displayed in Fig. 5.42. In both isotopic chains, a good overall agreement is observed around neutron number $N = 60$ ($A = 102$ for Mo and $A = 104$ for Ru). For Ru isotopes, the S_{2n} values follow a nearly linear trend, which is well reproduced by the model. In Mo isotopes, a slight flattening appears at $A = 102$, corresponding to the crossing of regular and intruder configurations. Although the IBM-CM results remain largely linear, this point signals the same structural change identified in other observables.

It should be noted that $A = 108$ in Mo already lies beyond the midpoint of the neutron shell, even though the same linear coefficients determined from the first half of the shell are employed. The deviation observed for ^{110}Mo is therefore related to the known differences between the linear trends in the first and second halves of the shell, as discussed in Ref. [151].

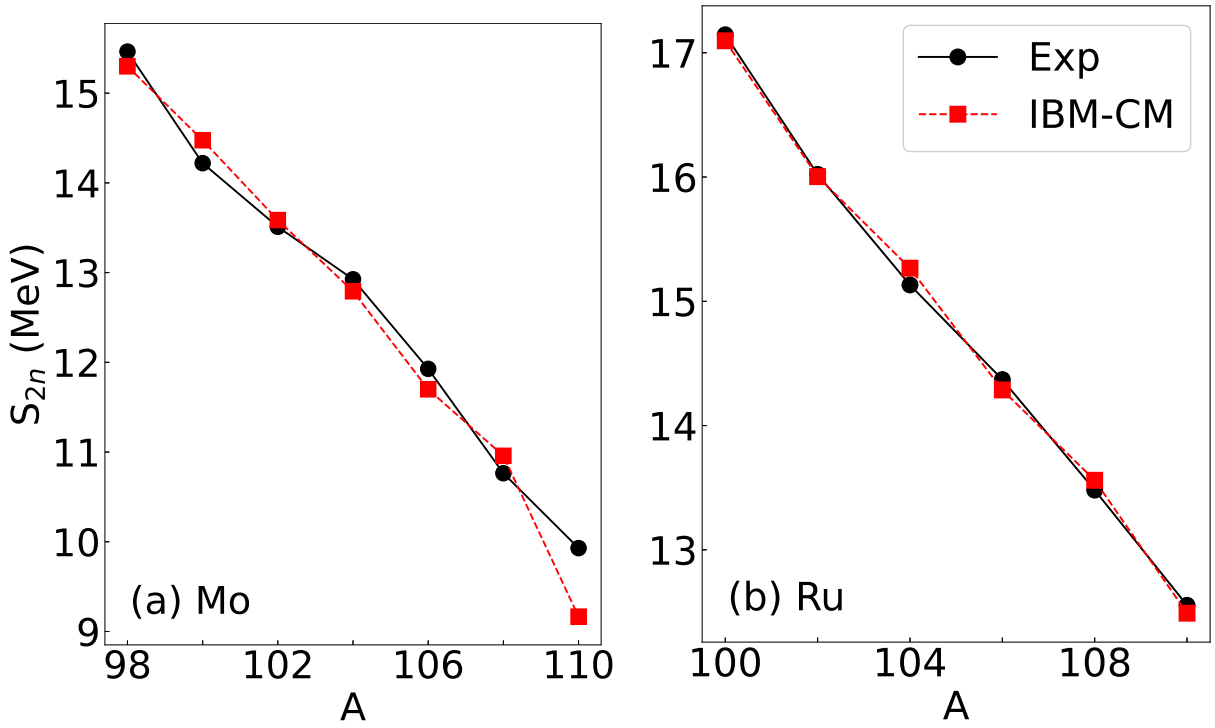

Figure 5.42: Comparison of experimental and theoretical two-neutron separation energies in Mo (panel (a)) and Ru (panel (b)) isotopes.

5.9 Nuclear Deformation and Mean-Field Energy Surfaces

One of our goals is to obtain information about the deformation along the different isotope chains considered, taking into consideration that the deformation (β) cannot be directly measured. Moreover, the use of different methods to determine the deformation will allow us to analyze the consistency of the obtained values.

The first way to get information about deformation is through the use of the intrinsic state formalism of the IBM. This formalism was presented in the set of seminal works [63, 72, 64, 153] and it provides a geometric interpretation of the model, defining, in particular, a deformation parameter. This intrinsic state formalism cannot be used directly for the IBM-CM, but the formalism should be enlarged. Frank *et al.* introduced almost twenty years ago the matrix coherent-state method [68, 69, 41, 154] which allows to calculate the total energy surface for a system where regular and intruder configurations exist. In Refs. [155, 144, 145, 88], a detailed description of the method and its application to Pt, Hg, Po, and Zr isotopes, respectively, has been given.

5.9.1 Sr Isotopes

The evolution of the nuclear deformation can also be approached by the study of the mean-field energy curves in a chain of isotopes, which can be calculated also using the IBM-CM formalism [68]. This is depicted in Fig. 5.43 for Sr isotopes, where we present these axial energy curves for the regular and the intruder configurations, as well as the one for the complete system. Concerning the regular configuration (red dotted line), it presents a smooth evolution being spherical for A = 92 − 96, becoming very flat and finally axially oblate deformed for A = 98 − 102. Regarding the intruder configuration (green dashed line), it starts being also spherical for A = 92 and 94, but rapidly becomes axially prolate deformed from A = 96 and onwards. Finally, the IBM-CM full calculation (black full line), which essentially follows the lowest of the intruder and regular curves, starts also with a spherical minimum in A = 92 − 96 and then becomes an axially prolate deformed for A = 98 − 102. A very relevant feature is that both configurations evolve separately from a spherical to a deformed shape, more rapidly in the case of the intruder configuration. Therefore, most probably in both configurations separately, regular and intruder, a QPT is present.

Moreover, the fact that both configurations cross at A = 98 makes much more abrupt the change of deformation, also inducing a QPT in the whole system. The QPT present in the separated regular and the intruder configurations is called type-I QPT [35] and involves the existence of a single configuration energy surface where several minima are present. On the other hand, for the whole energy surface a type-II QPT [35] appears because two energy surfaces that cross are present. A type-II QPT is expected to induce much more abrupt changes than the type-I and it will own the typical phenomenology of a first order QPT. It is worthy to mention that this is not the only mechanism to induce a discontinuity in the S_{2n}, as happens, for instance, in the rare-earth region at $N \approx 90$.

To complete the analysis, the IBM-CM mean-field energy surfaces calculated for the $^{92-102}$Sr isotopes are displayed in Fig. 5.44, where again a clear evolution of the nuclear shape is observed along the isotopic chain. Regarding the cited figure, the lightest nuclei, ^{92}Sr, ^{94}Sr, and ^{96}Sr, exhibit nearly spherical energy surfaces. In particular, ^{94}Sr shows a weakly deformed minimum, while ^{96}Sr presents a very flat potential, indicating in that way a transitional character.

In contrast, the heavier isotopes are clearly deformed. Showing the ^{98}Sr isotope clear signs of shape coexistence, with prolate and oblate minima lying very close in energy. For ^{100}Sr and ^{102}Sr, a pronounced prolate minimum becomes dominant, while an oblate minimum persists at higher excitation energy. These results are fully consistent with self-consistent mean-field calculations based on the Gogny interaction within the HFB

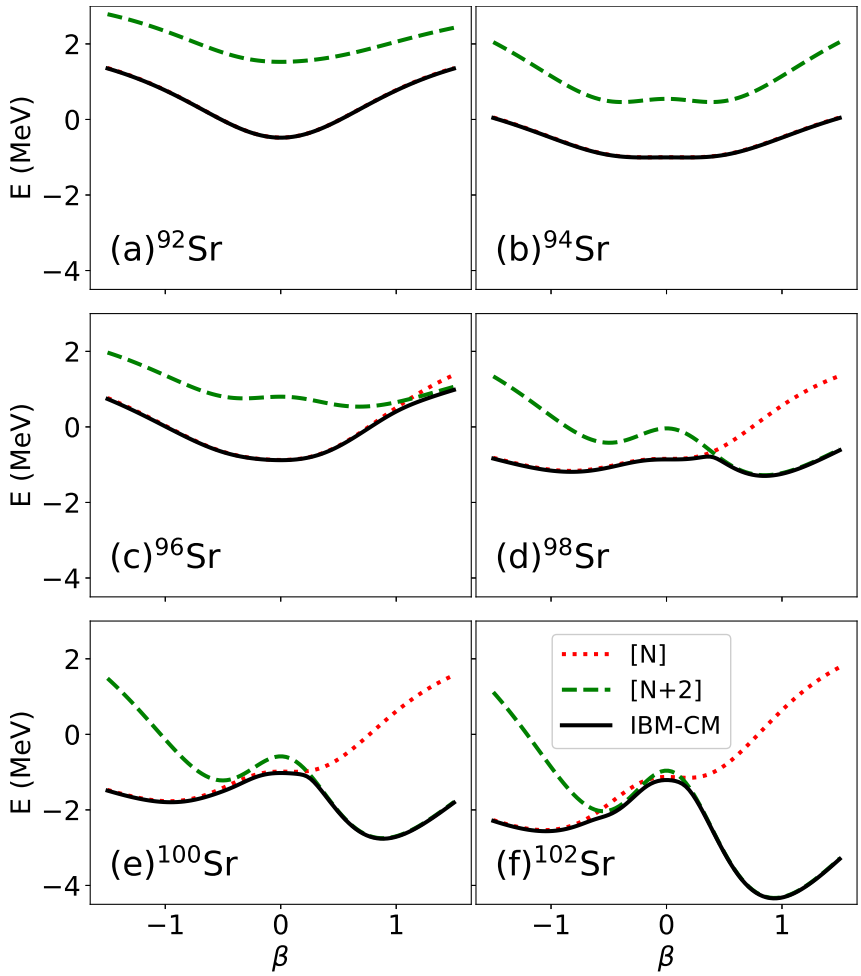

Figure 5.43: Axial IBM-CM mean-field energy surfaces for $^{92-102}$Sr isotopes. Red dotted line stands for the unperturbed regular configuration, [N], green dashed one for the unperturbed intruder configuration, [N+2], while the black continuous line for the full IBM-CM calculation.

framework [92, 91]. In those studies, ^{92}Sr remains spherical, a shallow oblate minimum appears in ^{94}Sr, and both oblate and prolate shapes coexist in ^{96}Sr, with the oblate minimum being energetically favored. For $^{98-102}$Sr, the prolate minimum becomes the lowest one, in agreement with the present IBM-CM results.

It is worth noting that, although a similar evolution is observed in the Zr isotopic chain, the nature of the coexisting shapes differs: in Zr isotopes the competition occurs mainly between spherical and prolate configurations, whereas in Sr isotopes the coexistence involves oblate and prolate shapes.

To quantify the evolution of deformation, Fig. 5.45 presents the value of the deformation parameter β associated with the absolute minimum of the energy surface. It is important to keep in mind that although the IBM deformation parameter β is not identical to the collective-model variable, an approximate correspondence can be established [63]. The figure displays separately the results obtained for the regular ($[N]$) and intruder ($[N+2]$)

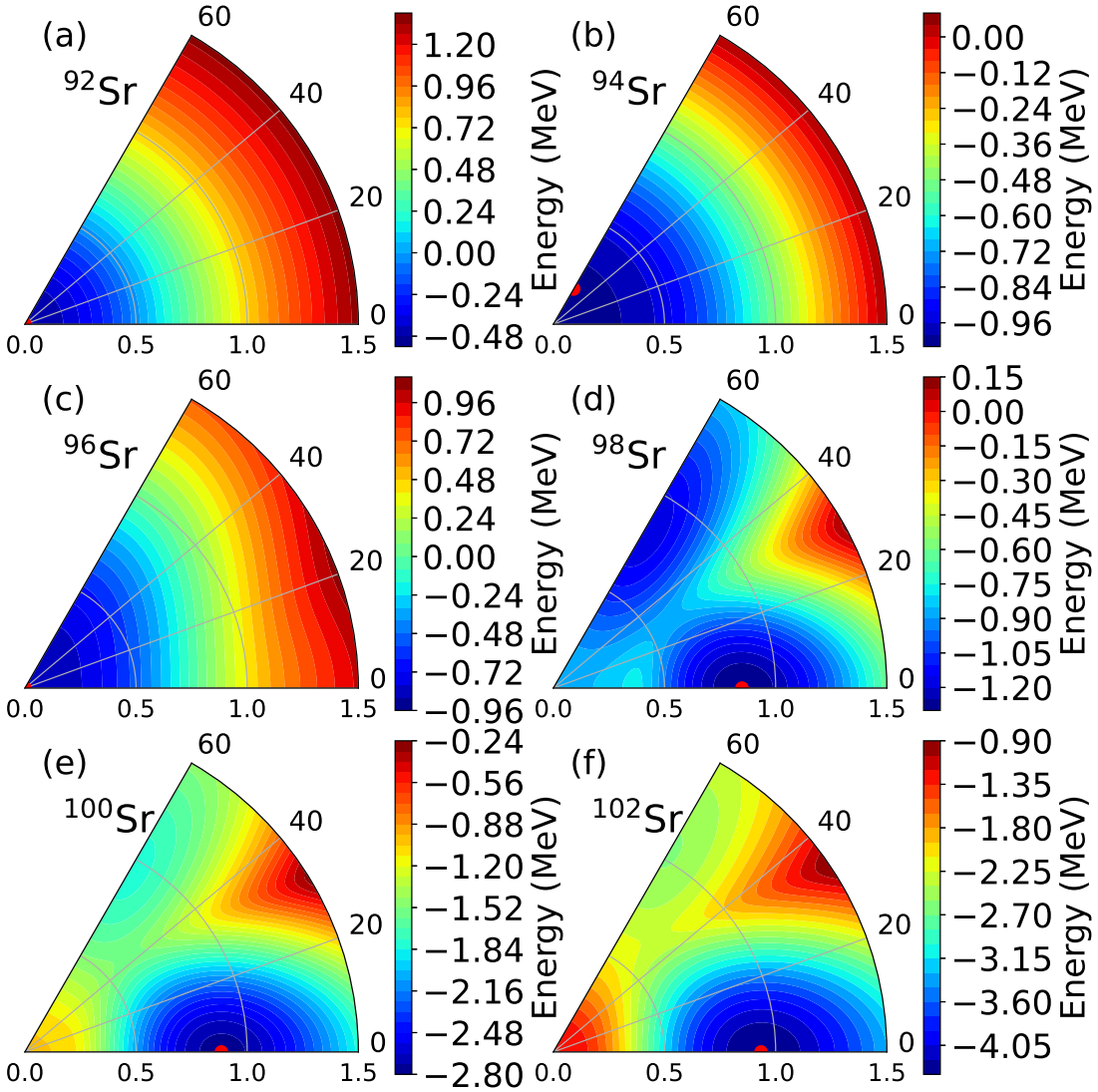

Figure 5.44: Matrix coherent-state calculation for $^{92-102}$Sr, corresponding with the present IBM-CM Hamiltonian (table 5.1). The red dot marks the position of the absolute minimum.

configurations by setting the mixing strength to zero ($\omega = 0$), as well as the outcome of the full IBM-CM calculation.

We can observe that both configurations evolve from near-spherical shapes at low mass numbers toward deformed ones at higher masses. The regular configuration develops an oblate deformation, while the intruder configuration becomes prolate. The onset of deformation is more abrupt in the regular configuration, whereas the intruder configuration evolves more smoothly. When configuration mixing is included, the ground state of the first three isotopes is dominated by the regular configuration, while for $^{98-102}$Sr the intruder configuration becomes dominant, leading to a prolate ground state.

Although nuclear shape is not a direct observable, Coulomb excitation experiments provide nearly model-independent access to deformation properties, as demonstrated by Ku-

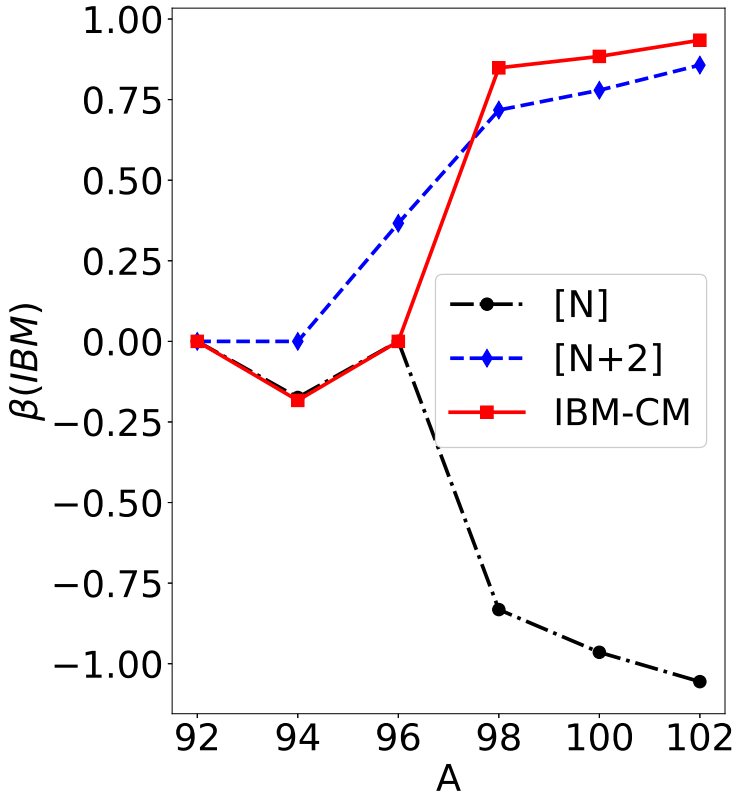

Figure 5.45: Value of β extracted from the IBM-CM energy surface. $[N]$, $[N+2]$, and IBM-CM correspond to a pure regular configuration, a pure intruder configuration, and to the complete calculation for Sr isotopes.

mar, Cline, and collaborators [156, 157]. This method relies on the concept of an "equivalent ellipsoid", defined as a uniformly charged ellipsoid reproducing the charge radius and E2 moments of a given nuclear state. From measured electromagnetic matrix elements, it is possible to extract effective deformation parameters β and γ for states with definite angular momentum. More recently, deformation properties have also been explored in the laboratory frame using auxiliary-field Monte Carlo techniques, extending the analysis to excited states [158, 159, 160].

From a theoretical perspective, nuclear deformation can be characterized using quadrupole shape invariants. For 0^+ states, these invariants are defined as

$$q_{2,i} = \sqrt{5}\left\langle 0_i^+ \left| [\hat{Q}\times\hat{Q}]^{(0)} \right| 0_i^+ \right\rangle, \tag{5.8}$$

$$q_{3,i} = -\sqrt{\frac{35}{2}}\left\langle 0_i^+ \mid [\hat{Q}\times\hat{Q}\times\hat{Q}]^{(0)} \mid 0_i^+ \right\rangle. \tag{5.9}$$

The deformation parameters are directly connected with the ones of the triaxial rigid rotor, q and δ, accordingly to,

$$q = \sqrt{q_2}, \tag{5.10}$$

Table 5.8: Values of deformation, q^2 and γ, extracted from the quadrupole shape invariants, together with the value of w^k ([N] content) for Sr isotopes.

A	State	q^2 (e^2b^2)	γ	w^k	A	State	q^2 (e^2b^2)	γ	w^k
92	0_1^+	0.10	29	0.999	98	0_1^+	1.33	10	0.109
	0_2^+	0.06	17	0.995		0_2^+	0.31	15	0.888
	0_3^+	1.18	19	0.003		0_3^+	0.14	27	0.947
94	0_1^+	0.10	30	0.996	100	0_1	1.46	10	0.109
	0_2^+	0.05	30	0.989		0_2^+	0.25	48	0.981
	0_3^+	0.32	30	0.013		0_3^+	0.98	18	0.039
96	0_1^+	0.17	39	0.996	102	0_1^+	1.84	9	0.001
	0_2^+	0.14	49	0.981		0_2^+	0.81	19	0.507
	0_3^+	0.16	15	0.020		0_3^+	0.83	18	0.493

$$\delta = \frac{60}{\pi} \arccos \frac{q_3}{q_2^{3/2}}, \tag{5.11}$$

where δ coincides with the parameter γ of the Bohr-Mottelson model up to first order approximation. It is worth mentioning the work [161] where a method to calculate the fluctuations of β and γ is presented.

The theoretical values of γ and q^2 are presented in Table 5.8 simultaneously with the fraction of wave function belonging to the regular sector w^k, for every 0_1^+, 0_2^+ and 0_3^+ of the whole chain of Sr isotopes. According to this table, one readily observe the coexistence of different deformations, typically less deformed for the regular than for the intruder states. Another interesting feature is the fact that the nature of the deformation of the ground state suddenly increase when passing from $^{92-96}$Sr to $^{98-102}$Sr. Regarding triaxiality, the three first isotopes present clear triaxial shapes, while in the three last ones the ground state is close to a prolate shape and the rest of states remain rather triaxial.

The deformation parameter β can also be obtained from the quadrupole shape invariant (5.8) (see, e.g., references [140, 162, 134]),

$$\beta = \frac{4\pi\sqrt{q_2}}{3Zer_0^2A^{2/3}}, \tag{5.12}$$

where e is the proton charge and $r_0 = 1.2$ fm.

The values of β extracted from equation (5.12) for the corresponding ground state, 0_1^+, and the 0_2^+ and 0_3^+ states, are shown in Fig. 5.46(a), where β for the ground state presents a rapid increase, passing from a value around 0.15 for $^{92-96}$Sr to another around 0.45 for $^{98-102}$Sr. The value of β for the 0_2^+ state steadily increase while for the 0_3^+ state there also exists a sudden increase for $^{100-102}$Sr. It is illustrative to present the value of the deformation for the first 0^+ state belonging to the regular sector, 0_{reg}^+, and the one of the

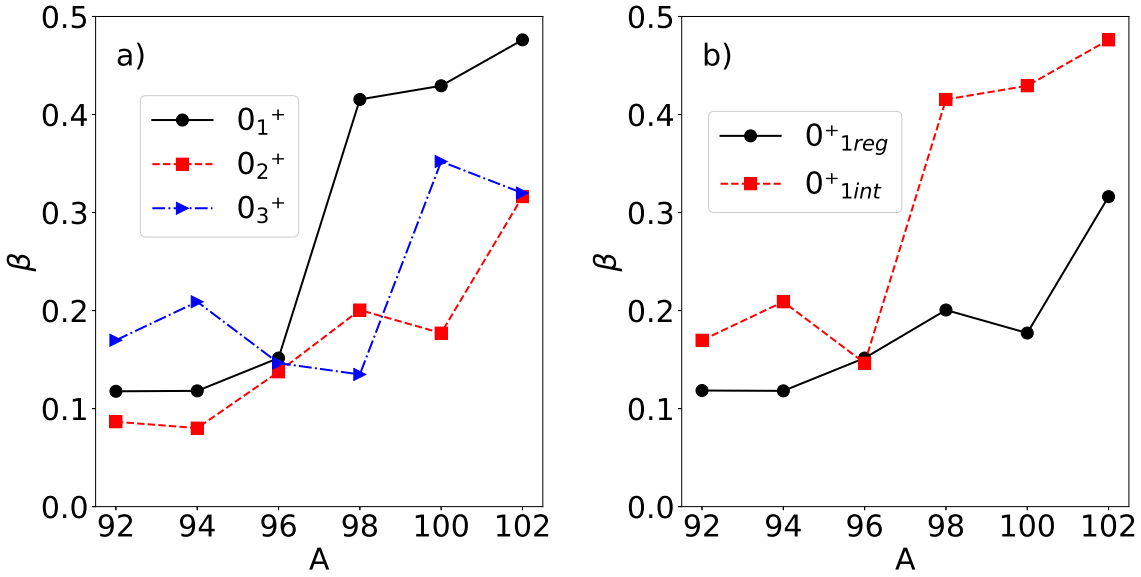

Figure 5.46: Value of the deformation, β, extracted from the value of the quadrupole shape invariants for Sr isotopes. In (a) we plot the value for the first three 0^+ states. In (b) we plot the same but for the first regular and the first intruder 0^+ state.

first 0^+ state which belongs to the intruder sector, 0^+_{int}, as shown in Fig. 5.46(b) which is done simply taking into account the regular content of the states presented in the last column of Table 5.8. The 0^+_{reg} state shows a smooth increase of deformation over the whole chain of isotopes and it corresponds to the 0^+_1 state for $^{92-96}$Sr and to the 0^+_2 for $^{98-102}$Sr, while the state 0^+_{int} shows the sudden increase of the deformation previously explained and it corresponds to the states 0^+_3 and 0^+_1 for $^{92-96}$Sr and $^{98-102}$Sr, respectively.

To conclude the analysis of the nuclear deformation of Sr Isotopes, we can say that both approaches presented provide a consistent view of the deformation of the two families of states, intruder and regular, with both configurations close to a spherical shape in $^{92-96}$Sr and an increase in deformation when entering in the region of $^{98-102}$Sr. The mean-field energy surfaces point to the coexistence of a prolate and an oblate shape in $^{98-102}$Sr, corresponding the deepest minimum to the prolate shape. The abrupt onset of deformation, specially for the ground state, which is the result of the crossing of the regular and the intruder configurations, points to the existence of a QPT around ^{98}Sr. The behavior of the S_{2n} and the nuclear radii, presented in previous section, point to the existence of a QPT, as well. This is a case that resembles the situation in even-even Zr isotopes where also two configurations coexist and they cross at ^{100}Zr. Therefore, the study of both chain of isotopes suggests the presence of a first order QPT at neutron number 60 associated to the crossing of two configurations.

5.9.2 Zr Isotopes

The evolution of the nuclear shape along the Zr isotopic chain can be analyzed in detail studying the energy curves and energy surfaces shown in Figs. 5.47 and 5.48, respectively. Both representations provide complementary information on the onset of deformation and the coexistence of different shapes.

Firstly, the energy curves displayed in Fig. 5.47 clearly illustrate the gradual change in the equilibrium configuration as the neutron number increases. For the lighter isotopes, the minimum of the energy curve is located at $\beta = 0$, indicating a spherical shape. However, as neutrons are added, the spherical minimum evolves into a more deformed configuration. Moreover, in all deformed cases, the minimum corresponds to a prolate shape.

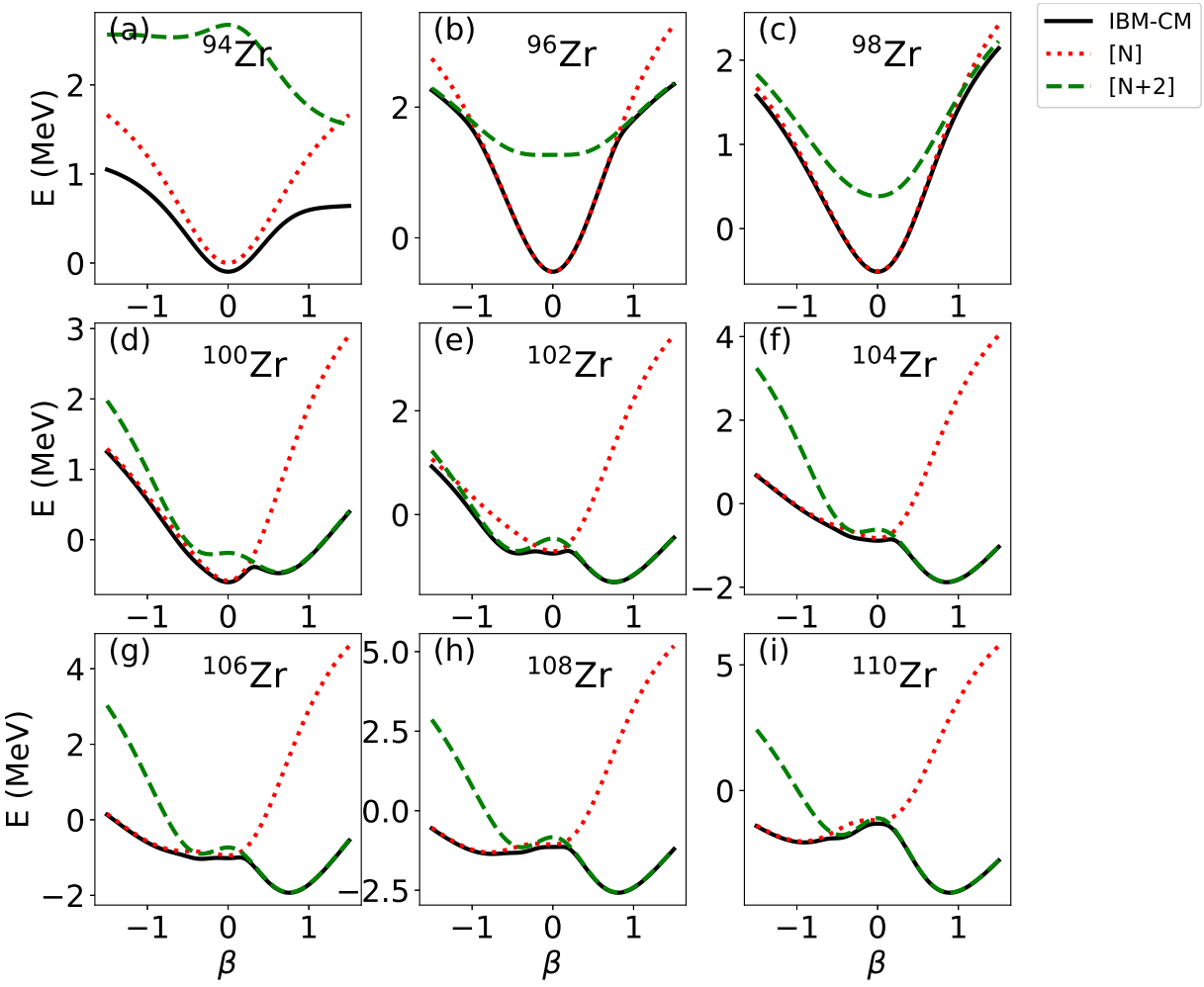

Figure 5.47: Matrix coherent-state potential energy surface along the axial axis for even-even Zr isotopes. Data extracted from [88]

The same physics is reflected in the energy surfaces shown in Fig. 5.48, where it can be observed that these nuclei exhibit a rapid transition from spherical configurations to well-deformed shapes as neutrons are added.

In Fig. 5.48, lighter isotopes corresponding to $^{94-98}$Zr, the energy surface displays a well-defined spherical minimum, while for ^{100}Zr, two competing minima are observed: a spherical minimum and a prolate-deformed one, which are nearly degenerate in energy, that is a feature of shape coexistence. Moreover, in $^{102-110}$Zr, the energy surface is dominated by a deep prolate-deformed minimum, although a shallow spherical minimum still persists. In addition, it is worth noting that, within the mean-field framework, the spherical configuration remains the lowest minimum in ^{100}Zr, although it lies very close in energy to the prolate one.

Furthermore, in the same way as we have previously performed, more information about the deformation can be extracted from the study of the quadratic quadrupole invariant, from which the β values are determined for the lowest 0^+ states along the zirconium isotopic chain.

The resulting deformation parameters for the first three 0^+ states are displayed in Fig. 5.49(a). The ground-state deformation exhibits a pronounced maximum around $A = 104$, whereas the deformation associated with the 0_2^+ state shows a more irregular behavior. In contrast, the deformation of the 0_3^+ state remains approximately constant throughout the isotopic chain.

An also meaningful representation is obtained by distinguishing between regular and intruder configurations. Selecting the lowest 0^+ state dominated by the regular configuration and the lowest 0^+ state dominated by the intruder configuration, the corresponding β values are shown in Fig. 5.49(b), where we notice that the intruder state is systematically more deformed than the regular one, as expected. Both configurations reach a maximum deformation around $A = 104$, although the regular configuration exhibits a much flatter behavior along the isotopic chain and whereas the deformation associated with the regular configuration remains nearly constant, except near mid-shell, the intruder configuration shows a more abrupt increase as mid-shell is approached. Additionally, a sudden increase in deformation is observed when moving from $A = 94$ to $A = 96$ and beyond.

5.9.3 Mo Isotopes

Firstly, we show in Fig. 5.50 the axial energy surfaces while in Fig. 5.51 appears the full $\beta - \gamma$ plane energy surfaces for Mo isotopes. In the axial case, the unperturbed calculations for regular (red dotted line) and intruder (green dashed line) configurations are presented, along with the full calculations (black solid line). It is evident that the intruder configuration evolves from a spherical shape to a flat surface in ^{100}Mo, transitioning into an oblate deformed shape and eventually becoming nearly γ-unstable. This configuration gains correlation energy more rapidly than the regular configuration. On the other hand, the regular configuration evolves slowly from a spherical shape to a shallow prolate de-

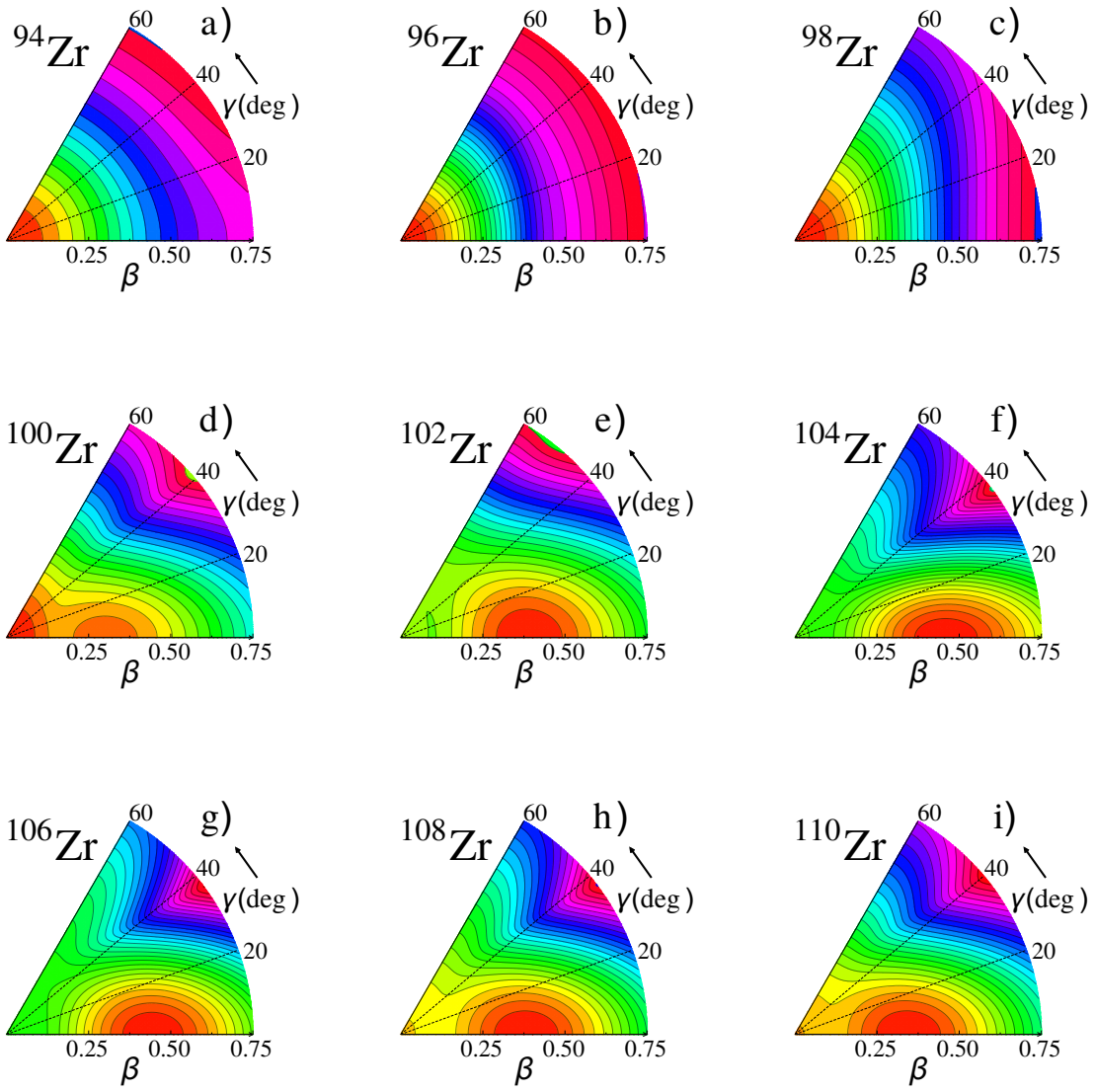

Figure 5.48: Matrix coherent-state calculation for $^{94-110}$Zr, corresponding with the present IBM-CM Hamiltonian. The β variable has been rescaled and it corresponds to the one of the collective model. The energy spacing between adjacent contour lines equals 100 keV and the deepest energy minimum is set to zero, corresponding to the red color[88]

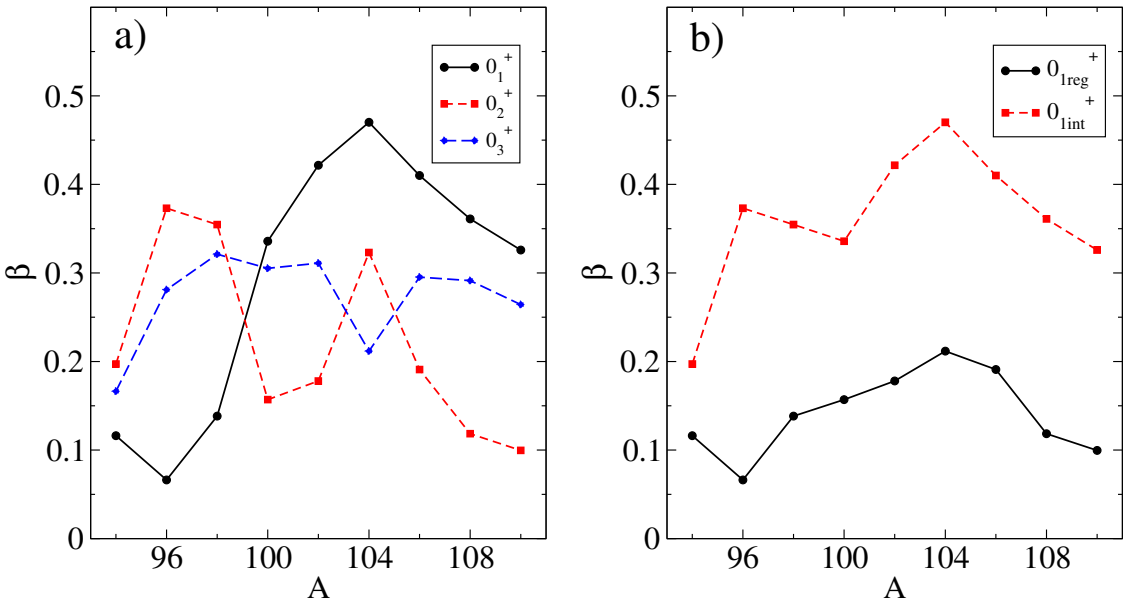

Figure 5.49: Value of the deformation parameter β extracted from the value of the quadrupole shape invariants for Zr isotopes. In panel (a) the first value for the 0^+ states is presented, while in panel (b) we plot the same but for the first regular and the first intruder 0^+ state [88]

formed energy surface. The full calculation clearly depicts the transition from a regular to an intruder ground state.

When analyzing the energy surfaces in the $\beta - \gamma$ plane (Fig. 5.51), the transition from a spherical to a prolate shape can be observed in ^{102}Mo, although also a secondary prolate minimum appears in ^{104}Mo, and the nuclei become almost γ-unstable in $^{108-110}$Mo. Previous HFB calculations using a Gogny interaction [92, 91] exhibit similar energy surfaces to the present results, although there ^{100}Mo is already prolate deformed. From ^{102}Mo onwards, the shape is predominantly oblate, with triaxial minima and shallow valleys in the γ direction. The coexistence of two minima, one oblate and the other prolate, is present in ^{104}Mo. Note that the situation is similar to the case of Sr where the coexistence of a prolate and an oblate minimum exists [36], but differs from the Zr nuclei where an spherical and a prolate minimum coexist [96].

To gain a clearer understanding on the evolution of nuclear shape, it is useful to represent the value of β corresponding to the minimum in the energy functional (indicated by red dots in Fig. 5.51). It is important to note that the β variable defined in the IBM does not directly correspond to the one used in the collective model. However, there exists a linear relationship [63] connecting both variables. Therefore, the variables presented should be understood as being proportional to the Bohr-Mottelson ones. Note that positive values corresponds to prolate shapes while negative to oblate.

Moreover, Fig. 5.52 illustrates the IBM β values for Mo isotopes, here the values corre-

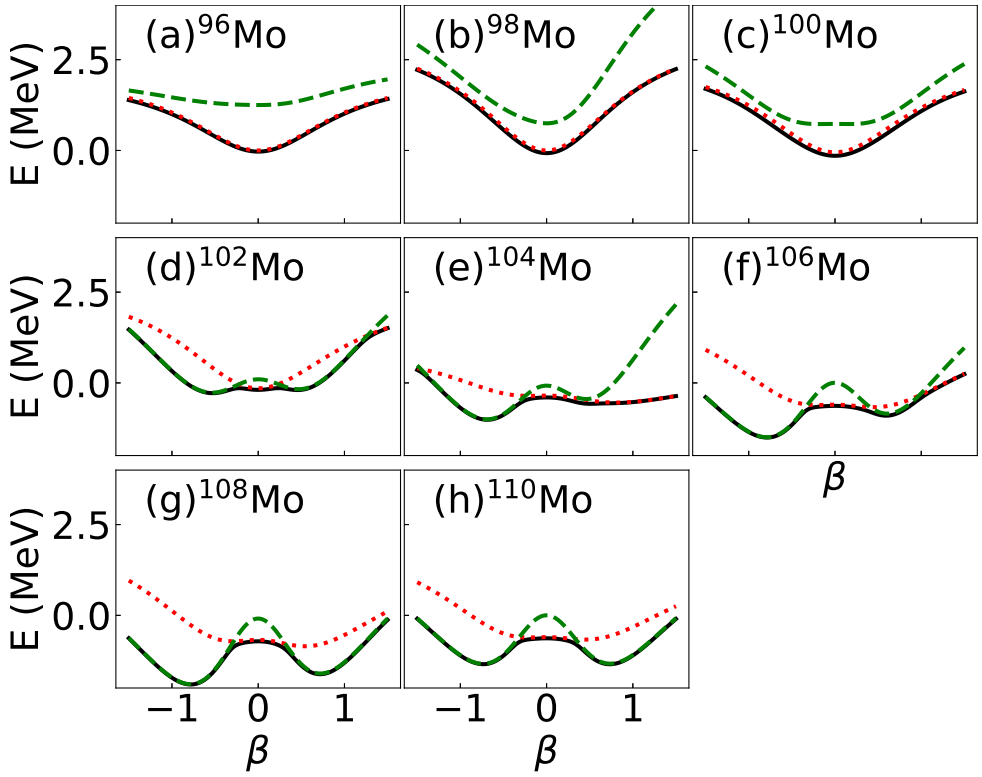

Figure 5.50: Axial symmetry energy for $^{96-110}$Mo, corresponding to the IBM-CM Hamiltonian provided in Table 5.3. The full configuration mixing calculation (full black line) is shown together with the unperturbed calculations for the regular sector (red dotted line) and for the intruder configuration (green dashed line).

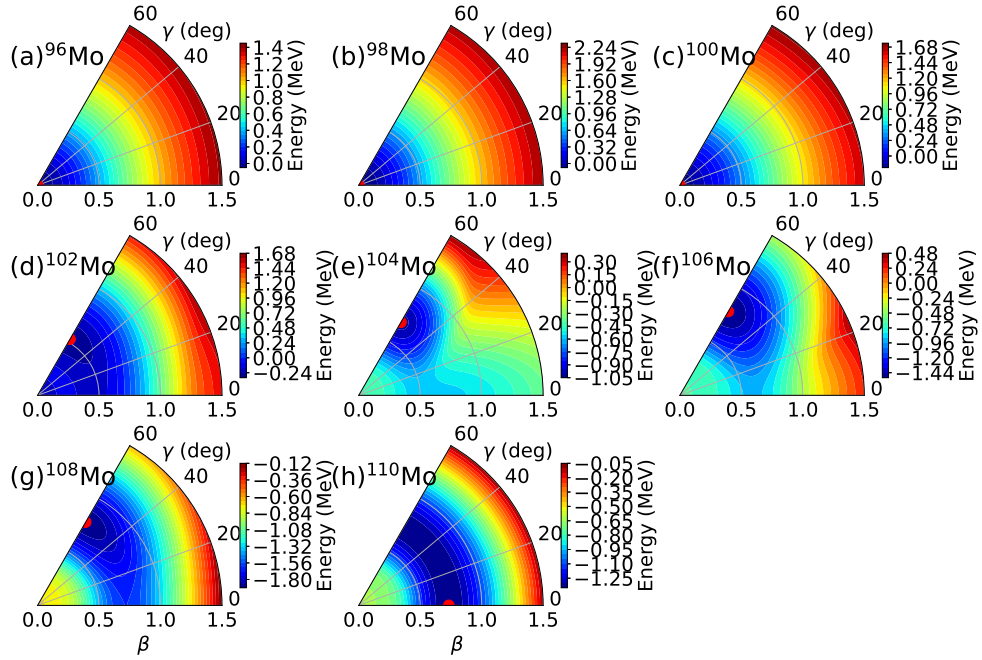

Figure 5.51: Matrix coherent-state calculation in the $\beta - \gamma$ plane for $^{96-110}$Mo, corresponding to the IBM-CM Hamiltonian provided in Table 5.3. The red dot marks the position of the absolute minimum.

spond to the full calculation (IBM-CM) as well as the regular ($[N]$) and intruder ($[N+2]$) configurations, assuming that no interaction exists between the two configurations.

In the present chain of isotopes, the regular configuration is spherical in the range $A = 96 - 102$, transitioning to a prolate shape for $A = 104 - 110$. On the other hand, the intruder configuration is spherical until $A = 100$, but then it rapidly increases its value, becoming oblate. The full calculation exhibits a similar behavior to the intruder configuration, transitioning rapidly from spherical to prolate deformation around $A = 102$. It is worth noting that although the obtained deformation for $A = 110$ is oblate, the potential is almost γ-unstable. Therefore, the sign of β for ^{110}Mo is unimportant. In both configurations, the deformation develops quite rapidly.

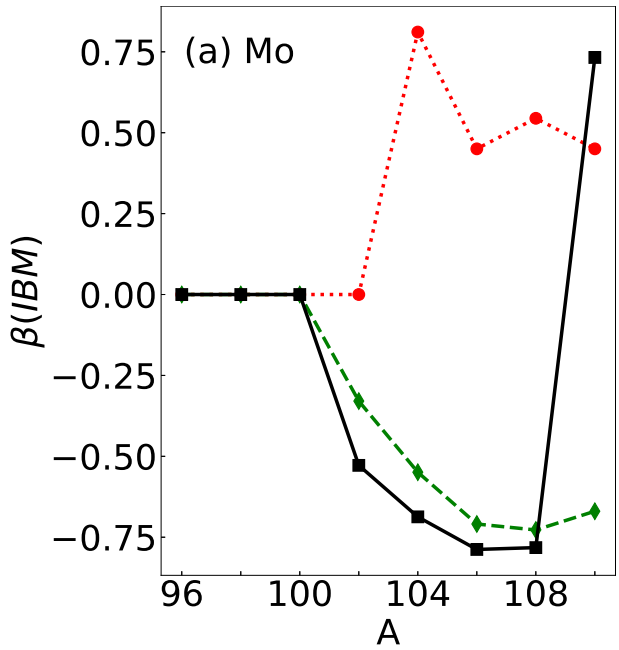

Figure 5.52: Value of β extracted from the IBM-CM energy surface for Mo isotopes. $[N]$, $[N+2]$, and IBM-CM correspond to a pure regular configuration, a pure intruder configuration, and to the complete calculation.

Lastly, we will also calculate the value of the deformation using the quadrupole shape invariants (see equations (5.9)). For doing so, by analyzing measured data from various transitions obtained through Coulomb excitation techniques, it is possible to extract the values of collective model variables, namely β and γ, for a given state. This approach provides valuable experimental insights into the deformation of nuclei.

The theoretical values of β, γ, q^2, and the fraction of wave function belonging to the regular sector, w^k, are presented in Table 5.9 for each 0_1^+, 0_2^+, and 0_3^+ state across the entire chains of Mo isotopes. This table reveals the coexistence of different deformations within the same nucleus, with the regular states typically exhibiting less deformation compared to the intruder states.

Table 5.9: Values of deformation parameters, q^2, β and γ, extracted from the quadrupole shape invariants, together with the value of w^k ([N] content), for Mo isotopes.

State	Iso	q^2 (e^2b^2)	β	γ (deg)	w^k
0_1^+	^{96}Mo	0.28	0.17	48	0.971
0_2^+		1.63	0.42	50	0.158
0_3^+		0.62	0.26	46	0.579
0_1^+	^{98}Mo	0.37	0.20	14	0.881
0_2^+		0.12	0.11	14	0.122
0_3^+		0.49	0.23	0	0.730
0_1^+	^{100}Mo	0.53	0.23	25	0.825
0_2^+		1.22	0.35	31	0.241
0_3^+		0.64	0.26	13	0.763
0_1^+	^{102}Mo	1.16	0.34	26	0.018
0_2^+		1.48	0.39	18	0.968
0_3^+		0.90	0.30	23	0.020
0_1^+	^{104}Mo	1.45	0.38	43	0.013
0_2^+		1.35	0.36	55	0.946
0_3^+		1.01	0.32	44	0.430
0_1^+	^{106}Mo	1.61	0.39	43	0.010
0_2^+		1.16	0.33	30	0.297
0_3^+		0.99	0.31	24	0.694
0_1^+	^{108}Mo	2.23	0.46	36	0.008
0_2^+		1.95	0.43	28	0.016
0_3^+		1.29	0.35	27	0.603
0_1^+	^{110}Mo	1.91	0.42	30	0.013
0_2^+		1.68	0.39	30	0.012
0_3^+		0.96	0.30	21	0.910

In this case, the intruder states generally display a significant oblate deformation that increases with the mass number. However, an exception is observed in ^{98}Mo, where a low deformation is observed. This is consistent with the "collapse" of the B(E2) values observed in its yrast band, possibly related to the closure of the neutron number 56 subshell. The deformation of the first regular state steadily increases until ^{100}Mo, but for ^{102}Mo, there is a sudden increase, and the deformation remains relatively constant for the remaining isotopes. Regarding the value of γ, clear conclusions can only be drawn in a few cases, such as ^{96}Mo and ^{98}Mo, where the states are oblate and prolate, respectively. In other cases, the deformation is compatible with triaxiality.

As a complement to Table 5.9, the trend of the value of β for the first two 0^+ states in Mo and Ru isotopes is depicted in Fig. 5.53, where we can observe that the situation is more complex for the 0_2^+ state. The 0_1^+ state exhibits a rapid increase in β at $A = 102$, rising from 0.23 to 0.34, and then showing a more gradual increase up to the mid-shell region where it reaches its maximum value of 0.42.

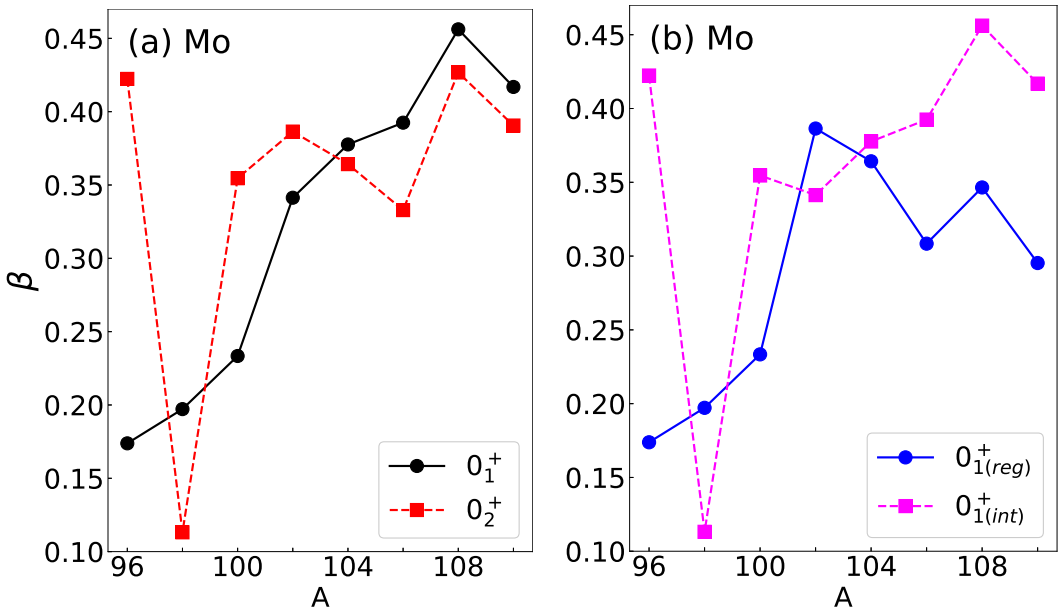

Figure 5.53: Value of the deformation, β, extracted from the value of the quadrupole shape invariants for Mo (panel(a)). Panel (b) is also for Mo but here the β values for the first regular and the first intruder 0^+ states are shown.

In addition, it is also of interest to plot the value of β for the first 0^+ state belonging to the regular sector (0^+reg) and the first 0^+ state belonging to the intruder sector (0^+int) in Mo isotopes, as shown in panel (b) It can be observed that the regular state exhibits a rapid increase in deformation at $A = 102$ and subsequently shows a steady decrease. On the other hand, the intruder state maintains a relatively high and constant value of β, except for the aforementioned exception observed at $A = 98$.

5.9.4 Ru Isotopes

In Fig. 5.54, the axial energy surfaces for Ru isotopes are shown and the full $\beta - \gamma$ plane energy surfaces are displayed in Fig. 5.55. In the axial case (Fig. 5.54), both the unperturbed and full calculations are presented. It is noteworthy that the intruder configuration remains well separated from the regular configuration throughout, and this is consistent with the full calculation. The nuclei start out as spherical but gradually evolve into flatter shapes, reaching full flatness at ^{104}Ru. Subsequently, they transform into γ-unstable shapes, with the deepest minimum occurring at ^{110}Ru.

When examining the energy surfaces in the $\beta-\gamma$ plane (Fig. 5.55), similar conclusions can be drawn. The flattest energy surface is observed at ^{104}Ru, which serves as a boundary between the spherical and γ-unstable shapes. In a previous study [91], it was found that the lightest Ru isotopes exhibit a slightly prolate shape, while a very shallow triaxial minimum is observed in $^{104-106}$Ru. In $^{108-114}$Ru, oblate minima are obtained, albeit with a very flat γ direction, and in certain cases, they become almost triaxial.

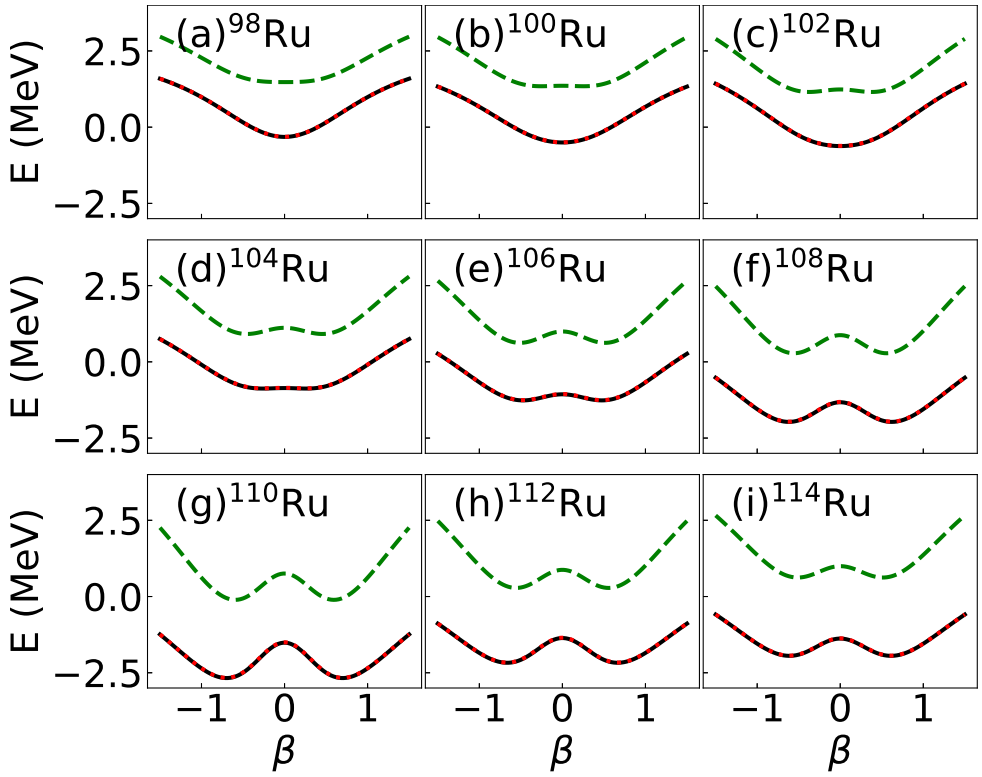

Figure 5.54: Same as Fig. 5.50 but for $^{98-114}$Ru and Table 5.4.

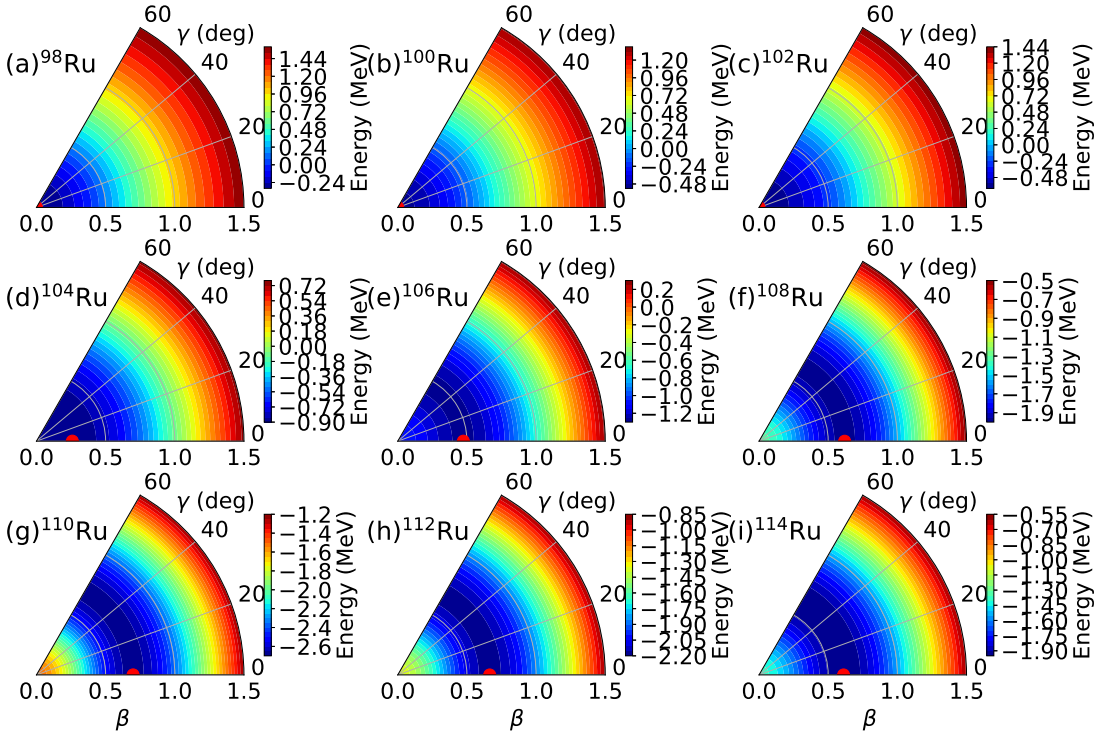

Figure 5.55: Same as Fig. 5.51 but for $^{98-114}$Ru and Table 5.4.

Here again we represent the β corresponding to the minimum in the energy functional (indicated again with red dots in Figs. 5.55). It is also convenient to remember that positive values corresponds to prolate shapes while negative to oblate. Fig. 5.56 illustrates the

IBM β values the isotopes considered in this section, with values corresponding to the full calculation (IBM-CM) as well as the regular ($[N]$) and intruder ($[N+2]$) configurations, assuming no interaction exists between the two configurations.

Here, in the case of Ru isotopes, the regular configuration, as well as the full calculation, corresponds to spherical shapes for $^{98-102}$Ru. However, they undergo a sudden transition to γ-unstable deformation for $^{104-114}$Ru, with the maximum deformation occurring at the mid-shell. The intruder configuration exhibits a similar behavior, but it is important to remember that the intruder Hamiltonian remains fixed throughout the entire isotope chain.

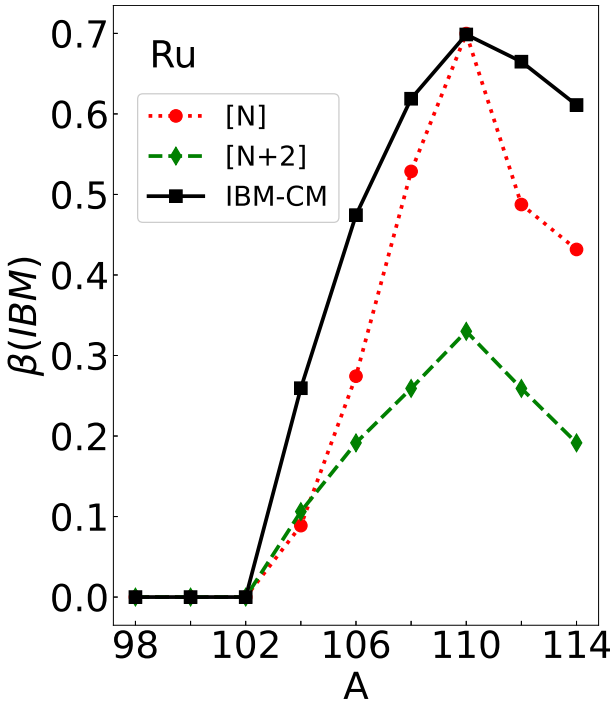

Figure 5.56: Value of β extracted from the IBM-CM energy surface for Ru isotopes. $[N]$, $[N+2]$, and IBM-CM correspond to a pure regular configuration, a pure intruder configuration, and to the complete calculation.

Lastly, we will also calculate the value of the deformation using the quadrupole shape invariants from equations (5.9). Where again, analyzing measured data from various transitions obtained through Coulomb excitation techniques, the values of collective model variables, namely β and γ, for a given state are extracted. In this way, the theoretical values of β, γ, q^2, and the fraction of wave function belonging to the regular sector, w^k, are presented in Table 5.10 for each 0_1^+, 0_2^+, and 0_3^+ state across the entire chains of Ru isotopes, where a situation relatively straightforward is observed, with a steady increase in deformation for the regular states, with a fixed γ value of 30 degrees throughout. Only in two cases are intruder states observed, exhibiting a large deformation.

Finally, as a complement to Table 5.10, the trend of the value of β for the first two

Table 5.10: Values of deformation parameters, q^2, β and γ, extracted from the quadrupole shape invariants, together with the value of w^k ([N] content), for Ru isotopes.

State	Iso	q^2 (e^2b^2)	β	γ (deg)	w^k
0_1^+	^{98}Ru	0.40	0.20	30	0.997
0_2^+		0.35	0.18	30	0.988
0_3^+		2.05	0.45	30	0.012
0_1^+	^{100}Ru	0.50	0.22	30	0.996
0_2^+		0.40	0.19	30	0.995
0_3^+		2.76	0.51	30	0.006
0_1^+	^{102}Ru	0.64	0.24	30	0.994
0_2^+		0.54	0.22	30	0.992
0_3^+		3.60	0.57	30	0.010
0_1^+	^{104}Ru	0.84	0.27	30	0.994
0_2^+		0.56	0.22	30	0.996
0_3^+		0.73	0.26	30	0.996
0_1^+	^{106}Ru	1.00	0.29	30	0.994
0_2^+		0.62	0.23	30	0.995
0_3^+		0.86	0.27	30	0.996
0_1^+	^{108}Ru	0.96	0.29	30	0.995
0_2^+		0.83	0.27	30	0.997
0_3^+		0.61	0.23	30	0.995
0_1^+	^{110}Ru	1.05	0.30	30	0.996
0_2^+		0.92	0.28	30	0.997
0_3^+		0.71	0.24	30	0.995
0_1^+	^{112}Ru	1.14	0.30	30	0.996
0_2^+		0.97	0.28	30	0.998
0_3^+		0.73	0.24	30	0.996
0_1^+	^{114}Ru	0.98	0.28	30	0.997
0_2^+		0.82	0.25	30	0.998
0_3^+		0.60	0.22	30	0.997

0^+ states in Ru isotopes is depicted in Fig. 5.57. Here again, a relatively straightforward behavior can be observed, with a constant increase in β up to around the mid-shell region, reaching a value of approximately 0.30, similar to the one shown in Fig. 5.56, concluding that both states belong to the regular sector.

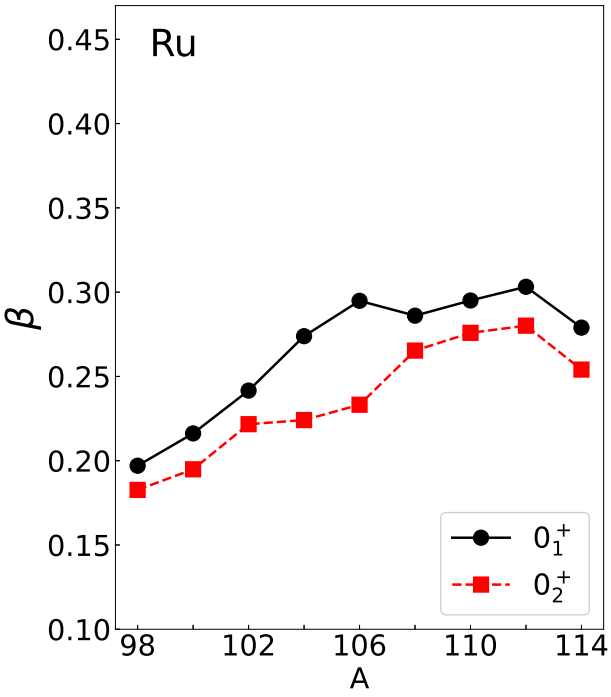

Figure 5.57: Value of the deformation, β, extracted from the value of the quadrupole shape invariants for Ru (panel (b)). Panel (c) is also for Mo but here the β values for the first regular and the first intruder 0^+ states are shown.

5.9.5 Direct Comparison of the β Parameter

To finish the analysis of the deformation in this mass area, we will present information about the quadrupole deformation, β, extracting it from a known B(E2) value as,

$$\beta = \frac{4\pi\sqrt{B(E2 : I_i \rightarrow I_f)}}{3\langle I_i 020|I_f 0\rangle ZeR_0^2}, \tag{5.13}$$

where $R_0 = 1.2A^{1/3}$ fm and $\langle ....|..\rangle$ is the Clebsch-Gordan coefficient and for the case of the yrast band we use $I_i = 2$ and $I_f = 0$.

In Fig. 5.58, we depict the extracted values of the deformation parameter, β, for the ground state bands in the four isotopic chains. It is evident that these chains exhibit distinct and contrasting systematics. In the cases of Sr and Zr, there is a clear and rapid onset of deformation at neutron number N=60. For Mo, the increase in deformation is more gradual. In the case of Ru, the value of β remains nearly constant. In the instances of Sr and Zr, the sudden increase in deformation arises from the crossing of regular and intruder

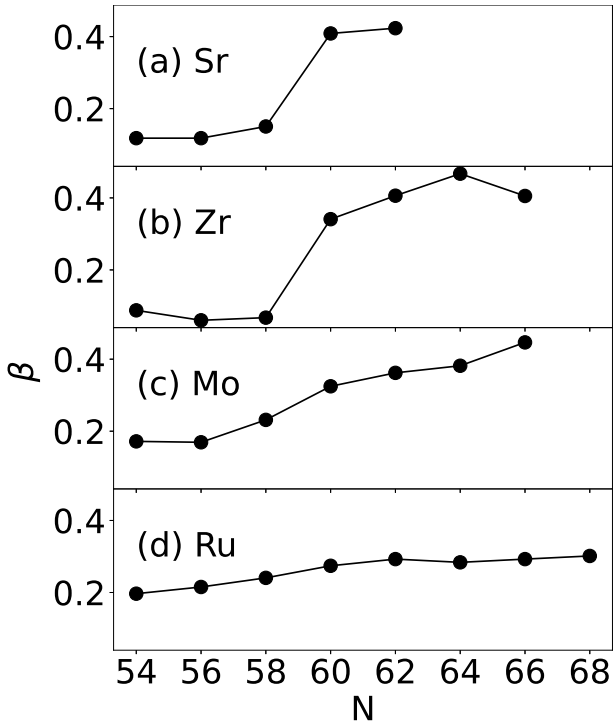

Figure 5.58: Value of the deformation parameter, β, for the ground state band in Sr, Zr, Mo, and Ru isotopes extracted from $B(E2 : 2_1^+ \rightarrow 0_1^+)$ as a function of the neutron number.

configurations, as previously shown in Fig. 5.2. Notably, the intruder configuration has a significantly larger deformation, contributing to the rapid change in β. However, in the case of Mo, although the crossing of regular and intruder configurations exists, the strong interaction between these configurations effectively smooths out the variation in β [37]. This smoothing effect has also been observed in Pt [143]. These observations are further corroborated by the systematics of the two-neutron separation energy [88, 36, 37]. In the language of QPTs, Sr and Zr exhibit a first order Type II QPT, as seen in the behavior of β [35, 110]. Similarly, Mo showcases a second order Type II QPT. In contrast, Ru provides ample evidence of a second-order QPT of Type I [37].

5.10 Shape Coexistence and Quantum Phase Transitions: Faces of a Single Phenomenon?

Shape coexistence in nuclear physics was first proposed by Morinaga in the 1950's [23] and considered as limited to very limited areas, but nowadays becomes a concept that appears throughout the entire nuclear landscape, especially in those nuclei at or near shell or subshell closures [30]. Shape coexistence presents certain key experimental features: an U shape pattern in the energy systematics of a set of states, the lowering of certain excited 0^+ states (intruder states), a rapid change in the value of the spectroscopic quadrupole

moments, and the existence of strong E0 transitions. All of them show an almost symmetric trend with respect to the corresponding mid-shell and they are enhanced at this place.

Shape coexistence can be understood in terms of two well-known theoretical approaches: the spherical shell model and the mean field. According to the shell model approach, the intruder configurations correspond to the promotion of pairs of nucleons across the shell or subshell gap closures. The other major approach is the mean-field theory where, roughly speaking, one obtains an energy surface depending on certain deformation parameters. In this landscape, the ground band will correspond to the deepest minimum (regular states), but the other local minima can be interpreted as intruder configurations, each of them owning to different deformations.

The concept of QPT [38] implies the sudden change of the ground state structure of the system as a function of a control parameter. Such a control parameter can be in the case of the atomic nucleus, e.g., the neutron number. Therefore, a QPT can appear in an isotopic chain where the ground state deformation varies in an abrupt way when passing from isotope to isotope. Of course, the latter should be considered as an approximation because a control parameter should be, strictly speaking, continuous. A QPT is characterized by the discontinuity of some derivative of the system energy. Assuming that the two-neutron separation energy (S_{2n}) is somehow proportional to the derivative of the energy with respect to the neutron number, a first-order QPT involves a discontinuity in S_{2n}, while a second-order one a discontinuity in the derivative of S_{2n}. The even-even Sr isotope chain, as will be shown along the text, corresponds to the case of a first-order QPT.

An ideal framework to deal with QPTs is the IBM [11] which is a paradigmatic example of a nuclear algebraic model. In that framework, a QPT can be understood considering a Hamiltonian that is a combination of two given symmetries, combined through a control parameter, $H = x\ H_{\mathrm{sym1}} + (1 - x)\ H_{\mathrm{sym2}}$ that allows to go from one to the other limit. The presence of a QPT is revealed by the existence of a critical value of the control parameter, x_c, for which the underlying structure of the system (phase) passes from symmetry 1 to symmetry 2.

We know that the IBM can be also used to deal with shape coexistence, allowing to define a framework where different particle-hole excitations are present in the spectrum. The formalism is known as IBM with configuration mixing, IBM-CM in short [31, 65].

When questioning the connection between QPTs and shape coexistence, first, one should note several similarities, namely, both phenomena involve a rapid change in the structure of certain set of states, either ground or excited states and, in both cases, at the mean-field level, several minima coexist. In the case of shape coexistence, the regular and the intruder configurations can be thought as having independent energy surfaces that interact

among them, especially when their minima are close in energy, while under a QPT a single energy surface exists where two or more minima are present. The evolution of the relative position of the minima as a function of the neutron number is at the origin of the change of the nuclear deformation and it can be understood in terms of either shape coexistence or a QPT. On the other hand, from a quantum point of view clear differences should exist between both approaches. The most obvious one is the existence of a larger Hilbert space when two configurations are present, because of the extra nucleons that occupy the single particle levels. This extra set of levels presents a different energy systematics than the regular one because for them the effective nuclear interaction is different. Moreover, the intruder configuration is expected to be found at low energy when the number of valence nucleons is large, i.e. around mid shell, therefore a parabolic-like energy systematics for the intruder states appears frequently. However, the situation can be blurred due to the interaction between intruder and regular configurations or because their crossing [150]. When a QPT exist without the presence of multiple particle-hole excitations, a larger density of states can be also observed at low energy as for configuration mixing, but it never happens around mid-shell [96].

5.10.1 Sr and Zr Isotopes Versus Pt and Hg Nuclei

The regions around the sub-shell closure Z = 40 are, together with the area around Z = 82, two of the best examples of shape coexistence in nuclei. In Hg and Pt nuclei, two types of configurations show up with a clear presence of low lying 0^+ states, combined with a parabolic-like shape in the spectra of Hg, whereas this behavior is not so obvious in Pt. On the other hand, Zr and Sr are known to exhibit the faster change in deformation in an isotope chain at N = 60, with two particle-hole configuration coexisting and crossing at this point.

From the point of view of a QPT, there are two key observables that can be used as indicators of its presence, namely, the two-neutron separation energy, S_{2n}, that will experience a discontinuity at a first-order transition point and the ratio $E(4_1^+)/E(2_1^+)$ which provides a hint for the appearance of deformation or, in a qualitative way, it is connected with the order parameter of the QPT. In Fig. 5.59, we present the systematics of S_{2n} and $E(4_1^+)/E(2_1^+)$, for Sr and Zr, on the one hand and, for Pt and Hg, on the other. Regarding the value of S_{2n}, one notices a clear change of slope in Sr and Zr, but a fully linear behavior in Hg and Pt. On the other hand, $E(4_1^+)/E(2_1^+)$ shows for Sr and Zr the typical rapid change that is expected in a QPT, passing from a value close to 2 (even 1.5 for $^{96-98}$Zr) to another close to 3.3. However, in Pt and Hg the interpretation of the systematics is not so evident and the physics involved in these cases seems to be quite different from the one of Sr and Zr.

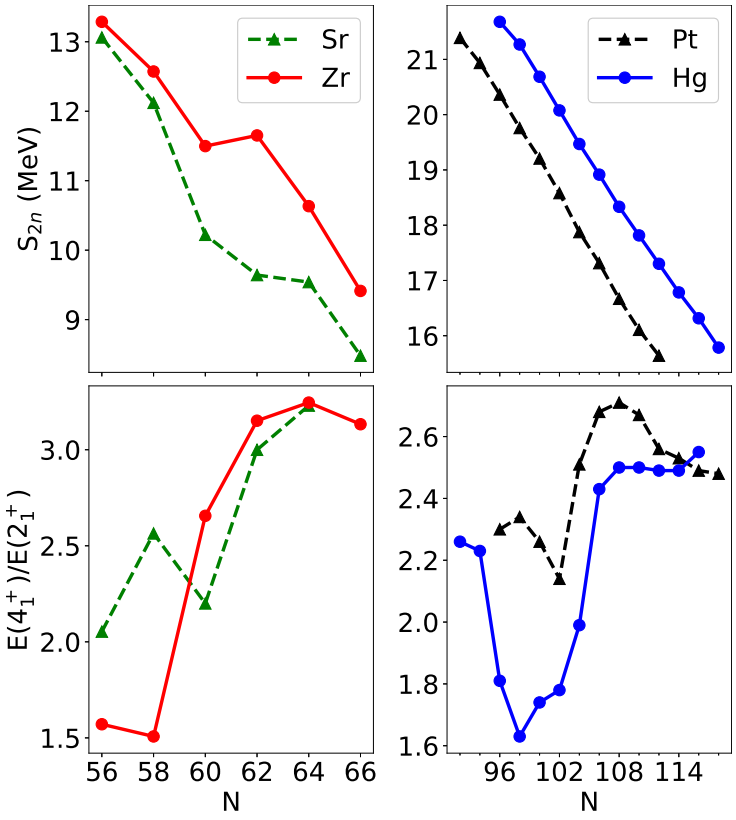

Figure 5.59: Experimental vales of S_{2n} and $E(4_1^+)/E(2_1^+)$ as a function of the neutron number, N, for Sr, Zr, Pt and Hg isotopes.

To have a more clear view of the analogies and differences between both situations, we present in Fig. 5.60 some relevant IBM calculations based on [36] for Sr, [96] for Zr, [143] for Pt, and [144] for Hg. In particular, the results correspond to the value of the IBM deformation parameter β for the regular ([N]), the intruder configuration ([N+2]) and the complete system (IBM-CM) (panels a), c), e), and g)). Moreover, the unperturbed energy for the lowest regular, intruder, and ground state (IBM-CM) are depicted in panels b), d), f), and h). Concerning Sr and Zr, the distinctive feature is the crossing of the regular and the intruder configurations at A = 98 and 100, respectively, corresponding to N = 60, inducing a change in the slope of the ground state energy and also a rapid onset of deformation, which has a dramatic effect on the trend of the radii [88, 36]. In the case of Pt and Hg, both configurations remain quite close, without crossing in the case of Hg, and crossing before and after the mid-shell (N = 104) in the case of Pt. The ground state energy is hardly modified, but the deformation parameter β passed from the less deformed configuration (the regular one) to the most deformed one (the intruder one) around mid-shell. The crossing or the close approaching of regular and intruder configurations in Pt and Hg, respectively, have also a noticeable influence in the radii of these nuclei, as shown in [150, 144]. In summary, in Sr, Zr and Pt nuclei, a intruder state becomes the ground state when approaching the mid-shell, while it never happens in Hg.

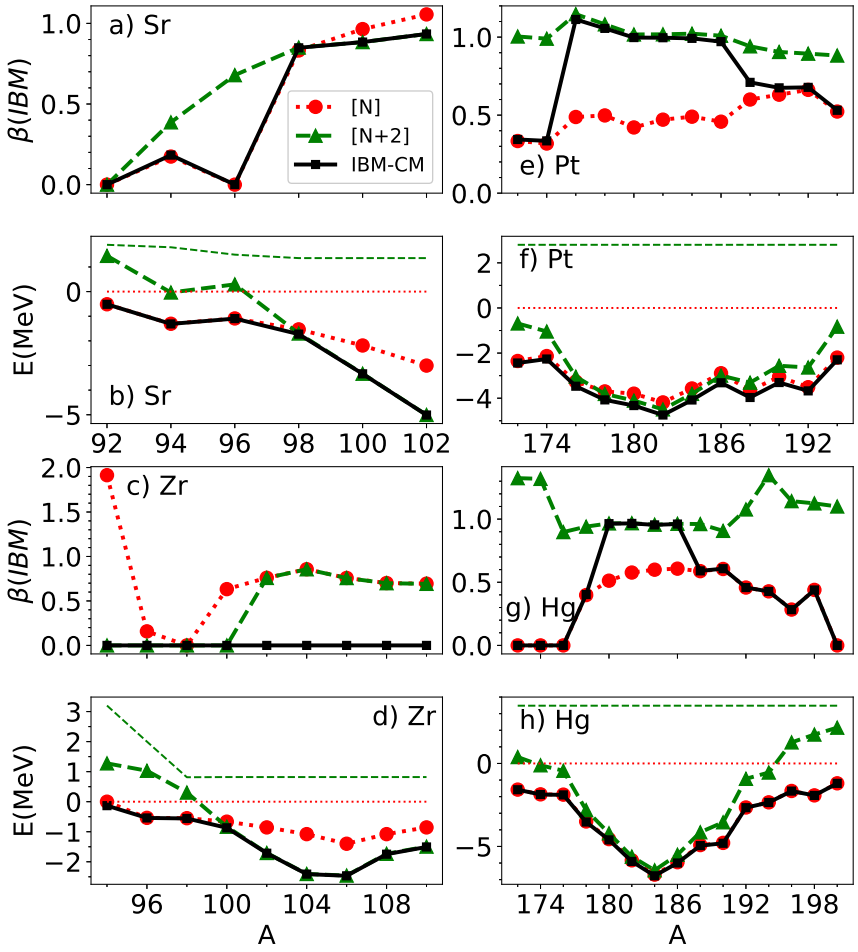

Figure 5.60: a), c), e), and g) panels: IBM value of β for the unperturbed regular, $[N]$, and intruder configurations, $[N+2]$, and full calculation, IBM-CM. b), d), f), and h) panels: ground state energy for the unperturbed regular and the intruder configurations and for the full calculation. The green thin dashed line stands for the energy needed to create a particle-hole excitation and the red thin dotted one stands for the reference level.

Note that in Pt, due to the strong mixing between both configurations [143], no dramatic effect are observed in the spectra, although the energy crossing exists.

The above features have direct consequences in the systematics of S_{2n} and $E(4_1^+)/E(2_1^+)$. In the case of Sr and Zr, what it is observed in Fig. 5.59 can be easily understood in terms of the crossing of configurations. Indeed, the change in the nature of the ground state produces a sudden change in the slope of the energy systematics and therefore a discontinuity in the value of S_{2n}. On the other hand, because the crossing is so fast, not only the ground state presents an intruder character, but also the rest of low-lying members of the yrast band involved in the energy ratio $E(4_1^+)/E(2_1^+)$, which makes that for $N < 60$ all the states present a vibrational character, while for $N \geq 60$ a rotational one appears. On the other hand, in the case of Hg, because the ground state presents all the way a regular character and, moreover, there is no interaction between intruder and regular sector, it can be understood the linear tendency of the S_{2n} even at the mid-shell.

Besides, the crossing between 2_1^+ and 4_1^+ regular and intruder states can explain the drop of the ratio $E(4_1^+)/E(2_1^+)$ around the mid-shell. Finally, to explain the systematics of Pt in Fig.5.59 is a challenge. First, the crossing of regular and intruder 0^+ energies would suggest a discontinuity in S_{2n} as the observed one in Sr and Zr. However, experimental values show a fully linear systematics. The reason for such a behavior is the strong mixing between the regular and the intruder sectors (see [143]). Note that according to [155] and Fig. 5.60, the deformation changes as it should be in a QPT, however the strong mixing somehow hides its effect in both the S_{2n} and $E(4_1^+)/E(2_1^+)$ observables.

Chapter 6

Structure and shape evolution in odd–even nuclei: an intrinsic-frame approach

The region around N=60 and Z=40 is highly known for the sudden appearance of deformation. As discussed previously in this thesis for even-even nuclei, this fact was nicely explained in terms of the simultaneous occupation of neutrons and protons of spin-orbit partners, namely $1g_{9/2}$ for protons and $1g_{7/2}$ for neutrons, leading to proton 2p-2h excitations highly favored thanks to the spin-orbit partner interaction, this has been also explained more recently in [163] in terms of the nuclear tensor interaction.

While these mechanisms were introduced in the context of even-even isotopes, they also provide the underlying framework to understand the behavior of odd-even nuclei in this region [164]. As in the even-even case, nuclear deformation in odd-even nuclei is not a direct observable. However, its presence can be inferred from experimental quantities that are sensitive to changes in the nuclear shape.

In particular, the systematics of the mean-square charge radii can provide a hint of deformation effects. Moreover, odd-even nuclei are expected to display a distinct behavior when compared to the even-even isotopes. For this reason, in order to study the specific effects associated with the unpaired nucleon, the experimental radii are presented separately for isotopes with an even and an odd number of neutrons, as shown in Fig. 6.1.

More information can be obtained from the two-neutron separation energies S_{2n} in Fig. 6.2, which are also indicator of structural changes along an isotopic chain. In this way, it is expected that odd-even and even-even nuclei will behave distinctly, being the changes in this parameter even larger for odd-even isotopes.

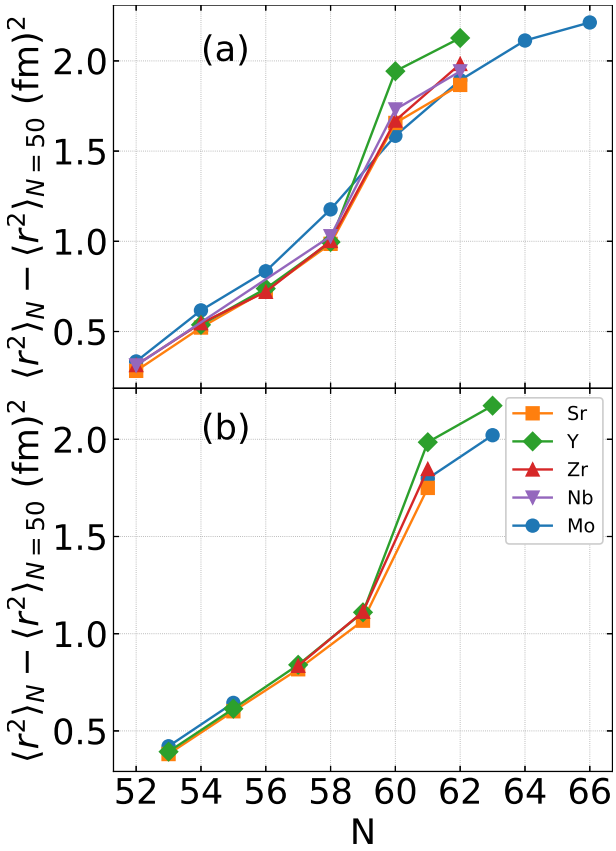

Figure 6.1: Experimental mean-square radii for Sr, Y, Zr, Nb, and Mo isotopes as a function of the neutron number. a) Even number of neutrons. b) Odd number of neutrons.

In order to expose these expected differences between odd-even and even nuclei, we present a comparison in Fig. 6.1, of the experimental mean-square radii for Sr, Y, Zr, Nb, and Mo are presented. In the case of even number of neutrons, corresponding with panel a), it is clearly remarkable the change in N=60, where there is a sudden increase in the radius. This is, that is noticeable in Sr and Zr isotopes (which also have an even proton number) is specially abrupt in Y and Nb (with an odd proton number). Finally, in Mo a smooth trend is observed, which is not due to the presence of an odd or even number of nucleons, but marks the end of the area of the onset of deformation [37]. When moving into the odd neutron number case, panel b), one observes a remarkable resemblance with the even case, with a rapid increase of the radius at N=60. Note that in the case of Y and Nb the nuclei are odd-odd and that for Mo there is no data for the central area. In summary, there are not huge differences between the even and the odd neutron number cases regarding the radius.

In Fig. 6.2, the S_{2n} is depicted, separating, once more, the cases of even and odd neutron numbers. In both panels, one can easily note a sudden change in the slope of S_{2n} at N=60, being much more abrupt in the case of odd neutron number (panel b)). In addition, it is interesting to notice that, even in the case of Mo, it is observed the flattening of the

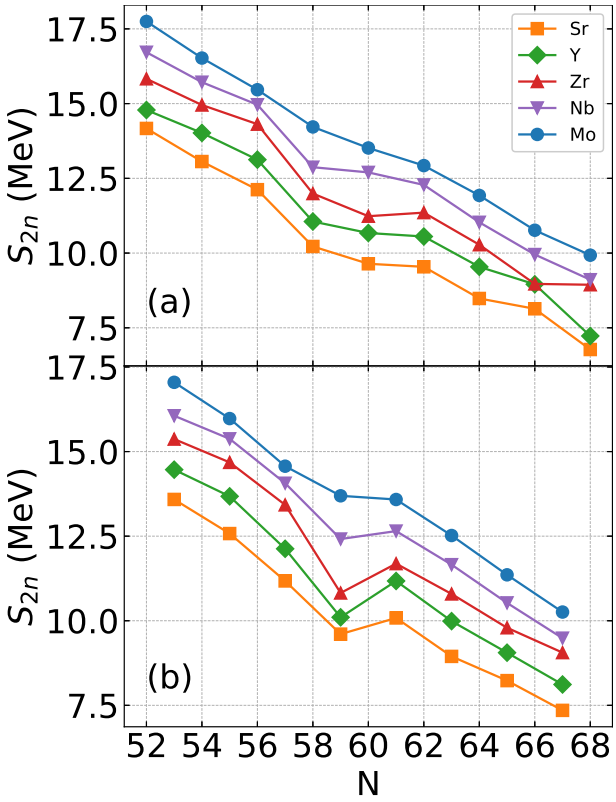

Figure 6.2: Experimental S_{2n} for Sr, Y, Zr, Nb, and Mo isotopes as a function of the neutron number. a) Even number of neutrons. b) Odd number of neutrons.

slope at N=60 for odd neutron number. In general, no differences are observed between the even and odd proton cases.

Hence, the onset of deformation in this area is a little more strong in the odd neutron case. Note that this is similar in Y and Nb isotopes that are also odd in the proton number. In other words, nuclei with either even or odd neutron number behave similarly regardless their proton character. This suggests that in this mass region the fastest changes appear for odd number of neutrons.

It is worth mentioning that this behavior observed in S_{2n} is also connected with the existence of a QPT [72], either of type I or Type II [35].

6.1 Application to a Crossing of Configurations

As we introduced previously in Section 4.11, the new intrinsic state formalism presented in this thesis introduces many advantages, as it allows incorporating all the three different components of the boson-fermion interaction, multiple j values, the triaxial degree of freedom and also considering configuration mixing.

To test the formalism, we choose in the first place as an illustrative application of the

formalism, a scenario inspired by Ref. [165], in which spherical and deformed configurations coexist in even-even Pt isotopes [81]. We focus on a hypothetical chain of even-even nuclei extending from $A = 172$ to $A = 192$, with the mid-shell located at $A = 182$.

For the regular part of the Hamiltonian, we fix $\varepsilon^N = 1$ MeV, while all remaining regular parameters are set to zero. In the intruder configuration, the parameters are chosen as $\kappa^{N+2} = -0.044$ MeV and $\chi^{N+2} = -\sqrt{7}/2$, with the rest of the intruder parameters also taken to be zero. The mixing interaction between both configurations is characterized by $\omega = 0.15$ MeV, and the energy offset of the intruder configuration is set to $\Delta^{N+2} = 14.2$ MeV.

With this parametrization, the regular configuration corresponds to the vibrational U(5) limit, whereas the intruder configuration presents a rotational SU(3) character. For our analysis the number of bosons is assumed to evolve along the isotopic chain, increasing from $N = 8$ to $N = 13$ at mid-shell and then decreasing back to $N = 8$ toward the end of the chain. In addition, we assign $N = 8$ to $A = 172$, $N = 13$ to the mid-shell nucleus at $A = 182$, and again $N = 8$ to $A = 192$. We illustrate the evolution of this bosonic part in Fig. 6.3, where we present the evolution of the energy, and the deformation parameters β and γ before adding the contribution of the fermion.

Thus, the value of Δ^{N+2} is deliberately chosen to induce a crossing between the U(5) regular configuration and the SU(3) intruder configuration in the region between $A = 176$ and $A = 178$, corresponding to $N = 10$ and $N = 11$ as is clearly illustrated in Fig. 6.3.

As a consequence of this configuration crossing, a Type II QPT emerges in this region (see Section 6.2), consistently with the behavior observed in Fig. 6.5a.

Moreover, it is useful to show the axial energy curves for this very schematic case. As will be seen, although the inclusion of a fermion clearly modifies these curves, the evolution of the nuclear shapes is still largely governed by the bosonic core. In this way, we present in Fig. 6.4 the evolution of the axial energy curves of the schematic Pt isotopes considered, separating the regular an the intruder part for an easier understanding of the total contribution of the bosonic core.

To illustrate the effect of adding one fermion, Fig. 6.5 shows the case where the fermion can occupy the $j = \frac{5}{2}, \frac{3}{2}$, or $\frac{1}{2}$ orbitals, where panel (a) displays the single-particle energies, and panels (b) and (c) show the corresponding equilibrium values of β and γ, respectively.

Here, we introduce a specific case involving two configurations, and although, many dif-

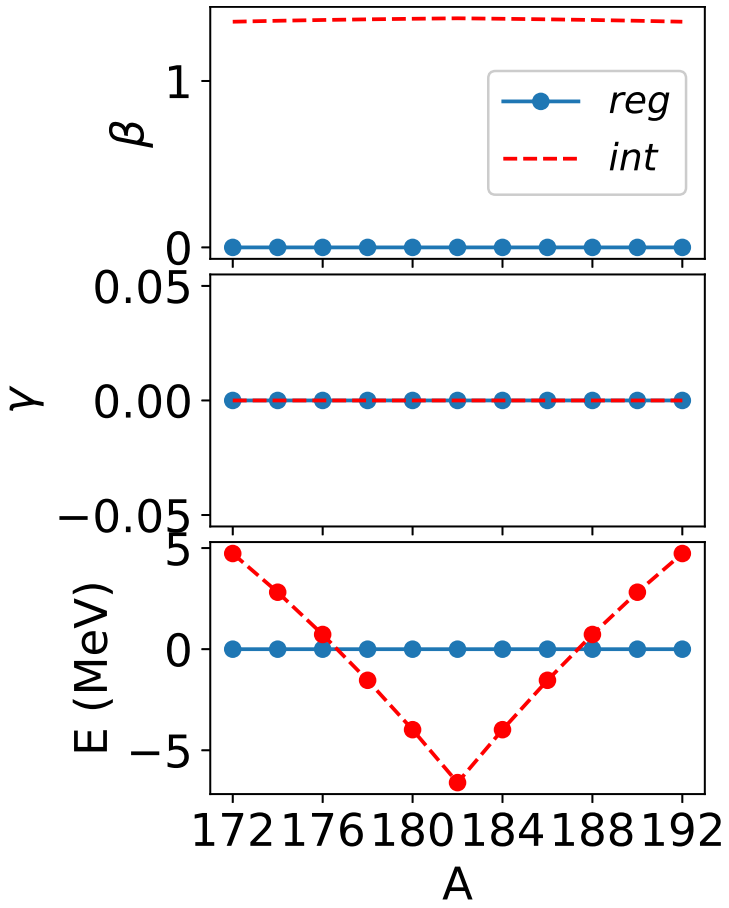

Figure 6.3: Schematic representation of the crossing of a regular U(5) vibrational limit with an intruder SU(3) rotational limit. Deformation parameters β, γ and the corresponding energies are included

ferent sets of parameters have been tested, we begin with the following set,

$$\begin{aligned} \epsilon_j^N &= \epsilon_j^{N+2} = 0\,\text{MeV}, \\ A_0^N &= A_0^{N+2} = 1.0\,\text{MeV}, \\ \Gamma_0^N &= \Gamma_0^{N+2} = -5.0\,\text{MeV}, \\ \Lambda_0^N &= \Lambda_0^{N+2} = 1.0\,\text{MeV}, \\ \chi^N &= -\chi^{N+2} = \sqrt{7}/2, \end{aligned} \tag{6.1}$$

Note that we closely follow the microscopic interpretation of the IBFM proposed in [79] that has been presented earlier, in which for our schematic calculation, we impose $v_j = v$ ($v^2 + u^2 = 1$), with $N_p = \sum_j (2j+1)v_j^2$ and $N_p = 7$.

Moreover, considering that we are working with even-even Pt isotopes as basis, the odd fermion added to the system will be a proton hole, hence, the hypothetical isotope chain correspond to Ir and therefore a unit should be subtracted to A.

It is important to notice that in Fig. 6.5a, 12 levels appear, although they are doubly

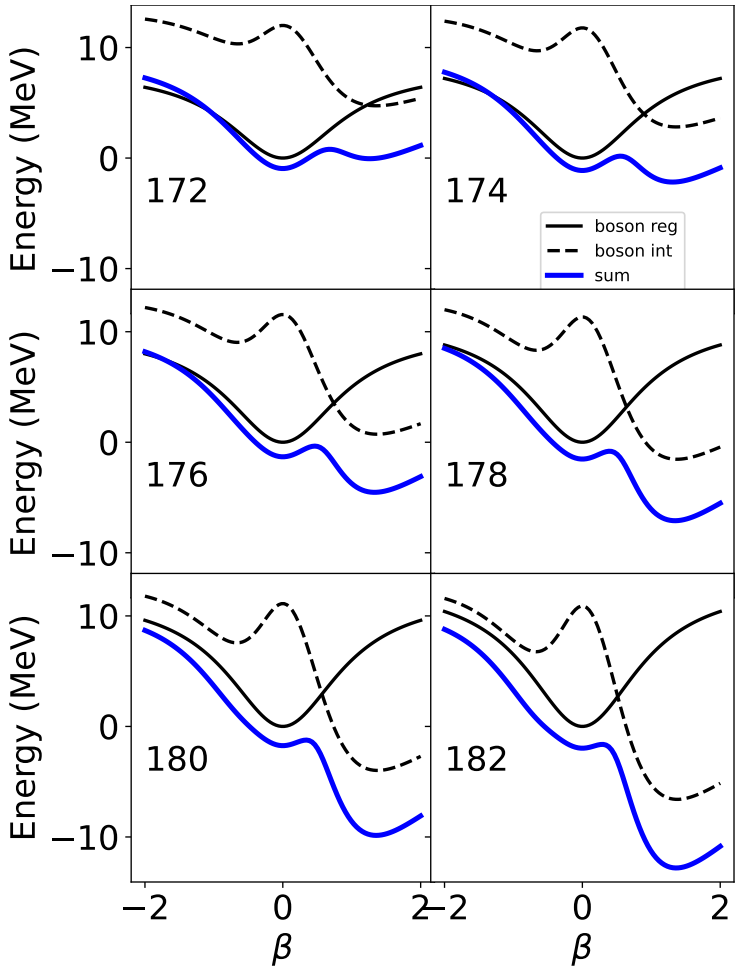

Figure 6.4: Axial energy curves corresponding to the crossing of U(5) and SU(3) configurations

degenerated, and as we have not imposed the condition of axial symmetry, different colors represent just the order of the levels. Each energy level corresponds to a distinct equilibrium value of β and γ; therefore, different states can exhibit different shapes or degrees of deformation. The key observation in the trend is that only the lowest energy level undergoes a transition from a regular (approximately spherical) to an intruder (more deformed) configuration. In contrast, the other low-lying states maintain a predominantly spherical character throughout. Additionally, the six higher-lying states (represented by dashed lines) are primarily associated with the intruder configuration and exhibit a prolate deformation.

The equilibrium deformation values and the corresponding energies in Fig. 6.5 alone do not fully capture the complexity of the energy surface topology. Therefore, in Fig. 6.6, we present the axial fermion energy curves across the entire isotope chain, alongside the unperturbed boson energy curves used as a reference (note that the second half of the shell is symmetric with respect to the first).

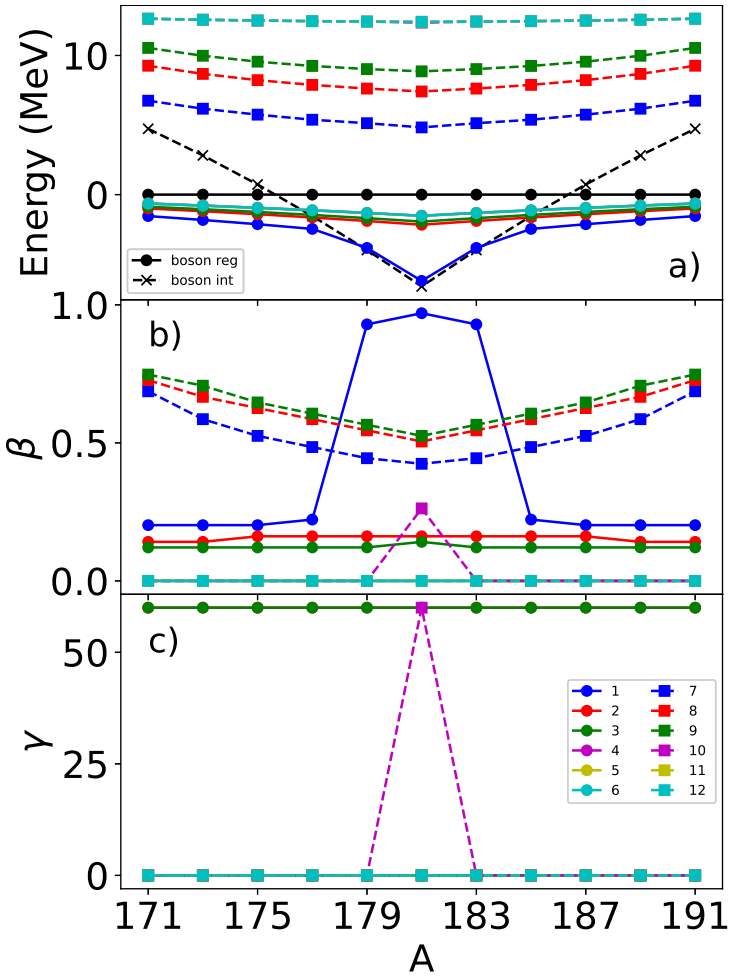

Figure 6.5: Equilibrium value of energies and β and γ deformation parameters for the schematic isotope chain. a) Unperturbed boson energies (black lines) and fermion energies of the different orbits. b) Equilibrium value of β for the fermion orbits. c) Equilibrium value of γ for the fermion orbits. Full lines with full circles for the six lower levels, dashed lines with full squares for the six upper ones. Colors stand to distinguish the order of the levels.

One of the main difference with the single particle energies represented before is that here, the levels are labeled with the K quantum number, which is actually preserved for the case of $\gamma = 0$. By construction, regarding the schematic case that we have chosen, the regular states exhibit a spherical shape, while the intruder states are associated with more deformed shapes. The deformation observed in the lower states arises from the lowering of the intruder levels toward mid-shell, as well as from the interaction between the regular and intruder configurations. It is also quite interesting to notice that, secondary minima appear in several of the energy curves, which can become nearly degenerate and may even exchange order as we move along the isotope chain.

In order to obtain a more complete picture of the evolution of the single-particle levels, it is convenient to analyze the behavior of the energy surface in the β-γ plane. In this context, we detail the evolution of the energy surface corresponding with the lowest energy

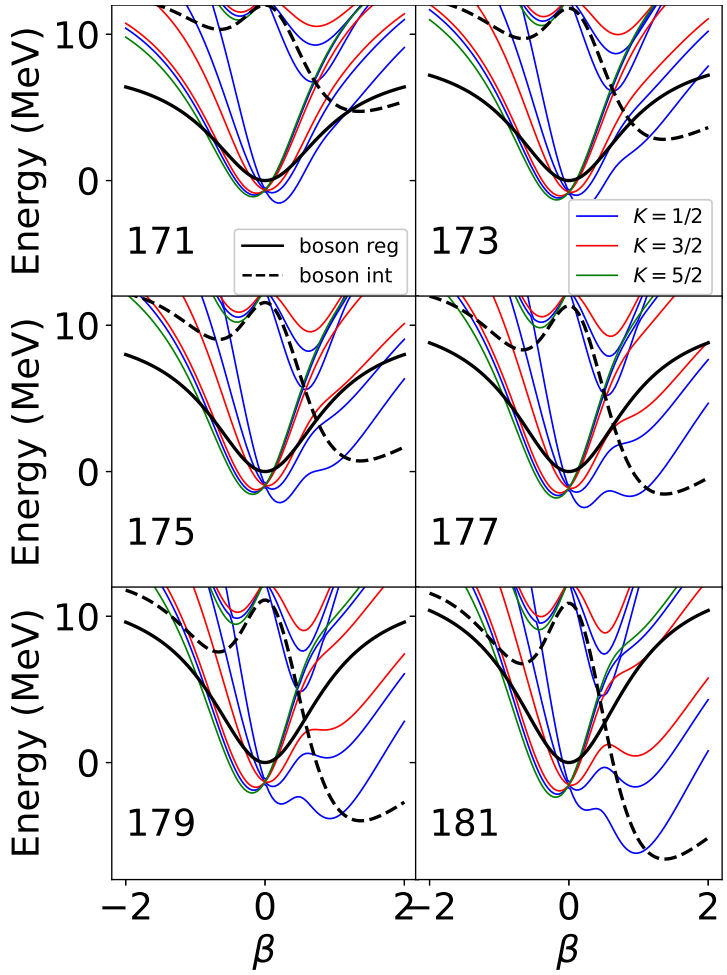

Figure 6.6: Axial energy curves for the fermion orbits over the isotope chain. The fermion lines are marked with its K value. The thick black lines correspond to the unperturbed boson energy curves, full for the regular and dashed lines for the intruder configuration.

value obtained after performing the complete calculation, in Fig. 6.7. The results indicate a smooth structural evolution, starting from a spherical configuration in nuclei with $A =$ 171-173 and gradually evolving to present a more clearly deformed shapes for $A =$ 179-181.

In the intermediate region, corresponding to nuclei with $A =$ 175-177, it is possible to distinguish two coexisting minima (see also Fig. 6.6). The appearance of these coexisting minima is a characteristic feature of the present formalism. Nevertheless, the specific boson-fermion Hamiltonian adopted in this work tends to hinder the formation of the second minimum and postpone the onset of deformation. However, this behavior is not a general property, but rather a consequence of the particular choice of the boson-fermion interaction employed in the calculation.

Another interesting case that we can exploit is the one in which the parameters considered are instead,

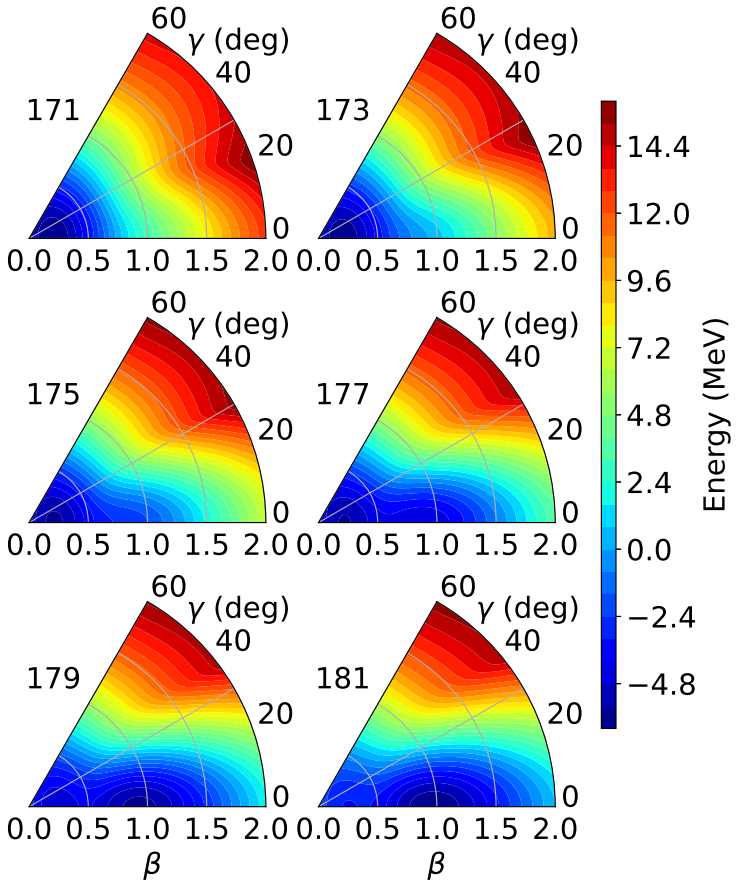

Figure 6.7: Triaxial energy surface for the first orbit along the isotope chain.

$$\begin{aligned} \epsilon_j^N &= \epsilon_j^{N+2} = 0\,\text{MeV}, \\ A_0^N &= A_0^{N+2} = 1.0\,\text{MeV}, \\ \Gamma_0^N &= \Gamma_0^{N+2} = -5.0\,\text{MeV}, \\ \Lambda_0^N &= \Lambda_0^{N+2} = -1.0\,\text{MeV}, \\ \chi^N &= -\chi^{N+2} = \sqrt{7}/2, \end{aligned} \tag{6.2}$$

where the difference can be found in the parameter $\Lambda_0^N = \Lambda_0^{N+2} = -1.0$MeV. Here, the key observation is that while in Fig. 6.5 the trend showed that only the lowest energy eigenvalue could undergo a transition from regular and approximately spherical to intruder and more deformed configuration, here in Fig. 6.8 are both the lowest and the second lowest the ones that can undergo such a transition, being of course more pronounced for the first one. Moreover, it is interesting to notice that although in Fig. 6.5 there was no sign of γ values different from 0° or 60°, in Fig. 6.8 there are some hints pointing towards a possible triaxiality.

Again, it is illustrative to present the axial energy curves for this schematic case in Fig. 6.9, where again the deformation observed in the lower states comes from the lowering of the

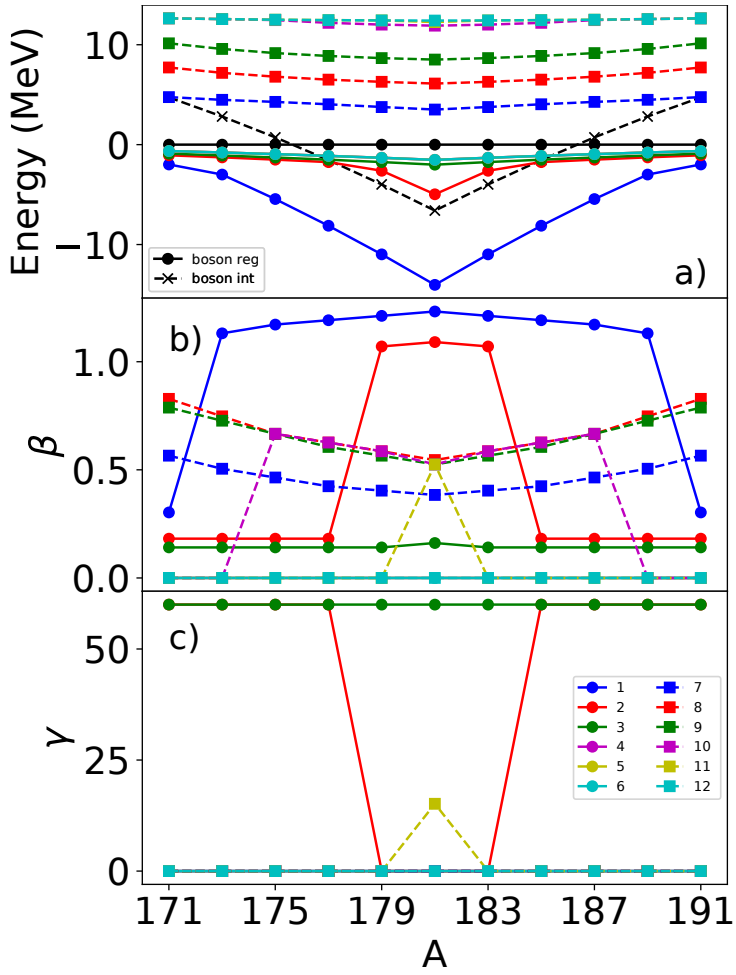

Figure 6.8: Equilibrium value of energies and β and γ deformation parameters for the second schematic isotope chain proposes. Labels and colors follow the same logic as Fig. 6.5

intruder levels as we approach midshell together with the interaction between regular and intruder configurations. Moreover, also in this case secondary minima appear and can also become degenerate, however, what it is interesting to notice it is that in this case the value of the absolute minimum for the heaviest isotopes, namely $A = 178$ and $A = 181$ is by far lower than the minima that would correspond to the bosonic core and the one presented in Fig. 6.6.

Finally, in Fig. 6.10 we present the behavior in the $\beta - \gamma$ plane for the lowest eigenvalue, where it is interesting to notice how the change in parameters leads to a set of surface that for this time do not evolve from an almost spherical case, as in $A = 171 - 173$, nearly two prolate minima can be found almost coexisting. The presence of this minimum is less prominent in the cases $A = 175 - 177$, resulting in a completely prolate deformed $A = 179 - 181$ isotopes with no hints of triaxiality.

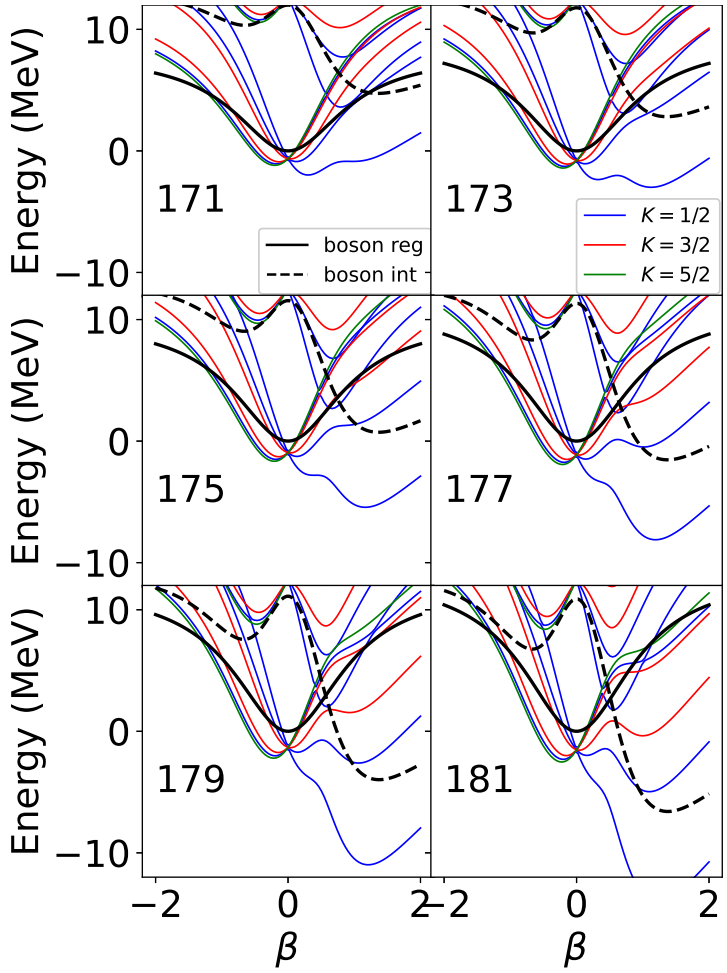

Figure 6.9: Axial energy curves for the fermion orbits over the isotope chain in the second schematic case. Lines and colors follow the same logic as in Fig. 6.6

6.2 About the Presence of Quantum Phase Transitions

Now, we specifically aim to interpret the behavior observed in Fig. 6.6, where the low-lying states exhibit increasing deformation as the system approaches mid-shell, despite the Hamiltonian remaining constant. This trend can be attributed to the increasing number of bosons along the isotopic chain, which enhances the binding energy of the deformed configuration. As a result, the spherical and deformed configurations eventually cross and become nearly degenerate. This crossing mechanism is schematically illustrated in Fig.1.2.

The presence of the odd fermion modifies the crossing behavior in several ways. First, the boson energy levels are split according to the K-projection of the fermion (within the axial approximation), which can either raise or lower the energy depending on the specific boson-fermion interaction. Second, the deformation associated with each configuration is slightly modified by the coupling to the fermion. Furthermore, the mixing between the

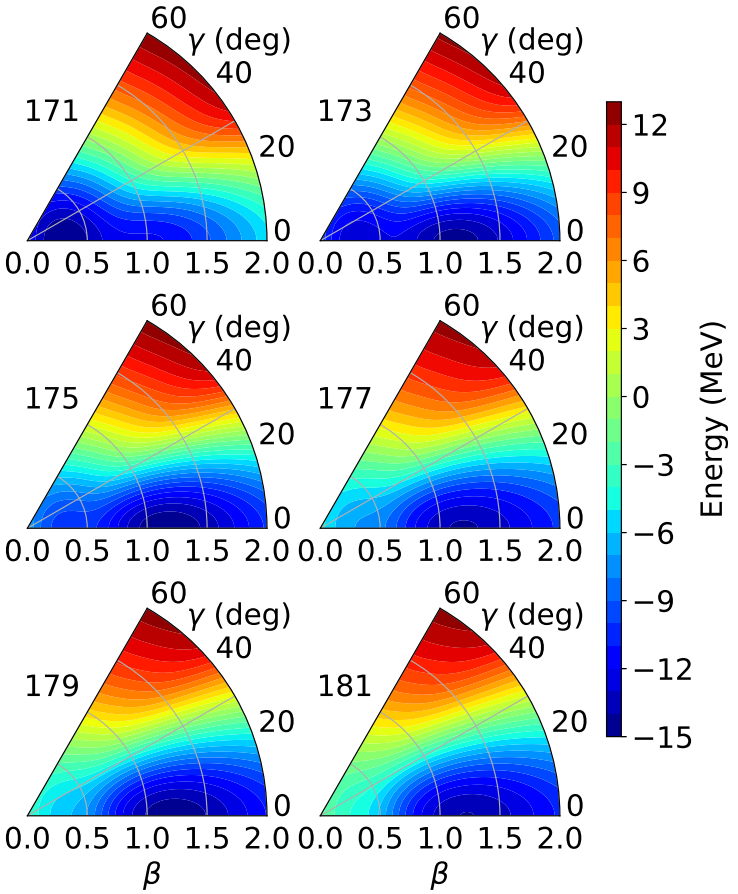

Figure 6.10: Triaxial energy surface for the first orbit along the isotope chain in the second schematic case.

regular and intruder configurations induces level repulsion, which can affect the relative ordering of states.

Taken together, this schematic picture suggests that a Type II QPT can be induced in the IBFM-CM framework, as previously proposed in Refs. [67, 66, 166]. Importantly, the precise mass number at which the QPT occurs is shifted relative to the purely bosonic case, due to the influence of the odd fermion. Given the coexistence of multiple minima in the energy surface, the resulting QPT is expected to be of first order.

In the second schematic case, the modification of the exchange term $\Lambda_0^N = \Lambda_0^{N+2} = -1.0$ MeV leads to a different manifestation of the QPT. Where, as shown in Fig. 6.8, both the lowest and the second-lowest eigenvalues undergo a structural change from a regular configuration to an intruder and more deformed one as mid-shell is approached. This, that is supported by the axial energy curves in Fig. 6.9 and by the triaxial energy surfaces shown in Fig. 6.10 shows that lowering of the intruder configurations is enhanced by the coupling to the odd fermion, producing more deformed minima that become clearly dominant for the heaviest isotopes. The coexistence of competing minima together with the appearance of the deformed shape, is consistent with a type-II QPT of first-order

character. The appearance of non-axial equilibrium points further suggests that triaxial degrees of freedom may also play a role, even though the final deformed phase remains predominantly prolate.

6.3 Nuclear Shapes of Nb Isotopes

The isotope chain $^{93\text{-}103}$Nb has been previously described in Refs. [67, 66], where the value of the Hamiltonian parameters of the IBFM-CM were determined by carrying out a laboratory-frame calculation. In particular, the parameters were obtained by fitting the theoretical results to the available experimental data. Here, we take those parameters as fixed inputs and use them to analyze the same isotope chain within the intrinsic-state formalism of the IBFM-CM [167, 164].

Within this approach, the odd-mass niobium isotopes are described as a boson core coupled to a single unpaired proton. For negative-parity states, the proton occupy the $1f_{5/2}$, $2p_{3/2}$, and $2p_{1/2}$ orbitals, while positive-parity states are generated by placing the proton in the $1g_{9/2}$ shell.

The consideration of this isotope chain within the intrinsic-state formalism provides a way of testing the performance of the formalism in both single-j and multiple-j scenarios, using a complete and realistic set of Hamiltonian and transition-operator parameters. All the coefficients entering the Hamiltonian and the electromagnetic transition operators are taken from Refs. [67, 66], where they were obtained through a least-squares fit to the available experimental information.

6.3.1 Positive Parity States

We begin our analysis by considering the case in which the odd proton occupies the $1g_{9/2}$ orbit, which gives rise to positive-parity states. Under these conditions, the Hamiltonian matrix to be diagonalized has dimension 10, that originates from the simultaneous inclusion of both regular and intruder configurations within the model space.

The first step of the study consists in determining the equilibrium values of the deformation parameters, as we did previously with the schematic case, in order to better understand the role played by the mixing between regular and intruder configurations, it is convenient to analyze two different scenarios. Firstly, we consider the case in which configuration mixing is switched off ($V_{\text{mix}} = 0$) and then, we study the more general situation in which the mixing interaction is included ($V_{\text{mix}} \neq 0$).

The results obtained, not considering configuration mixing, are shown in the left column of Fig. 6.11. In this case, the regular (solid lines) and intruder (dashed lines) configurations

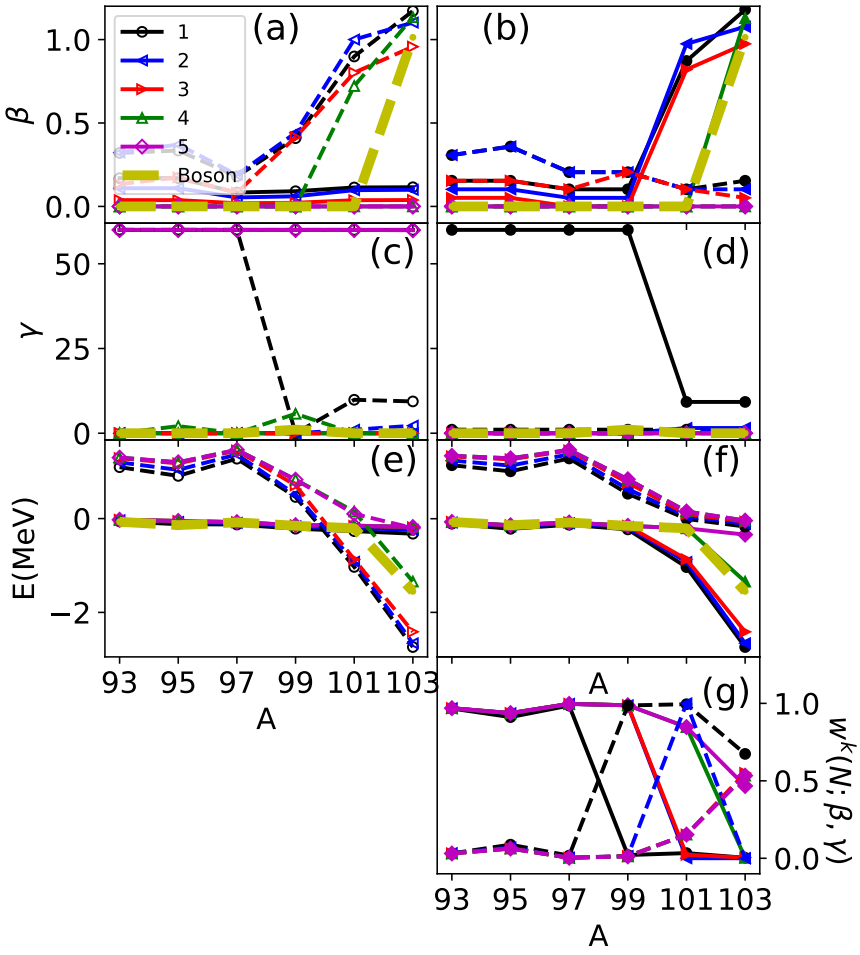

Figure 6.11: Equilibrium deformation values, excitation energies, and regular content of the wavefunction for the positive parity states. (a) equilibrium values of β for the unmixed case ($V_{mix} = 0$), full lines for the regular states and dashed for the intruder ones, thick dashed yellow line for the IBM-CM result; (b) equilibrium value of β for $V_{mix} \neq 0$, full lines for the first five states and dashed for the last five ones; (c) equilibrium value of γ for $V_{mix} = 0$; (d) equilibrium value of γ for $V_{mix} \neq 0$; (e) excitation energies for $V_{mix} = 0$; (f) excitation energies for $V_{mix} \neq 0$; (g) regular content of the wave function for $V_{mix} \neq 0$.

remain clearly separated, both in terms of their excitation energies [panel (e)] and their equilibrium deformation properties [panels (a) and (c)]. Panel (e) shows the eigenvalues obtained for each configuration, where the lowest five eigenvalues correspond to the regular sector, while the next five belong to the intruder sector. The thick dashed yellow line represents the reference energy associated with the boson core, that is, the IBM-CM result. For each state, the equilibrium values of the deformation parameters β and γ, obtained by minimizing the energy, are shown in panels (a) and (c), respectively.

A key feature emerging from these results is the presence of a crossing between the regular and intruder configurations, which are characterized by markedly different equilibrium deformations. As the neutron number increases along the isotopic chain, the intruder

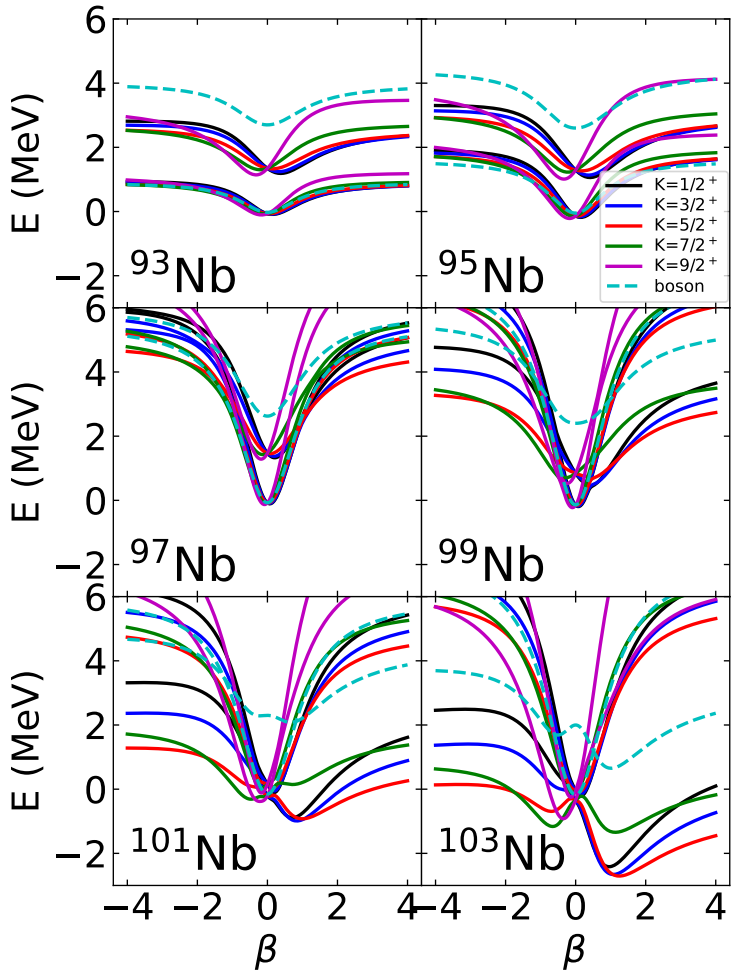

Figure 6.12: Axial energy curves as a function of K^π for positive-parity states with $V_{mix} \neq 0$. For reference, the unmixed regular and intruder energy surfaces are also included.

configuration progressively decreases in energy relative to the regular one, being this a behavior that provides a natural explanation for the sudden onset of deformation observed experimentally in this region.

The equilibrium deformation parameters also support this interpretation. As shown in panel (a), intruder states are associated with larger values of the β deformation parameter, indicating a more pronounced deformation, that also becomes particularly significant from $A = 99$ onwards, where the intruder configuration begins to dominate the low-energy part of the spectrum. Moreover, for the heaviest isotopes, $A = 101$ and 103, the calculated values of the γ parameter differ significantly from 0° and 60°, which signals the development of triaxial shapes in this mass region.

Since configuration mixing is not included in this calculation, both regular and intruder sets of states remain well separated throughout the isotopic chain, that allows us to unambiguously identify the point at which the crossing between configurations occurs and the intruder configuration becomes the ground state of the system, which is found to

take place between $A = 99$ and $A = 101$.

The situation changes when configuration mixing is taken into account ($V_{\text{mix}} \neq 0$), as shown in the right column of Fig. 6.11. In this case, the spectrum exhibits a more complex structure, since regular and intruder configurations can no longer be distinguished as clearly as in the unmixed calculation. The five lowest eigenvalues are now plotted with solid lines, while the next five are shown with dashed lines.

Despite this increased complexity, the overall behavior of the excitation energies and of the equilibrium deformation parameters β and γ remains qualitatively similar to that observed in the unmixed case. However, the inclusion of configuration mixing leads to a fragmentation of the wave functions between the regular and intruder sectors. This effect is illustrated in panel (g), which shows the fraction of the wave function in the regular sector, $w^k(N; \beta_0, \gamma_0)$, as defined in Eq. (4.106).

From this panel, it is easily observed that for $^{93\text{-}97}$Nb the lowest-lying states retain a predominantly regular character, while the higher-lying ones are mainly intruder in nature. This situation starts to change when the configurations approach each other and begin to cross. In particular, significant mixing is observed for the first and second states (black and blue lines) in ^{99}Nb, for the third state (red line) in ^{101}Nb, and finally for the fourth state (green line) in ^{103}Nb. As additional neutrons are added, the distinction between regular and intruder states becomes progressively less clear, and the wave functions become increasingly fragmented, indicating strong configuration mixing.

An additional consequence of the configuration crossing is the reduction of the regular content of the states. In fact, the sum of $\omega^k(N; \beta_0, \gamma_0)$ over all states turns out to be smaller than half the total number of states, as would be expected if orthogonality were strictly preserved. In other words, the regular content of the states is lower than anticipated due to the non-orthogonality induced by the large differences in deformation between the lowest and highest states. This observation suggests that, for the heaviest isotopes, intruder configurations play an increasingly dominant role in shaping the low-lying spectrum.

This evolution of the nuclear deformation can be visualized more clearly in Fig. 6.12, which displays the axial energy curves as a function of K^π, where we add the reference of unmixed regular and intruder boson lines. Here it is interesting to observe that for the lighter isotopes, the spectrum is organized into two well-defined sets of states: On the one hand, the lowest-lying levels, that are mainly associated with regular configurations and correspond to nearly spherical shapes, while on the other hand the higher states are dominated by intruder configurations, in which small deformations begin to develop. Moreover, as neutrons are added along the isotopic chain, these two sets of configurations progressively approach each other, interact, and eventually cross.

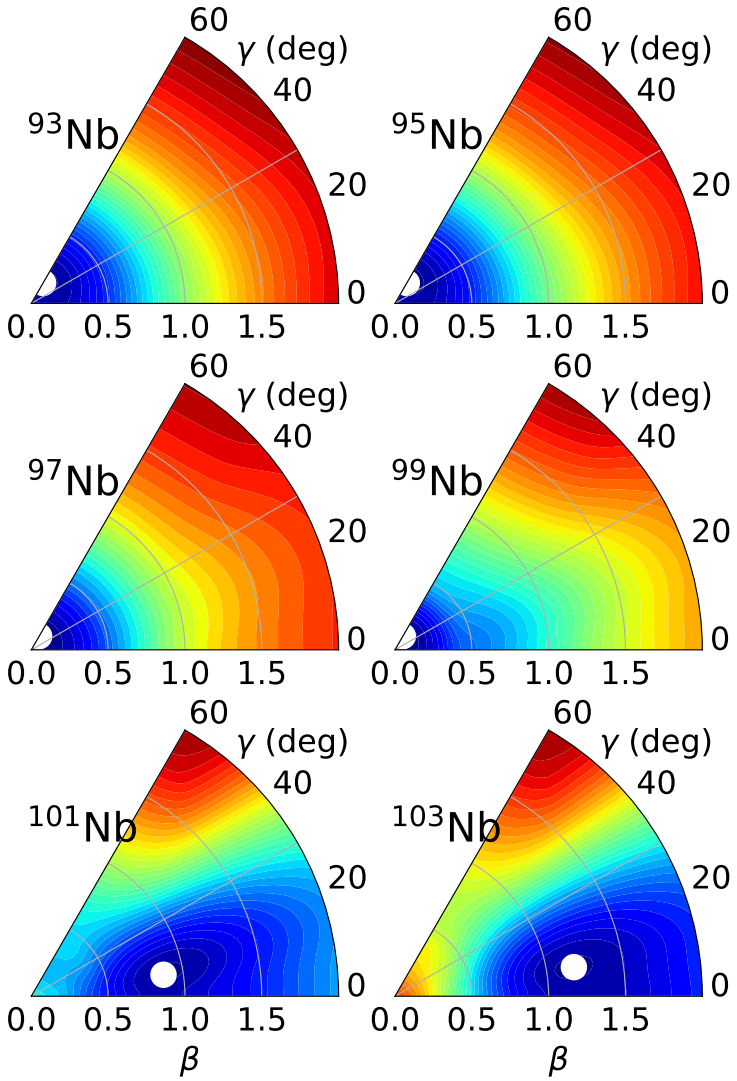

Figure 6.13: Ground-state energy surfaces in the β–γ plane for positive-parity states along the isotopic chain. White dots indicate the minimum of the energy surfaces. The energy scale varies across panels, with blue representing the minimum and red the maximum, divided into 40 contour levels.

When studying the isotopes $^{93\text{-}99}$Nb, we observe that the ground state remains spherical and the energy curves corresponding to different K^π values are almost degenerate, reflecting the absence of any axial deformation. In contrast, for the heaviest isotopes, $^{101\text{-}103}$Nb, the lowest states associated with each K^π value develop pronounced energy minima that are linked to intruder configurations. Among these, the lowest minimum corresponds to $K^\pi = 5/2^+$, followed by the associated with $K^\pi = 3/2^+$ and $K^\pi = 1/2^+$. It should be noted that the presence of these minima does not necessarily imply the existence of stable axial shapes, since their nature may change once the γ degree of freedom is explicitly taken into account. Finally, it is also worth emphasizing that no energy curve exhibits the coexistence of two distinct minima.

Additional insight into the evolution of nuclear shapes can be obtained by examining the

energy surfaces in the β-γ plane, in the same sense that we studied those surfaces in the schematic cases. In this way, Fig. 6.13 illustrates the evolution of the ground-state energy surface along the isotopic chain, while a more complete set of results, including excited states, is presented in Fig. 6.14, supporting in addition this interpretation, since for the isotopes with $A = 93$-97, all states exhibit essentially spherical shapes, although the highest-lying states are characterized by broader and flatter minima. In contrast, for $A = 99$-103, the lowest-lying states display clearly deformed shapes, while the highest-lying ones remain closer to spherical configurations. The calculations reveal a smooth but well-defined structural evolution, where the lighter isotopes ($A = 93$-97) are characterized by nearly spherical shapes, the nucleus with $A = 99$ develops a modest axial deformation, and the heaviest isotopes ($A = 101$-103) exhibit pronounced triaxial minima located around $\gamma \approx 20°$.

Altogether, these results indicate that the interplay between regular and intruder configurations is responsible for driving the onset of deformation along the isotopic chain. However, the emergence of triaxial shapes toward the end of the chain is largely driven by the presence of the unpaired proton, as is clearly illustrated in Fig. 6.11(c), which corresponds to a calculation performed without configuration mixing ($V_{\rm mix} = 0$).

6.3.2 Negative Parity States

We now turn to the analysis of the negative-parity states, which correspond to configurations in which the odd proton occupies one of the $1f_{5/2}$, $2p_{3/2}$, or $2p_{1/2}$ orbits. In this case, the Hamiltonian matrix to be diagonalized has dimension 12, reflecting the larger model space associated with the inclusion of these different orbitals altogether.

As in the positive parity case, the first step of the analysis consists on determining the equilibrium values of the deformation parameters and the corresponding energies, both in the absence of configuration mixing ($V_{\rm mix} = 0$) and when configuration mixing is included ($V_{\rm mix} \neq 0$). The main results of this analysis are summarized in Fig. 6.15, where in an equivalent way, the left column of the figure shows the results obtained without configuration mixing, while the right column presents those obtained when mixing is taken into account. In both cases, solid lines represent regular configurations, whereas dashed lines denote intruder configurations. The thick dashed yellow lines correspond to the IBM-CM results, which are included as a reference for the underlying boson core just as it was made for the positive parity case.

One of the most relevant results that can be extracted from Fig. 6.15 is the behavior of the β deformation parameter shown in panel (a). Here, for the heavier isotopes ($^{99\text{-}103}$Nb), different low-lying states are associated with distinct equilibrium deformations, indicating a richer and more complex structural behavior. In contrast, for the lightest isotopes, most

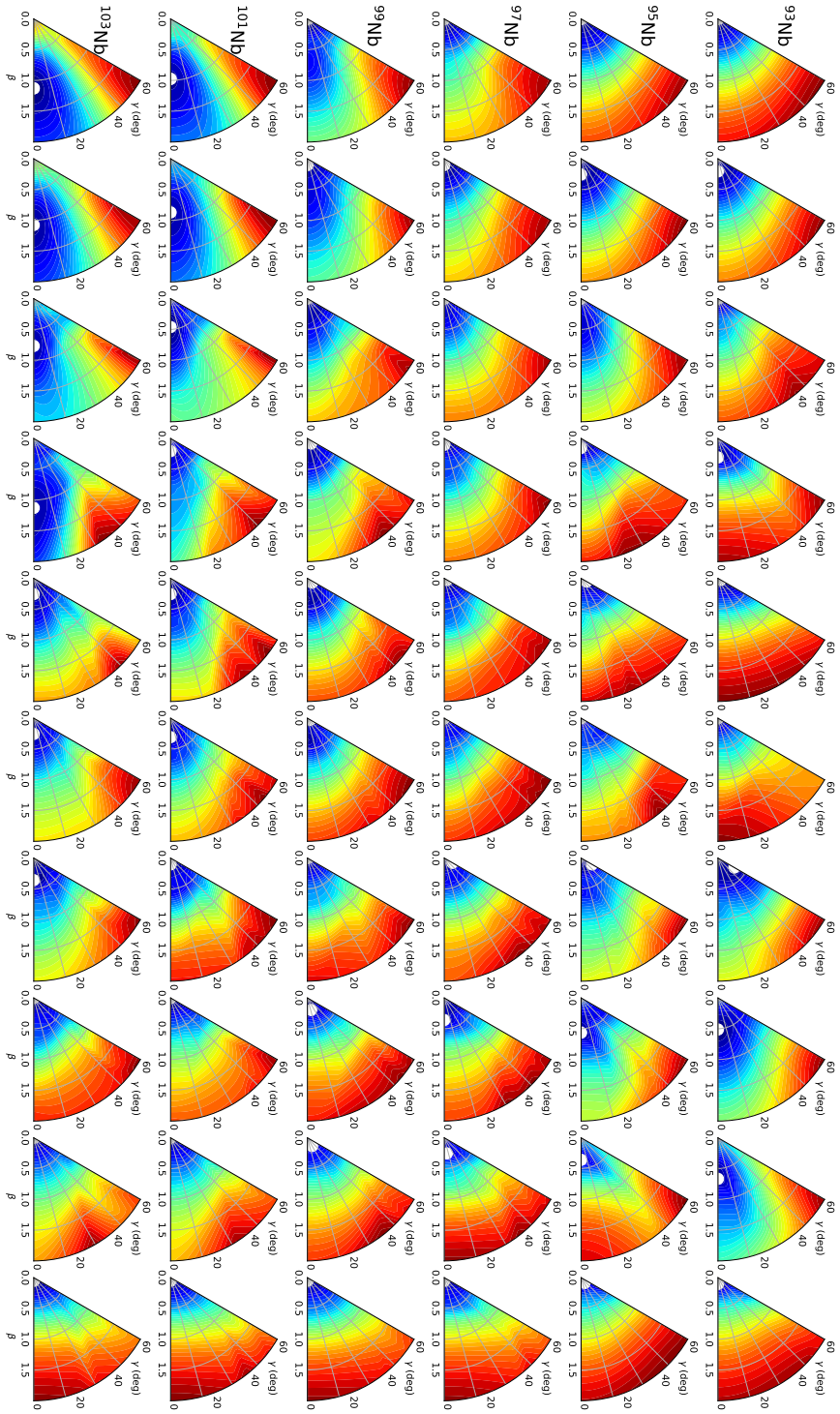

Figure 6.14: Energy surfaces in the β–γ plane for positive-parity states across the isotopic chain. Rows correspond to the isotope while column to the ordering. White dots indicate the minimum of the energy surfaces. The energy scale varies among the panels, blue color for the minimum and red for the maximum with 40 divisions among them.

states remain essentially spherical or exhibit only a small deformation. This evolution is closely related to the systematics of the excitation energies displayed in panel (e): in the unmixed calculation, the crossing between regular and intruder configurations marks the onset of a structural change along the isotopic chain.

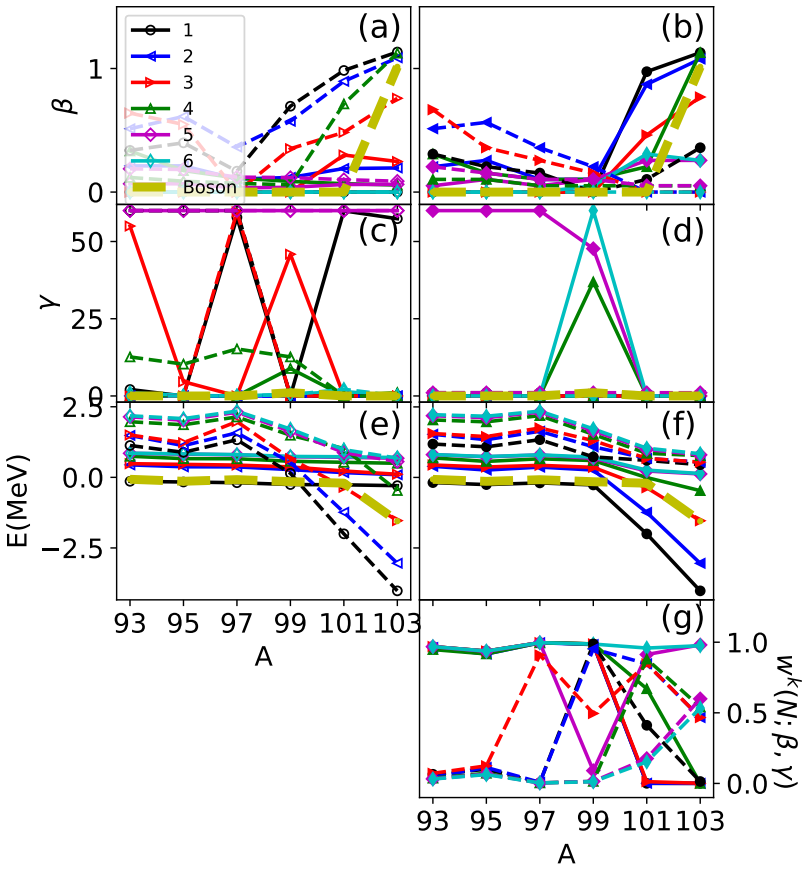

Figure 6.15: Same as Fig. 6.11 but for negative-parity states.

Regarding the γ deformation parameter, the oscillatory behavior observed in panel (c) should be regarded as purely artificial, since all cases in which $\gamma \neq 0$ correspond to situations with $\beta \approx 0$, where the γ degree of freedom is not physically meaningful.

When configuration mixing is included ($V_{\text{mix}} \neq 0$), the overall behavior remains qualitatively similar. However, the values of the β deformation parameter in the lightest isotopes are systematically slightly larger than those obtained in the unmixed calculation. In this mixed case, the six lowest eigenvalues are plotted with solid lines, while the next six are shown with dashed lines. The analysis of the regular content of the wave functions reveals that, for the lighter isotopes, regular and intruder states remain well separated and can still be individually identified. In contrast, for the heavier isotopes, the wave functions acquire a strongly mixed character, indicating an enhancement of configuration mixing as the neutron number increases.

Additional insight into the evolution of nuclear shapes is provided by the axial energy curves shown in Fig. 6.16, in which for the lightest isotopes, the ground-state energy surfaces exhibit a nearly spherical minimum associated with $K^\pi = \frac{1}{2}^-$, together with a secondary minimum corresponding to $K^\pi = \frac{5}{2}^-$. As neutrons are added along the

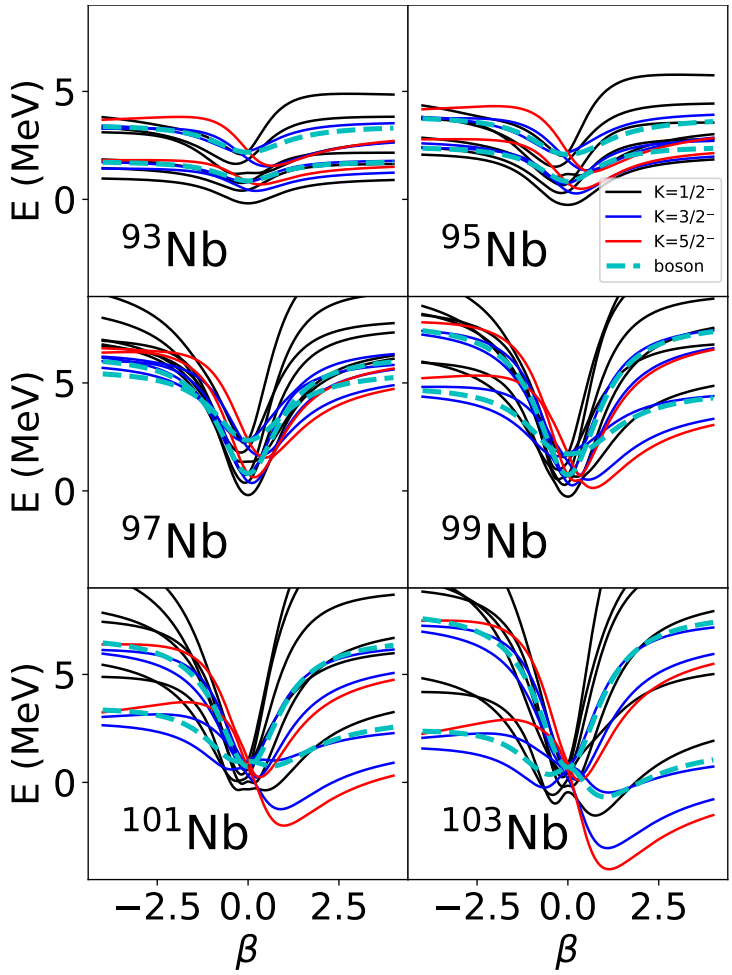

Figure 6.16: Same as Fig. 6.12 but for negative-parity states.

isotopic chain, the minimum associated with $K^\pi = \frac{5}{2}^-$ gradually increases its deformation and becomes the ground state, a behavior that is particularly evident for $^{101\text{-}103}$Nb, that indicates a progressive stabilization of a prolate shape in the heavier isotopes. Indeed, for these nuclei, the energy curves corresponding to $K^\pi = \frac{3}{2}^-$ and $K^\pi = \frac{1}{2}^-$ also develop deformed minima. It is worth noting that this situation closely mirrors the behavior observed in the positive-parity case.

This evolution provides additional evidence for the configuration crossing inferred from the excitation energies. However, it should be emphasized that the observed minima do not coexist simultaneously within a single energy curve. Instead, one minimum progressively replaces the other as the dominant configuration as the neutron number increases.

A more comprehensive picture of the structural evolution is obtained from the full energy surfaces in the β-γ plane, shown in Fig. 6.17. In contrast to the positive-parity case, no triaxial minima are found for negative parity states. Instead, the heavier isotopes develop well-defined prolate minima, in agreement with the behavior inferred from the axial energy curves, which demonstrates that, although the interplay between regular and

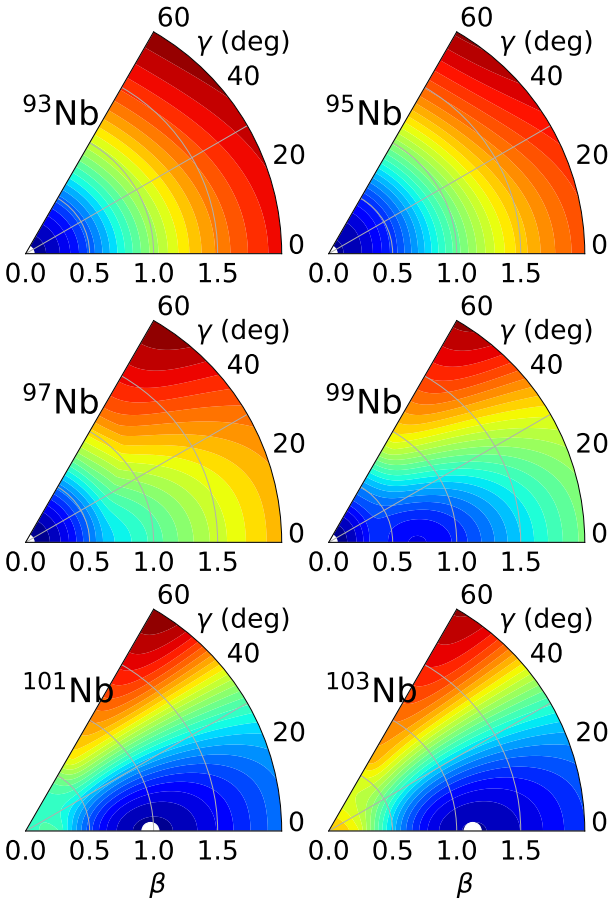

Figure 6.17: Same as Fig. 6.13 but for negative-parity states.

intruder configurations plays a central role in both parity sectors, the resulting equilibrium shapes differ significantly. Finally, while the positive parity states evolve toward triaxiality at the end of the isotopic chain, the negative-parity states stabilize into axially symmetric prolate configurations.

For completeness, the β-γ energy surfaces corresponding to all states and isotopes are shown in Fig. 6.18, from which is evident that no triaxial minima are present in the negative parity sector. Most of the energy surfaces exhibit spherical minima, except for the higher-energy surfaces in the lightest isotopes and the lowest-energy surfaces in the heaviest ones, which display clearly deformed prolate shapes.

Finally, this analysis reveals that the structural evolution of $^{93\text{-}103}$Nb depends of the parity of the unpaired nucleon. Moreover, in both positive and negative-parity sectors, the interplay between regular and intruder configurations plays a key role in driving the onset of deformation, as evidenced by the systematic crossing of configurations and the associated changes in the excitation spectra.

However, the resulting equilibrium shapes differ markedly between the two parity considered, since positive-parity states, associated with $1g_{9/2}$ orbital, evolve from nearly spherical

configurations in the lighter isotopes toward pronounced triaxial shapes in the heaviest nuclei, but in contrast, negative-parity states, built on the $1f_{5/2}$, $2p_{3/2}$, and $2p_{1/2}$ orbitals, display a more robust axial character, with the heavier isotopes stabilizing into prolate shapes and no evidence for triaxial minima. This comparison highlights the crucial role of the single-particle structure of the unpaired proton in shaping the collective behavior of the nucleus and demonstrates how the odd particle can qualitatively modify the deformation behavior, even when the same underlying boson core and configuration mixing mechanisms are at play.

6.4 Discussion: Quantum Phase Transitions and Excited-State Energy Curves

As previously discussed in Ref. [66], the structural evolution of the Nb isotopes can be interpreted in terms of an intertwined QPT. However, in that work, the analysis was restricted to the laboratory-frame formulation of the model and did not include mean field or intrinsic state results. Here we focus on extending that picture by providing a detailed intrinsic state formalism analysis, which allows for a direct comparison with the case of the Zr isotopes that constitute the boson core of the Nb system.

As shown in Figs. 6.11(e) and 6.11(f) for positive-parity states, and in Figs. 6.15(e) and 6.15(f) for negative-parity states, a clear crossing between the regular and intruder configurations takes place between $A = 99$ and $A = 101$. This crossing is accompanied by a sudden increase in the equilibrium deformation parameter, as shown in panels (a) and (b) of the same figures (and also in Fig. 6.15 for the negative-parity sector). For the ground state, this behavior is characteristic of a Type II QPT, which is driven by the interplay between two distinct configurations. Interestingly, this transition occurs at a lower mass number than in the Zr isotopes, as indicated by the reference IBM-CM boson line (yellow line).

At the same time, the intruder configuration itself undergoes a structural evolution, changing from an almost spherical shape to a clearly deformed one, as can be noticed in panel (a) of Figs. 6.11 and 6.15. This evolution is moreover noticeably more rapid for positive-parity states than for negative-parity ones. Therefore, in addition to the Type II QPT affecting the ground state, the intruder configuration experiences a Type I QPT, associated with a shape change within a single configuration. As a result, both types of QPTs coexist and are intertwined in the Nb isotopes, in close analogy with the behavior previously identified in the Zr isotopic chain.

It is also relevant to mark that the intrinsic-state results obtained in the present work for the odd-even Nb system go somewhat beyond the conventional mean-field approach, as

they indeed provide information not only on the ground state but also on excited states associated with different single-particle orbits, as well as on both regular and intruder configurations. Moreover, for each orbit, a distinct equilibrium set of deformation parameters β and γ is obtained. Also a direct consequence of this procedure is that the resulting intrinsic states are no longer orthogonal, and in addition, the presence of two configurations leads to the appearance of two families of states characterized by markedly different equilibrium deformations.

In purely bosonic systems, the highest eigenvalue obtained from the diagonalization of the intrinsic Hamiltonian has received little attention, mainly because its physical interpretation is often ambiguous. In principle, one would expect a clear correspondence between the unperturbed results and those obtained from the full diagonalization. However, this correspondence may break down when the unperturbed intruder configuration manifests itself as a secondary local minimum of the lowest eigenenergy surface. In such cases, the absolute minimum associated with the highest eigenvalue becomes only weakly connected to the unperturbed intruder configuration and is instead largely influenced by an artificial minimum that emerges from the crossing of the two configurations.

In the obtained results for Nb, both families of eigenvalues appear to exhibit a clear correspondence with the unperturbed results. Consequently, the interpretation of the energy curves is relatively straightforward, including both the lowest and highest eigenvalues. For bosonic systems, this type of analysis has been carried out only for the even-even Pt isotopes in [154]; in general, however, only the lowest eigenvalue is usually considered [41, 39, 40].

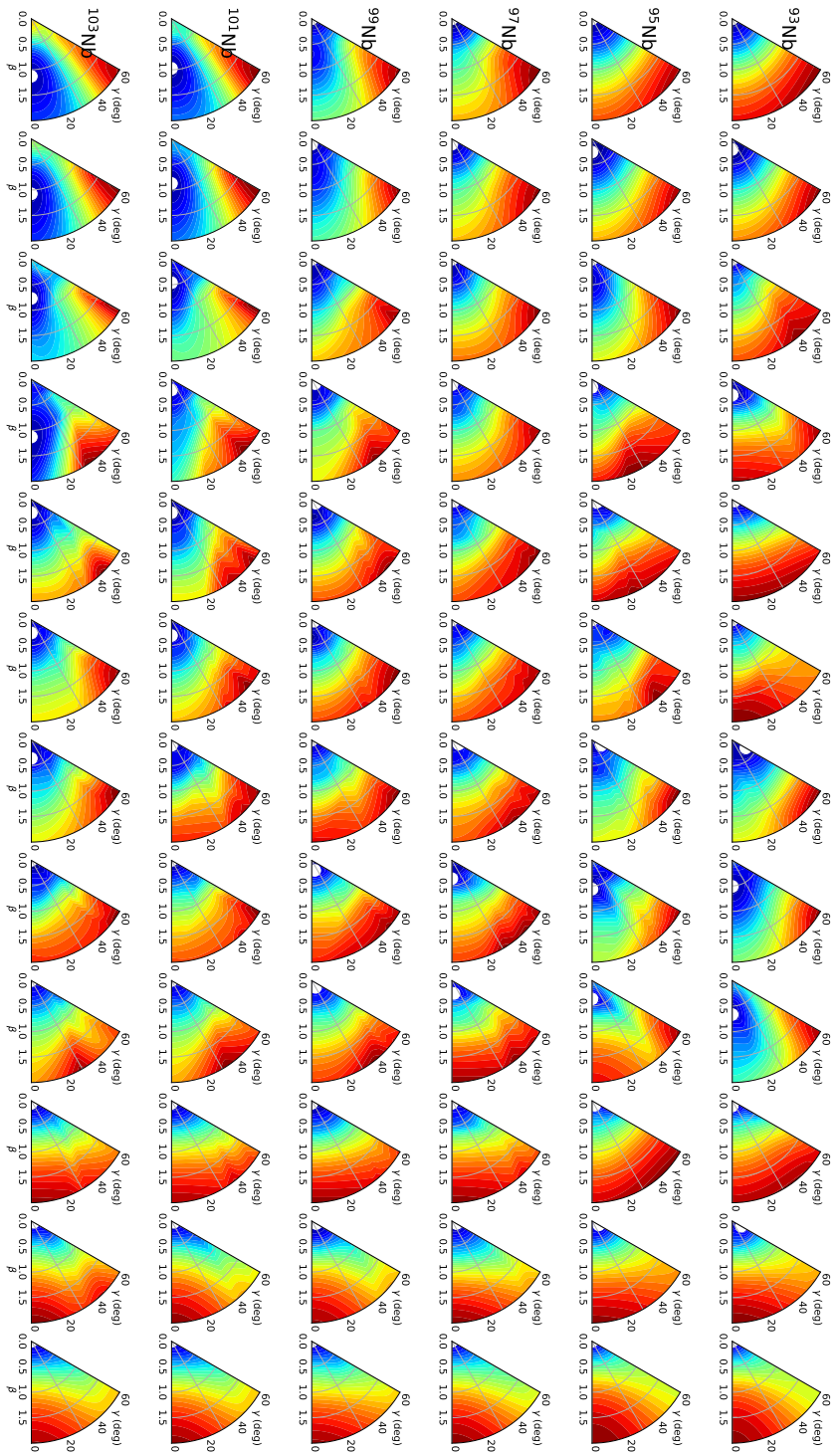

Figure 6.18: Same as Fig. 6.14 but for negative-parity states.

Chapter 7

Conclusions

Throughout this thesis the following aspects have been studied in depth:

- A comprehensive study of shape coexistence, the onset of nuclear deformation and their connection with QPTs in in medium-mass nuclei around the $Z \approx 40$ region within the framework of the IBM-CM.
- For the even–even Sr isotopes, detailed IBM-CM calculations have been performed for $^{92\text{-}102}$Sr, where the Hamiltonian parameters were determined throughout a fitting procedure to resemble to the available experimental excitation energies below and the corresponding B(E2) transition rates.
- The performed calculations for the Sr isotope chain also reproduce the rapid structural changes observed around $A = 98$, and the analysis of unperturbed regular and intruder configurations reveals a clear crossing around neutron number $N = 60$, with the intruder configuration gaining correlation energy and becoming dominant in the low-lying states. This is additionally supported by the evolution of the wave functions, which show an abrupt change from predominantly regular to predominantly intruder character. The mean-field energy surfaces and equilibrium deformation parameters extracted from the IBM-CM calculations are also in agreement with the laboratory frame results.
- With respect to the analysis of QPTs these features can be interpreted as fingerprints of the onset of deformation driven by configuration crossing, corresponding to a Type II QPT.
- The results obtained for Sr isotopes naturally complement earlier studies of Zr isotopes in this region, for which also a more extensive experimental data set is available. Taken together, Sr and Zr isotopes define a picture in which regular and intruder configurations cross at $N = 60$, marking the onset of deformation.

- The extension of the study to the Mo and Ru isotopic chains has allowed to mark the limits of the shape coexistence region around $Z = 40$. In Mo isotopes, a crossing between regular and intruder configurations is found to occur in the ground state around $N = 60$, indicating that shape coexistence still plays a significant role.
- In contrast, for Ru isotopes the intruder configurations remain at higher excitation energies and do not significantly influence the low-lying structure. As a result, the behavior of Mo and Ru isotopes points to Mo as the borderline nucleus for the relevance of shape coexistence in this region.
- From the perspective of QPTs, the analysis indicates that Mo isotopes undergo a Type II QPT of second order, induced by configuration crossing, whereas Ru isotopes exhibit a Type I second-order QPT associated with a single configuration.
- Additional insight has been obtained from the analysis of nuclear radii and two-neutron separation energies in all even-even isotope chains, which not only are useful to study the the structural evolution around $Z = 40$ but also serve as a test for the theoretical results obtained using the IBM-CM fitting procedure.
- Experimental nuclear radii and two-neutron separation energies have been compared for both even-even and odd-even isotope chains, showing that while nuclear radii mark only minor differences between even and odd neutron numbers, the systematics of S_{2n} display more pronounced effects in odd-neutron nuclei, including a clear dip at $N = 60$, emphasizing the sensitivity of two neutron separation energies to structural changes.
- A central contribution of this thesis is the development and application of the intrinsic-frame formalism for the IBFM-CM, valid for both single and multiple j shells and applicable to axial and triaxial shapes.
- This intrinsic frame formalism has been applied to an schematic multiple-j shell case, using an IBFM Hamiltonian that includes U(5) and SU(3) boson terms for the regular and the intruder configurations, respectively. Moreover, the considered boson-fermion interaction contains the monopole, the quadrupole and the exchange components.
- For this schematic case axial and $\beta - \gamma$ fermion energy surfaces are calculated along with the corresponding equilibrium values, where a type II QPT and clear signatures of shape coexistence are observed.
- The formalism has also been employed to study odd–even Nb isotopes using realistic Hamiltonian parameters obtained from a laboratory frame calculation.
- For positive-parity states associated with the $1g_{9/2}$ orbit, a clear crossing between

regular and intruder configurations is observed, leading to a structural evolution from nearly spherical shapes in the lighter isotopes to triaxial minima in the heavier ones. In this case, the emergence of triaxiality is primarily driven by the presence of the odd proton rather than by shape coexistence alone.

- For negative-parity states, involving the $1f_{5/2}$, $2p_{3/2}$, and $2p_{1/2}$ orbits, the configuration crossing results in an evolution toward prolate axial shapes in the heavier isotopes without appearance of triaxiality. Consequently, the energy minima evolve from nearly spherical configurations in the lighter nuclei to prolate shapes in the heaviest ones, namely $^{101-103}$Nb.
- For this more realistic case, in both parity sectors, the interplay between regular and intruder configurations gives rise to a Type II QPT in the ground state, with the odd proton enhancing how abrupt the transition appears.
- The results obtained for both positive and negative parities demonstrate that the interplay between the regular and intruder configurations plays a crucial role in driving the structural evolution along the $^{93-103}$Nb isotopic chain, providing a consistent explanation for the onset of deformation.
- In both positive- and negative-parity states, a Type II QPT is observed for the ground state, while the intruder configuration also undergoes an evolution from spherical to deformed shapes, proceeding more rapidly in positive parity and more slowly in negative parity.
- The capability of the IBFM-CM intrinsic-frame formalism has been shown, as it has allowed us to describe the shape evolution of an isotopic chain using realistic Hamiltonian parameters.

Chapter 8

Conclusiones

A lo largo de esta tesis se han estudiado los siguientes aspectos:

- En primer lugar se ha realizado un estudio de la coexistencia de forma, el inicio de la deformación nuclear y su relación con las transiciones de fase cuánticas (QPTs) en núcleos en torno a $Z \approx 40$, dentro del marco del IBM y el IBM-CM.
- Para los isótopos par-par de Sr se han realizado cálculos detallados dentro del marco del IBM-CM para $^{92\text{-}102}$Sr, hallándose los parámetros del Hamiltoniano mediante un procedimiento de ajuste a las energías de excitación y B(E2) experimentales.
- Los cálculos realizados para los isótopos del Sr muestran resultados coherentes con los cambios en la estructura nuclear observados en torno a $A = 98$. El análisis de las configuraciones regulares e intrusas no perturbadas muestra además un cruce para $N = 60$, donde la configuración intrusa gana energía de correlación y pasa a dominar los estados de baja energía. Este comportamiento se comprueba además observando la evolución de las funciones de onda, que muestran un cambio abrupto desde un carácter predominantemente regular a uno mayoritariamente intruso. Además las superficies de energía y los parámetros de deformación extraídos del IBM-CM concuerdan asimismo con los resultados obtenidos en el sistema laboratorio.
- Desde el punto de vista de las QPTs, estos resultados se interpretan como pruebas del inicio de deformación, que además está inducida por el cruce de configuraciones, y que puede identificarse con una QPT de Tipo II.
- Los resultados obtenidos para los isótopos de Sr complementan además los estudios previos sobre los isótopos de Zr en esta región. Considerados conjuntamente, los isótopos de Sr y Zr muestran un escenario en el que las configuraciones regulares e intrusas se cruzan para $N = 60$.
- El estudio de los isótopos de Mo y Ru permite además delimitar los limites de la

región donde puede encontrarse coexistencia de forma en torno a $Z = 40$.De esta forma, en los isótopos de Mo se observa un cruce entre configuraciones regulares e intrusas en el estado fundamental alrededor de $N = 60$, indicando que la coexistencia de formas sigue desempeñando un papel relevante.

- Por otro lado, en los isótopos de Ru las configuraciones intrusas permanecen a energías de excitación más elevadas y no influyen de manera significativa en la estructura de los estados que se encuentran más bajos en energía. Como resultado, el comportamiento de los isótopos de Mo y Ru muestra que los isótopos de Mo marcan la frontera en cuanto a la aparición de coexistencia de forma.

- Analizando las posibles QPTs, los isótopos de Mo experimentan una QPT de Tipo II de segundo orden, inducida por el cruce de configuraciones, mientras que los isótopos de Ru presentan una QPT de Tipo I de segundo orden, asociada en esta ocasión a una única configuración.

- Se han analizado además los radios nucleares y de las energías de separación de dos neutrones para todos los isótopos par-par considerados, ya que no solo resultan útiles para estudiar la evolución de la estructura nuclear en torno a $Z = 40$, sino que también sirven como prueba de la calidad de los resultados teóricos obtenidos mediante el IBM-CM.

- Además han comparado los radios nucleares experimentales y las energías de separación de dos neutrones tanto para los isótopos par-par como impar-par, mostrando que, aunque los radios nucleares presentan solo diferencias menores para núcleos con un número de neutrone par o impar, por otro lado las S_{2n} muestran efectos más pronunciados en los núcleos con número impar de neutrones, con un mínimo claro en $N = 60$, manifestando asímismo la sensibilidad de las energías de separación de dos neutrones a los cambios en la estructura.

- Además se ha desarrollado y la aplicado un nuevo formalismo en el sistema intrínseco para el IBFM-CM, válido tanto para capas con una sola j como con múltiples j, y aplicable a formas axiales y triaxiales.

- Este formalismo intrínseco se ha aplicado a un caso esquemático con múltiples capas j, utilizando un Hamiltoniano IBFM con términos bosónicos U(5) y SU(3) para las configuraciones regular e intrusa, respectivamente. Además, la interacción bosón-fermión considerada contiene todos los componentes monopolar, cuadrupolar y de intercambio.

- Para este caso esquemático se han calculado curvas y superficies de energía en el plano β–γ, junto con los valores de equilibrio correspondientes, observándose una QPT de Tipo II y señales de coexistencia de forma.

- El formalismo se ha empleado también para un caso más realista centrado en el estudio de los isótopos impar-par de Nb utilizando parámetros de Hamiltoniano obtenidos a partir de cálculos en el sistema laboratorio.
- Para los estados de paridad positiva asociados a $1g_{9/2}$, se observa un cruce claro entre configuraciones regulares e intrusas, lo que conduce a una evolución desde formas casi esféricas en los isótopos más ligeros hasta mínimos triaxiales en los más pesados. En este caso, la aparición de la triaxialidad tiene su origen principalmente en la presencia del protón impar, más que en la coexistencia de forma por sí sola.
- Para los estados de paridad negativa, que incluyen las órbitas $1f_{5/2}$, $2p_{3/2}$ y $2p_{1/2}$, el cruce de configuraciones da lugar a una evolución hacia formas axiales prolatas en los isótopos más pesados, sin aparición de triaxialidad. En consecuencia, los mínimos de energía evolucionan desde configuraciones casi esféricas en los núcleos más ligeros hasta formas prolatas en los más pesados, concretamente en $^{101-103}$Nb.
- En este último caso más realista, para ambas paridades, la interacción entre configuraciones regulares e intrusas da lugar a una QPT de Tipo II en el estado fundamental, siendo la presencia del protón impar la responsable de acentuar dicha transición.
- Los resultados obtenidos para ambas paridades demuestran que la interacción entre configuraciones regulares e intrusas desempeña un papel clave en la evolución de la estructura a lo largo de la cadena de isótopos $^{93-103}$Nb, explicando el inicio de la deformación.
- Tanto en los estados de paridad positiva como negativa se observa una QPT de Tipo II en el estado fundamental, mientras que la configuración intrusa experimenta también una evolución desde formas esféricas a deformadas, más pronunciada en paridad positiva y más gradual en paridad negativa.
- Finalmente, se pone de manifiesto la capacidad descriptiva del formalismo intrínseco del IBFM-CM, que ha permitido describir la evolución de las formas nucleares de una cadena de isóyopos utilizando parámetros de Hamiltoniano realistas.

Appendix A

Procedure to fit the IBM-CM parameters

Here we provide a detailed explanation of the fitting strategy followed to determine the parameters of an IBM-CM Hamiltonian using the package MINUIT [168] which allows to minimize any multi-variable function. The procedure is focused on obtaining a global agreement between calculated results and experimental data, including both excitation energies and B(E2) transition rates.

In this way, the fitting strategy, does not aim at reproducing only the physical data with maximal precision, but rather at achieving an overall description of the energy structure, and even though the fit is performed independently for each nucleus, we impose the constraint that the resulting parameters should vary smoothly from case to case. Additionally, as many parameters as possible are kept fixed or at least constrained within physically meaningful ranges.

As we already introduced, two types of experimental data are included,

- Excitation energies (typically under 3 MeV).
- Reduced B(E2) transition rates.

In the case of **excitation energies**, an example of the input considered, for the case of ^{98}Sr is,

```
0  1      0.00000      1.00000
2  1      0.14470      0.00010
0  2      0.21564      0.00100
4  1      0.43407      0.01000
6  1      0.86737      0.01000
2  2      0.87134      0.01000
```

```
 8  1       1.43365       0.01000
10  1       2.12315       0.01000
 6  2       2.53430       0.01000
```

Where the third column correspond to a determinate theoretical error (σ), which do not correspond with any experimental value or error bars, but are instead related with the expected accuracy of the IBM-CM to reproduce a certain experimental value. That is also the reason why the 2_1^+ level present such a little value of σ, as it is our reference value for the rest of the chain. Moreover, the magnitude this parameter is adjusted recursively for each level according with the fitting result to ensure a correct reproduction of all the data. However, we try to maintain it constant at least for the different bands. It is important to note, that imposing the minimum value of σ for all the levels does not ensure a correct reproduction of the data.

While for the case of B(E2) transition rates our input is:

```
2  1  0  1  2   096.00000       0.01000
0  2  2  1  2   062.00000       1.00000
4  1  2  1  2   124.00000       12.0000
6  1  4  1  2   174.80000       18.0000
2  2  4  1  2   012.00000       06.0000
2  2  0  2  2   013.00000       00.1000
2  2  0  1  2   000.80000       00.0500
8  1  6  1  2   122.80000       25.0000
10 1  8  1  2   126.00000       25.0000
6  2  4  1  2     0.00010       0.00004
```

Here the uncertainties are usually of the order of 10%, unless the experimental uncertainty is larger. Moreover, the transition $2_1^+ \to 0_1^+$ is assigned a very small uncertainty and is used to fix the absolute scale of the effective charge. Again, this value can be adjusted in every fitting for ensuring a better fitting. However it is important try keeping it as close as possible to the experimental uncertainties or the 10% order of magnitude.

The optimal parameter set is obtained by minimizing a χ^2 function, defined as

$$\chi^2 = \frac{1}{N_{\text{data}} - N_{\text{par}}} \sum_{i=1}^{N_{\text{data}}} \left(\frac{X_i^{(\text{data})} - X_i^{(\text{calc})}}{\sigma_i} \right)^2 , \tag{A.1}$$

where N_{data} is the number of experimental data points, N_{par} is the number of free parameters, $X_i^{(\text{data})}$ represents an experimental excitation energy or B(E2) value, $X_i^{(\text{calc})}$ is the corresponding calculated quantity, and σ_i is the assigned theoretical uncertainty. Moreover, the normalization factor ensures that the χ^2 value can be meaningfully compared

between fits involving different numbers of data points or parameters.

Finally, this minimization of the χ^2 function is performed using the MINUIT package, which iteratively explores the parameter, taking into account parameter correlations and imposed constraints, until a minimum is reached. For doing this we also included the IBM-CM Hamiltonian,

```
    1     'Ed         '  526.15000000      0.001
2     'K          '  0.00000000000     0.001
3     'PP         '  0.00000000000     0.001
4     'LL         '  18.58500000       0.001
5     'QQ         '  0.00000000000     0.001
6     'T3T3       '  0.0000000000      0.001
7     'T4T4       '  0.0000000000      0.001
8     'kappa      '  -28.18800000      0.001
9     'chi        '  1.87720000        0.001
10    'Unused     ' -0.0000E+3         0.001
11    'Ed-int     '  279.09000000      0.001
12    'K-int      '  0.00000000000     0.001
13    'PP-int     '  0.00000000000     0.001
14    'LL-int     '  0.23361000        0.001
15    'QQ-int     '  0.00000000000     0.001
16    'T3T3-int   '  0.0000000000      0.001
17    'T4T4-int   '  0.0000000000      0.001
18    'kappa-int  '  -34.96300000      0.001
19    'chi-int    '  -0.72311000       0.001
20    'Unused     ' -0.0000E+3         0.001
21    'alpha      '  15.00000000       0.001
22    'beta       '  15.00000000       0.001
23    'delta      '  680.00000000      0.001
24    'BE2:e      '  0.782530000       0.001
25    'BE2:e-int  '  2.217500000       0.001
```

where in order to improve numerical stability, several parameters are fixed during the fit. For the remaining parameters, lower and upper bounds are imposed based on physical considerations. In our example,

```
fix 2 3 5 6 7 10 12 13 15 16 17 20 21 22 23
set limit 1 0 2000
set limits 9 -2 2
set limits 8 -30 0
```

```
set limits 11 0 1000
minimize
call 3
```

The fitting procedure is inherently iterative. This means that an initial minimization is first performed to obtain a rough description of some data, and then the agreement with individual energies and transition rates is inspected. If certain observables are poorly reproduced, their assigned uncertainties can be temporarily reduced to guide the minimization towards the desired region of parameter space. Once a satisfactory agreement is reached, the original uncertainties are restored and a final minimization is performed.

Appendix B

Differentiation method to calculate expectation values in the intrinsic state formalism

In this thesis, expressions for the expectation values of the IBM-CM and IBFM-CM Hamiltonians in the coherent state have been extensively used. In this appendix, we summarize the differentiation method proposed in [169], that we have applied to our particular cases to obtain such expectation values.

In first place, let $b_i^\dagger$ (b_i) be some generic creation (annihilation) operators, together with a polynomial function of such operators that we call $f(b)$. For them, it can be proven that:

$$[b_i, f(b)] = \frac{\partial}{\partial b_i^\dagger} f(b), \tag{B.1}$$

Together with:

$$\left[f(b), b_i^\dagger\right] = \frac{\partial}{\partial b_i} f(b). \tag{B.2}$$

Now, we introduce the operator B as a linear combination of different possible kinds of bosons,

$$B = \sum_i \alpha_i b_i. \tag{B.3}$$

Moreover, we introduce the identity, 1, as well as the one-body and two-body opera-

tors,

$$\begin{aligned} A_1 &= \sum_{ij} \xi_{ij} b_i^\dagger b_j \\ A_2 &= \sum_{ijkl} \eta_{ijkl} b_i^\dagger b_j^\dagger b_k b_l. \end{aligned} \tag{B.4}$$

That according to the property that we have defined in (B.1) and (B.2) let us write:

$$N_n \equiv \left\langle B^n \right| 1 \left| B^{\dagger n} \right\rangle = \left\langle B^{n-1} \right| \sum_i \alpha_i \frac{\partial}{\partial b_i^\dagger} \left| B^{\dagger n} \right\rangle = n\alpha^2 \left\langle B^{n-1} \mid B^{\dagger n-1} \right\rangle, \tag{B.5}$$

which means that $N_n = n!\alpha^{2n}$ and $\alpha^2 = \sum_i \alpha_i^2$.

Finally, for the one-body and two body operator we find:

$$\begin{aligned} \langle A_1 \rangle \equiv N_n^{-1} \left\langle B^n \right| A_1 \left| B^{\dagger n} \right\rangle &= N_n^{-1} \sum_{ij} \xi_{ij} \left\langle \frac{\partial}{\partial b_i} B^n \middle| \frac{\partial}{\partial b_j^\dagger} B^{\dagger n} \right\rangle \\ = N_n^{-1} \sum_{ij} n^2 \alpha_i \alpha_j \xi_{ij} N_{n-1} &= \frac{n}{\alpha^2} \sum_{ij} \alpha_i \alpha_j \xi_{ij}, \end{aligned} \tag{B.6}$$

and

$$< A_2 >= \frac{n(n-1)}{\alpha^4} \sum_{ijk\ell} \alpha_i \alpha_j \alpha_k \alpha_\ell \eta_{ijkl}. \tag{B.7}$$

Resulting in a method that can be easily applied to our case, as our Hamiltonians are made of linear combinations of boson creation and annihilation operators.

Appendix C

Angular-Momentum Algebra Tools Used in this Thesis

For the development of this thesis, it has been very necessary the use of algebraical tools such as the Clesbsch-Gordan coefficients, together with Wigner-3j, -6j and -9j symbols [170]. In this appendix we summarize the most recurrent properties used in this thesis.

Clebsch-Gordan Coefficients:

They are defined as:

$$\psi\left(j_1 j_2 JM\right) = \sum_{m_1 m_2} \left(j_1 m_1 j_2 m_2 \mid j_1 j_2 JM\right) \psi\left(j_1 m_2\right) \psi\left(j_2 m_2\right). \tag{C.1}$$

Where their value is 0 unless $j_1 + j_2 \geq J \geq |j_1 - j_2|$ and $M = m_1 + m_2$, being also specially important its symmetry property:

$$\left(j_1 m_1 j_2 m_2 \mid j_1 j_2 JM\right) = (-1)^{j_1 + j_2 - J} \left(j_2 m_2 j_1 m_1 \mid j_2 j_1 JM\right) \tag{C.2}$$

Wigner-3j symbols

They are defined in terms of the Clebsch Gordan coefficients as:

$$\begin{pmatrix} j_1 & j_2 & j_3 \\ m_1 & m_2 & m_3 \end{pmatrix} = \frac{(-1)^{j_1 - j_2 - m_3}}{\sqrt{2j_3 + 1}} \left(j_1 m_1 j_2 m_2 \mid j_1 j_2 j_3 - m_3\right), \tag{C.3}$$

presenting also the following symmetry properties:

$$\begin{pmatrix} j_1 & j_2 & j_3 \\ m_1 & m_2 & m_3 \end{pmatrix} = \begin{pmatrix} j_2 & j_3 & j_1 \\ m_2 & m_3 & m_1 \end{pmatrix} = \begin{pmatrix} j_3 & j_1 & j_2 \\ m_3 & m_1 & m_2 \end{pmatrix} = (-1)^{j_1+j_2+j_3} \begin{pmatrix} j_1 & j_3 & j_2 \\ m_1 & m_3 & m_2 \end{pmatrix}$$
$$\begin{pmatrix} j_1 & j_2 & j_3 \\ -m_1 & -m_2 & -m_3 \end{pmatrix} = (-1)^{j_1+j_2+j_3} \begin{pmatrix} j_1 & j_2 & j_3 \\ m_1 & m_2 & m_3 \end{pmatrix} \tag{C.4}$$

Wigner-9j symbols

They are defined in terms of the Wigner-3j symbols in the following manner:

$$\begin{Bmatrix} j_{11} & j_{12} & j_{13} \\ j_{21} & j_{22} & j_{23} \\ j_{31} & j_{32} & j_{33} \end{Bmatrix} = \sum_{m_{ij}} \begin{pmatrix} j_{11} & j_{12} & j_{13} \\ m_{11} & m_{12} & m_{13} \end{pmatrix} \begin{pmatrix} j_{21} & j_{22} & j_{23} \\ m_{21} & m_{22} & m_{23} \end{pmatrix} \begin{pmatrix} j_{31} & j_{32} & j_{33} \\ m_{31} & m_{32} & m_{33} \end{pmatrix}$$
$$\begin{pmatrix} j_{11} & j_{21} & j_{31} \\ m_{11} & m_{21} & m_{31} \end{pmatrix} \begin{pmatrix} j_{12} & j_{22} & j_{32} \\ m_{12} & m_{22} & m_{32} \end{pmatrix} \begin{pmatrix} j_{13} & j_{23} & j_{33} \\ m_{13} & m_{23} & m_{33} \end{pmatrix}, \tag{C.5}$$

With 0 value in the following case:

$$\begin{Bmatrix} l_1 & l_2 & l_3 \\ l_1 & l_2 & l_3 \\ j_1 & j_2 & j_3 \end{Bmatrix} = 0 \quad \text{if} \quad 2\,(l_1 + l_2 + l_3) + j_1 + j_2 + j_3 \quad \text{is odd} \tag{C.6}$$

Racah coefficients

That are defined as:

$$\begin{Bmatrix} j_1 & j_2 & J \\ j_2' & j_1' & k \end{Bmatrix} \equiv (-1)^{j_2+J+j_1'+k} \sqrt{(2J+1)(2k+1)} \begin{Bmatrix} j_1 & j_2 & J \\ j_1' & j_2' & J \\ k & k & 0 \end{Bmatrix}, \tag{C.7}$$

following these symmetry properties:

$$\begin{Bmatrix} j_1 & j_2 & j_3 \\ l_1 & l_2 & l_3 \end{Bmatrix} = \begin{Bmatrix} j_2 & j_3 & j_1 \\ l_2 & l_3 & l_1 \end{Bmatrix} = \begin{Bmatrix} j_3 & j_1 & j_3 \\ l_3 & l_1 & l_2 \end{Bmatrix} = \begin{Bmatrix} j_2 & j_1 & j_3 \\ l_2 & l_1 & l_3 \end{Bmatrix} = \begin{Bmatrix} l_1 & l_2 & j_3 \\ j_1 & j_2 & l_3 \end{Bmatrix} \tag{C.8}$$

Change of coupling

It has also been useful to known that the transformation for a change of coupling is:

$$\psi\left(j_1 j_3\left(J_{13}\right) j_2 j_4\left(J_{24}\right) J\right)=\sum_{J_{12},J_{34}}\left\langle J_{13}J_{24};J\mid J_{12}J_{34};J\right\rangle \psi\left(j_1 j_2\left(J_{12}\right) j_3 j_4\left(J_{34}\right) J\right), \quad \text{(C.9)}$$

where:

$$\left\langle J_{13}J_{24};J\mid J_{12}J_{34};J\right\rangle =\sqrt{\left(2J_{13}+1\right)\left(2J_{24}+1\right)\left(2J_{12}+1\right)\left(2J_{34}+1\right)}\left\{\begin{array}{ccc} j_1 & j_2 & J_{12} \\ j_3 & j_4 & J_{34} \\ J_{13} & J_{24} & J \end{array}\right\}. \quad \text{(C.10)}$$

Finally, we stress that these expressions are the most employed, however, more relevant relations can be found in [170].

Bibliography

[1] Aage Bohr. On the quantization of angular momenta in heavy nuclei. *Physical Review*, 81(1):134, 1951.

[2] Aage Bohr. *The coupling of nuclear surface oscillations to the motion of individual nucleons*. Munksgaard, 1952.

[3] Aage Niels Bohr and Benjamin Roy Mottelson. Collective and individual-particle aspects of nuclear structure. *Dan. Mat. Fys. Medd.*, 27(CERN-57-38):1–174, 1953.

[4] James Rainwater. Nuclear energy level argument for a spheroidal nuclear model. *Physical Review*, 79(3):432, 1950.

[5] Maria G Mayer. On closed shells in nuclei. *Physical Review*, 74(3):235, 1948.

[6] Maria Goeppert Mayer. Nuclear configurations in the spin-orbit coupling model. ii. theoretical considerations. *Physical Review*, 78(1):22, 1950.

[7] Otto Haxel, J Hans D Jensen, and Hans E Suess. On the" magic numbers" in nuclear structure. *Physical Review*, 75(11):1766, 1949.

[8] Peter Ring and Peter Schuck. *The nuclear many-body problem*. Springer Science & Business Media, 2004.

[9] A Bohr, BR Mottelson, Gregory Breit, and Gerald E Brown. Nuclear structure, vol. 2: nuclear deformations, 1977.

[10] Maria Goeppert Mayer. The shell model. *Science*, 145(3636):999–1006, 1964.

[11] F. Iachello and A. Arima. *The interacting boson model*. Cambridge University Press, Cambridge, 1987.

[12] Herman Feshbach and Francesco Iachello. The interacting boson model. *Annals of Physics*, 84(1-2):211–231, 1974.

[13] H Feshbach and F Iachello. The interacting boson model structure of 16O. *Physics Letters B*, 45(1):7–11, 1973.

[14] A Arima and F Iachello. Collective nuclear states as representations of a su (6) group. *Physical Review Letters*, 35(16):1069, 1975.

[15] A Arima, T Otsuka, F Iachello, and Igal Talmi. Collective nuclear states as symmetric couplings of proton and neutron excitations. *Physics Letters B*, 66(3):205–208, 1977.

[16] T Otsuka, A Arima, F Iachello, and Igal Talmi. Shell model description of interacting bosons. *Physics Letters B*, 76(2):139–143, 1978.

[17] JP Elliot and JA Evans. An intrinsic spin for interacting bosons. *Physics Letters B*, 101(4):216–218, 1981.

[18] JP Elliot and AP White. An isospin invariant form of the interacting boson model. *Physics Letters B*, 97(2):169–172, 1980.

[19] F Iachello and O Scholten. Interacting boson-fermion model of collective states in odd-a nuclei. *Physical Review Letters*, 43(10):679, 1979.

[20] F. Dickmann and K. Dietrich. Coexistence and mixing of spherical and deformed states in the region of light hg-isotopes. *Zeitschrift für Physik*, 271(4):417 – 426, 1974.

[21] D. Kolb and C.Y. Wong. Shape isomerism in mercury isotopes. *Nuclear Physics A*, 245(2):205–220, 1975.

[22] S Frauendorf, FR May, and VV Pashkevich. Future directions in studies of nuclei far from stability, 1980.

[23] H. Morinaga. Interpretation of Some of the Excited States of $4n$ Self-Conjugate Nuclei. *Phys. Rev.*, 101:254–258, Jan 1956.

[24] G.E. Brown. *in Comptes Rendus du Congres International de Physique Nucléaire de Paris (Editions du Centre National de la Recherche Scientifique, Paris)*, 1:129, 1964.

[25] G.E. Brown and A.M. Green. Even parity states of ^{16}O and ^{17}O. *Nuclear Physics*, 75(2):401–417, 1966.

[26] G.E. Brown and A.M. Green. Nuclear coexistence in the oxygen region and realistic nucleon-nucleon forces. *Nuclear Physics*, 85(1):87–96, 1966.

[27] E. Caurier, J. Menéndez, F. Nowacki, and A. Poves. Coexistence of spherical states with deformed and superdeformed bands in doubly magic ^{40}Ca: A shell-model challenge. *Phys. Rev. C*, 75:054317, May 2007.

[28] A Poves. Shape coexistence: the shell model view. *Journal of Physics G: Nuclear and Particle Physics*, 43(2):024010, jan 2016.

[29] Alfredo Poves. Shape Coexistence and Islands of Inversion Monopole vs Multipole. *JPS Conf. Proc.*, 23:012015, 2018.

[30] Kris Heyde and John L. Wood. Shape coexistence in atomic nuclei. *Rev. Mod. Phys.*, 83:1467–1521, Nov 2011.

[31] Philip D. Duval and Bruce R. Barrett. Configuration mixing in the interacting boson model. *Phys. Lett. B*, 100(3):223 – 227, 1981.

[32] Paul E. Garrett, Magda Zielińska, and Emmanuel Clément. An experimental view on shape coexistence in nuclei. *Progress in Particle and Nuclear Physics*, 124:103931, 2022.

[33] John A. Hertz. Quantum critical phenomena. *Phys. Rev. B*, 14:1165–1184, Aug 1976.

[34] Pavel Cejnar, Jan Jolie, and Richard F. Casten. Quantum phase transitions in the shapes of atomic nuclei. *Rev. Mod. Phys.*, 82:2155–2212, Aug 2010.

[35] N. Gavrielov, A. Leviatan, and F. Iachello. Intertwined quantum phase transitions in the Zr isotopes. *Phys. Rev. C*, 99:064324, Jun 2019.

[36] E. Maya-Barbecho and J. E. García-Ramos. Shape coexistence in Sr isotopes. *Phys. Rev. C*, 105:034341, Mar 2022.

[37] E. Maya-Barbecho, S. Baid, J. M. Arias, and J. E. García-Ramos. At the borderline of shape coexistence: Mo and Ru. *Phys. Rev. C*, 108:034316, Sep 2023.

[38] Pavel Cejnar and Jan Jolie. Quantum phase transitions in the interacting boson model. *Progress in Particle and Nuclear Physics*, 62(1):210 – 256, 2009.

[39] V. Hellemans, P. Van Isacker, S. De Baerdemacker, and K. Heyde. Criticality in the configuration-mixed interacting boson model: (1) U(5)–$Q(\chi) \cdot Q(\chi)$ mixing. *Nucl. Phys. A*, 789(1):164 – 181, 2007.

[40] V. Hellemans, P. Van Isacker, S. De Baerdemacker, and K. Heyde. Criticality in the configuration-mixed interacting boson model: (2) $Q(\chi_1) \cdot Q(\chi_1) - Q(\chi_2) \cdot Q(\chi_2)$ mixing. *Nuclear Physics A*, 819(1):11 – 26, 2009.

[41] A. Frank, P. Van Isacker, and F. Iachello. Phase transitions in configuration mixed models. *Phys. Rev. C*, 73:061302, Jun 2006.

[42] R. Gilmore. *Catastrophe theory for scientists and engineers*. Wiley, New York, 1981.

[43] F. Iachello, A. Leviatan, and D. Petrellis. Effect of a fermion on quantum phase transitions in bosonic systems. *Phys. Lett. B*, 705(4):379–382, 2011.

[44] D. Petrellis, A. Leviatan, and F. Iachello. Quantum phase transitions in bose–fermi systems. *Ann. Phys.*, 326(4):926–957, 2011.

[45] JP Elliott and AM Lane. The nuclear shell-model. In *Structure of Atomic Nuclei/Bau der Atomkerne*, pages 241–410. Springer, 1957.

[46] Niels Bohr. Neutron capture and nuclear constitution. *Uspekhi Fizicheskikh Nauk*, 16(4):425–435, 1936.

[47] Frederick Seitz. Li schiff, quantum mechanics. 1950.

[48] Roger D Woods and David S Saxon. Diffuse surface optical model for nucleon-nuclei scattering. *Physical Review*, 95(2):577, 1954.

[49] David Lawrence Hill and John Archibald Wheeler. Nuclear constitution and the interpretation of fission phenomena. *Physical Review*, 89(5):1102, 1953.

[50] Sven Gösta Nilsson. Binding states of individual nucleons in strongly deformed nuclei. *Dan. Mat. Fys. Medd.*, 29(CERN-55-30):1–69, 1955.

[51] John Bardeen, Leon N Cooper, and J Robert Schrieffer. Microscopic theory of superconductivity. *Physical Review*, 106(1):162, 1957.

[52] A Frank, S Pittel, DD Warner, and J Engel. The pseudo-l scheme in strongly deformed bose-fermi systems and its relation to the nilsson model. *Physics Letters B*, 182(3-4):233–238, 1986.

[53] A Arima, A Gelberg, and Olaf Scholten. Coriolis coupling in the interacting boson fermion model. *Physics Letters B*, 185(3-4):259–264, 1987.

[54] I. Talmi. *Simple models of complex nuclei*. Harwood Academic Pubishers (Chur, Switzeriand), 1993.

[55] P Van Isacker, A Frank, and J Dukelsky. Phase ambiguities in the o (6) limit of the interacting boson model. *Physical Review C*, 31(2):671, 1985.

[56] D. D. Warner and R. F. Casten. Predictions of the interacting boson approximation in a consistent Q framework. *Phys. Rev. C*, 28:1798–1806, Oct 1983.

[57] A Arima and F Iachello. Interacting boson model of collective states i. the vibrational limit. *Annals of Physics*, 99(2):253–317, 1976.

[58] A Arima and F Iachello. Interacting boson model of collective nuclear states ii. the rotational limit. *Annals of Physics*, 111(1):201–238, 1978.

[59] JP Elliot. Collective motion of the nuclear shell model i, ii. *Proc. Roy. Soc*, 245(128):562, 1958.

[60] JD Vergados. Su (3) r (3) wigner coefficients in the 2s-1d shell. *Nuclear Physics A*, 111(3):681–754, 1968.

[61] A Arima and F Iachello. Interacting boson model of collective nuclear states iv. the o (6) limit. *Annals of Physics*, 123(2):468–492, 1979.

[62] Aage Bohr and Ben R Mottelson. Features of nuclear deformations produced by the alignment of individual particles or pairs. *Physica Scripta*, 22(5):468, 1980.

[63] J.N. Ginocchio and M.W. Kirson. An intrinsic state for the interacting boson model and its relationship to the Bohr-Mottelson model. *Nucl. Phys. A*, 350(1):31 – 60, 1980.

[64] A. E. L. Dieperink, O. Scholten, and F. Iachello. Classical Limit of the Interacting-Boson Model. *Phys. Rev. Lett.*, 44:1747–1750, Jun 1980.

[65] Philip D. Duval and Bruce R. Barrett. Quantitative description of configuration mixing in the interacting boson model. *Nucl. Phys. A*, 376(2):213 – 228, 1982.

[66] N. Gavrielov. Configuration mixing and intertwined quantum phase transitions in odd-mass niobium isotopes. *Phys. Rev. C*, 108:014320, Jul 2023.

[67] N. Gavrielov, A. Leviatan, and F. Iachello. Mixed configurations and intertwined quantum phase transitions in odd-mass nuclei. *Phys. Rev. C*, 106:L051304, Nov 2022.

[68] A. Frank, O. Castaños, P. Van Isacker, and E. Padilla. The Geometry of the IBM with Configuration Mixing. *AIP Conf. Proc.*, 638(1):23, 2002.

[69] Alejandro Frank, Piet Van Isacker, and Carlos E. Vargas. Evolving shape coexistence in the lead isotopes: The geometry of configuration mixing in nuclei. *Phys. Rev. C*, 69:034323, Mar 2004.

[70] A. Leviatan. A geometric interpretation for the interacting-boson-fermion model. *Phys. Lett. B*, 209(4):415–419, 1988.

[71] C.E. Alonso, J.M. Arias, F. Iachello, and A. Vitturi. Intrinsic frame description of interacting boson-fermion systems. *Nucl. Phys. A*, 539(1):59–74, 1992.

[72] A.E.L. Dieperink and O. Scholten. On shapes and shape phase transitions in the interacting boson model. *Nucl. Phys. A*, 346(1):125 – 138, 1980.

[73] A Arima, M Harvey, and K Shimizu. Pseudo ls coupling and pseudo su3 coupling schemes. *Physics Letters B*, 30(8):517–522, 1969.

[74] Karl T Hecht and A Adler. Generalized seniority for favored j≠ 0 pairs in mixed configurations. *Nuclear Physics A*, 137(1):129–143, 1969.

[75] R Bijker and VKB Kota. Interacting boson-fermion model of collective states ii. boson-fermion symmetries connected with the u (5) limit. *Annals of Physics*, 156(1):110–141, 1984.

[76] BH Flowers. Studies in jj-coupling. i. classification of nuclear and atomic states. *Proceedings of the Royal Society of London. Series A. Mathematical and Physical Sciences*, 212(1109):248–263, 1952.

[77] Morton Hamermesh. *Group theory and its application to physical problems*. Courier Corporation, 2012.

[78] O Scholten. The computer program code odda. *University of Groningen*, 1979.

[79] O. Scholten. Single particle degrees of freedom in the interacting boson model. *Prog. Part. Nucl. Phys.*, 14:189–229, 1985.

[80] T Otsuka and A Arima. A new seniority scheme for non-degenerate single particle orbits. *Physics Letters B*, 77(1):1–5, 1978.

[81] Esperanza Maya-Barbecho and José-Enrique García-Ramos. An intrinsic-state formalism for the Interacting Boson-Fermion Model with configuration mixing. *Physics Letters B*, 868:139724, 2025.

[82] P. Federman and S. Pittel. Towards a unified microscopic description of nuclear deformation. *Phys. Lett. B*, 69(4):385 – 388, 1977.

[83] P. Federman, S. Pittel, and R. Campos. Microscopic study of the shape transition in the zirconium isotopes. *Phys. Lett. B*, 82(1):9 – 12, 1979.

[84] P. Federman and S. Pittel. Unified shell-model description of nuclear deformation. *Phys. Rev. C*, 20:820–829, Aug 1979.

[85] K. Heyde, P. Van Isacker, M. Waroquier, J.L. Wood, and R.A. Meyer. Coexistence in odd-mass nuclei. *Physics Reports*, 102(5):291 – 393, 1983.

[86] J.L. Wood, K. Heyde, W. Nazarewicz, M Huyse, and P. van Duppen. Coexistence in even-mass nuclei. *Physics Reports*, 215(3):101 – 201, 1992.

[87] B. A. Marsh, T. Day Goodacre, S. Sels, Y. Tsunoda, B. Andel, A. N. Andreyev, N. A. Althubiti, D. Atanasov, A. E. Barzakh, J. Billowes, K. Blaum, T. E. Cocolios, J. G. Cubiss, J. Dobaczewski, G. J. Farooq-Smith, D. V. Fedorov, V. N. Fedosseev, K. T. Flanagan, L. P. Gaffney, L. Ghys, M. Huyse, S. Kreim, D. Lunney, K. M. Lynch, V. Manea, Y. Martinez Palenzuela, P. L. Molkanov, T. Otsuka,

A. Pastore, M. Rosenbusch, R. E. Rossel, S. Rothe, L. Schweikhard, M. D. Seliverstov, P. Spagnoletti, C. Van Beveren, P. Van Duppen, M. Veinhard, E. Verstraelen, A. Welker, K. Wendt, F. Wienholtz, R. N. Wolf, A. Zadvornaya, and K. Zuber. Characterization of the shape-staggering effect in mercury nuclei. *Nature Physics*, 14(12):1163–1167, Dec 2018.

[88] J. E. García-Ramos and K. Heyde. Quest of shape coexistence in Zr isotopes. *Phys. Rev. C*, 100:044315, Oct 2019.

[89] H. Mei, J. Xiang, J. M. Yao, Z. P. Li, and J. Meng. Rapid structural change in low-lying states of neutron-rich Sr and Zr isotopes. *Phys. Rev. C*, 85:034321, Mar 2012.

[90] J. Xiang, Z.P. Li, Z.X. Li, J.M. Yao, and J. Meng. Covariant description of shape evolution and shape coexistence in neutron-rich nuclei at N≈60. *Nuclear Physics A*, 873:1–16, 2012.

[91] K. Nomura, R. Rodríguez-Guzmán, and L. M. Robledo. Structural evolution in $A \approx 100$ nuclei within the mapped interacting boson model based on the Gogny energy density functional. *Phys. Rev. C*, 94:044314, Oct 2016.

[92] R. Rodríguez-Guzmán, P. Sarriguren, L.M. Robledo, and S. Perez-Martin. Charge radii and structural evolution in sr, zr, and mo isotopes. *Physics Letters B*, 691(4):202 – 207, 2010.

[93] H. Abusara, Shakeb Ahmad, and S. Othman. Triaxiality softness and shape coexistence in mo and ru isotopes. *Phys. Rev. C*, 95:054302, May 2017.

[94] Smriti Thakur, Pankaj Kumar, Virender Thakur, Vikesh Kumar, and Shashi K. Dhiman. Shape transitions and shell structure study in zirconium, molybdenum and ruthenium. *Nuclear Physics A*, 1014:122254, 2021.

[95] J. E. García-Ramos, J. M. Arias, J. Barea, and A. Frank. Phase transitions and critical points in the rare-earth region. *Phys. Rev. C*, 68:024307, Aug 2003.

[96] J. E. García-Ramos and K. Heyde. Subtle connection between shape coexistence and quantum phase transition: The Zr case. *Phys. Rev. C*, 102:054333, Nov 2020.

[97] Ridham Bakshi, Rajat Gupta, Surbhi Gupta, Amit Kumar, Suram Singh, Arun Bharti, G. H. Bhat, and J.A. Sheikh. Microscopic insights into the nuclear structure of 98-106ru nuclei. *European Physical Journal A*, 58:89, 2022.

[98] H. Jiang, B. Li, and Y. Lei. Low-lying states of ruthenium isotopes within the nucleon pair approximation. *Phys. Rev. C*, 93:054323, May 2016.

[99] A. Giannatiempo, A. Nannini, A. Perego, and P. Sona. Spectroscopy of ^{98}Ru. *Phys. Rev. C*, 94:054327, Nov 2016.

[100] A. Giannatiempo. Structure of ^{98}Ru in the iba-2 interacting boson model. *Phys. Rev. C*, 96:044326, Oct 2017.

[101] S. Kisyov, D. Bucurescu, J. Jolie, and S. Lalkovski. Algebraic approach to the structure of the low-lying states in $a \approx 100$ ru isotopes. *Phys. Rev. C*, 93:044308, Apr 2016.

[102] A. Giannatiempo. Gyromagnetic factors in the even ru and pd chains. *The European Physical Journal A*, 49(3):37, Mar 2013.

[103] M A Jafarizadeh, A Jalili Majarshin, N Fouladi, and M Ghapanvari. Investigation of quantum phase transitions in the spdf interacting boson model based on dual algebraic structures for the four-level pairing model. *Journal of Physics G: Nuclear and Particle Physics*, 43(9):095108, aug 2016.

[104] M Böyükata, P Van Isacker, and I Uluer. Description of nuclei in the $a \approx 100$ mass region with the interacting boson model. *J. Phys. G*, 37(10):105102, jul 2010.

[105] G. Lévai and J.M. Arias. Extended analytical solutions of the bohr hamiltonian with the sextic oscillator. *Journal of Physics G: Nuclear and Particle Physics*, 48(8):085102, jul 2021.

[106] A. Frank, C. E. Alonso, and J. M. Arias. Search for e(5) symmetry in nuclei: The ru isotopes. *Phys. Rev. C*, 65:014301, Nov 2001.

[107] Esperanza Maya-Barbecho and José-Enrique García-Ramos. Sr isotopes: the interplay between shape coexistence and quantum phase transitions. In *EPJ Web of Conferences*, volume 290, page 02022. EDP Sciences, 2023.

[108] Esperanza Maya-Barbecho, Samira Baid, José-Manuel Arias, and José-Enrique García-Ramos. At the edge of shape coexistence in the z= 40 region. In *EPJ Web of Conferences*, volume 329, page 02011. EDP Sciences, 2025.

[109] A. Bohr and B. R. Mottelson. *Nuclear Structure, Vol. II.* W. A. Benjamin, Reading MA, 1975.

[110] N. Gavrielov, A. Leviatan, and F. Iachello. Zr isotopes as a region of intertwined quantum phase transitions. *Phys. Rev. C*, 105:014305, Jan 2022.

[111] Coral M. Baglin. Nuclear Data Sheets for A = 92. *Nuclear Data Sheets*, 113(10):2187 – 2389, 2012.

[112] D. Abriola and A.A. Sonzogni. Nuclear Data Sheets for A = 94. *Nuclear Data Sheets*, 107(9):2423 – 2578, 2006.

[113] A. Negret and A. A. Sonzogni. Nuclear Data Sheets for ^{94}Sr. http://www.nndc.bnl.gov/ensdf, 2011.

[114] D. Abriola and A.A. Sonzogni. Nuclear Data Sheets for A = 96. *Nuclear Data Sheets*, 109(11):2501 – 2655, 2008.

[115] Balraj Singh and Zhiqiang Hu. Nuclear Data Sheets for A = 98. *Nuclear Data Sheets*, 98(2):335 – 513, 2003.

[116] Jun Chen and Balraj Singh. Nuclear Data Sheets for A=98. *Nuclear Data Sheets*, 164:1–477, 2020.

[117] Balraj Singh. Nuclear Data Sheets for A = 100. *Nuclear Data Sheets*, 109(2):297 – 516, 2008.

[118] D. DeFrenne. Nuclear Data Sheets for A = 102. *Nuclear Data Sheets*, 110(8):1745 – 1915, 2009.

[119] T. Rzaca-Urban, K. Sieja, W. Urban, F. Nowacki, J. L. Durell, A. G. Smith, and I. Ahmad. $(h_{11/2}, g_{7/2})_{9^-}$ neutron excitation in ^{92,94,96}Sr. *Phys. Rev. C*, 79:024319, Feb 2009.

[120] J. Park, A. B. Garnsworthy, R. Kruecken, C. Andreoiu, G. C. Ball, P. C. Bender, A. Chester, A. Close, P. Finlay, P. E. Garrett, J. Glister, G. Hackman, B. Hadinia, K. G. Leach, E. T. Rand, S. Sjue, K. Starosta, C. E. Svensson, and E. Tardiff. Shape coexistence and evolution in ^{98}Sr. *Phys. Rev. C*, 93:014315, Jan 2016.

[121] E. Clément, M. Zielińska, A. Görgen, W. Korten, S. Péru, J. Libert, H. Goutte, S. Hilaire, B. Bastin, C. Bauer, A. Blazhev, N. Bree, B. Bruyneel, P. A. Butler, J. Butterworth, P. Delahaye, A. Dijon, D. T. Doherty, A. Ekström, C. Fitzpatrick, C. Fransen, G. Georgiev, R. Gernhäuser, H. Hess, J. Iwanicki, D. G. Jenkins, A. C. Larsen, J. Ljungvall, R. Lutter, P. Marley, K. Moschner, P. J. Napiorkowski, J. Pakarinen, A. Petts, P. Reiter, T. Renstrøm, M. Seidlitz, B. Siebeck, S. Siem, C. Sotty, J. Srebrny, I. Stefanescu, G. M. Tveten, J. Van de Walle, M. Vermeulen, D. Voulot, N. Warr, F. Wenander, A. Wiens, H. De Witte, and K. Wrzosek-Lipska. Spectroscopic Quadrupole Moments in ^{96,98}Sr: Evidence for Shape Coexistence in Neutron-Rich Strontium Isotopes at $N = 60$. *Phys. Rev. Lett.*, 116:022701, Jan 2016.

[122] E Clément and M Zielińska. Shape coexistence in neutron-rich strontium isotopes at N = 60. *Physica Scripta*, 92(8):084002, jul 2017.

[123] J.-M. Régis, J. Jolie, N. Saed-Samii, N. Warr, M. Pfeiffer, A. Blanc, M. Jentschel, U. Köster, P. Mutti, T. Soldner, G. S. Simpson, F. Drouet, A. Vancraeyenest, G. de France, E. Clément, O. Stezowski, C. A. Ur, W. Urban, P. H. Regan, Zs. Podolyák, C. Larijani, C. Townsley, R. Carroll, E. Wilson, L. M. Fraile, H. Mach, V. Paziy, B. Olaizola, V. Vedia, A. M. Bruce, O. J. Roberts, J. F. Smith, M. Scheck, T. Kröll, A.-L. Hartig, A. Ignatov, S. Ilieva, S. Lalkovski, W. Korten, N. Mărginean, T. Otsuka, N. Shimizu, T. Togashi, and Y. Tsunoda. Abrupt shape transition at neutron number $N = 60$: $B(E2)$ values in ^{94,96,98}Sr from fast $\gamma - \gamma$ timing. *Phys. Rev. C*, 95:054319, May 2017.

[124] S. Cruz, P.C. Bender, R. Kruecken, K. Wimmer, F. Ames, C. Andreoiu, R.A.E. Austin, C.S. Bancroft, R. Braid, T. Bruhn, W.N. Catford, A. Cheeseman, A. Chester, D.S. Cross, C.Aa. Diget, T. Drake, A.B. Garnsworthy, G. Hackman, R. Kanungo, A. Knapton, W. Korten, K. Kuhn, J. Lassen, R. Laxdal, M. Marchetto, A. Matta, D. Miller, M. Moukaddam, N.A. Orr, N. Sachmpazidi, A. Sanetullaev, C.E. Svensson, N. Terpstra, C. Unsworth, and P.J. Voss. Shape coexistence and mixing of low-lying 0+ states in ^{96}Sr. *Physics Letters B*, 786:94–99, 2018.

[125] A. Esmaylzadeh, J.-M. Régis, Y. H. Kim, U. Köster, J. Jolie, V. Karayonchev, L. Knafla, K. Nomura, L. M. Robledo, and R. Rodríguez-Guzmán. Lifetime measurements and shape coexistence in ^{97}Sr. *Phys. Rev. C*, 100:064309, Dec 2019.

[126] W. Urban, T. Rzaca-Urban, J. Wiśniewski, I. Ahmad, A. G. Smith, and G. S. Simpson. Structure of 0^+ excitations in the mass $A \approx 100$ region: 0_2^+ bands in ^{98}Sr and ^{100}Zr. *Phys. Rev. C*, 99:064325, Jun 2019.

[127] Jean Blachot. Nuclear Data Sheets for A = 104. *Nuclear Data Sheets*, 108(10):2035 – 2172, 2007.

[128] D. De Frenne and A. Negret. Nuclear data sheets for a = 106. *Nuclear Data Sheets*, 109(4):943–1102, 2008.

[129] Jean Blachot. Evaluated Nuclear Structure Data File for A= 108. http://www.nndc.bnl.gov/ensdf, 2008.

[130] S. Lalkovski and F.G. Kondev. Nuclear Data Sheets for A = 112. *Nuclear Data Sheets*, 124:157–412, 2015.

[131] Jean Blachot. Nuclear Data Sheets for A = 114. *Nuclear Data Sheets*, 113(2):515–714, 2012.

[132] T. Thomas, V. Werner, J. Jolie, K. Nomura, T. Ahn, N. Cooper, H. Duckwitz, A. Fitzler, C. Fransen, A. Gade, M. Hinton, G. Ilie, K. Jessen, A. Linnemann,

P. Petkov, N. Pietralla, and D. Radeck. Nuclear structure of 96,98mo: Shape coexistence and mixed-symmetry states. *Nucl. Phys. A*, 947:203–233, 2016.

[133] M. Zielińska, T. Czosnyka, J. Choiński, J. Iwanicki, P. Napiorkowski, J. Srebrny, Y. Toh, M. Oshima, A. Osa, Y. Utsuno, Y. Hatsukawa, J. Katakura, M. Koizumi, M. Matsuda, T. Shizuma, M. Sugawara, T. Morikawa, H. Kusakari, A.D. Efimov, and V.M. Mikhajlov. Electromagnetic structure of 98mo. *Nucl. Phys. A*, 712(1):3–13, 2002.

[134] K. Wrzosek-Lipska, L. Próchniak, M. Zielińska, J. Srebrny, Hadynska-Klek K., J. Iwanicki, Kisielinski M., M. Kowalczyk, P. J. Napiorkowski, D. Pietak, and T. Czosnyka. Electromagnetic properties of ^{100}Mo: Experimental results and theoretical description of quadrupole degrees of freedom. *Phys. Rev. C*, 86:064305, Dec 2012.

[135] J. Ha, T. Sumikama, F. Browne, N. Hinohara, A. M. Bruce, S. Choi, I. Nishizuka, S. Nishimura, P. Doornenbal, G. Lorusso, P.-A. Söderström, H. Watanabe, R. Daido, Z. Patel, S. Rice, L. Sinclair, J. Wu, Z. Y. Xu, A. Yagi, H. Baba, N. Chiga, R. Carroll, F. Didierjean, Y. Fang, N. Fukuda, G. Gey, E. Ideguchi, N. Inabe, T. Isobe, D. Kameda, I. Kojouharov, N. Kurz, T. Kubo, S. Lalkovski, Z. Li, R. Lozeva, H. Nishibata, A. Odahara, Zs. Podolyák, P. H. Regan, O. J. Roberts, H. Sakurai, H. Schaffner, G. S. Simpson, H. Suzuki, H. Takeda, M. Tanaka, J. Taprogge, V. Werner, and O. Wieland. Shape evolution of neutron-rich ^{106,108,110}Mo isotopes in the triaxial degree of freedom. *Phys. Rev. C*, 101:044311, Apr 2020.

[136] S. J. Freeman, D. K. Sharp, S. A. McAllister, B. P. Kay, C. M. Deibel, T. Faestermann, R. Hertenberger, A. J. Mitchell, J. P. Schiffer, S. V. Szwec, J. S. Thomas, and H.-F. Wirth. Experimental study of the rearrangements of valence protons and neutrons amongst single-particle orbits during double-β decay in ^{100}Mo. *Phys. Rev. C*, 96:054325, Nov 2017.

[137] P.E. Garrett, L. Makhathini, R.A. Bark, T.R. Rodríguez, S. Valbuena, V. Bildstein, T.D. Bucher, C. Burbadge, R. Dubey, T. Faestermann, R. Hertenberger, M. Kamil, E.A. Lawrie, K.G. Leach, A.D. MacLean, C. Mehl, S.H. Mthembu, N.J. Mukwevho, C. Ngwetsheni, S.S. Ntshangase, J.C. Nzobadila Ondze, J.N. Orce, B. Rebeiro, B. Singh, S. Triambak, E.C. Vyfers, and H.-F. Wirth. Observation of the 0_2^+ and γ bands in ^{98}ru, and shape coexistence in the ru isotopes. *Physics Letters B*, 809:135762, 2020.

[138] D. Radeck, V. Werner, G. Ilie, N. Cooper, V. Anagnostatou, T. Ahn, L. Bettermann, R. J. Casperson, R. Chevrier, A. Heinz, J. Jolie, D. McCarthy, M. K. Smith, and E. Williams. Simultaneous deorientation and lifetime measurement in ^{98}ru using

the recoil distance doppler shift method in inverse coulomb excitation. *Phys. Rev. C*, 85:014301, Jan 2012.

[139] W. Urban, M. Jentschel, R. F. Casten, J. Jolie, Ch. Bernards, B. Maerkisch, Th. Materna, P. Mutti, L. Próchniak, T. Rzaca-Urban, G. S. Simpson, V. Werner, and S. Ahmed. 0_2^+ band in ^{102}Ru and the evolution of nuclear deformation in ru isotopes. *Phys. Rev. C*, 87:031304, Mar 2013.

[140] J. Srebrny and T. Czosnyka and Ch. Droste and S.G. Rohoziński and L. Próchniak and K. Zajac and K. Pomorski and D. Cline and C.Y. Wu and A. Bäcklin and L. Hasselgren and R.M. Diamond and D. Habs and H.J. Körner and F.S. Stephens and C. Baktash and R.P. Kostecki. Experimental and theoretical investigations of quadrupole collective degrees of freedom in ^{104}Ru. *Nucl. Phys. A*, 766:25 – 51, 2006.

[141] M. J. Taylor, G. Gürdal, G. Kumbartzki, N. Benczer-Koller, A. E. Stuchbery, Y. Y. Sharon, M. A. Bentley, Z. Berant, R. J. Casperson, R. F. Casten, A. Heinz, G. Ilie, R. Lüttke, E. A. McCutchan, J. Qian, B. Shoraka, V. Werner, E. Williams, and R. Winkler. Low-energy structure of the even-a $^{96-104}$Ru isotopes via g-factor measurements. *Phys. Rev. C*, 83:044315, Apr 2011.

[142] P. E. Garrett, M. Zielińska, A. Bergmaier, T. R. Rodríguez, D. Kalaydjieva, M. Siciliano, H. Bidaman, V. Bildstein, C. Burbadge, A. Diaz Varela, D. T. Doherty, T. Faestermann, K. Hadyńska-Klęk, R. Hertenberger, N. Keeley, A. Laffoley, A. D. MacLean, M. Mahgoub, A. J. Radich, M. Rocchini, P. Spagnoletti, S. Triambak, M. Vandebrouck, and K. Wrzosek-Lipska. Coulomb excitation of ^{102}Ru with ^{12}C and ^{16}O. *Phys. Rev. C*, 106:064307, Dec 2022.

[143] J.E. García-Ramos and K. Heyde. The Pt isotopes: Comparing the Interacting Boson Model with configuration mixing and the extended consistent-Q formalism. *Nucl. Phys. A*, 825(1):39 – 70, 2009.

[144] J. E. García-Ramos and K. Heyde. Nuclear shape coexistence: A study of the even-even Hg isotopes using the interacting boson model with configuration mixing. *Phys. Rev. C*, 89:014306, Jan 2014.

[145] J. E. García-Ramos and K. Heyde. Nuclear shape coexistence in Po isotopes: An interacting boson model study. *Phys. Rev. C*, 92:034309, Sep 2015.

[146] V. Hellemans, R. Fossion, S. De Baerdemacker, and K. Heyde. Configuration mixing in ^{188}Pb: Band structure and electromagnetic properties. *Phys. Rev. C*, 71:034308, Mar 2005.

[147] V. Hellemans, S. De Baerdemacker, and K. Heyde. Configuration mixing in the neutron-deficient $^{186-196}$Pb isotopes. *Phys. Rev. C*, 77:064324, Jun 2008.

[148] S. Zerguine, P. Van Isacker, and A. Bouldjedri. Consistent description of nuclear charge radii and electric monopole transitions. *Phys. Rev. C*, 85:034331, Mar 2012.

[149] I. Angeli and K.P. Marinova. Table of experimental nuclear ground state charge radii: An update. *Atomic Data and Nuclear Data Tables*, 99(1):69 – 95, 2013.

[150] J. E. García-Ramos, V. Hellemans, and K. Heyde. Platinum nuclei: Concealed configuration mixing and shape coexistence. *Phys. Rev. C*, 84:014331, Jul 2011.

[151] R. Fossion, C. De Coster, J.E. García-Ramos, T. Werner, and K. Heyde. Nuclear binding energies: Global collective structure and local shell-model correlations. *Nucl. Phys. A*, 697(3):703 – 747, 2002.

[152] S. Sachdev. *Quantum Phase Transitions*. Cambridge University Press, Cambridge, UK, 2011.

[153] R. Gilmore. *Lie groups, Lie algebras and some applications*. Wiley, 1974.

[154] Irving O. Morales, Alejandro Frank, Carlos E. Vargas, and P. Van Isacker. Shape coexistence and phase transitions in the platinum isotopes. *Phys. Rev. C*, 78:024303, Aug 2008.

[155] J. E. García-Ramos, K. Heyde, L. M. Robledo, and R. Rodríguez-Guzmán. Shape evolution and shape coexistence in Pt isotopes: Comparing interacting boson model configuration mixing and Gogny mean-field energy surfaces. *Phys. Rev. C*, 89:034313, Mar 2014.

[156] Krishna Kumar. Intrinsic Quadrupole Moments and Shapes of Nuclear Ground States and Excited States. *Phys. Rev. Lett.*, 28:249–253, Jan 1972.

[157] Douglas Cline. Nuclear shapes studied by coulomb excitation. *Ann. Rev. Nucl. Part. Sci.*, 36:683–716, 1986.

[158] Y. Alhassid, C. N. Gilbreth, and G. F. Bertsch. Nuclear Deformation at Finite Temperature. *Phys. Rev. Lett.*, 113:262503, Dec 2014.

[159] C. N. Gilbreth, Y. Alhassid, and G. F. Bertsch. Nuclear deformation in the laboratory frame. *Phys. Rev. C*, 97:014315, Jan 2018.

[160] M. T. Mustonen, C. N. Gilbreth, Y. Alhassid, and G. F. Bertsch. Statistical theory of deformation distributions in nuclear spectra. *Phys. Rev. C*, 98:034317, Sep 2018.

[161] A. Poves, F. Nowacki, and Y. Alhassid. Limits on assigning a shape to a nucleus. *Phys. Rev. C*, 101:054307, May 2020.

[162] E. Clément, A. Görgen, W. Korten, E. Bouchez, A. Chatillon, J.-P. Delaroche, M. Girod, H. Goutte, A. Hürstel, Y. Le Coz, A. Obertelli, S. Péru, Ch. Theisen,

J. N. Wilson, M. Zielińska, C. Andreoiu, F. Becker, P. A. Butler, J. M. Casandjian, W. N. Catford, T. Czosnyka, G. de France, J. Gerl, R.-D. Herzberg, J. Iwanicki, D. G. Jenkins, G. D. Jones, P. J. Napiorkowski, G. Sletten, and C. N. Timis. Shape coexistence in neutron-deficient krypton isotopes. *Phys. Rev. C*, 75:054313, May 2007.

[163] Tomoaki Togashi, Yusuke Tsunoda, Takaharu Otsuka, and Noritaka Shimizu. Quantum Phase Transition in the Shape of Zr isotopes. *Phys. Rev. Lett.*, 117:172502, Oct 2016.

[164] E. Maya-Barbecho and J.E. García-Ramos. The enhancement of deformation in odd-even nuclei around A = 100. *EPJ Web Conf.*, 324:00027, 2025.

[165] M.K. Harder, K.T. Tang, and P. Van Isacker. An IBM description of coexistence in the platinum isotopes. *Phys. Lett. B*, 405(1):25 – 30, 1997.

[166] N. Gavrielov. Competing shape evolution, crossing configurations, and single particle levels in nuclei. *Phys. Rev. Res.*, 7:L022022, Apr 2025.

[167] E. Maya-Barbecho and J. E. García-Ramos. Nuclear shapes of Nb isotopes. *Physical Review C*. To be published.

[168] Minuit: Function Minimization and Error Analysis Reference Manual, Version 94.1, CERN. 1994.

[169] Jin-Quan Chen and Pieter Van Isacker. A general formula for the classical limit of the interacting boson hamiltonian. In *Interacting Bose-Fermi Systems in Nuclei*, pages 193–199. Springer, 1981.

[170] Amos De-Shalit and Igal Talmi. *Nuclear shell theory*, volume 14. Academic Press, 2013.